Optical Variability with the Palomar Transient Factory

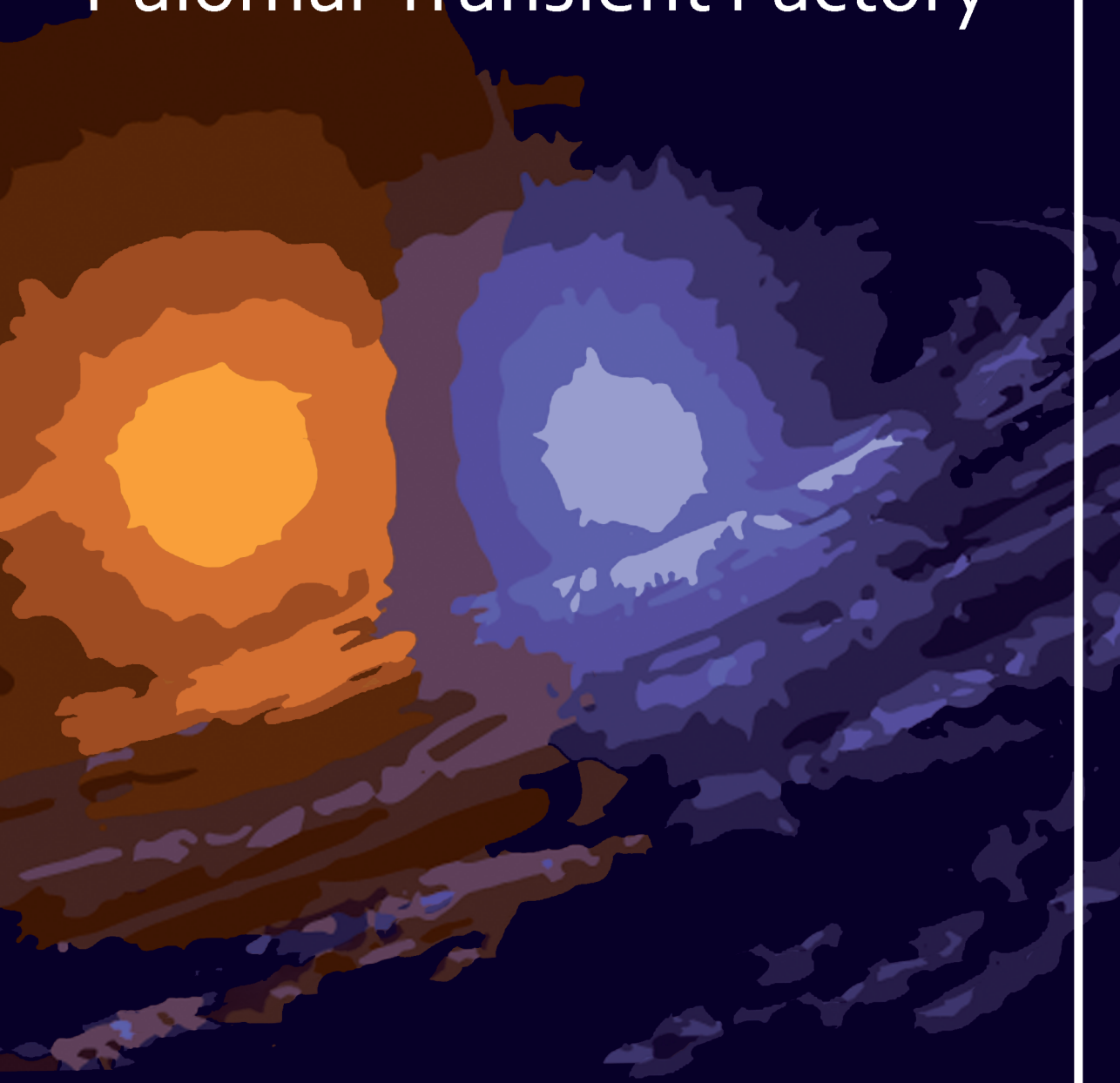

Jan van Roestel

Optical Variability with the Palomar Transient Factory

Proefschrift

ter verkrijging van de graad van doctor
aan de Radboud Universiteit Nijmegen
op gezag van de rector magnificus prof. dr. J.H.J.M. van Krieken,
volgens besluit van het college van decanen
in het openbaar te verdedigen op
dinsdag 27 november 2018
om 10.30 uur precies

door

Joannes Christiaan Josephus van Roestel

geboren op 2 april 1990
te Tilburg

Promotoren:	Prof. dr. Paul Groot	
	Prof. dr. Tom Prince	(California Institute of Technology, VS)
Manuscriptcommissie:	Prof. dr. Bas van de Meerakker	
	Prof. dr. Rudy Wijnands	(Universiteit van Amsterdam)
	Prof. dr. Frank Verbunt	
	Prof. dr. Peter Jonker	
	Dr. Raffaella Margutti	(Northwestern University, VS)

Optical Variability with the Palomar Transient Factory
Thesis, Radboud University Nijmegen
Illustrated; with bibliographic information and Dutch summary
Cover design: Femke Boezen
Front cover image: Binary stars
Image credit: Casey Reed/NASA

ISBN: 978-94-028-1279-4

Contents

Chapter 1

Introduction

1.1 The optical variable sky

Even though it may seem so to the naked eye and on human time scales, stars are not eternal and static but vary on all time scales and energy scales. Variability is either intrinsic to the source, in which case the energy output varies as a function of time, or extrinsic, in which case the environment is the cause of changes in the observed luminosity. This means that by studying the variability in the luminosity of objects, we can learn more about the physics that is involved in the generation or transport of energy (typically gravitational energy or nuclear energy) and/or learn more about the immediate environment of the objects.

The nuclear fusion processes in the cores of stars change over the course of time as the reservoir of hydrogen gets depleted, leading to *secular* variability. If the hydrostatic equilibrium that keeps stars in balance is disturbed the structure of a star changes, sometimes on *cataclysmic* ways, on timescales of seconds, as in a supernova explosion at the end of the lives of stars with masses exceeding eight times that of the Sun (8 Solar Masses, $8\,M_\odot$). In the outer layers of stars, the intricate interplay between radiation and plasma can cause large-scale instabilities leading to stellar *pulsations*, and the interaction with magnetic fields can lead to *eruptive* events. Solar flares are an extremely low-energy and mild example of these magnetic reconnection events. In lower mass stars the luminosity of the star can be increased by >500 times over the course of an hour, thereby posing a real obstacle for the habitability of planets around these stars. As many stars are part of a binary system, interactions between the two components can lead to a different type of *eruptive* variability, induced by accretion, the mass overflow from one star to another.

Next to these *intrinsic* changes, *extrinsic* variability can be induced, in particular in binary systems when the orbital plane of the binary is favourably oriented towards our line of sight and the two stars are eclipsing each other in their orbit. The regularity of the eclipses is a very powerful tool, when coupled with the laws of physics, to determine masses, radii and surface brightnesses of stars.

The optical wavelength regime (300-1000 nm) is still central to the study of most celestial objects. It is the regime where we have the largest body of knowledge on the Universe, and it is the regime where most of the atomic transitions are located, allowing us to use the tools of

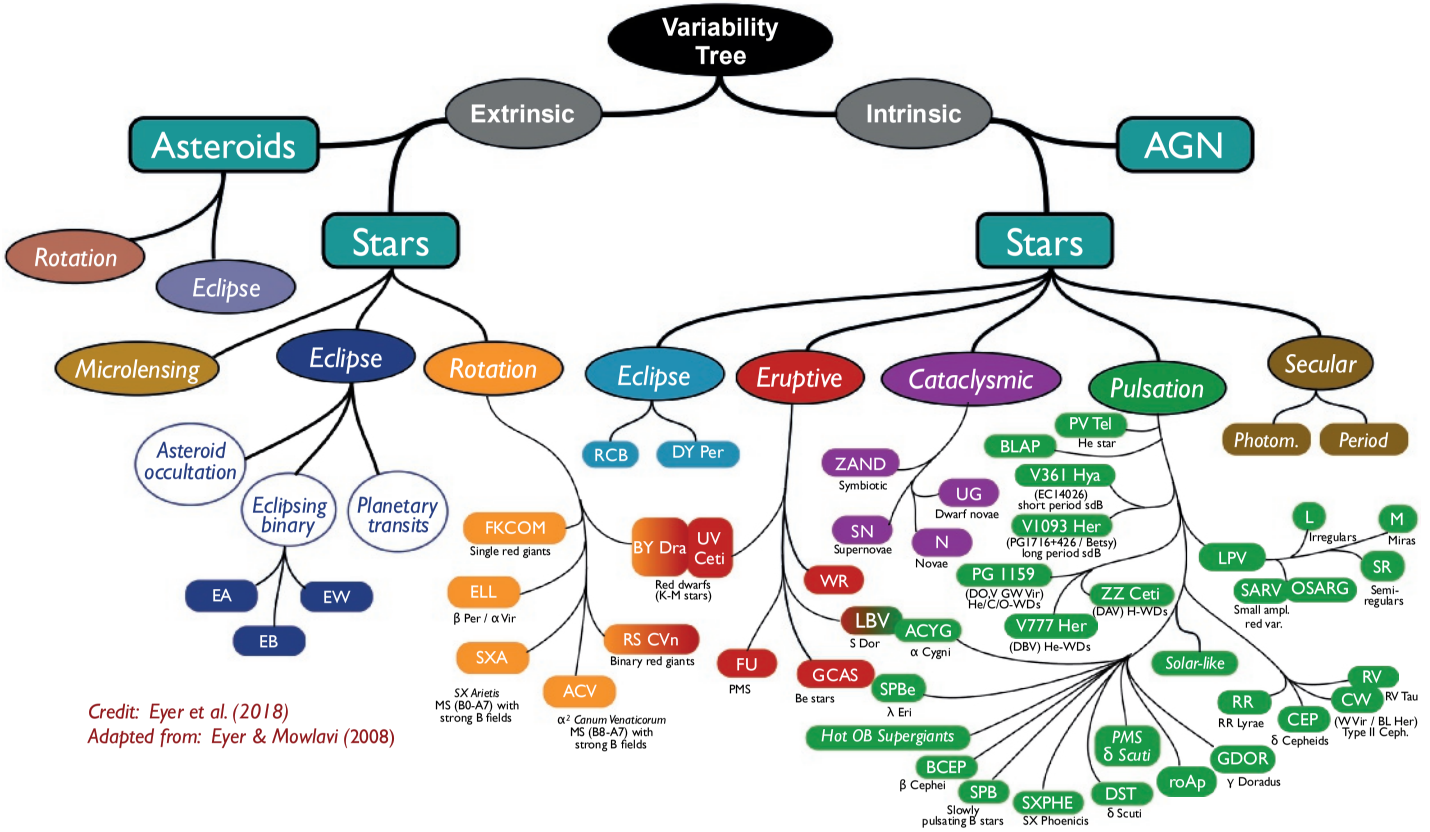

Figure 1.1: An overview of different kinds of variability that can be observed in the night sky (Gaia Collaboration et al., 2018b)

spectroscopy to gain insight into the physical conditions in the Universe.

Figure 1.1 (Gaia Collaboration et al., 2018b) shows an overview of all the different kinds of variability that we can observe in the optical sky.

1.2 Stellar evolution; the life and death of stars

To understand the variable optical sky, we need to understand the physics of stars and their environments. Stars are formed when a gas cloud collapses. At the core of the condensing ball of gas, the temperature and pressure will reach conditions under which hydrogen can be fused to helium. This is the moment a 'star is born'. Hydrogen-fusing stars are called 'main-sequence stars', after their location in a plot of luminosity versus surface temperature; the Hertzsprung-Russell diagram (Hertzsprung, 1911; Russell, 1914).

The mass of main-sequence stars ranges from $\approx 0.08\,\mathrm{M}_\odot$ (the hydrogen burning limit; Kumar, 1962) to $\approx 100\mathrm{M}_\odot$, with the birth mass function $N(M) \propto M^{-2.35}$ (Salpeter, 1955). At the lower end of this mass range the temperature and pressure in the core never get above the fusion ignition conditions. At the upper end of the mass range, radiation pressure causes strong instabilities in the star, leading to an intense mass loss. The subsequent disappearance of gravitational pressure on the core causes the fusion processes to be (slightly) quenched, which may lead to a new equilibrium. A clear example is the very massive star η Carinae, which lost more than 10 $\mathrm{M}_\odot$ of gas in an 'eruption' around 1837 (Herschel, 1847). Stars spend most of their lifetime in the main-sequence phase; $\tau_{MS} \approx 10^{10} \left(\frac{M}{M_\odot}\right)^{-2.5}$ yr. What happens to the star after its main-sequence phase, when the hydrogen in the core has been converted to helium, depends on its initial mass.

When hydrogen in the core has been converted to helium, the inert helium core shrinks and the outer layers expand; a red giant. In a thin shell around the core, hydrogen is fused to helium, which increases the mass of the helium core. Once the core reaches a mass of $\approx 0.48\,\mathrm{M}_\odot$ (Sweigart & Gross, 1978), the temperature and pressure in the core become high enough for helium fusion to commence, which causes the envelope to shrink again. Once all helium in the core is converted to carbon and oxygen (CO[1]), the envelope expands again. But for stars with a mass of $< 8\mathrm{M}_\odot$, the pressure and temperature in the core will never be high enough to start carbon fusion. The envelope of the star is slowly lost (the planetary nebula phase) and what remains is the inert CO-core of the star; a white dwarf. A white dwarf does not produce any energy, and degenerate electron pressure instead of gas pressure prevents further collapse.

For the few stars more massive than $8\,\mathrm{M}_\odot$ ($\sim$0.1 per cent) the pressure and temperature in the core are high enough to fuse carbon and oxygen into heavier elements. This process continues until the core is made of nickel and iron. Fusing iron and nickel does not produce any energy as the nuclear binding energy per atom is maximal for these elements. A lack of any energy source to sustain the gas pressure against the gravitational pressure of the overlying gas layers means that the core collapses. The core is compressed to a ball of neutrons about 12 km in size, which is supported by degenerate neutron pressure. In the case of really massive stars ($>25\,\mathrm{M}_\odot$), even degenerate neutron pressure is not enough and the core becomes a black hole. The collapse of the

[1]Note that astronomers are not chemists and 'CO' therefore stands for a mix of atomic carbon and oxygen, and not for the molecule carbonmonoxide

dense core releases huge amounts of (gravitational) energy and momentum, which is transferred to the envelope. The infalling outer envelope 'bounces' on the neutron star core and is ejected, while energy is deposited in the envelope by a large neutrino flux and converted gravitational potential energy, which is generated during the neutron-core formation (Colgate & White, 1966).

1.3 Binary star evolution

So far, we have assumed that stars evolve in isolation. However, a large fraction of stars, 57 per cent of G-stars (Duquennoy & Mayor, 1991), and close to 100 per cent of massive stars (Sana et al., 2012) have a gravitationally bound companion (Lada, 2006). Binary star systems are two stars that are bound by gravity and orbit a common centre of mass. Their orbital distance (a) and period (P) are related to the total mass of the stars ($M_1 + M_2$) via Kepler's Third Law (equation 1.1; Kepler 1619, modified by Newton 1687).

$$\frac{a^3}{P^2} = \frac{G(M_1 + M_2)}{4\pi^2} \tag{1.1}$$

Typically, binary stars are born together and have the same age. The initial orbital period of binary stars ranges from just a few days to up to millions of years (Kroupa & Petr-Gotzens, 2011). If stars are in a wide orbit, their evolution will not be any different to that of a single star. However, binary stars in narrow orbits ($a \lesssim 1000\,\mathrm{R}_\odot$) will interact at some point during their evolution, changing the mass and orbital period, which results in a wealth of phenomena.

Both stars initially evolve as single stars. The more massive star evolves faster, and at some point becomes too large and starts to transfer mass to its companion. This can happen either as the donor is still a main-sequence star, when the donor is a giant, or when the donor is a more evolved AGB-giant star (case A, B, and C binary evolution, e.g. Paczyński, 1971). The different cases result in a different kind of remnant of the donor star.

Mass-transfer can be stable or unstable. In the case of stable mass transfer, the envelope of the donor is slowly transferred to the companion star. Because angular momentum is conserved, the mass flow often forms an accretion disk around the accretor. The mass transfer process continues until only the core of the donor star remains. Stable mass transfer (of case A) is involved in the formation of 'EL CVn' binaries (proto-WD–A stars), the topic of Chapter 5.

Mass-transfer is unstable if the accreted matter piles up on the accreting star. This causes the envelope of the accretor to expand and ends up engulfing both stars, a common-envelope (CE). Orbital angular momentum is transferred to the common envelope and the common envelope is ejected and as a result the orbital period of the components decreases. Common envelope evolution is important in the formation of short period white dwarf binaries as discussed in Chapter 4.

Besides the individual stars changing in size, the orbital separation of a binary can also change due to angular momentum loss. The above described common envelope ejection is one example of this. For very compact binary stars, angular momentum loss in the form of gravitational wave radiation is the most important. The binary coalescence timescale due to gravitational wave angular momentum loss is:

$$\tau = \frac{c^5}{G^3} \frac{5a^4}{256 M_1 M_2 (M_1 + M_2)} \tag{1.2}$$

As can be seen in the equation, this process depends strongly on the semi-major axis (a) and the masses, and is therefore most important in massive, compact binary systems: short period white dwarf, neutron star and black hole binaries. A prime example of this is the 'Hulse-Taylor' pulsar (Hulse & Taylor, 1975); a double neutron star binary for which the orbital decrease has been observed. In $\approx$ 300 million years, these two neutron stars will collide and merge together. Mergers of stellar objects are not limited to just neutron stars. Mergers between any type of star (main-sequence, white dwarf, neutron star, black hole) are possible as e.g. seen in the recent detections in gravitational waves of merging black holes

In many of the binary evolution processes (stable or unstable mass transfer and stellar mergers), gravitational or nuclear energy is released. We observe these events as transients. In addition, binary evolution can result in objects which do not occur in single star evolution. The final fate of these exotic stars can also result in unusual transients.

1.4 The transient zoo

Optical transients (*stellae novae*) have been observed since ancient times with notable events happening throughout history, e.g. a (possible) supernova in 185 (Fan et al., 445) and Kepler's supernova (e.g. Kepler, 1606). Baade & Zwicky (1934) started to systematically study optical transients. By plotting the absolute luminosity versus timescale (a 'Zwicky diagram'), they discovered that not all novae are alike.

Figure 1.2 shows the 'Zwicky diagram' with the currently known types of transients. Core-collapse supernovae have already been introduced as the end point of massive star evolution. However, many other types of transients are observed, and many are the result of interaction between binary stars.

1.4.1 Classical transients

Supernovae are cataclysmic explosions of stars. They have traditionally been divided into two groups; the 'Type Ia' supernovae and core-collapse supernova (Type II, Ib and Ic).

Type Ia supernovae are the result of a thermonuclear detonation of a CO white dwarf. Once nuclear fusion of carbon starts, a nuclear runaway reaction occurs. All carbon and oxygen (almost the entire star) is rapidly converted to Ni^{56} and energy. As the thermonuclear energy being released is higher than the binding energy of the white dwarf star, the star unbinds (explodes), ejecting all matter (including Ni^{56} and Fe) into space at high velocity ($v \approx 10.000$ km s^{-1}).

Observationally, Type Ia supernovae (SNIae) are intrinsically bright (compared to core-collapse supernovae). SNIae light curves have a typical rise and decay time of a few weeks and are all very similar in shape (Phillips, 1993). The shape of the lightcurve is consistent with being powered by radioactive decay of Ni^{56} (half-life decay time of $\tau_{\frac{1}{2}} = 6.1$ days) and its product Co^{56} ($\tau_{\frac{1}{2}} = 77.1$ days). Type Ia supernovae have proven to be 'standardise-able candles' and are therefore important in cosmology because they can be used to measure the expansion rate of the universe (Riess et al., 1998). Although they are very important tools, it is still not understood how the thermonuclear reactions in the white dwarfs are triggered, but all scenarios involve interactions with nearby stars. Either in a mass-accreting binary where mass is slowly accumulated onto the

white dwarf from a companion, or in a merger event of two white dwarfs, where mass is added to the more massive CO white dwarf in a rapid event (Webbink, 1984).

In contrast to Type Ia supernovae which are powered by nuclear energy, core-collapse supernovae are powered by gravitational energy released by the collapse of the core. This also ejects radioactive nuclei, among others Ni^{56}, which power the optical transient. The ejected material also contains all the material of the envelope of the star. This gives rise to a large variety of transients due to the varied structure and chemical composition of the outer layers of massive stars just before core collapse. For example, Types Ib and Ic do not show any hydrogen in the ejecta, while type II supernovae do.

Core-collapse supernova lightcurves therefore span a larger range of luminosities and timescales (Smartt, 2009). Lightcurves can stay at a steady brightness for some time (a 'plateau' phase, type IIP) or even re-brighten. In addition, they can show interactions with material which had been ejected by the star earlier.

At the faint end of the Zwicky diagram, we find transients that are commonly detected in our own Milky Way Galaxy (or nearby galaxies): the classical novae and dwarf novae outbursts. These both occur in binary systems where a white dwarf is accreting mass from another star in a stable fashion, *Cataclysmic Variables* (Warner, 2003). A (classical) *nova* occurs when enough mass has been accreted by the white dwarf to start hydrogen fusion in the surface layer of the white dwarf. This results in a runaway thermonuclear reaction that rapidly consumes the accreted material and ejects burnt and unburnt material in an expanding envelope at velocities of thousands of kilometers per second. Novae can increase the brightness of a system by more than a factor of 1000, and slowly decay to pre-explosion brightness on timescales of months to years.

Dwarf novae are fainter transients that also occur in Cataclysmic Variables, when an accretion disk surrounding a white dwarf in a mass-transferring binary becomes unstable (Warner, 1976). The suddenly increased mass-transfer rate through the disk, and mass accretion onto the white dwarf, causes a rapid (days timescale) brightening of the system by a factor of 10-100 in luminosity. The system will fade back to quiescence on time scale of days to weeks.

Stellar flares are similar to solar flares and are a result of magnetic reconnection. Reconnection of magnetic fields of the star accelerate particles which impact and rapidly heat the stellar photosphere (Pettersen, 1989). Flares occur on stars of different masses (especially magnetically active stars) but are most often observed to occur on low mass M-dwarfs because of the high contrast with the steady state luminosity. Stellar flares rise quickly (1–10 s) and disappear on timescales of 10 s to a few hours, with high energy flares lasting longer than low energy flares.

1.4.2 New transients

In the last few decades, new types of optical transients have been discovered. Some of these are because of a detection of a high energy counterpart (X-ray, gamma-rays), which are then observed at optical wavelengths. The other large driver of the new discoveries are automated telescopes with a large field of view. The advances in automated survey telescopes are mainly driven by cheap, large CCD chips and also the availability of computing resources to process all the data. These advances have driven the exploration of the transient sky, and the Zwicky diagram is slowly being populated with more rare and difficult to detect transients.

The fastest and brightest of the optical transients are *gamma-ray burst* (GRB) afterglows. GRBs are fast gamma-ray transients which are caused by relativistic jets, possibly launched when a neutron star collapses into a black hole. The optical afterglow is the result of shockwaves as the high energy particles in the jet collide with ejected, circumbinary and interstellar material (Piran, 1999). GRBs are divided into two classes, long and short bursts (with the division at $\tau \approx 2\,s$). Long bursts often occur in starforming galaxies and their light curves sometimes also show the signature of a core-collapse supernova. They are therefore associated with the death of massive stars and are also called *hypernovae* (e.g. Galama et al., 1998). Short bursts often occur in galaxies without any recent star formation and are therefore not directly related to the death of massive stars. They are thought to be the result of a binary neutron star merger, a link that is now confirmed by the coincident detection of a short GRB with the gravitational wave merger signal of two neutron stars in the event recorded on August 17, 2017 (GW170817, see further down in this section). In the optical, GRB-afterglows fade rapidly, on timescales of hours to days. Because they fade very fast they have almost exclusively been found after the gamma-ray burst was detected. The Palomar Transient Factory (PTF; Section 1.5.1) has now found a very small number of *orphan* afterglows where we see the optical signal but not the associated gamma-ray burst (Cenko et al., 2013, 2015).

A *tidal disruption event* (Rees, 1988) is a transient that is caused by the disruption of a star by a black hole. When a star gets too close to a black hole, it is ripped apart by tidal forces. During the accretion process of gas, it is heated and can be observed as an optical transient, but also at shorter wavelengths like UV, X-ray and gamma-rays. The optical discovery of TDEs began to take off about a decade ago (van Velzen et al., 2011; Gezari et al., 2012), and high energy TDE discoveries some years earlier. The transients typically show rise times of tens of days and long decay times of hundreds of days (Kochanek, 2016).

In recent years, additional subtypes of supernovae have been discovered. These include the *superluminous supernovae* (SLSNe), which are $\gtrsim 5$ times brighter than Type Ia supernovae and are defined to have to have an absolute luminosity $M > -21$ (Quimby et al., 2011; Gal-Yam, 2012). Superluminous supernovae show a diverse range of properties. Some are thought to be the result of the collapse of very massive stars (Type Ic SLSNe), while others are thought to be bright because of interactions with circumstellar material (Type IIn SLSNe). Others are expected to be/remain bright by the continued energy injection of a central object, e.g. newly born highly-magnetized neutron star (a magnetar). Superluminous supernovae are very bright by definition and evolve on longer timescales (∼months) than regular supernovae.

Recent searches have uncovered transients that are brighter than novae but fainter than supernovae ('gap transients'; Kasliwal, 2011). One type are the Calcium-rich transients which show strong calcium emission lines in their spectra and typically occur in the outskirts of their host galaxies. They are likely associated with white dwarfs, but the exact nature is unknown. They are slightly fainter ($M_{\rm R} \approx -16$) than supernovae and evolve faster, ∼10 days (Kasliwal et al., 2012). *Luminous red novae* are also fainter than supernovae and brighter than novae ($M_{\rm R} \approx -12$) and evolve on slightly longer timescales (∼100 d). A few transients of this class have been detected in the last few decades, but in 2002 a nearby example was observed, V838 Monocerotis (Soker & Tylenda, 2003). Observations showed a that the outer layers of the star were rapidly expanding, and reached a size of $1200\,{\rm R}_\odot$. The progenitor of the transients was a blue main-sequence star, but after the

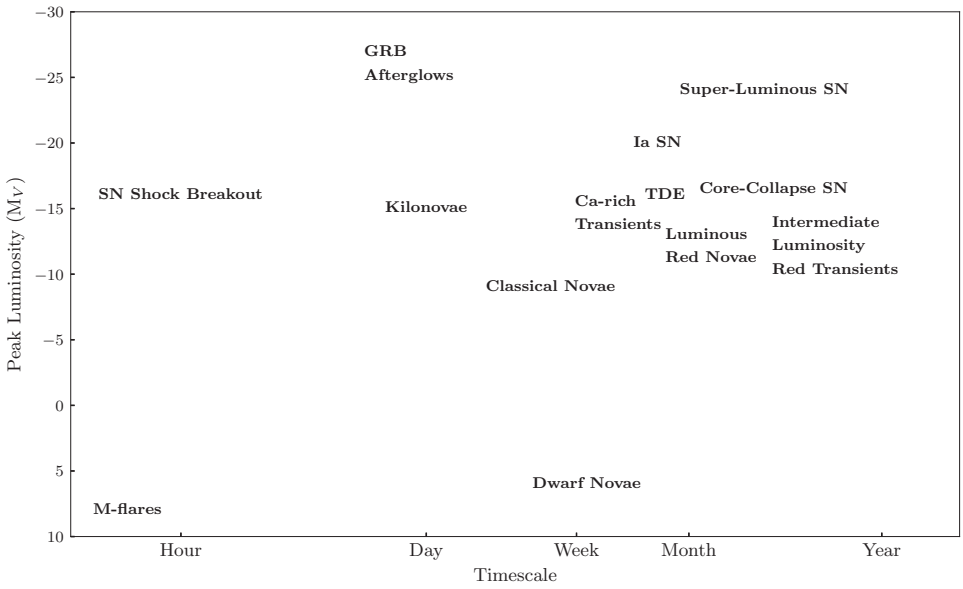

Figure 1.2: The transient phase space ('Zwicky diagram').

transient faded, a red giant was observed. In 2008, luminous red novae V1309 Scorpii was discovered (Tylenda et al., 2011). This transient had a contact-binary star as a progenitor. Therefore, at least some of the luminous red novae are the result of a merger of two stars. *Intermediate luminosity red transients* are similar to the luminous red novae in brightness, but evolve on a longer timescale. This type of transient is caused by accretion by AGB stars, e.g. NGC 300 OT (Bond et al., 2009). Kashi & Soker (2016) give an overview of all the different types of intermediate luminosity transients.

Most recently, in 2017, the aLIGO/aVirgo gravitational wave observatories (LIGO Scientific Collaboration et al., 2015; Acernese et al., 2015) detected gravitational waves of a binary neutron star (BNS) merger for the first time (Abbott et al., 2017). Rapid optical follow up of this event resulted in the discovery of the optical transient AT2017gfo (Abbott et al. 2017 and Abbott et al. 2017) The optical counterpart, called a kilonova, had been theorized to accompany a BNS merger by Li & Paczyński (1998); Kulkarni (2005). AT 2017gfo is consistent with the kilonova model predictions; fainter than a supernova and only visible for a short time (<a week). The rise time of AT2017gfo is less than a few hours and it faded within a few days while it rapidly became redder. Almost coincident with the gravitational wave detection was the detection of a short GRB, which supports the hypothesis that short GRBs are the result of binary neutron star mergers.

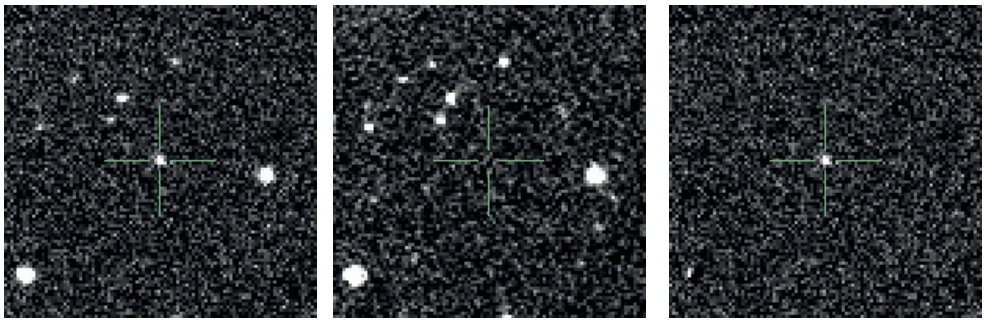

(a) New image (b) Old image (c) Difference image

Figure 1.3: An example PTF images which contains a transient (PTF14yb). The left panel shows the new image which contains a transient in the middle but also some stars. The middle panel shows an older image of before the transient appeared. The right panel shows the difference between the new and old image, in which only the transient remains.

1.5 Telescopes

1.5.1 The Palomar Transient Factory

In all Chapters of this thesis, I have used data obtained with the Palomar Transient Factory (PTF, Mar 2009 – 2012) and its successor, the intermediate PTF (iPTF[2], 2013-2017). PTF was a fully-automated, wide-field survey for a systematic exploration of the optical transient sky (Law et al., 2009a; Rau et al., 2009a). PTF used the Palomar Samuel Oschin 48-inch Schmidt Telescope ('P48') equipped with the 7.26-square degree CFHT12k mosaic camera. The nominal survey is in $R_{\rm mould}$ band, but additional observations are also made at g-band. The standard exposure time per frame is 60 seconds, yielding a 5-sigma limiting magnitude of $R_{\rm mould} \approx 20.5$ and $g \approx 21$. How often a field was observed and after how much time it was revisited (the cadence) varied greatly, since PTF was used to perform many different kinds of experiments.

The PTF used an automated image processing pipeline which performed bias and flatfield corrections and automatically finds and measures the position and brightness of all light sources (stars, galaxies, asteroids) in the image (Laher et al., 2014). To find transients, the images are further processed by an automated image differencing pipeline. This pipeline subtracts an old image from each new image to create a difference image, as shown in Fig. 1.3 (Laher et al., 2014). In principle, only transients should be visible on the difference images, but the process is not perfect and many false positive are also present on the difference images. The sources present on difference images are therefore analysed using a machine learning method to identify the real transients (Real-Bogus, Bloom et al. 2012, Cao et al. 2016, and also Smith et al. 2011). The best candidates are presented to human scanners which have to inspect the images by eye and determine the nature of the transient.

[2]in the rest of this chapter, PTF is used to refer to both PTF and iPTF

During a typical night, PTF could obtain 300 images. While in principle these could be 300 different fields, PTF almost always observed each field at least twice per night with some time in between (typically half an hour). The main motivation for this is to identify main belt asteroids, which move at a rate of a few arcseconds per hour and appear at a different position on the two images. In addition, two detections of a transient can be used to determine if a transient is rapidly rising or fading, and help to identify the type of transient. On a typical night, a few hundred candidate transients are interesting enough to be presented to humans scanners. The majority of these are variable stars or bad subtractions of stars. Another large group are the so-called 'nuclear' transients, transient-like signals which are located at the center of a galaxy. These are either bad subtractions or are the result of activity of the central blackhole of the galaxy (Active Galactic Nucleus, AGN). Out of the hundreds of candidates that are detected, only a few are real. These are supernovae of all types and also faint (beyond the detection limit) outbursting stars like dwarf novae. Using the light curve and archival data (SDSS, Abolfathi et al. 2018; Pan-STARRS, Chambers et al. 2016) the human scanner decides if the transient should be followed up with other telescopes.

1.5.2 Spectroscopic followup of PTF sources

After objects of interest have been identified with PTF they can be studied in more detail. The first step is often to obtain an optical spectrum of the source. A major part of the follow-up spectroscopy presented in this thesis has been obtained with the Isaac Newton Telescope (INT, Pagel, 1986), the William Herschel Telescope (WHT; Boksenberg, 1985) and the Hale Telescope (Hubble, 1949). The INT and WHT are located on La Palma, Spain and operated by the Isaac Newton Group of telescopes. The Hale telescope is situated at Palomar Mountain.

The INT telescope has a 2.5 m mirror and is mounted on an equatorial mount. It is equipped with the long-slit Intermediate Dispersion Spectrograph (IDS). IDS has a spectral resolution of $R \approx 500$ to ≈ 10000. Data from the INT was used in Chapters 3 and 5.

The WHT is a 4.2 m telescope and mounted on an alt-azimuth mount. The main spectrographs of the WHT are the Intermediate dispersion Spectrograph and Imaging System (ISIS) and the low-resolution spectrograph and camera ACAM (Benn et al., 2008). ISIS is a double beam spectrograph which can use a range of different setups. The advantage of ACAM is that it has a high efficiency and is therefore ideal for faint sources. It is mounted at a bent Cassegrain focus and always available to the observer. Data obtained with the WHT was used in Chapters 2 and 4.

The Hale telescope has a mirror of a diameter of a 5.1 m (200 inch) and uses a horse mount. The main spectrograph of the Hale telescope is the Double Spectrograph (Oke & Gunn, 1982) with a resolution between R=1000 to ∼10000. I have used data from the Hale telescope in Chapters 3 and 4.

1.6 Methods

1.6.1 Measuring binary star parameter

If the inclination angle (i) of a binary star is close to 90° and therefore the orbital plane is perpendicular with the plane of the sky and the stars, the stars move periodically in front of each

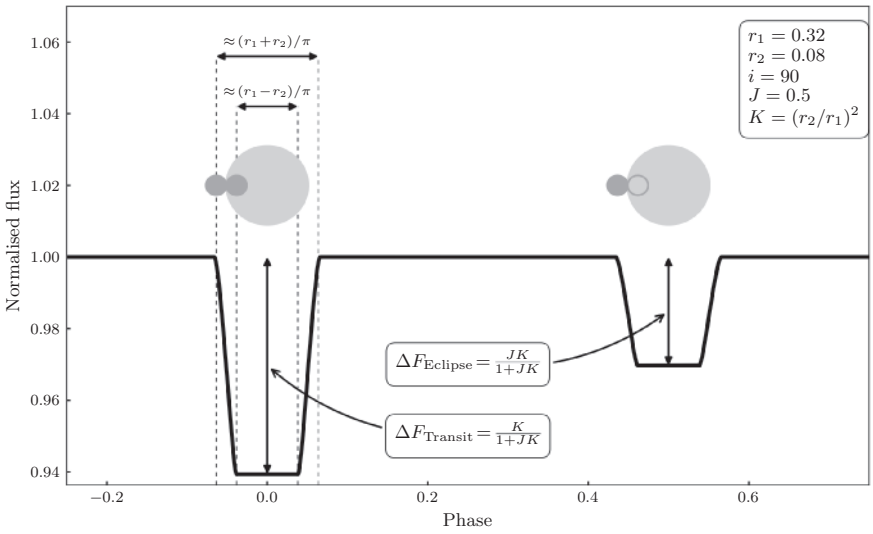

Figure 1.4: A simplified model of an eclipsing binary star. The large, light grey sphere represents star 1, the smaller, darker grey sphere is star 2. In this example, star 1 is four times larger than star 2, and the surface brightness of star 2 is half that of star 1 ($J = S_2/S_1 = 0.5$). How the light curve depends on these parameters is indicated in the figure. For simplicity, we have assumed that the inclination (i) is 90 degrees (edge-on) and gravity and radiation has been turned off in the model. The light curve has been generated using ellc (Maxted, 2016).

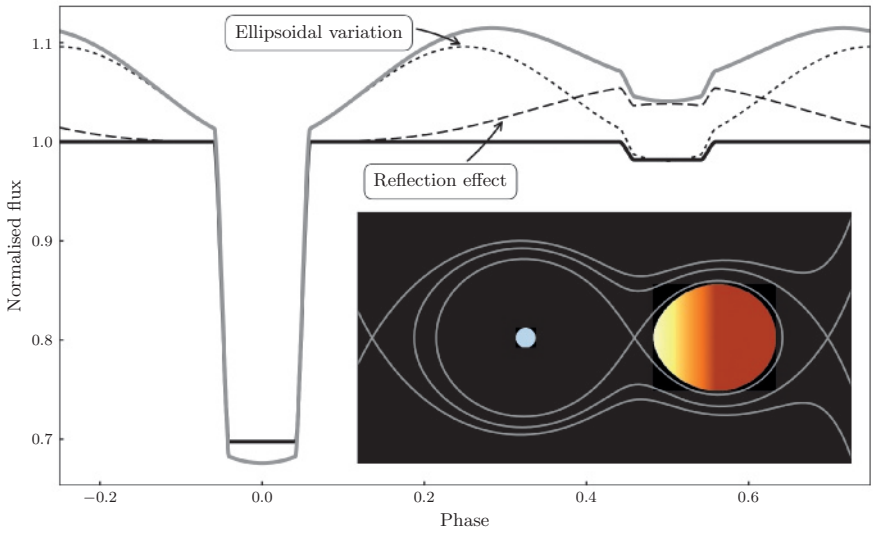

Figure 1.5: The light curves of an eclipsing binary. The black line shows the basic model, while the grey line shows a model for which heating and ellipsoidal included. The dashed and dotted lines show the basic model plus the individual contribution of reflection and ellipsoidal variation. The inset panel shows the binary in the x-z plane (i.e. viewed from above). The colours indicate the difference in temperature, with one side of star 2 being heated by star 1. The grey lines show equipotential lines in the Roche potential at critical potential levels.

other; an eclipsing binary. Light curves (a time sequence of brightness measurements) of eclipsing binary stars can be used to infer physical properties of the binary stars. The duration and depth of the eclipses in the light curve are a function of the radii and relative brightness of the stars. This means that from simple geometry alone, we can determine the stellar parameters of both stars without using any stellar structure models. For this reason, eclipsing binary stars are important in astrophysics.

A basic, simplified example of an eclipsing binary is shown in Fig. 1.4. The figure shows the light curve for two spherical stars in a circular orbit. The parameters which determine the shape of the light curve are: the scaled radii ($R_{1,2}/a \equiv r_{1,2}$): the stellar radii of the two stars divided by the orbital separation (a), the inclination of the orbital axis with respect to the observer (i) and the surface brightness ratio of the two stars ($J = S_2/S_1$). As is shown in the figure, the depth of the eclipse (the small star disappearing behind the large star) and transit (the small star moving in front of the large star) is determined by the ratio between the radii and surface brightnesses. For the edge-on case ($i = 90°$), the duration (in units of phase) of the eclipse and transit are determined by the sum and difference between the scaled radii ($r_{1,2}$). The duration is shorter as the inclination gets lower, as is shown in equation 1.3.

$$\Delta\phi = \pi^{-1} \arcsin \sqrt{\frac{(r_1 \pm r_2)^2 - \cos^2 i}{\sin^2 i}} \tag{1.3}$$

In the example above, we made a number of simplifications. First of all, if the radius of a star is large compared to the semi-major axis, its shape is distorted by the gravitational pull of the other star. The star becomes tear-drop shaped: elongated along the axis that intersects the centre of the two stars (x) and squashed in the other two directions (y and z). The shape of the star can be described by an equipotential surface in the Roche-potential (Roche, 1859):

$$\Omega = \frac{2}{1+q}\frac{1}{\sqrt{x^2+y^2+z^2}} + \frac{2q}{1+q}\frac{1}{\sqrt{(x-1)^2+y^2+z^2}} + \left(x - \frac{q}{1+q}\right)^2 + y^2 \tag{1.4}$$

with the mass ratio as $q \equiv \dfrac{M_2}{M_1}$. The result is that a different-sized surface area can be observed as function of phase. The surface area that can be seen from the side is larger than the area seen from the front or back. Fig. 1.5 shows a light curve in which the ellipsoidal variation can be seen. The inset in Fig. 1.5 shows the elongated shape of star 2.

If the temperature of the two stars is very different, the hot star will heat one side of the other star, called the 'reflection effect'. This is however a misnomer, and most light is absorbed and re-emitted instead of simply reflected. The reflection effect adds a sinusoidal modulation in the light curve, as can be seen in Fig. 1.5.

The total mass and semi-major axis of the binary both do not have any effect on the shape of the light curve, except for subtle relativistic effects (e.g. Bloemen et al., 2011). Since relativistic effects are rarely observable, additional observations are needed to measure the total mass and semi-major axis. As can be seen in equation 1.1, by measuring either the semi-major axis or the total mass, the other can be calculated assuming the orbital period is known.

The most common method to solve this problem is to obtain phase-resolved spectroscopy and measure the redshift of spectral features to determine the radial velocity amplitude of one or both

stars. The radial velocity of the stars is given by equation 1.5. The radial velocity depends on the period and inclination, but these can be measured by fitting the light curve. Therefore, with both K_1 and K_2 measured, both masses can be calculated.

$$K_{1,2}^3 = \frac{2\pi G}{P} \frac{M_{2,1}^2}{(M_1 + M_2)^3} \sin^3 i \tag{1.5}$$

It is not always possible to measure the radial velocity of both stars, if one star outshines the other for example. In such a case, other information can be used, for example the mass ratio (q). However, this is generally less accurate and requires more model assumptions. Another problem is the assumption that the measured radial velocity is the radial velocity of the centre of mass of the star. For example, spectra of strongly irradiated stars only show emission lines when the irradiated side of the star is visible. The Appendix of Chapter 4 describes this problem in more detail.

1.6.2 Fitting data

In this thesis, I have compared observational data to models by 'fitting' data; a statistical method more accurately called χ^2-regression of least-squares regression (Legendre, 1806; Gauss, 1809). The χ^2 function is:

$$\chi^2 = \sum_{i=1}^{N} \frac{(y_i - m_p(x_i))^2}{\sigma_i^2} \tag{1.6}$$

where y_i represents the measurements, σ_i the Gaussian uncertainty on the measurements, and $m_p(x_i)$ is the model with parameters (p) which is a function of the independent variable (x_i). Fitting a function involves finding the parameters for which χ^2 has the lowest value.

The choice to use χ^2 as the objective function seems a little ad-hoc. However, it can be shown that minimizing χ^2 is equivalent to maximizing the likelihood that the data has been generated by the model. The full derivation can be found in e.g. Hogg et al. (2010), with the final equation of the likelihood of the parameters

$$\ln P = -\frac{1}{2} \sum_{i=1}^{N} \ln(2\pi\sigma_i^2) - \sum_{i=1}^{N} \frac{(y_i - m_p(x_i))^2}{2\sigma_i^2} = C - \frac{1}{2}\chi^2 \tag{1.7}$$

were C is a constant value.

This mathematical derivation depends on a number of assumption. First, to arrive at this result, the uncertainties on the measurements are assumed to be normally distributed, a.k.a. 'Gaussian'. In addition, the data is assumed to be generated from the model and therefore can be explained in full by the model. Any residual difference between the data and model are due to the measurement uncertainty only.

Only if all these assumptions are satisfied, can the uncertainties on the model parameters be correctly estimated. Unfortunately, this is not always the case. In this thesis, a number of examples can be found were the measurement uncertainties could not explain the residual differences between the data and the model. In most cases, this additional uncertainty is due to calibration uncertainties which are not accounted for by the uncertainty estimates. To properly handle this, the model can be expanded to take into account this extra uncertainty by replacing σ_i^2 with $\sigma_i^2 + \sigma_{\text{extra}}^2$. By

treating σ_{extra} as an additional model parameter, we can estimate calibration uncertainties in a statistically correct way[3].

1.6.3 Machine learning and its applications in astronomy

With telescopes like PTF producing huge amounts of data, traditional data analysis techniques have become non-viable. Traditional approaches are often too labour intensive and cannot be scaled up to orders of magnitude more data. For example, it is impossible for a single person to inspect hundreds of images produced by PTF each night in search for transients. Traditional methods are often to narrow in scope and work only for one specific goal and cannot be (easily) adapted. For example, a method to identify eclipsing binary light curves cannot be used to find other types variables.

Machine learning techniques are algorithms which mimic the way humans find patterns in data. Instead of using a pre-programmed, rigid algorithm, the algorithm is adjusted based on the input data. Machine learning techniques are typically used for tasks which are difficult to program but that humans can do in seconds, and needs to be repeated on a large scale. Examples in astronomy include the classification of variables star light-curves, finding transients in images, and estimating a galaxy red-shift from colours only. In each of these cases, known examples are used to 'teach' a computer to perform a task and is called supervised machine learning[4].

Supervised machine learning can be understood more mathematically as techniques to construct a function (f) which takes input (x) and produces output (y). If y is categorical ($a, b, c, ...$), f is called a classifier, if y is continuous ($1, 2, 3, ...$), f is called a regressor. A machine learning model is 'trained' on a training sample; a function f is estimated using known input (x_{train}) and known output (y_{train}). Once the function f has been learned using training data, it can be applied to other data (x) to get an output (y). The critical difference between classical techniques is that function f is not programmed by a human (using e.g. physical knowledge) but estimated from the data itself.

Many different machine learning algorithms exist. In Chapter 5 of this thesis, I have used 'decision tree' classifiers. These use a sequence of 'if' statements to construct a classifier. However, a single decision tree is not a very flexible classifier. The latest version of decision tree classifiers combines a series of decision trees. Random Forest (Breiman, 2001) combines a large number (a few hundred to thousands) of decision trees which have been constructed by using random subsets of the training data. Random Forest classifiers are one of the best performing classifiers but are also easy to understand and do not require much fine tuning to get working. Machine learning is a very active field, and new methods are constantly being developed. Currently, artificial neural networks (LeCun et al., 2015) are increasingly being used to analyse astronomical images and other types of data.

[3] assuming that the calibration uncertainties are uncorrelated and follow a Gaussian distribution.

[4] as opposed to unsupervised machine learning methods, which do not require any examples, but are more limited in what they can do.

1.7 This thesis

In this thesis, I have used the Palomar Transient Factory to study the variable sky. The first part of the thesis focusses on transients, specifically on the question of what the rate of fast transients is. Chapter 2 presents the Sky2Night-I survey. A survey with PTF, combined with spectroscopic follow-up, in search for fast optical transients. Chapter 3 presents the Sky2Night-II project, which is similar in setup to the first Sky2Night project but aimed at the Galactic plane in search of fast transients.

The second part of the thesis focusses on a more detailed study of eclipsing binary stars. The main aim is to use binary stars to understand the binary evolution processes involved in their formation and evolution. Chapter 4 presents the discovery and analysis of a short period white dwarf binary. The main question in this chapter is if the binary is a detached Cataclysmic Variable or not. In Chapter 5, I used machine learning techniques to search the PTF data for a relatively new type of eclipsing binary; pre-He white dwarf–dA binaries. The sample I found more than doubles the known number of EL CVn binaries and presents the largest population study of these systems so far.

Chapter 2

The Palomar Transient Factory Sky2Night programme

J. van Roestel, P.J. Groot, T. Kupfer, K. Verbeek, S. van Velzen, M. Bours, P. Nugent, T. Prince, D. Levitan, S. Nissanke, S.R. Kulkarni, Russ R. Laher

MNRAS submitted

Abstract

We present results of the Sky2Night project: a systematic, unbiased search for fast optical transients with the Palomar Transient Factory. We have observed 407 $\deg^2$ in R-band for 8 nights at a cadence of 2 hours. During the entire duration of the project, the 4.2 m William Herschel Telescope on La Palma was dedicated to obtaining identification spectra for the detected transients. During the search, we found 12 supernovae, 10 outbursting cataclysmic variables, 9 flaring M-stars, 3 flaring active Galactic nuclei and no extragalactic fast optical transients. Using this systematic survey for transients, we have calculated robust observed rates for the detected types of transients, and upper limits of the rate of extragalactic fast optical transients of $\mathcal{R} < 37 \times 10^{-4}$ $\deg^{-2}\,\mathrm{d}^{-1}$ and $\mathcal{R} < 9.3 \times 10^{-4}$ $\deg^{-2}\,\mathrm{d}^{-1}$ for timescales of 4 h and 1 d. We use the results of this project to determine what kind of and how many astrophysical false positives we can expect when following up gravitational wave detections in search for kilonovae.

2.1 Introduction

Fast optical transients are transients which appear and disappear within 24 hours or less. The rate of fast optical transients is not well known (see Fig. 2.1). The reason why the fast transient sky has not yet been systematically explored is due to technical limitations. To find fast transients a high cadence is required, which means that area and/or depth need to be sacrificed. For example, a 3-day cadence supernova survey can cover an area 100 times larger than a survey of optical transients

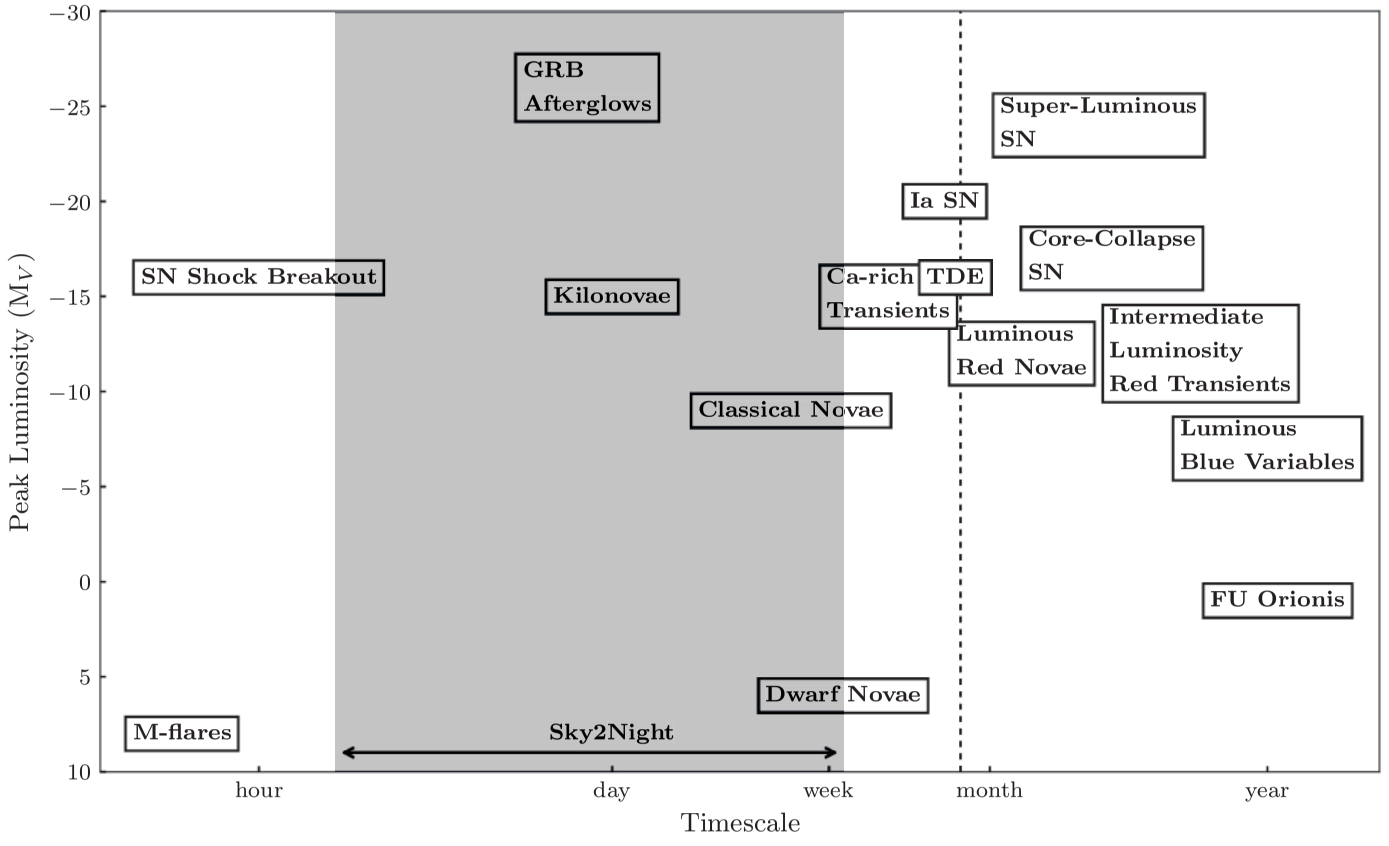

Figure 2.1: The absolute luminosity versus the typical timescale of transients. The grey area shows the timescales which are probed by the Sky2Night project. The dashed line shows the time between the acquisition of the reference images and the end of the survey. This figure is adapted from Kasliwal (2011).

with a cadence of 1 hour (using the same setup). In addition, follow up of fast optical transients is difficult since it requires rapid detection and identification of the transient and triggering of a follow-up telescope.

For this reason, almost all known extragalactic fast optical transients (timescales of less than 1 day) have been found as a counterpart of a transient detected at another wavelength where larger solid angle facilities are possible, e.g. X-ray or gamma-ray satellites. The most well studied are gamma-ray burst afterglows: interactions between highly relativistic outflows (jets) and their environment (e.g. Piran, 1999). Although they can be bright, because of the low rate ($\approx 1000\,\mathrm{yr}^{-1}$ with $R < 20$, Cenko et al., 2015) and in particular because of their rapid fading ($\sim$ magnitudes per hour, e.g. Singer et al., 2015; Fong et al., 2015) they are very difficult to find in blind searches. So far, only one[1] GRB afterglow has been found in a blind search: iPTF14yb (Cenko et al., 2015).

In searches for fast extragalactic transients, many Galactic fast optical transients are detected: outbursts of stars in our Galaxy with short ($\sim$1 d) timescales. These are sometimes considered a 'foreground fog', but they are also interesting to study in their own right. Flaring M-dwarfs are the most common Galactic fast optical transients with typical time scales of 10-100 minutes (Hawley et al., 2014; Silverberg et al., 2016) up to 7 hours (Kowalski et al., 2010) and outburst magnitudes up to 9 magnitudes in V-band (e.g. Schmidt et al., 2014). Understanding M-flare rates and intensities have recently become important with regards to planetary habitability (e.g. Vida et al., 2017). The other type of common Galactic transients are eruptions in compact binary systems with an accretion disk. The most common are dwarf novae (DN), caused by accretion disc instabilities in systems where a white dwarf accretes mass from a main sequence companion. These outbursts can brighten the system by up to 8 magnitudes (e.g. WZ Sge, Harrison et al., 2004), with short rise timescales ($\sim$ 1 day) and can last for a few days to weeks (Warner, 2003).

In 2017, the aLIGO/aVirgo gravitational wave observatories (LIGO Scientific Collaboration et al., 2015; Acernese et al., 2015) detected the first binary neutron star (BNS) merger (Abbott et al., 2017). Rapid optical follow up of this event resulted in the discovery of the optical counterpart AT 2017gfo (Abbott et al. 2017, Abbott et al. 2017, see also: Andreoni et al. 2017; Arcavi et al. 2017; Coulter et al. 2017; Cowperthwaite et al. 2017b; Díaz et al. 2017; Drout et al. 2017; Evans et al. 2017; Hu et al. 2017; Kasliwal et al. 2017; Lipunov et al. 2018; Pian et al. 2017; Pozanenko et al. 2018; Shappee et al. 2017; Smartt et al. 2017; Tanvir et al. 2017; Troja et al. 2017; Utsumi et al. 2017; Valenti et al. 2017). The optical counterpart, called a kilonova, had been theorized to accompany a BNS merger by Li & Paczyński (1998); Kulkarni (2005); Metzger et al. (2010); Roberts et al. (2011); Barnes & Kasen (2013); Tanaka & Hotokezaka (2013); Metzger & Fernández (2014); Kasen et al. (2015). AT 2017gfo is consistent with the kilonova model predictions: it was fading rapidly ($\Delta r \approx 1.2\,\mathrm{mag\,d}^{-1}$), had a peak absolute magnitude of $M_r \approx -16$ mag and displayed rapid reddening ($\approx 0.8\,\mathrm{mag\,d}^{-1}$ in $g-r$).

The models predict that the optical signal is comprised of either two or three components. The two-component models are a combination of a rapidly fading 'blue' component, emitted by fast-moving, low opacity material, and a slower fading 'red' component emitted by slower-moving, high opacity material. Three component models add an addition 'purple' component, with intermediate velocity and opacity. Villar et al. (2017) show that a three-component model is the best explanation

[1] a strong candidate without a gamma-ray detection is described by Cenko et al. (2013)

for kilonova AT 2017gfo. However, we should be aware that future kilonovae can be quite different than AT 2017gfo. For example, a lower amount of ejected mass and a different viewing angle results in a kilonovae which is significantly fainter, from $M_R = -16$ down to $M_R = -12$ (e.g. Kasen et al., 2015; Rosswog et al., 2017).

Currently, the aLIGO/aVirgo detectors are being upgraded, increasing the distance (and thus volume) at which they can detect BNS mergers. However, the localisation of the events will remain relatively poor (120-180 deg^2, depending on the SNR of the event, Abbott et al., 2016). This means after the detection of a BNS merger, optical telescopes will still have to search a large area to find the faint optical counterpart, $R \approx 19.5$ mag at 200 Mpc if it is similar to AT 2017gfo. One of the problems is that in such a large area and magnitude limit, many other (fast) transients will appear which can be confused for a kilonova; a 'needle-in-the-haystack' problem.

In the last decade, there have been a few studies that performed a blind search for fast transients in an attempt to determine the observed rate of fast optical transients. One of the earliest attempts was by Becker et al. (2004). They carried out an unbiased transients search on the data from the Deep Lensing Survey (DLS, Wittman et al., 2002) and found two M-flares and one potential extragalactic transient (OT20030305). However, follow up of the quiescent counterpart by Kulkarni & Rau (2006) shows that OT20030305 is also a flaring M-star. Other searches also found only Galactic transients, mainly cataclysmic variables (CVs) and M-dwarf flares. For example, Rykoff et al. (2005) used the ROTSE-II survey to search for untriggered GRBs but found only six outbursting cataclysmic variables. Rau et al. (2008) performed a high cadence survey on the Fornax galaxy cluster (cadence 32 min, depth B=22 mag). They also did not find any extragalactic fast optical transients in their search. The first multi-colour search for fast optical transients was performed by Berger et al. (2013), who showed that colours are very useful in identifying the transients. In their search for fast transients, they only found flares on faint M-stars and slow-moving asteroids. More recently, Cowperthwaite et al. (2017a) and Utsumi et al. (2018) performed multi-colour surveys with the goal to measure the rate of false positives when searching for kilonovae.

In this paper, we present an 8-day unbiased search for all transients in 407 deg^2 of the sky. The search was combined with rapid, unbiased spectroscopic follow-up. To identify the transients we used the Palomar Transient Factory (PTF) and for immediate (within 24 hours) spectroscopic follow-up we used the William Herschel Telescope (WHT, Boksenberg, 1985). The main goals of the project are to measure the rate of intra-night transients (Galactic and extragalactic) and to determine the expected types of false positives when searching for the optical counterpart of gravitational waves by BNS mergers. The survey design is discussed in Section 2.2. The execution of the observations and data reduction are described in Section 2.3. The results: the survey characteristics, an overview of all detected transients, and the observed transient rates are presented in Section 2.4. We discuss the results in Section 2.5. The last section summarizes the paper and lists the main conclusions.

2.2 Survey design

The project consists of two parts: identification of transients with PTF, and rapid spectroscopic classification with the WHT.

To search the sky for transients, PTF used the 48-inch Oschin Schmidt Telescope at Palomar Observatory (P48), equipped with the CFH12K camera. The mosaic camera consists of 11 working CCDs with 4k×2k pixels each. The system has a pixel scale of 1.01″/pixel and a total field of view of 7.26 square degrees (Rau et al., 2009a; Law et al., 2009a). P48 was available for 8 nights of dark time on 2010 November 1–8 (in MJD range 55501.08–55508.85). We used the standard PTF setup of 60 s exposure times and the $R_{\rm Mould}$ filter (R in the rest of the paper). We chose a target cadence of 2 hours and observed the same 59 PTF fields every night (see Table 2.4 for an overview). The fields are adjacent to each other on the sky and slightly overlapping, so the effective area covered is 407 deg^2. The fields were selected such that they were observable the entire night and are located at an intermediate Galactic latitude ($-45^\circ < b < -25^\circ$), allowing us to study both Galactic and extragalactic transients (see Fig. 2.1). The ecliptic latitude of the fields is between $-3^\circ < \lambda < 15^\circ$.

To be able to rapidly identify fast transients, PTF used an automated image processing pipeline which does bias and flatfield corrections, source extraction and image subtraction on all new images (Cao et al., 2016). Reference images of the target fields were obtained 14–16 days before the start of the project. Each reference image was constructed using at least 5 individual images. The difference images were presented to human scanners to identify transient candidates of interest and reject false positives. The best candidates were marked for follow-up spectroscopy.

We used the 4.2 m William Herschel Telescope (WHT) on La Palma, Spain, to obtain classification spectra of new transients. The WHT was dedicated for this purpose for 7 nights starting after the first night of PTF observations (MJD 55501.75). The instrument used to observe the transients was ACAM (Benn et al., 2008). ACAM is both an imager and low-resolution spectrograph (R ≈ 500, 4000–9000 Å) and is therefore ideally suited for rapid transient identification. We first observed the candidate transients with ACAM in imaging mode to confirm if they are real and to determine the brightness, followed by an identification spectrum.

2.3 Observations

During the project, the weather at the P48 was mostly good. Fifteen per cent of the time was lost due to bad weather, mostly during nights 2, 7, and 8. The seeing was typically 2.5″, but it was highly variable and regularly increased up to 4″ (Table 2.5). A total of 1974 exposures were obtained, with a median of 5 exposures per field per night. Fewer observations were obtained during nights 2, 7, and 8; with a median of 3, 3, and 2 observations per field. A full overview of all PTF observations can be found in Table 2.6.

Fig. 2.2 shows a schematic overview of the data reduction and transient detection process. The new images were processed and difference images were created by the PTF pipeline as quickly as possible (see Sec. 2.2). This ranged from half an hour to a few hours after the observation because the image processing pipeline could not keep up with the flow of incoming images. As soon as the difference images were available they were analysed by multiple human scanners to identify new transients. Identifying the real transients on the difference images was not trivial since the

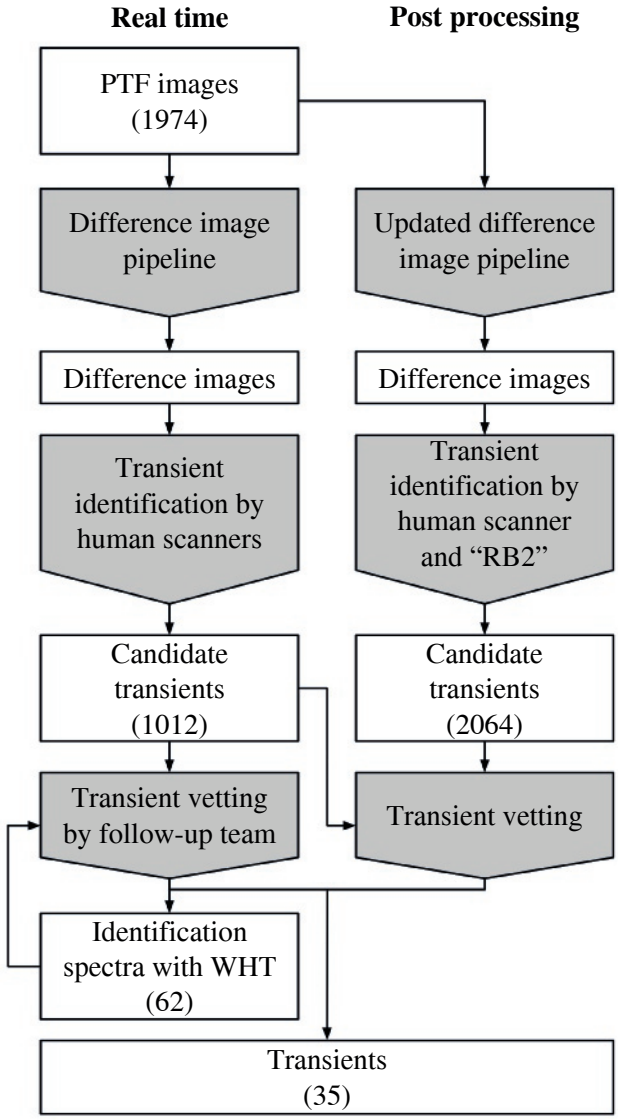

Figure 2.2: The Sky2Night data analysis and transient detection procedure. The left column shows the real-time analysis of the data, the right column shows the re-analysis of the data. White boxes show data products, within brackets the number of items, grey boxes indicate operations/filters which are applied to the data.

Table 2.1: The different types of transient candidates found in the real-time search.

Type	#
Point-source counterpart	
- Star	873
- QSO	15
- Faint star ($R \gtrsim 20.5$)	3
Galaxy counterpart	
- Nuclear	48
- Near galaxy	12
Artefact	26
Moving object	35
Total	1012

difference images contained many artefacts (e.g. slight misalignments of the images, bad pixels). To reduce the number of targets we need to inspect. We only inspected candidate transients which had two or more detections. This was done to get rid of asteroids but also filtered out some of the artefacts. In addition, the human scanners were assisted by a machine learning algorithm to get rid of the most obvious false positives (a rudimentary version of the 'RealBogus' pipeline, see Bloom et al. 2012, Cao et al. 2016 and also Smith et al. 2011). A total of 1012 candidate transients were judged by the human scanners to be potentially real, and these were passed on for further inspection by the follow-up team at the WHT.

The 1012 candidate transients were more carefully vetted by the follow-up team by inspecting the images obtained by PTF and, if available, SDSS images (Abazajian et al., 2009). In addition, we checked if the target corresponded to a known object in SIMBAD database[2]. An overview of the different kinds of transient candidates is given in Table 2.1. The bulk of the potential transients were associated with a known point-like source. The majority (873) of these were either due to bad subtraction of a star or low amplitude variability of a star. Besides variable stars, there were also 15 QSOs which brightened significantly during the project. We found three transient candidates without a counterpart in the PTF images, but for which a point-source was detected in the SDSS images. A number of potential transients (60) were found near a galaxy. The majority of these (48) were at the core of the galaxy, and it is difficult to determine if this is a bad subtraction, AGN activity, or a supernova in the core of a galaxy. Five of these could be matched to a known AGN. Experience with other PTF data indicates that the remaining nuclear transients are likely bad subtractions or AGN. The 12 remaining transients with a nearby galaxy were strong supernova candidates. A few objects (35) were initially flagged as transients but were later identified as moving objects. In addition, 26 candidates were caused by artefacts (bad pixels, very bright stars and 'ghosts').

The PTF imaging data was thoroughly re-analysed in 2014 to make sure no transients were missed during the initial search (the right column in Fig. 2.2). The images were reprocessed using an improved version of the image processing pipeline. New difference images were made. All

[2] `http://simbad.u-strasbg.fr/simbad/`

sources present on the new difference images were analysed using the 'RealBogus2' pipeline (Brink et al., 2013; Cao et al., 2016). We used a lower than normal threshold value of 0.3, compared to the 0.53 advised in the paper. This lower threshold corresponds to a missed detection rate of 5 per cent (compared to 10 per cent for a threshold of 0.53). This second search resulted in 2064 candidates transients, of which 105 overlap with the initial sample of 1012 sources. All these transient candidates were vetted using PTF, SDSS and Pan-STARRS (Chambers et al., 2016) images and CRTS light curves (Drake et al., 2009) and also using the SIMBAD database. This re-analysis recovered all real transients identified by the human scanners during the Sky2Night run. However, we also identified 2 faint supernovae and 5 flaring M-stars in the overlapping sample of transients. In addition, one new flaring M-star was found that was missed entirely during the initial search.

The most promising candidate transients found during the real-time search, typically transients candidates which were bright or were rapidly getting brighter, or were located off-centre from a galaxy, were observed with the WHT telescope. During the spectroscopic follow-up, the weather was variable. Most nights were clear, but during nights 2 and 3 time was lost due to passing clouds. Although night 7 was clear, about half the time was lost due to high humidity. The seeing during the nights varied between $0.8''$and $4''$. Table 2.5 shows an overview of the weather conditions at the WHT. A total of 62 transient candidates were observed. A quick reduction of the spectra was performed within 24 hours in order to identify any events which might need additional follow-up. The data were later reduced using standard procedures using IRAF.

2.4 Results

2.4.1 Survey characteristics

An overview of the most important metrics of the survey is given in Fig. 2.3. The time between observations, generally referred to as cadence, is given in the top left panel in Fig. 2.3. The median time between observations is 2.0 h within a night and almost all fields have been revisited within 3 hours. There is also a longer delay of about 16.8 h between revisits, which is due to the day-night cycle.

The limiting magnitude of the observations are shown in the top right panel. To estimate the limiting magnitude, we use the 95^{th} percentile magnitude of all stars detected in the image. The median limiting magnitude of all observations is $R = 20.18$ mag, with 95 per cent of the observations in the range of $R = 18.92$ mag and $R = 20.70$ mag (top right panel in Fig. 2.3). The figure also shows the distribution of the limiting magnitude of the deepest image per night (median $R = 20.41$ mag) and the second deepest image per night (median $R = 20.27$ mag), which is the relevant measure for transients which are visible for longer than 1 day. In addition, the distribution for individual nights is plotted, which shows that the nights are comparable, except for nights 2 and 8, due to clouds. Note that the limiting magnitudes are not randomly distributed in each night, but vary as a function of time in the night (see Fig. 2.10). This is caused by the airmass related extinction as the fields are tracked from horizon to horizon. At the beginning of the night, the limiting magnitude is about $R \approx 20.0$ mag per exposure and increases to $R \approx 20.4$ mag during the middle of the night, and then decreases again to $R \approx 20.0$ mag toward the end of the night.

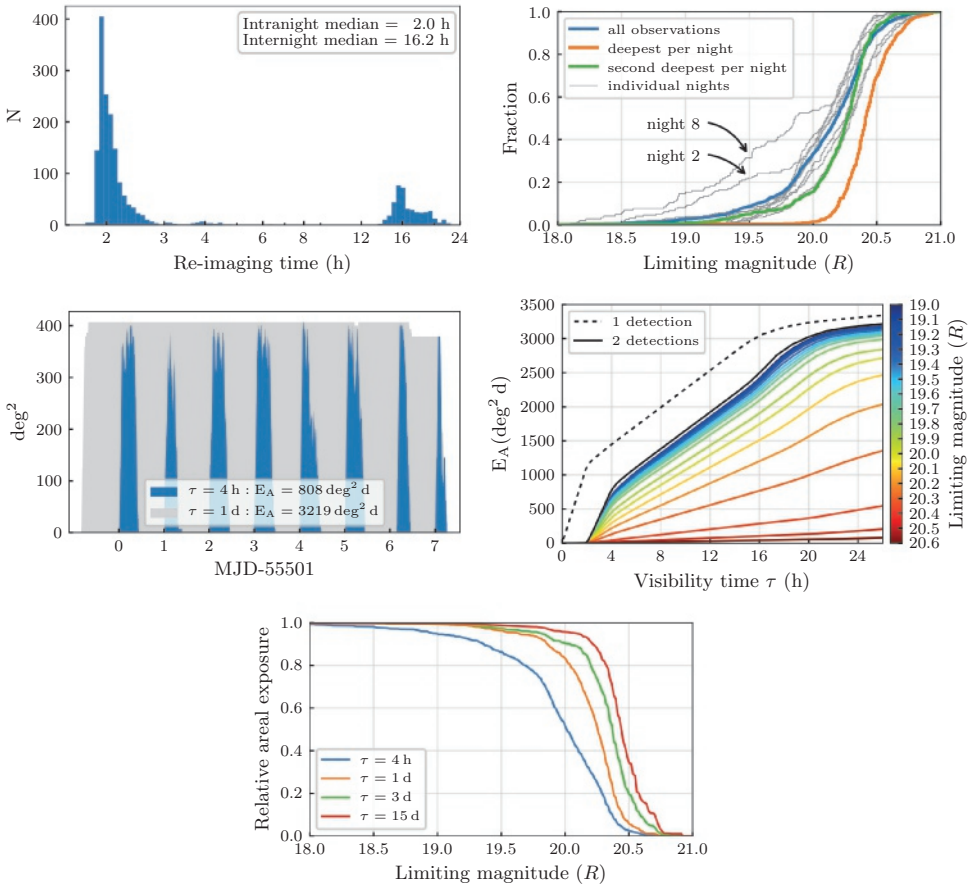

Figure 2.3: The survey characteristics. (*top-left*) The distribution of time between observations for all fields. (*top-right*) The cumulative histogram of the limiting magnitudes of all observations. (*mid-left*) The number of square degrees in which we are able to find transients with 2 detections as a function of time. The area under the curve is the areal exposure (E_A). (*mid-right*) The areal exposure (E_A) as function of visibility time (τ). The black line is the areal exposure if all observations are used, while the coloured lines show the areal exposure if observations that reach a certain limiting magnitude are used. (*bottom*) The fraction of the total areal exposure (the black line in the mid-right panel) as function of magnitude for different visibility times.

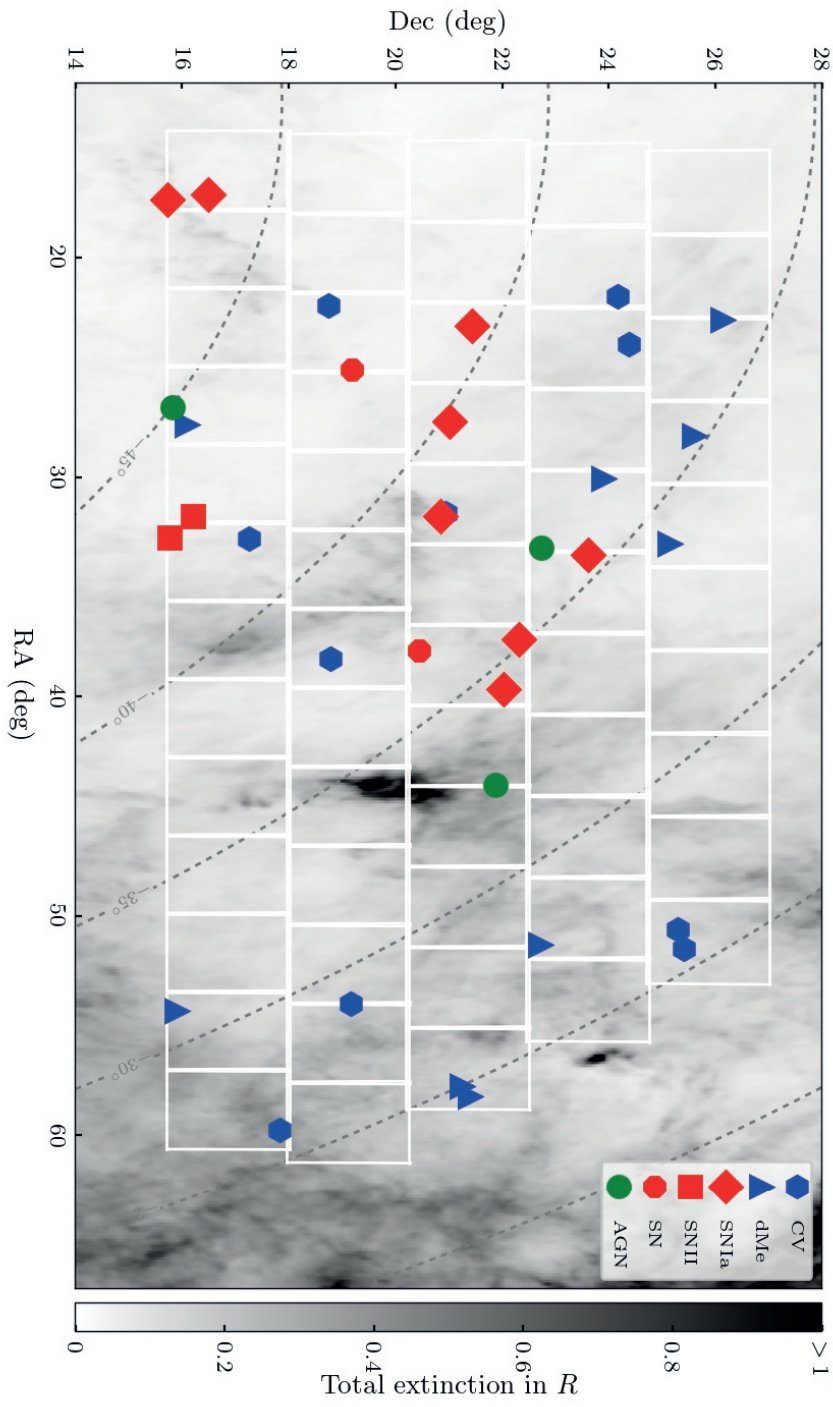

Figure 2.4: The observed area and all transients found during the project. The white rectangles indicate the 59 PTF fields. The dashed lines indicate different Galactic latitudes. The grey background indicates the total amount of Galactic extinction (Schlegel et al., 1998).

A few spikes can be seen in the limiting magnitudes as a function of time which are caused by passing clouds.

In order to calculate an observed rate of transients, we need to determine how much area we have effectively monitored and for how long: the areal exposure $E_{\rm A}(\tau)$ (units: $\deg^2\,{\rm d}$), which is a function of how long a transient is visible (τ). To calculate the areal exposure for Sky2Night, we test if a transient (visible for a set duration τ) would have been detected at least twice in our survey. The result for transients visible for τ=4 h and τ=1 d is shown as the shaded area in the mid-left panel in Fig. 2.3. The total areal exposure for a given visibility time can be calculated by integrating over time (i.e. the area of the shaded surface in the mid-left panel). The areal exposure as a function of visibility time (τ) is shown in the mid-right panel. Here we also show the areal exposure if we take the limiting magnitude of the images into account. The bottom panel shows the same information in a different way: the fraction of areal exposure that is available as a function of magnitude. This shows that there is almost no loss of areal exposure for long timescale transient before magnitude $R = 19.5$, but for the short timescale transients, the areal exposure already starts to decrease at $R \approx 18$. This shows that the areal exposure on short timescales is more sensitive to low limiting observations than the longer times scales. In the rest of the paper, we will use the areal exposure assuming that all images can be used (the black line in the mid-right panel, 1 in the bottom panel) to calculate the observed rate of transients.

2.4.2 Transients

All transients that were identified as real are listed in Table 2.2 and shown in Fig. 2.4. We found a total of 12 supernovae, 10 cataclysmic variables, 9 flaring M-stars, and 3 flaring AGN. We will discuss each class separately in the following sections.

Table 2.2: Overview of all transients found, sorted by discovery date. Shaded rows indicate extragalactic transients. The first detection column lists the time when the transient was first detected on an image. The discovery column shows the time when the transient was identified by the human scanners. The counterpart column lists the magnitude of the quiescent counterpart with R indicating the PTF R magnitude, and r the SDSS or Pan-STARRS r magnitude (the faintest of the two) for points sources. The spectrum column lists the sources of the spectra; 'ACAM': observations with ACAM at the WHT (see Sec. 2.2), 'KPNO': R.C. Spectrograph at the 4 meter Mayall telescope at KPNO (Arcavi et al., 2010), 'Kast': Kast spectrograph at the 3 meter Shane telescope at Lick Observatory, 'LRIS': LRIS at Keck-1 (Oke et al., 1995). The superscript above the name refers to one of the following papers: a: Pan et al. (2014), b: Arcavi et al. (2010), c: Drake et al. (2010a), d: Drake et al. (2010b), e: D'Abrusco et al. (2014), f: Szkody et al. (2014), g: Maguire et al. (2012), h: Paturel et al. (2003), i: Drake et al. (2014), j: Kato et al. (2009), k: Ackermann et al. (2015), l: Oliveira et al. (2017), m: Mickaelian et al. (2006).

Name PTF ...	Ra (°)	Dec (°)	First detection (MJD-55501)	Discovery (MJD-55501)	Type	counterpart	spectrum
10vey	21.734133	24.188559	-46.5	-46.5	CV	R=19.37	
10aaqh	58.242271	21.424262	-3.76	-1.78	M-flare	R=16.50	ACAM
10zbk[a]	37.393757	22.333575	-1.76	-1.72	SN/Ia	galaxy	KPNO, Kast
10zcd[b]	17.137369	16.502957	-1.76	0.13	SN/Ia	galaxy	ACAM, KPNO
10zej[c,d]	31.760443	20.853715	0.1	0.19	SN/Ia-"91bg"?	galaxy	ACAM
10zeb[e]	26.82027	15.82885	-1.82	0.22	QSO/BL Lac	r=19.20	
10zhi[b]	23.101224	21.455835	0.19	0.27	SN/Ia	galaxy	KPNO
10zfe	30.067678	23.926279	0.34	0.34	M-flare	R=18.15	
10zdq	27.478711	21.033048	0.19	0.36	SN/Ia	galaxy	ACAM
10zdi[f]	31.639451	20.952067	0.1	0.44	CV	R=18.44	ACAM
10zdk[g]	33.530525	23.630602	0.12	0.46	SN/Ia	galaxy	ACAM, KPNO, Kast, LRIS
10zqz	25.085293	19.205094	0.60	0.86	SN	galaxy	
10aacy	27.623838	16.107371	1.17	1.17	M-flare	R=16.37	ACAM
10aadb[h]	35.64689	25.137566	-5.6	1.20	AGN	galaxy	
10zig[i]	22.159879	18.760014	1.31	1.31	CV	R=18.22	
10zix[j]	32.792509	17.273396	1.16	1.33	CV	R=19.61	ACAM
10zxs	37.87864	20.461258	0.20	1.89	SN	galaxy	
10aaop	33.024992	25.166939	1.1	2.18	M-flare	R=19.51	
10aaes[k]	31.791567	16.211025	-19.81	2.20	SN/IIn	galaxy	ACAM
10aaom	54.314202	15.914879	2.24	2.25	M-flare	R=18.58	
10aaho	32.755376	15.785523	0.14	2.27	SN/IIP	galaxy	ACAM, LRIS

10aaey	39.654895	22.056594	0.29	2.31	SN/Ia	galaxy	LRIS
10aafc[l]	51.512414	25.425869	2.33	2.40	CV	r=20.17	ACAM
10aagv	57.774944	21.256824	3.34	3.34	M-flare	R=18.34	
10aajr[m]	33.219913	22.748068	0.26	4.10	QSO/BL lac	r=17.83	
10aaiw[a]	17.338134	15.735881	-2.71	4.13	SN/Ia-“99T”	galaxy	ACAM, KAST
10aakm	51.319163	22.735708	0.14	4.51	M-flare	R=15.89	ACAM
10aaqc[i]	38.260974	18.806173	6.28	6.28	CV	r=22.03	ACAM
10aarq	28.098845	25.613108	6.34	6.34	M-flare	R=20.68	
10aaqt[i]	23.952331	24.400854	6.24	6.40	CV	r=23.02	
10aaqj	50.600737	25.309258	5.33	6.42	CV	R=20.16	ACAM
10aaqb[i]	59.774695	17.842959	6.38	6.46	CV	R=18.00	ACAM
10aaqu[i]	53.982354	19.188484	6.36	6.52	CV	R=20.34	
1401fi	22.82068	26.1559	1.29	>8	M-flare	r=21.37	

Supernovae

We found a total of 12 supernovae in the Sky2Night area. They are listed in Table 2.2 and the light curves and spectra are shown in Fig. 2.11. For most of the supernovae, we have at least 8 nights of photometry. For 10 supernovae, an ACAM spectrum is available. For some supernovae, additional spectra are available that were obtained as part of other programs in the PTF collaboration. For the 2 faint supernovae that were not found in the real-time search (PTF10zqz and PTF10zxs) no spectra are available.

To determine the type and sub-type of the supernovae, we use SNID (Blondin & Tonry, 2007) to cross-correlate the spectra with supernova template spectra. If possible, we determine the redshift from the host galaxy or use narrow emission lines in the supernova spectrum. If this is not possible, we use the average redshift from the SNID cross-correlation. For the supernovae without a spectrum, we use the SDSS photometric redshift. To determine the age of the supernovae, we fit a supernova light curve template to the PTF difference imaging photometry using the python package sncosmo (Barbary, 2014). For the Ia supernovae we use the template light curves from Hsiao et al. (2007) and for the core-collapse supernovae we use the templates from Gilliland et al. (1999)[3].

The results are shown in Table 2.7. The majority of the supernovae (8) are of type Ia. Since we obtained both a spectrum and an 8-day light curve, there is little uncertainty in the classification. The subtypes are more difficult to determine, but all except two, appear to be normal type Ia supernovae (for an overview of Ia subtypes, see for example Taubenberger, 2017). PTF10aaiw, for which we have two spectra, is a "91T"-like supernova (Filippenko et al., 1992b) according to the cross-correlation with template spectra. The spectra of PTF10aaiw show a shallow Si II 6355 Å absorption line and deep Fe III absorption features, which are the main features discriminating "91T"-type supernovae from normal SNIa supernovae. In addition, the absolute peak magnitude as determined from the light curve fit, $M_B \approx -19.5$, is consistent with being a "91T"-type supernova. PTF10zej could be a "91bg"-type supernova (Filippenko et al., 1992a); the obtained spectra match almost equally well with "91bg"-templates and normal Ia-template spectra. The estimated absolute magnitude is only $M_B \approx -18.0$, which puts it at the boundary between normal Ia supernova and "91bg"-type supernovae. With the available data, we cannot make a certain sub-classification of the subtype of PTF10zej.

PTF10aaho and PTF10aaes, are core-collapse supernovae. PTF10aaho is a supernova that exploded a few days before the start of the program in a faint, unresolved galaxy ($\mathrm{SDSS}_r = 21.36$ mag). The light curve shows a rapid rise during the Sky2Night project, and PTF kept observing the field containing this supernova for a long time. The light curve indicates that this is a normal type IIP supernova (e.g. Filippenko, 1997).

PTF10aaes is likely a core-collapse supernova that occurred off-centre in an elliptical galaxy. The spectrum best matches old type-II templates, of 80 days or older. The lack of any significant trend in the 8-day light curve and the faint absolute magnitude ($M_B = -15.8 \pm 0.5$) also indicate that this is most likely an old core-collapse supernova. The first detection was in only one of the images used to build a reference image, taken 15 days before the start of the project. Therefore, we would not expect the supernova to be detected during Sky2Night, as a transient present in the

[3] 'Nugent' supernovae templates available at `https://c3.lbl.gov/nugent/nugent_templates.html`

reference images should not show up in the difference images. One possibility is that the supernova re-brightened since the reference images were taken, and therefore does appear in the difference images.

We have been unable to identify two supernovae, PTF10zqz and PTF10zxs. They are transients that appeared close to a galaxy (but not in the nucleus of the galaxy). No spectrum is available for PTF10zqz and PTF10zxs, and the light curve does not show any significant evolution over the 8 days of data. With this information, it is not possible to classify these two supernovae.

We also found one false positive supernova, PTF10zfi, which turned out to be a processing artefact. It appeared close to a galaxy, which is why it was initially confused for a supernova. Two ACAM spectra were obtained of the host galaxy but did not show any sign of a supernova. Re-analysis of the imaging data with forced photometry (PSF-photometry with a fixed location) does not show the transient any more.

Outbursting Cataclysmic Variables

We found a total of 10 outbursting CVs in the Sky2Night survey area, see Table 2.8 and Fig. 2.12. Out of these systems, five were found by the human scanners during the Sky2Night project and for these five we obtained an ACAM spectrum. We confirmed that these objects are CVs by their spectra which show Balmer emission lines at a redshift of zero. For the remaining systems, we confirmed the CV nature by inspecting their CRTS light curves, which show many eruptions over the 10+ year baseline.

Dwarf nova outbursts are the most common type of large amplitude optical variation in CVs, and the majority of CVs we found feature dwarf nova outbursts. The amplitude of the outbursts are typically $R = 1 - 5$ mag and last approximately 4 to 6 days. Transients PTF10vey, PTF10zdi, PTF10zix, PTF10aafc, and PTF10aaqu are typical examples of dwarf novae outbursts. PTF10aaqb shows an outburst amplitude of only 1.2 magnitudes. However, CRTS archival data show many dwarf nova outbursts with an amplitude of typically 2 magnitudes. We, therefore, conclude that PTF10aaqb is also a dwarf nova outburst.

Transients PTF10aaqc and PTF10aaqt have no counterpart in the PTF images. However, deeper SDSS images and Pan-STARRS images both show a faint, unresolved object. Both transients appeared at the end of the project so the light curve only spans a few days and no spectra are available. Both transients are repeating; both in PTF data obtained years later and in CRTS data multiple outbursts of a few days duration can be seen for both objects. We therefore also classify PTF10aaqc and PTF10aaqt as dwarf novae.

Transient PTF10zig was in outburst long enough for it to be detected both in the reference image and during the survey. The PTF light curve shows rapid variability ($\sim$ hours) of $\sim$1.5 magnitudes. The few observations were taken before the start of the Sky2Night project hint that this system was already in outburst for 20 days, and possibly 80 days. The CRTS light curve, taken around the same time as the Sky2Night survey, also shows rapid variability of $\sim$1.5 magnitudes. Observations taken by CRTS years earlier and later only detected the source at $\sim$21 mag. The SDSS image also shows a faint source with a colour of $g - r \approx 0.3$ with $r = 21.55$. In addition, an SDSS spectrum is available which shows many Balmer emission lines and also the He I emission line at 5875 Å which confirms the CV nature of the object. However, the light curve does not

resemble that of a typical CV with dwarf nova outbursts. The PTF observations could be taken while it was in a super-outburst; long outbursts that can last months and can feature strong variability (e.g. Osaki & Kato, 2013). If indeed the Sky2Night light curve is part of a long duration superoutburst, PTF10zig can be classified as an SU UMa or WZ Sge subtype of dwarf nova CVs.

PTF10aaqj showed a slow brightening of about 1 magnitude during the Sky2Night project and was therefore saved as a candidate. The ACAM spectrum feature Balmer emission lines ($z = 0$) and confirms that this is a CV. The CRTS light curve shows non-periodic optical variability but with no clear outbursts. These characteristics match those of AM Her type CVs (Warner, 2003).

Flaring M-stars

A total of 9 flaring stars were identified in the Sky2Night data, see Fig. 2.13. All except PTFS1401fi were identified as candidate transients, and a spectrum was obtained for three of the objects. The quiescent counterparts of the flaring objects were also detected in PTF reference images, ranging from $R = 16$ mag to $R \approx 21$ mag. We use Pan-STARRS colours to determine the spectral type of the M-dwarfs, following the classification of Best et al. (2018), see Table 2.9 and Fig. 2.6. This shows that the majority of the flaring objects are of spectral type M4–M5. Two of the flaring stars were significantly redder and have later spectral types of M6 and M7.

We fit a simple outburst model (instant rise, exponential decay in flux) to the light curves to determine the outburst properties, such as flare magnitude and decay time scale, see Table 2.9. Here we have assumed that the highest detected magnitude corresponds to the observed peak magnitude, the most conservative approach. We calculated the energy emitted per flare in the R-band by first measuring the equivalent duration of the flare (Gershberg, 1972), and then calculate the absolute energy in the flare by using the absolute magnitudes of M-stars from Pecaut & Mamajek (2013).

The flare timescales are typically within 0.5 and 2 hours, with one longer flare with a timescale of almost 5 hours. The observed flare magnitudes are typically between 0.6 and 1.5 magnitudes, but three flares are significantly stronger, with the strongest flare of 3.5 magnitudes.

AGN activity

Three promising transient candidates were followed up with the WHT but were identified as an AGN. Their light curves and spectra are shown in Fig. 2.14.

PTF10aadb is a transient at the core of a face-on SAa spiral galaxy ($z \approx 0.062$, Huchra et al., 2012). The light curve during the Sky2Night project has an average of $R \approx 19.5$ mag and does not show a significant trend. The initial spectrum showed what seemed to be a weak Hα P-Cygni profile, and the object was initially identified as a type IIn supernova. However, there is evidence that the core of the galaxy is an AGN. First, a radio source has been detected in the NVSS survey (Condon et al., 1998). Second, observations by PTF three years after the Sky2Night project also show another brightening of the core of this galaxy, now up to $R \approx 18.8$ mag. This makes it more plausible that the transient seen during Sky2Night is due to AGN activity.

PTF10zeb and PTF10aajr both appear as unresolved sources which rapidly became brighter. For PTF10aajr a spectrum was obtained with ACAM. The spectrum shows a blue continuum without any prominent features. Both sources are known radio and X-ray sources and classified

Table 2.3: The observed rate of transients for the Sky2Night project. The uncertainties indicate the 95 per cent confidence interval. Upper-limits for fast optical transients are 95 per cent confidence upper-limits. These limits assume a detection efficiency of $\epsilon = 1$ (see equation 2.1) and assume that transients could have been detected in all of the images.

Type	N	$\mathcal{R}$ (10^{-4} deg^{-2} d^{-1})
Supernova - Ia	8	$10.0^{+8.2}_{-5.3}$
Supernova - CC	1	$2.0^{+4.4}_{-1.6}$
CV - DN	5	$12.8^{+13.6}_{-7.9}$
CV - DN - $R > 20.5$ mag	2	$6.0^{+10.3}_{-4.6}$
M-flares	9	118^{+94}_{-58}
M-flares - $R > 20.5$ mag	2	35^{+64}_{-26}
BL Lac flares	2	$6.7^{+11.6}_{-5.0}$
FOTs (4 h)	0	< 37
FOTs (1 d)	0	< 9.3

as BL Lac-type objects (Mickaelian et al., 2006; D'Abrusco et al., 2014), which agrees with our observations.

2.4.3 Observed transient rates

The observed rate of transients is calculated as follows:

$$\mathcal{R} = \frac{N}{\epsilon^2 E_A(\tau)} \text{ (deg}^{-2}\text{ d}^{-1}\text{)} \tag{2.1}$$

with N the number of transients, ϵ the detection efficiency per image, and E_A the effective exposure (see Sec. 2.3). Since N is a small number, we use Poisson statistics to calculate the uncertainty (e.g. Gehrels, 1986).

The detection efficiency (ϵ) occurs in the equation squared because we required a transient to be detected in two images. The efficiency is difficult to estimate and is a function of the magnitude, the background (e.g. a galaxy), and the subjective nature of human scanners. We tried to be as complete as possible by saving candidate transients when in doubt. However, the efficiency will always gradually decrease as the brightness approaches the detection limit. In the calculation of the rates, we will assume $\epsilon = 1$ for transient brighter than the magnitude limit. This should be kept in mind when interpreting the results: if the real efficiency is lower than 1, the real observed transient rates will be higher than reported in this work.

The effective exposure (E_A) depends on the visibility time of the transient, as can be seen in Fig. Fig. 2.3. We, therefore, need to estimate how long a transient would have been visible during the project. We then use the areal exposure assuming that the transients could have been detected in all images (the black line in the bottom-left panel in Fig. 2.3). For supernovae, we assume

that they are all visible for longer than 15 days. This maximum results from the requirement of a non-detection in the reference images obtained 15 days before the start of the project. For the dwarf novae and BL Lac flares we estimate the visibility time by eye from the light curves, ranging between 3–5 d. For the M-dwarf flares, we have used the fitted curve to estimate the visibility time, which are typically detectable as transient for 3-6 h. We assume an uncertainty on our estimates of the visibility time (τ) 10% (log-normal distributed).

We calculate the observed rate and uncertainty for each type of transient by numerically combining the Poisson distribution for N, with the distribution we calculated for E_A. The final values are shown in Table 2.3 with the uncertainties indicating the 95 per cent confidence interval. In addition, we calculate an upper limit for transients visible for 4 h and 1 d. We use the 95 percentile upper limit, which corresponds approximately to 3 detections (Gehrels, 1986).

2.5 Discussion

2.5.1 Expected number of transients

Supernovae

The expected number of supernovae Ia in the survey are easy to determine since their light curves are very uniform and the volumetric rate for Ia supernovae is well-known (e.g. Graur et al., 2014). In addition, they can be assumed to be uniformly distributed across the sky. We use sncosmo to simulate a large number of supernova Ia light curves of uniformly distributed supernovae (in co-moving volume). We use SALT2 supernova light curve templates (Guy et al., 2007) with parameters and host galaxy extinction parameters according to Mandel et al. (2017). We also take into account Galactic extinction (Schlegel et al., 1998). We simulate our survey by checking if the supernovae are in the Sky2night field and if it is above the detection limit during the survey and not detected in the reference image. For a limiting magnitude of R=20.21 mag (the magnitude at which the fractional areal exposure is 90 per cent, see the bottom panel of Fig. 2.3) and volumetric rate of $\mathcal{R}_{\rm volume} = 2.5 \times 10^{-5}{\rm yr}^{-1}{\rm Mpc}^{-3}$ (Graur et al., 2014), we would expect to find 13.4 supernovae during our project, marginally consistent with 8 confirmed detections taking into account Poisson uncertainty. Or, the other way around, we find a volumetric rate of $\mathcal{R}_{\rm volume} = 1.50^{1.46}_{-0.73} \times 10^{-5}{\rm yr}^{-1}{\rm Mpc}^{-3}$. This suggests that we have missed some supernovae in our search or the effective magnitude limit was about $R \approx 19.8$ mag. Adams et al. (2018), who also used PTF data, also found that the efficiency started to drop of about 0.5 magnitudes above the detection limit. This could be explained due to the fact that Ia supernovae occur in galaxies, which makes their detection more difficult.

We compare the relative number of different types of supernovae to the fraction of supernovae found by the Lick Supernova search (Li et al., 2011). They find that 74 per cent of their supernovae are of type Ia, with 17 per cent of type II and 9 per cent type Ibc. Our results are consistent with this result: with 8 out of 9 identified supernovae are of type Ia (we do not count PTF10aaes, as it is an old supernova). The distribution of Ia subtypes is also in agreement with the ratios found in the Lick Supernova search. With 8 detected Ia supernovae, the expectation value for "99T" and "91bg" types is both one, which is what we have found.

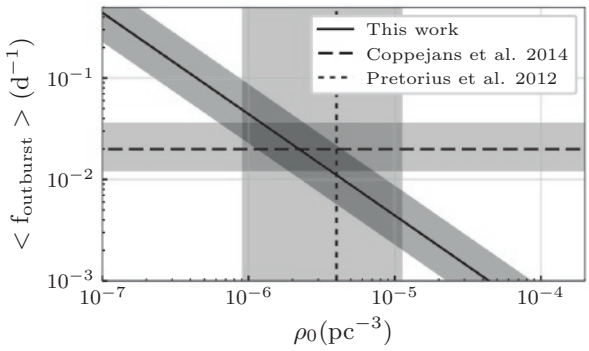

Figure 2.5: The CV space density versus the average dwarf nova outburst frequency. The dwarf nova volumetric rate we derived in this paper is shown as the diagonal line in the figure. The vertical line shows the space density as measured by Pretorius & Knigge (2012) and the horizontal line shows the average outburst frequency calculated from the dwarf nova sample by Coppejans et al. (2014). The shaded regions indicate a 95 per cent confidence interval.

Dwarf novae

We simulate the number of dwarf novae outbursts which we expect given the CV space density and outburst frequency. We use a simple Galaxy model with a thin and thick disk. We assume disks with an exponentially decreasing density profile with scale heights of 200 pc and 1000 pc and a Galaxy scale radius of 3000 pc (Nelemans et al., 2004). We assume a density ratio between the thin and thick disk population of cataclysmic variables of 1 to 56 (Groot et al., in prep.). We randomly populate the model Galaxy according to the space density distribution and keep only the objects that are in the field-of-view of the Sky2Night survey. We then estimate if each object would have been detected in the Sky2Night project if a dwarf nova outburst occurs. For this, we use the relation $M_V = 5.92 - 0.383P$ (Warner, 1987), and assume that $V - R = 0$ at peak. We randomly draw periods from a sample of periods as found in CRTS (see Coppejans et al., 2014). With this simulation and 8 detected dwarf novae, we derive a local dwarf nova volumetric rate of $4.6^{4.7}_{-2.4} \times 10^{-8}\,\mathrm{d^{-1}pc^{-3}}$. As this rate is the combination of a space density and an outburst frequency, we can compare our result to measurements of either of these, which is illustrated in Fig. 2.5. This shows that our finding is consistent with the combination of the measured space density of $2.3^{9.0}_{-1.4} \times 10^{-6}\,\mathrm{pc^{-3}}$ (approximated 95 per cent interval, Pretorius & Knigge, 2012) and, at the same time, an average outburst frequency of dwarf novae of $20^{+15}_{-8} \times 10^{-3}\,\mathrm{d^{-1}}$ (calculated from the sample of Coppejans et al., 2014).

Stellar flares

In order to make a more direct comparison with flare rates from other surveys, we calculate the average flare duty cycle per M-dwarf spectral type. First, we use *ri* and *iz* colours from Pan-STARRS (Flewelling et al., 2016) to determine the number of stars per spectral type in the

Sky2Night area, see Fig. 2.6. To calculate the average flare duty cycle we divide the number of flare epochs by the total number of observations per spectral type, see Fig. 2.7.

This shows that, on average, the late type M-dwarfs are more active, which confirms earlier findings by Kowalski et al. (2009) and Hilton et al. (2010) (both with SDSS data), also plotted in Fig. 2.7. All findings show a similar trend, but the absolute numbers are three orders of magnitude off. This is the result of different flare selection criteria: Kowalski et al. (2009) selected flares with $\Delta u > 0.7$ in Stripe 82 data, and Hilton et al. (2010) use Balmer emission lines in SDSS spectra to identify flares, but these lines can be a sign of persistent chromospheric activity as well. The main difference is that the contrast in the u-band and of emission lines of flares is much higher than in the R-band. Models by Davenport et al. (2012) can be used to convert ΔR to Δu (assuming $r = R$); a flare of $\Delta R = 0.6$ on an M4 star corresponds to a Δu of 4 magnitudes. This makes all flares which we found brighter than at least 99 per cent of the flares found in Kowalski et al. (2009). This explains the large difference in observed rates: Kowalski et al. (2009) reported an observed rate of 48 flares $\mathrm{deg}^{-2}\,\mathrm{d}^{-1}$, a factor 2600 higher than our results (see Table 2.3). This is also consistent with the difference between the duration and flare energy compared to the relation plotted in Fig. 5.8 of Hilton (2011). The flares found in the Sky2night project are all at the high-energy, long-decay time end of the distributions.

We compare the rate of flares with the 38 M-flares found in the entire iPTF survey by Ho et al. (2018). Using their estimate for $E_A = 22146\,\mathrm{deg}^2\,\mathrm{d}$, the rate of such flares is $\mathcal{R} = 17^{+6}_{-5} \times 10^{-4}\ \mathrm{deg}^{-2}\,\mathrm{d}^{-1}$. Ho et al. (2018) rejected any transients with a stellar counterpart in the PTF reference images, so we compare it to the rate of flares with a counterpart fainter than the detection limit: $35^{+64}_{-26} \times 10^{-4}\ \mathrm{deg}^{-2}\,\mathrm{d}^{-1}$(Table 2.3). The rate from Sky2Night is slightly higher but consistent with the flare rate by Ho et al. (2018).

2.5.2 Upper limit for fast optical transients

Since no unclassified fast optical transients were found in our search, we have calculated upper limits for the rate of fast optical transients visible for 4 hours and 1 day (see Sect. 2.4.3 and Tables 2.3). We compare our upper limits to upper limits determined by other searches for fast optical transients, see Fig. 2.8. Our result is most similar to the upper limit set by Cowperthwaite et al. (2017a): 0.07 $\mathrm{deg}^{-2}\,\mathrm{d}^{-1}$ down to 22.5 in i-band at a time scale of 3 hours. The Sky2Night upper limit is a factor of ≈ 15 lower, but at magnitude 19.7, 2.8 magnitudes lower. The Sky2night upper limit for 1 d transients is a factor 2.5 times deeper than the limit set by Berger et al. (2013) using g- and r-band data from Pan-STARRS. However, the PanSTARRS limiting magnitude is again 2.8 magnitudes deeper than the Sky2night search, making the Pan-STARRS upper limit slightly more constraining.

A lower limit to the rate of fast optical transients is set by GRB afterglows. During the entire duration of PTF, one GRB afterglow was found as a fast optical transient: PTF14yb (Cenko et al., 2015). The transient was bright enough to be detected by PTF for a total of five hours. Ho et al. (2018) did an archival search of all PTF transients and did not find any new fast optical transients besides flaring M-dwarfs. Given this one event, they calculated a rate for extragalactic fast optical transients (peak $m \leq 18$ and fade by $\Delta\mathrm{mag} > 2$ in $\Delta t = 3\,\mathrm{hrs}$) of $\mathcal{R} = 4.5^{+17.8}_{-4.4} \times 10^{-5}\ \mathrm{deg}^{-2}\,\mathrm{d}^{-1}$ (see also Cenko et al., 2015). This indicates that the limit set by

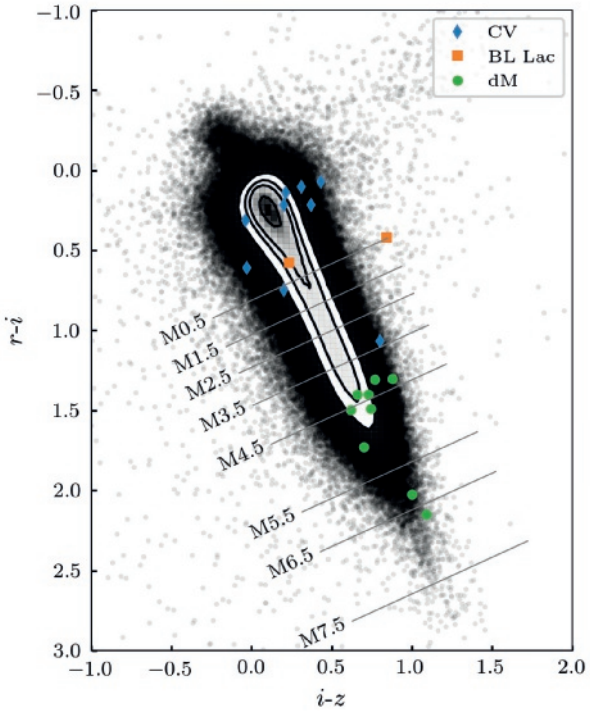

Figure 2.6: The Pan-STARRS colours of unresolved counterparts of transients. The black dots and contours show all point-sources in the Sky2Night area.

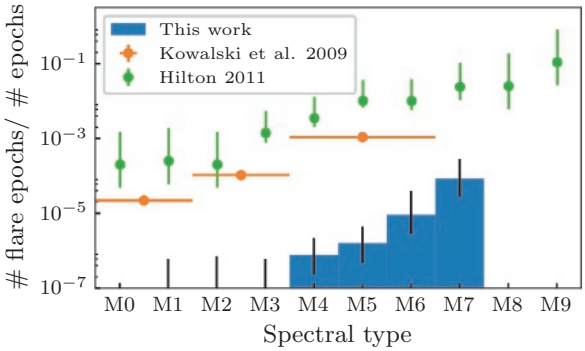

Figure 2.7: The fraction of time M-stars are in outburst for different spectral types. This is calculated by counting the number of flares per spectral type and dividing by the total number of M-stars of that spectral type in the S2N field, see Fig. 2.6. The error bars indicate the Poisson uncertainties only.

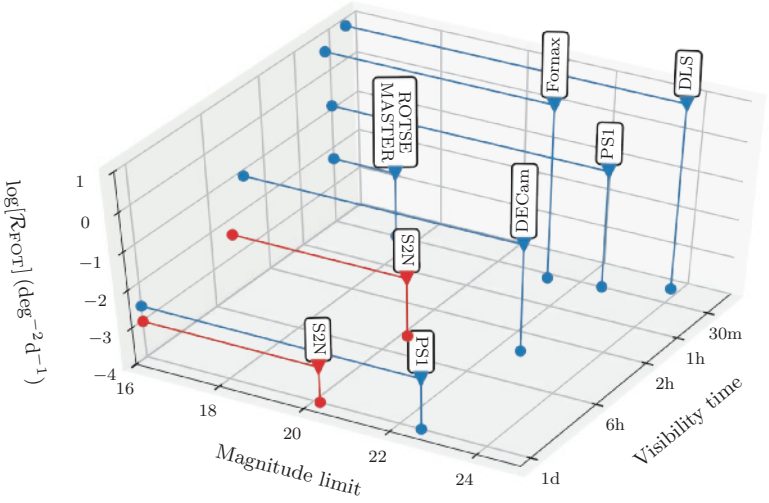

Figure 2.8: Upper-limit to the rate of fast optical transient versus time-scale and limiting magnitude (adapted from Berger et al., 2013). The limits set by this work are shown in red and are labelled 'S2N'. Upper-limits by other surveys are indicated in blue; Deep Lensing Survey (DLS, Becker et al., 2004), ROTSE/MASTER (Rykoff et al., 2005; Lipunov et al., 2007), Fornax Survey (Fornax, Rau et al., 2008), Pan-STARRS Berger et al. ('PS1', 2013), survey by the DECam (DECam Cowperthwaite et al., 2017a).

the Sky2Night survey is approximately 2 orders of magnitude above the rate of extragalactic fast optical transients.

2.5.3 False positives in the search for kilonovae

The aLIGO/aVirgo detectors are scheduled for another observing run, starting in early 2019 ("O3"). The estimated distance horizon to detect BNS mergers is 65-120 Mpc, and the expected number of BNS detections is 1 to 50 events (Abbott et al., 2016). Systematic follow-up of all BNS gravitational wave events allows us to study kilonovae in more detail using spectroscopy and also determine the characteristics of the population of kilonovae. In order to do this, optical survey telescopes need to quickly identify the kilonova counterpart in an area of 120-180 $\deg^2$ (Abbott et al., 2016). This will be more challenging than the search for the optical counterpart to GW170817, AT 2017gfo, which was well-localized (40 $\deg^2$), nearby ($\approx$ 40 Mpc) and bright ($r \approx 17$ mag at peak). For nearby kilonovae, a galaxy-targeted survey is more efficient than surveying the entire aLIGO/aVirgo error-box (e.g. Gehrels et al., 2016). However, because aLIGO/aVirgo will be more sensitive, the majority of the BNS events will be more distant and thus fainter. In those cases, a Galaxy targeted search is not viable any more as the surface density of galaxies on the sky is $\approx 1\,{\rm arcmin}^{-2}$ at these magnitudes (e.g. Yasuda et al. 2001). Instead, an untargeted search will be needed to locate kilonova counterparts. The different search strategy, but also the fainter

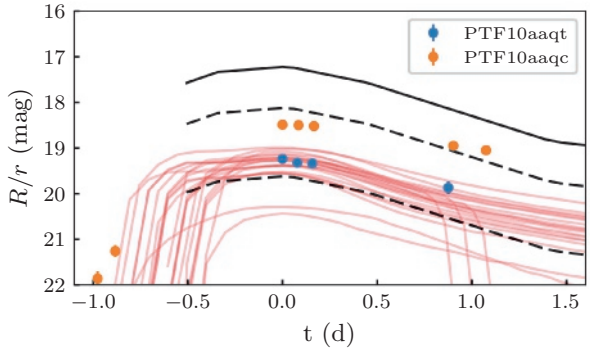

Figure 2.9: A comparison between the light curves of the DN detected in the Sky2Night project and kilonova light curves. All light curves have been shifted such that their peak occurs at t=0. The black line indicates the best fit light curve of AT2017gfo in r-band (Villar et al., 2017). The dashed and dotted lines show this light curve for distances of 60 Mpc and 120 Mpc, the expected range of aLIGO/aVirgo during 'O3'. The red lines show kilonovae models by Kasen et al. (2017) at a distance of 120 Mpc.

target, means that the number of false positives can become problematic. False positives delay the identification of the true kilonova counterpart and ruling them out requires valuable follow-up resources. In this section, we use results from the Sky2Night project to assess how problematic false positives are in a monochromatic kilonova search, and determine the best way to recognise false positives.

The Sky2Night survey area of the 407 $\deg^2$, 2–3 times the typical "O3" errorbox of aLIGO/aVirgo, contained a total of 1012 transient candidates. Most of these were associated with variable stars or bad subtractions of stars (873 out of 1012). These can be identified by the presence of a star in the reference images (or other surveys). During the execution of Sky2Night, the identification of stellar counterparts was done by human inspection, but an automated procedure is easy to implement and is now standard in many transient identification pipelines (e.g. Miller et al., 2017). In addition, better image subtraction techniques such as ZOGY (Zackay et al., 2016) and also more advanced 'RealBogus' methods (e.g. Gieseke et al., 2017) have been developed. Moreover, the increase in available training data for the machine learning based 'RealBogus' also improves the identification of real transients. Improvement of this processing step will eliminate, in particular, false positives due to poor subtractions of images, and should especially help in removing any nuclear transients which are the result of a slight misalignment of images. If we reject any candidate with a point-source counterpart (888), which is an improper subtraction (26), which is located at the core of a galaxy (48), or is moving (35), only 15 real transients remain out of the 1012 initial candidates.

The remaining 15 transients either have a nearby galaxy as a counterpart or no counterpart at all in the PTF images. The time evolution of a transient is one of the most discriminating properties of a transient, and Sky2Night light curves probe the evolution on timescales of 2 hours to 8 days. If we compare the light curves of the flare stars with that of a kilonova, we can easily

tell them apart as flares evolve much faster than any kilonova. On the other hand, kilonovae evolve significantly in a timespan of 8 days, while supernovae lightcurves generally change only slightly in an 8-day timespan. They are therefore also easy to distinguish with an 8-day light curve. However, the two outbursting CVs with a faint quiescent counterpart (PTF10aaqc and PTF10aaqt) evolve on a similar timescale as kilonovae, as shown in Fig. 2.9. The rise time is <1 d and the decay timescale is ≈ 1 mag d^{-1}. Although the dwarf novae in our example rise and decay slightly slower, the difference will be almost impossible to detect with just a few epochs of data. With only this short span of data and if no additional information, such as historic light curves that may identify previous dwarf nova outburst, making the distinction between a kilonova and a young dwarf nova will be problematic. To distinguish a kilonova and a dwarf nova we need to rely on additional information (if no counterpart is detected). In the case of PTF10aaqc and PTF10aaqt, PTF detected previous outbursts, which confirmed the dwarf nova nature of the transients.

With the complete light curves, we have been able to reject all transients as kilonova candidates. However, the goal of kilonova searches is to identify the kilonova as fast as possible so it can be targeted for follow-up observations. Therefore, we should consider the question: can we reject all transients with only one day of data? In that case, the transient light curves contain only a few epochs, and the time-span is only a few hours. Next to dwarf novae now also supernovae become problematic, depending on the time since the merger for the kilonova searches. Supernovae do not evolve significantly in an 8-hour timespan, and therefore can be confused with a kilonova at peak when it is relatively constant (approximately 10-24 hours after the merger, ≈ 24 hours for AT 2017gfo). This ambiguity can be solved if the host redshift is known, and the absolute magnitude of the transient can be calculated. However, this information is not always available at the moment the transient is first detected.

We conclude that the rapid (within 24 hour) unique identification of (faint) kilonovae using only a monochromatic transient light curve is difficult due to false positives. This is especially a problem if no counterpart can be identified and no recent pre-merger images are available. The latter issue can be solved by monitoring the entire (available) sky every night. This ensures that all repeating Galactic dwarf novae will be discovered and also that slowly evolving supernovae can be identified and can be discarded as kilonovae. However, this is resource intensive and not always possible (due to weather) and would still leave infrequent outbursting dwarf novae and young supernovae as potential false positives. The second solution is to obtain additional information by performing a two-band survey search to obtain instantaneous colours (e.g. $g-r$) of all transients. According to simulations kilonovae rapidly become redder within the first few days. This was also seen for AT2017gfo were the $g-r$ colour changed by $\approx 0.8\,\mathrm{mag\,d^{-1}}$. This means that within 8 hours it became redder by ≈ 0.3 mag which should be easily detectable, even at low signal-to-noise ratios.

Cowperthwaite et al. (2017a) have explored the colour solution and performed an empirical study of false positives with DECam (mounted at the 4 m Blanco telescope). They surveyed an area of $56\,\mathrm{deg^2}$ for 5 nights at a cadence of 3 h with $i-z$ colour information. Out of the 929 transient candidates they found, all but 21 can be rejected as a potential kilonova using static colour information. A further inspection of the luminosity and colour evolution is enough to reject all of them as kilonova candidates. Utsumi et al. (2018) empirically tested the number of false

positives expected in searches for kilonovae with the Hyper-SuprimeCam installed on the 8.2 m Subaru telescope. They obtained two sets of i and z images separated by 6 days covering 64 deg^2, in which they discovered a total of 1744 transient candidates. They applied colour and variability cuts aimed at identifying kilonovae. They concluded that all supernovae and AGN can be rejected as kilonovae candidates. However, two transients remained satisfying the kilonova criteria: a flare on a M-dwarf or M-giant and a CV outbursts.

The conclusion is that the automatic rejection of all false positives without any additional follow-up is difficult. We have shown that high-cadence (2 h) survey alone is not sufficient to identify all transients. A combination of high cadence, multicolour light curves combined with historical information are needed to quickly identify transients found in gravitational wave follow-up. We note that the biggest colour change is between the extremes of the optical regime (faster decay with bluer colour). Therefore a colour such as $(u - z)$ would have the highest diagnostic power when probing deep enough.

2.6 Summary and conclusions

In this paper, we present a systematic, unbiased survey of intra-night transients. We used PTF to survey 407 deg^2 at a cadence of 2 hours combined with large-scale, systematic follow up with the WHT telescope. We performed a thorough search for transients, both Galactic and extragalactic. Our search identified 35 transients: 8 type-Ia SN, 2 Core-collapse SN, 3 unknown SN, 10 outbursting CVs, 9 flaring M-stars and 3 AGN flares. For each of these types of transients, we have calculated an observed rate and confirmed these with simulations. We found no extragalactic fast optical transients and set a deeper upper limit on their observed rate.

Our main conclusions are that the rate of fast extragalactic transients is low, $\mathcal{R} < 37 \times 10^{-4}$ deg^{-2} d^{-1} and $\mathcal{R} < 9.3 \times 10^{-4}$ deg^{-2} d^{-1} for timescales of 4 h and 1 d, and that they are not a source of confusion when searching for kilonovae. In addition, a mono-chromatic survey with a cadence of 2 hours, combined with longer time baseline information and static colour information is sufficient to be able to identify common transients such as flaring star, outbursting CVs and supernovae. Difficulties arise if the transients need to be identified within a single night, with only single-band photometry. Transient surveys that aim to identify kilonovae within the first night should observe with at least two bands, preferably widely separated in wavelength, multiple times per night.

2.A Additional Figures and Tables

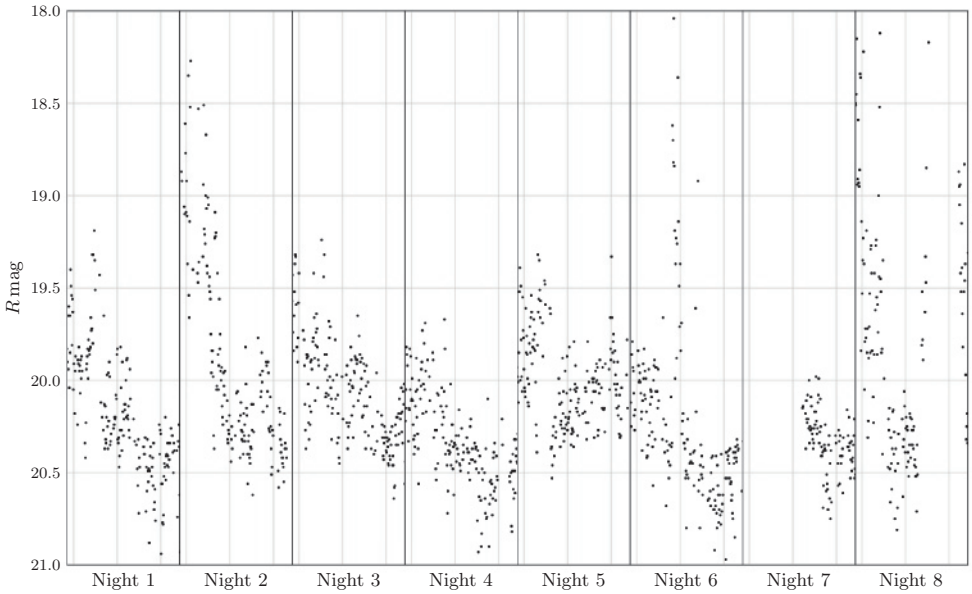

Figure 2.10: The limiting magnitude of the P48 images as function of time. Night 1 starts on MJD 55501.08.

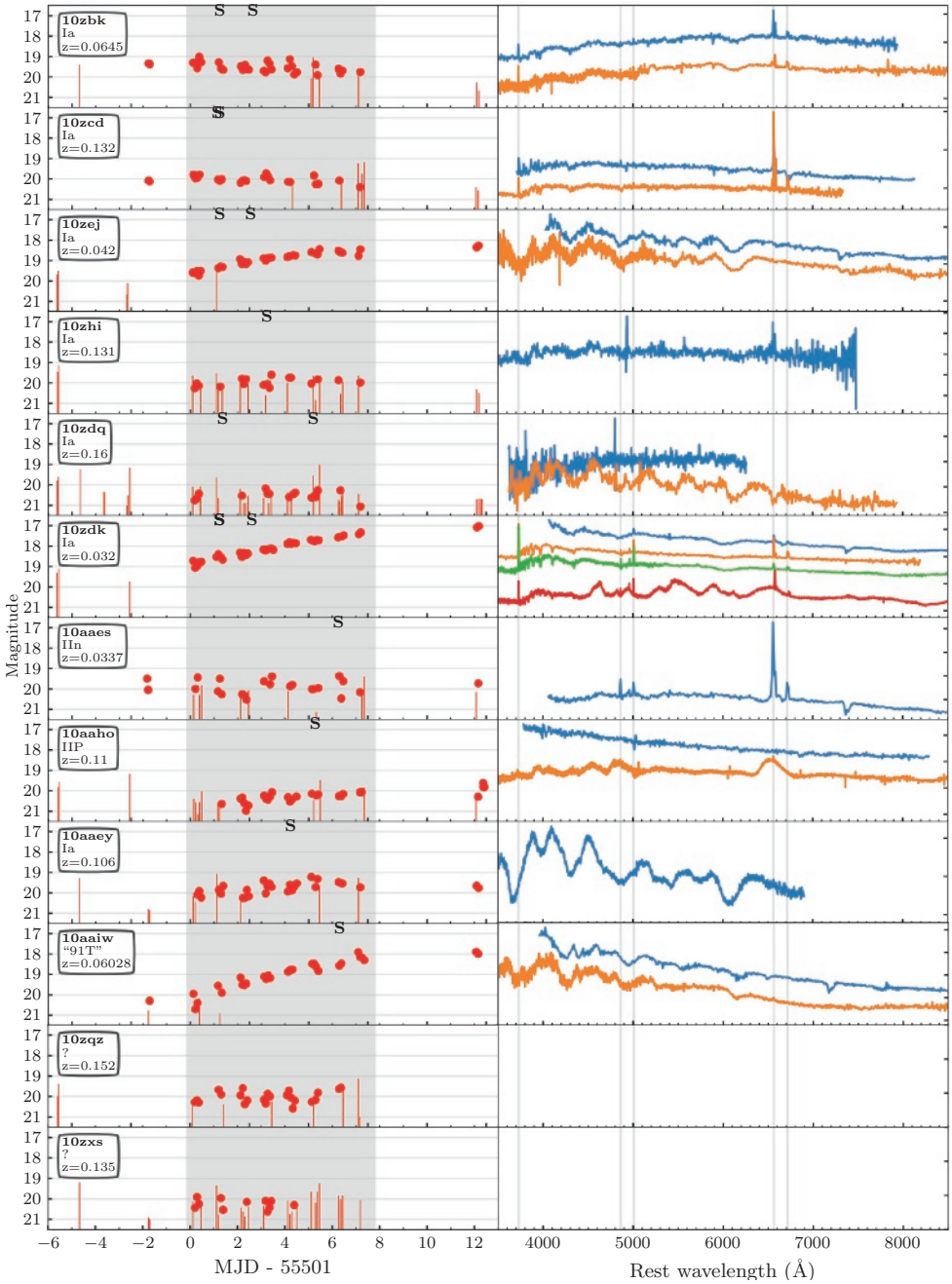

Figure 2.11: Light curves and spectra of all supernovae found during the project. The red dots indicate PTF photometry and vertical red lines indicate upper limits (R filter). The grey shaded area indicates the duration of the Sky2Night project. The spectra are normalised to the median and offset by 1, from high to low according to time obtained. The grey lines indicate common spectral lines: H α, H β, O II, O III and S II. Note that some improperly subtracted telluric lines are visible in the spectra of PTF10zhi (4940 Å) and for PTF10zdq (4800 Å). The last spectrum of PTF10zdk was taken 37 days after the start of the Sky2Night project (MJD 55538).

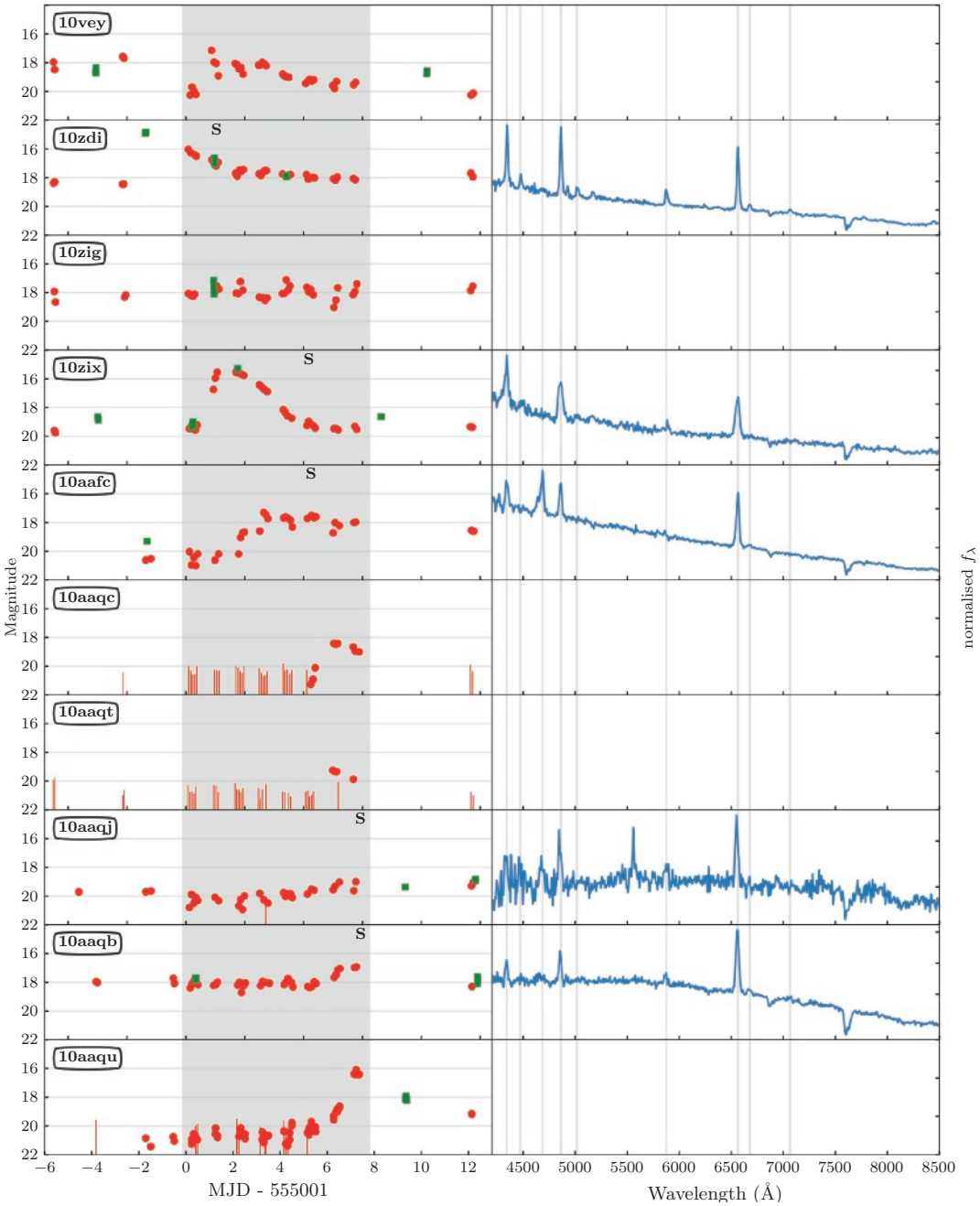

Figure 2.12: Light curves and spectra of all cataclysmic variables found during the project. The red dots indicate PTF photometry and vertical red lines indicate upper limits (R filter), green squares indicate CRTS photometry (no filter). The grey shaded area indicates the duration of the Sky2Night project. All spectra were obtained with ACAM and normalised to the mean value. Grey lines show the Balmer lines, He I, and He II lines. The emission feature at 5577 Å in the spectrum of PTF10aaqj is caused by a telluric line.

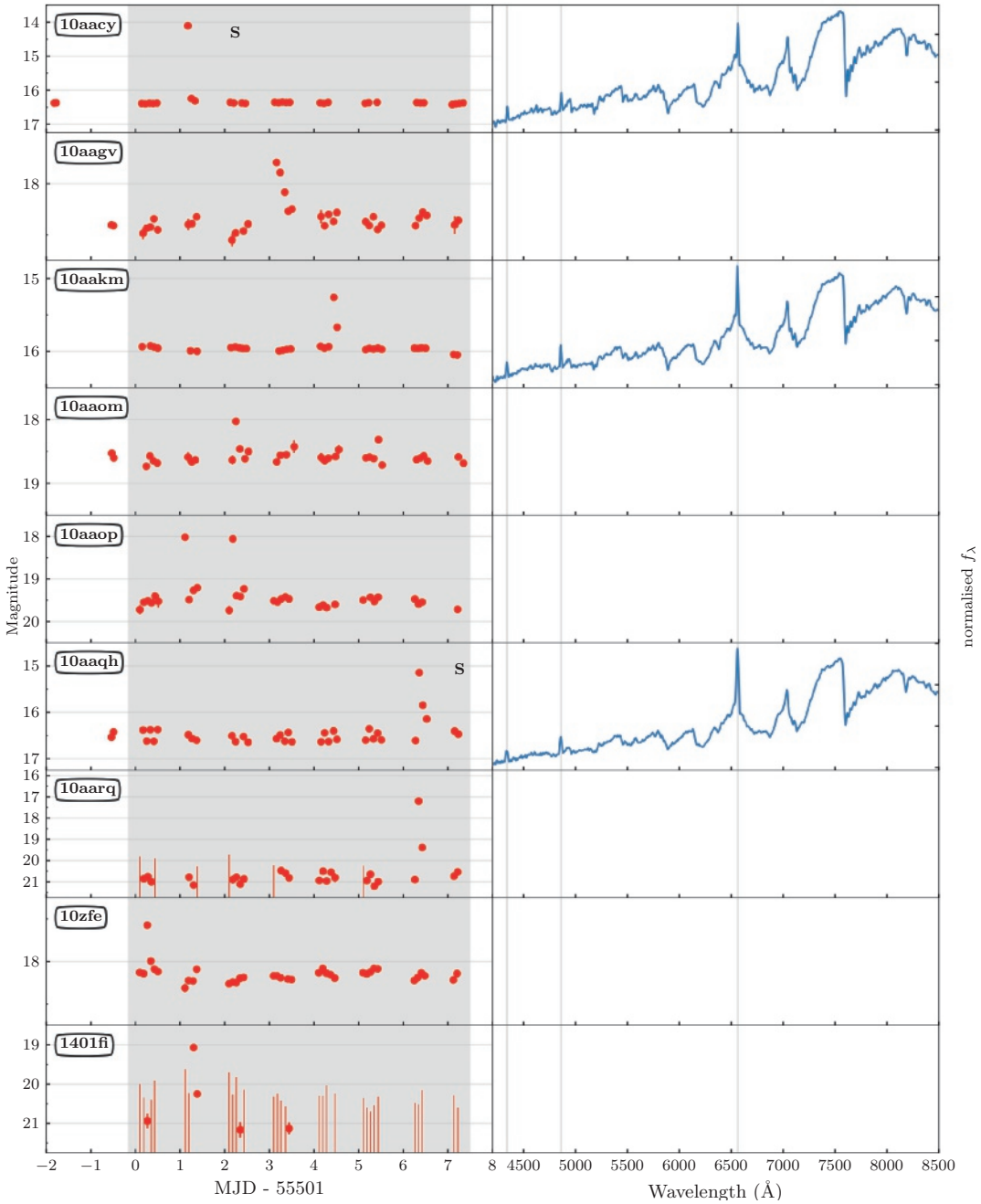

Figure 2.13: Light curves and spectra of all stellar flares. The red dots indicate PTF photometry (R filter), vertical lines indicate upper limits. The grey shaded area indicates the duration of the Sky2Night project. All spectra were obtained with ACAM and normalised to the mean value. Grey lines show the Balmer lines.

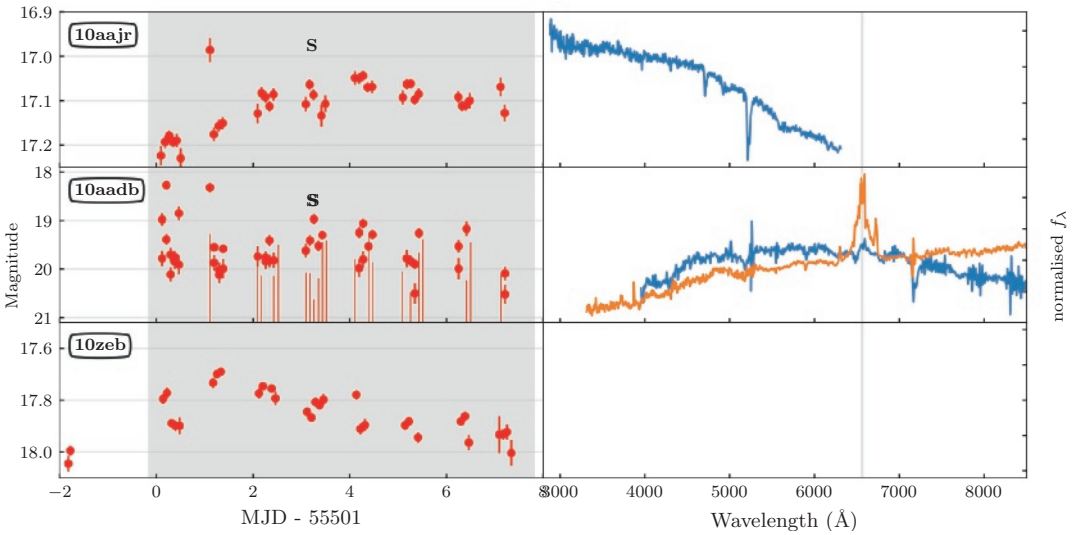

Figure 2.14: Light curves and spectra of flaring AGN. The red dots indicate PTF photometry (R filter), vertical lines indicate upper limits. The grey shaded area indicates the duration of the Sky2Night project. The light curve for extended object PTF10aadb is made using the difference images, the other two light curves (two QSOs) are made without subtraction of the reference image. Spectra were obtained with ACAM and LRIS and normalised to the mean value. The LRIS spectrum for PTF10aadb (yellow) was taken 28 days after the start of the project. The grey line indicates the Hα line.

Table 2.4: The coordinates, the average extinction and brightest stars of PTF fields observed during the project.

FieldID	RA (°)	Dec (°)	Ec. Lon. (°)	Ec. Lat. (°)	Gal. Lon. (°)	Gal. Lat. (°)	$E(B-V)$	Brightest star (mag)
3430	16.0396	16.875	21.2721	9.2741	127.306	-45.8887	0.045	5.68
3431	19.604	16.875	24.459	7.9678	132.161	-45.5128	0.078	3.71
3432	23.1683	16.875	27.6492	6.6942	136.916	-44.8742	0.089	3.71
3433	26.7327	16.875	30.8459	5.4573	141.528	-43.9839	0.053	5.21
3434	30.297	16.875	34.0516	4.261	145.96	-42.8563	0.061	5.21
3435	33.8614	16.875	37.2688	3.1092	150.189	-41.5079	0.098	5.89
3436	37.4257	16.875	40.4995	2.0057	154.198	-39.9567	0.454	6.05
3437	40.9901	16.875	43.7453	0.9542	157.982	-38.2211	0.1	5.32
3438	44.5545	16.875	47.0077	-0.0417	161.541	-36.319	0.224	5.32
3439	48.1188	16.875	50.2875	-0.9783	164.88	-34.2677	0.129	6.1
3440	51.6832	16.875	53.5855	-1.8524	168.01	-32.0832	0.123	6.26
3441	55.2475	16.875	56.9018	-2.6606	170.943	-29.78	0.221	6
3442	58.8119	16.875	60.2362	-3.3998	173.694	-27.3716	0.436	5.91
3531	16.2	19.125	22.3031	11.2882	127.294	-43.6335	0.04	4.77
3532	19.8	19.125	25.4973	9.9791	131.952	-43.26	0.054	4.77
3533	23.4	19.125	28.6931	8.7045	136.519	-42.6317	0.055	5.34
3534	27.0	19.125	31.8936	7.4682	140.956	-41.7586	0.059	5.21
3535	30.6	19.125	35.1015	6.2741	145.233	-40.6537	0.08	5.21
3536	34.2	19.125	38.3192	5.1263	149.324	-39.3323	0.136	5.28
3537	37.8	19.125	41.5487	4.0284	153.216	-37.8109	0.096	5.57
3538	41.4	19.125	44.7918	2.9841	156.9	-36.1066	0.085	5.17
3539	45.0	19.125	48.0498	1.9971	160.376	-34.2362	0.194	4.45
3540	48.6	19.125	51.3236	1.0707	163.647	-32.216	0.106	4.45
3541	52.2	19.125	54.614	0.2084	166.722	-30.0612	0.169	4.87
3542	55.8	19.125	57.921	-0.5867	169.611	-27.7861	0.405	5.67
3543	59.4	19.125	61.2446	-1.3117	172.326	-25.4034	0.321	5.62
3631	16.5306	21.375	23.4947	13.2383	127.489	-41.3668	0.041	4.5
3632	20.2041	21.375	26.7269	11.9154	132.004	-40.9786	0.048	4.77
3633	23.8775	21.375	29.9592	10.6295	136.434	-40.3384	0.07	5.34
3634	27.551	21.375	33.1947	9.3848	140.743	-39.4557	0.07	4.8
3635	31.2245	21.375	36.4363	8.1853	144.9	-38.3429	0.126	4.8

3636	34.898	21.375	39.6865	7.0349	148.883	-37.0148	0.101	5.04
3637	38.5714	21.375	42.9474	5.9376	152.679	-35.487	0.135	5.47
3638	42.2449	21.375	46.2206	4.897	156.279	-33.776	0.342	5.17
3639	45.9184	21.375	49.5076	3.9168	159.683	-31.898	0.432	4.45
3640	49.5918	21.375	52.8094	3.0004	162.892	-29.8688	0.333	4.45
3641	53.2653	21.375	56.1264	2.1513	165.913	-27.7033	0.185	5.22
3642	56.9388	21.375	59.4589	1.3726	168.757	-25.4154	0.191	5.43
3729	16.701	23.625	24.5571	15.2451	127.469	-39.1113	0.043	4.5
3730	20.4124	23.625	27.7929	13.9204	131.812	-38.7253	0.065	4.79
3731	24.1237	23.625	31.0272	12.6345	136.076	-38.0941	0.1	6.24
3732	27.835	23.625	34.263	11.3916	140.229	-37.2265	0.119	4.8
3733	31.5464	23.625	37.5033	10.1956	144.245	-36.1341	0.084	4.8
3734	35.2577	23.625	40.7507	9.0505	148.101	-34.8302	0.09	5.04
3735	38.9691	23.625	44.0071	7.9601	151.786	-33.3295	0.134	5.47
3736	42.6804	23.625	47.2745	6.9281	155.289	-31.6474	0.207	5.17
3737	46.3918	23.625	50.5542	5.958	158.61	-29.799	0.141	5.17
3738	50.1031	23.625	53.847	5.0533	161.748	-27.7994	0.212	5.46
3739	53.8144	23.625	57.1536	4.2172	164.71	-25.6627	0.22	3.6
3826	17.0526	25.875	25.7913	17.1841	127.647	-36.8431	0.086	4.75
3827	20.8421	25.875	29.0625	15.8464	131.867	-36.4421	0.119	4.75
3828	24.6316	25.875	32.3304	14.5504	136.012	-35.7978	0.1	6.25
3829	28.4211	25.875	35.5986	13.3004	140.052	-34.9189	0.116	4.8
3830	32.2105	25.875	38.87	12.1004	143.961	-33.8163	0.063	4.8
3831	36.0	25.875	42.1473	10.9545	147.72	-32.503	0.088	5.02
3832	39.7895	25.875	45.4327	9.8665	151.315	-30.9931	0.153	3.58
3833	43.5789	25.875	48.7279	8.8402	154.739	-29.3015	0.096	3.58
3834	47.3684	25.875	52.0342	7.8791	157.988	-27.443	0.197	5.46
3835	51.1579	25.875	55.3527	6.9866	161.063	-25.432	0.152	5.64

Table 2.5: Overview of the weather conditions during the observations. The time inbetween astronomical twilight was approximately 12.3 h for both PTF and WHT.

		Night 1	Night 2	Night 3	Night 4	Night 5	Night 6	Night 7	Night 8
PTF	time lost (h)	0.6	3.7	0.1	0.2	0.7	0.4	3.7	6.0
	seeing (″)	2.5-3.5	3.0	3.0	2.5	2.0-3.5	2.0	3.0	2.5-3.5
	cloud conditions	good	good	good	ok	ok	ok	bad/ok	bad
WHT	time lost (h)	0	3.0	10.3	0	0	0	6.7	
	seeing (″)	1.5-2.5	1.5-3.0	2.5	2.5	1.5-2.5	1.0	2-3	
	cloud conditions	good	ok-bad	bad	good	good	good	good	

Table 2.6: Number of observations of each field. Night 1 starts at MJD 55501.08.

FieldID	Night 1	Night 2	Night 3	Night 4	Night 5	Night 6	Night 7	Night 8	Total
3430	4	3	4	4	3	4	2	4	28
3431	4	3	5	5	3	4	2	4	30
3432	4	3	5	5	3	4	3	4	31
3433	5	3	4	5	3	3	3	4	30
3434	5	3	5	5	3	4	3	4	32
3435	5	3	5	5	4	5	3	4	34
3436	5	4	5	5	3	4	3	3	32
3437	5	3	5	4	3	5	3	3	31
3438	5	3	4	5	3	5	3	3	31
3439	5	3	5	5	4	5	3	3	33
3440	5	3	5	5	4	5	4	3	34
3441	4	3	5	5	5	5	4	3	34
3442	5	3	5	4	5	5	4	3	34
3531	5	5	4	5	5	4	2	3	33
3532	5	2	4	5	5	4	3	3	31
3533	4	3	4	5	5	4	3	3	31
3534	5	4	4	5	5	4	3	3	33
3535	5	4	5	5	5	5	3	4	36
3536	4	4	4	5	5	5	3	4	34
3537	5	4	5	5	5	5	3	4	36
3538	4	4	5	6	6	5	3	3	36
3539	5	3	5	5	4	5	4	3	34
3540	5	3	5	5	5	5	4	3	35
3541	5	3	5	5	5	5	4	3	35
3542	4	3	5	5	5	6	4	3	35
3543	4	3	5	5	5	5	4	2	33
3631	5	3	5	5	4	4	2	2	30
3632	5	4	5	5	4	4	3	3	33
3633	5	4	5	5	3	5	3	2	32
3634	5	2	5	5	5	5	3	2	32
3635	5	4	5	5	4	5	3	2	33
3636	6	3	5	6	5	5	3	1	34
3637	5	4	5	5	5	5	3	3	35
3638	5	2	5	6	5	5	4	3	35

3639	5	3	5	5	5	4	4	2	33
3640	5	3	5	5	5	5	4	2	34
3641	5	3	5	4	5	5	4	2	33
3642	5	3	5	5	5	5	4	2	34
3729	5	3	5	5	5	4	3	2	32
3730	4	4	5	5	4	5	3	2	32
3731	5	4	5	4	5	5	4	1	33
3732	6	4	5	5	4	5	4	2	35
3733	6	4	5	5	5	5	4	2	36
3734	5	4	5	6	5	5	4	2	36
3735	5	4	6	6	5	5	4	1	36
3736	5	4	5	5	5	6	4	2	36
3737	5	3	5	5	5	5	4	2	34
3738	5	3	5	5	5	5	4	2	34
3739	5	3	5	5	5	5	4	2	34
3826	5	4	5	5	4	5	3	2	33
3827	5	4	5	4	5	5	3	2	33
3828	5	4	5	5	4	5	3	2	33
3829	6	4	5	5	5	5	3	2	35
3830	6	4	5	5	4	5	3	1	33
3831	5	4	6	6	5	6	3	2	37
3832	5	4	4	6	5	6	4	2	36
3833	5	3	5	5	5	6	4	2	35
3834	5	3	4	5	5	5	4	2	33
3835	5	3	5	5	5	5	4	2	34
median	5	3	5	5	5	5	3	2	34
total	290	200	287	296	266	285	199	151	1974

Table 2.7: Properties of the supernovae discovered during the Sky2Night project.

Name PTF ...	Type	Redshift (z)	peaktime (MJD-55501)
10zbk	Ia	0.0645(5)	-9 ± 3
10zcd	Ia	0.132(2)	-1.9 ± 1.8
10zej	Ia "91bg":	0.048(6)	11.5 ± 0.2
10zhi	Ia	0.128(5)	5.5 ± 1.4
10zdq	Ia	0.161(4)	0.3 ± 3.0
10zdk	Ia	0.033(1)	14.2 ± 0.1
10aaes	IIn	0.0337(1)	< -80
10aaho	IIP	0.108(4)	6.5 ± 0.4
10aaey	Ia	0.107(2)	8.4 ± 1.0
10aaiw	Ia "99T"	0.06028(2)	16.3 ± 0.3
10zxs	?	0.135(34)	
10zqz	?	0.152(38)	

Table 2.8: Properties of the CVs found during the Sky2Night project. The quiescence magnitude is given in R if it is detected in PTF images. If the counterpart is too faint, the PanSTARRS r magnitude is given.

Name PTF ...	type	quiescence (mag)	Δr (mag)
10vey	U Gem	$R = 20.5$	3.4
10zdi	U Gem	$R = 18.4$	2.4
10zig	SU UMa:/WZ Sge:	$r = 21.6$	5.5
10zix	U Gem	$R = 19.61$	3.9
10aafc	U Gem	$R = 20.17$	2.5
10aaqc	U Gem	$r = 22.0$	3.5
10aaqt	U Gem	$r = 23.0$	4.5
10aaqj	AM Her:	$R = 20.5$	1.0
10aaqb	U Gem	$R = 18.00$	1.2
10aaqu	U Gem	$R = 20.34$	4.3

Table 2.9: Properties of the flaring M-stars discovered during the Sky2Night project. PTF10aaop showed two outbursts in different nights.

Name PTF ...	Sp type	quiescence R (mag)	ΔR (mag)	time scale (h)	$\log E_R$ ($ergs^{-1}$)
10aacy	M4	16.4	2.3	0.5(1)	32.0
10aagv	M5	18.3	0.6	4.6(4)	32.0
10aakm	M4	15.9	0.6	1.6(1)	32.0
10aaom	M5	18.7	0.7	1.3(2)	31.4
10aaop	M7	19.5	1.5/1.5	<0.3/<0.6	30.0/30.4
10aaqh	M5	16.5	1.3	1.9(1)	32.1
10aarq	M6	20.7	3.5	0.8(1)	31.6
10zfe	M4	18.2	0.6	1.4(1)	32.0
1401fi	M4	21.3	2.2	1.2(2)	34.0

Chapter 3

PTF-Sky2Night II: Fast Galactic transients with the Palomar Transient Factory

J. van Roestel, T. Kupfer, P.J. Groot, R.R. Laher

MNRAS submitted

Abstract

Sky2Night II is a survey with the Palomar Transient Factory for fast transients with timescales less than a day, at low Galactic latitudes. In two campaigns, in 2015 and 2016, we systematically searched for transients in areas spanning 982 and 482 square degrees. We used a cadence of 1 day and 1–2 hours. The duration of both campaigns was 8 days. Follow-up telescopes were used to spectroscopically classify all transients. We determined the rate of flaring M-type stars, outbursting Cataclysmic Variables, Type Ia supernovae and core-collapse supernovae. In addition, we calculated an upper limit to the rate of fast optical transients. We conclude that any population of fast optical transients without counterparts brighter than $R \lesssim 20.4$ and $g \lesssim 20.8$ that are concentrated towards low Galactic latitudes has to be exceedingly rare: $\mathcal{R} \lesssim 4 \times 10^{-5}$ deg^{-2} d^{-1}(timescale of 4 hours). We argue that the number of interlopers at low Galactic latitudes does not hinder the search for kilonova counterparts to binary neutron stars mergers.

3.1 Introduction

The rates and character of fast transients, on time scales of one day or less, are rapidly gaining interest, among others due to their importance for the identification of gravitational wave counterparts (e.g. AT2017gfo, Abbott et al., 2017), as well as for understanding the effects of stellar

flares on the habitability of exoplanets, especially around low-mass, magnetically-active stars (e.g. Airapetian et al., 2018). In the first paper in this series on the PTF-Sky2Night-I project (van Roestel et al., 2018), we explored the rate of fast extragalactic transients at high Galactic latitude to understand the number of possible interlopers in gravitational wave follow-up efforts.

Two additional Sky2Night campaigns, aimed at exploring the rate of intranight transients at lower Galactic latitude, have been performed in 2015 and 2016. The 2015 campaign was aimed at intermediate Galactic latitudes ($10° < |b| < 30°$), while the 2016 campaign explored the Galactic Plane itself ($0° < |b| < 25°$).

3.2 Observations

3.2.1 Survey design

The Sky2Night-II campaigns followed the same set-up as Sky2Night-I: transients were identified using the Palomar Transient Factory (PTF; Rau et al. 2009a; Law et al. 2009a) and rapid spectroscopic classification was obtained with dedicated follow-up telescopes.

The PTF project ran from 2009-2013 and was succeeded by the iPTF project until 2017. To search for transients the PTF and iPTF projects used the 48-inch Oschin Schmidt Telescope (P48) at Palomar Observatory, equipped with the CFH12K camera consisting of 11 working 4k×2k pixel CCDs. The system had a pixel scale of $1.01''$/pixel and a total field of view of 7.26 square degrees.

To rapidly identify transients PTF used an automated image processing pipeline which included bias and flatfield corrections, source identification and photometry. Image subtraction was performed on all new images after a reference image was constructed using at least five individual images for each PTF grid pointing. The subtracted difference images were processed using the 'Real-Bogus'-pipeline (Bloom et al., 2012; Cao et al., 2016) and the best candidate transients were presented to human scanners for confirmation or rejection of any remaining false positives (Cao et al., 2016). During the 2015 campaign, the transient pipeline at LBNL (Cao et al., 2016) was used, while processing of the 2016 data was done at IPAC (Laher et al., 2014). The pipelines are not identical, but they use the same methods and subroutines.

In 2015, the P48 was available for 8 nights (September 8–15, MJD 57273.0–57281.0). During the survey the g-band filter was used. Exposure times of 60 s were used, which was standard for PTF. The target cadence was 1 d, with each field being observed twice within an hour to identify any fast evolving transient and to reject any moving objects. On a perfect night, a total of 160 fields (1 161 deg^2) could have been observed. The Galactic latitudes of the target fields ranged between 10° and 30° (see the left panel of Fig. 3.2).

The 2.5 m Isaac Newton Telescope (INT) on La Palma, Spain, was used to obtain identification spectra. The INT was available for 8 nights, starting after the first night of PTF observations (MJD 57273.75). The Intermediate Resolution Spectrograph (IDS) with the R300B grating was used to obtain spectra of transients brighter than $g \approx 19.5$ mag.

For the 2016 campaign, the P48 was available for 8 nights (June 25–July 2, MJD 57564.0–57572.0). The R_{Mould}-band filter (R in the rest of the paper) and 60 s exposure times were used. The initial target cadence was 1 hr on 34 fields (245 deg^2). The Galactic latitude of the fields ranged between 0° and 13°. After 4 nights of observing, the cadence was halved to 2 hr, and 34

additional fields were included in the survey. The Galactic latitude of these additional fields ranged between 13° and 25° (see the right panel of Fig. 3.2).

The 5.2 m Hale Telescope on Palomar Mountain, US, was used as the follow-up telescope. It was available for 4 nights (29 June 2016 – 2 July 2016, MJD 57568.0–57572.0), equipped with the double beam spectrograph, DBSP (Oke & Gunn, 1982). The R316 grating, blazed at 7500Å was used in the red arm and the R600 grating, blazed at 4000Å, was used in the blue arm. The wavelength coverage for the blue and red arms are 3200–5800 Å and 5200–10500 Å, respectively, with a spectral resolving power of $R \approx 1400$ in both arms. In addition, the P60 telescope equipped with the SED Machine (SEDM, Blagorodnova et al., 2018) was available during the run to obtain low-resolution spectra of bright targets ($g \lesssim 19$).

3.2.2 Execution

Sky2Night-II-2015 campaign

During the 2015 campaign, the weather at PTF was substandard (Table 3.4). On the first two nights, only a few hours were lost, but the weather got steadily worse from night 3 onwards. Less than half of the fields were observed during nights 3 and 4, and no observations were carried out during night 5. Nights 6 and 7 were relatively good, and most fields were observed during these nights. The weather on night 8 prevented any observations altogether. At the end of the project, only 131 fields (950 deg^2) were observed for at least two nights (Table 3.5).

Transient candidates were visually inspected and flagged for follow up as soon as the images were processed ($\approx$ 1 hr after being obtained). At the end of the night, the observer at the INT independently searched the images for transient candidates and vetted any flagged transients. Any new transient brighter than magnitude $g \approx 19$, or any old transient that became brighter than $g \approx 19$, was put in the observing schedule of the INT for the upcoming night. The weather at the INT was good, with a typical seeing of $1''$. A few hours were lost during night 2 and night 4 due to high clouds. A total of 18 transients were observed with the INT. Some of the other (fainter) transients were observed with other PTF follow-up resources: the 4.3m Discovery Channel Telescope equipped with the DeVeny Spectrograph (Bida et al., 2014), the 200 inch Hale telescope equipped with the DBSP, and the Keck Telescope equipped with DEIMOS (Faber et al., 2003). For a total of 36 transients at least one spectrum has been obtained.

Sky2Night-II-2016 campaign

The weather at PTF during the 2016 campaign was excellent (Table 3.4). During the full eight nights, visibility was good and only 1.5 hours was lost during the entire run. The seeing was between $2''$ and $3''$, which is typical for PTF. Any transient candidates were visually inspected and flagged for follow-up observations. After 4 nights, only a few transients were found, partially because the automated pipeline had difficulties processing some of the high stellar density fields. We therefore doubled the number of fields and halved the cadence. During the last four nights, a total of 67 fields were observed at a cadence of 2 hr. See Table 3.6 for an overview.

For any transient that was found in real-time, we obtained a spectrum with P60 equipped with SEDM or the 200-inch Hale telescope equipped with DBSP. Because the telescopes are on

the same site as P48, the weather conditions were the same. For 9 transients we obtained at least one spectrum.

3.2.3 Transient classification

For all transients with a spectrum, we first determined if the transient is of Galactic or extragalactic origin from the wavelength of any emission/absorption lines. For extragalactic transients we used SNID (Blondin & Tonry, 2007) to perform a further spectroscopic classification. For the Galactic objects, we used the spectral energy distribution and Balmer (emission) lines to classify the transients.

For a significant fraction of the discovered transients, no spectrum is available, and we attempted to classify the transient using all other information at our disposal. First, we again visually inspected the PTF images to confirm the transients are real. We then inspected deeper SDSS (Abolfathi et al., 2018) and Pan-STARRS images (Chambers et al., 2016) to determine if a counterpart is present and the angular distance to the nearest object. There are three possibilities: the counterpart is a galaxy or a point source, or there is no (obvious) counterpart. If the transient is close to a galaxy (within $\approx 10''$), we classify it as a supernova. If the transient is closer than $1''$ to a galaxy nucleus, we classify it as a nuclear transient. If a nuclear transient shows activity over many years, or is listed in an AGN catalogue (Brescia et al., 2015; Secrest et al., 2015), we discard the transient for being an AGN. If it is not an obvious AGN, we further try to determine the nature of the transient from its PTF light curve. If the counterpart is a point source, we check if it is a known QSO. If it is not known as a QSO we classify it as a Galactic variable. If no (obvious) counterpart has been detected, or if the nature of the counterpart is uncertain, we simply classify it as a transient and try to infer the nature of the transient from its light curve.

3.3 Results

3.3.1 Survey characteristics

The upper panels of Fig. 3.1 show the distribution of the cadence of the projects. For the 2015 campaign, observations were typically separated by 45-60 minutes. However, fields were not observed regularly between nights due to bad weather, which is reflected in the revisit times of 2, 3, 4 and 5 d (Table. 3.5). The 2016 campaign was not affected by bad weather and therefore the cadence of the observations is close to the design cadence. The longest time between revisits was less than a day, and fields were observed every hour on the first 4 nights, and every 2 hours during the latter half of the project. A small peak can be seen at 4 hours, which is the result of images not being processed properly (usually due to a problem in the astrometric solution, which occurred more frequently at lower Galactic latitudes due to the high stellar density in the images).

The middle panels in Fig. 3.1 show the areal exposure as a function of timescale for the two campaigns. The areal exposure (E_A, in units of $\mathrm{deg}^2\,\mathrm{d}$) is the product of the area that has been surveyed and the effective time that transients (visible for a certain time) could have been detected. It is therefore closely related to the cadence of the survey. Whether a transient could have been detected depends on how many detections are required (two or more for Sky2Night-I), and on how long a transient is detectable. For a detailed explanation, see van Roestel et al. (2018).

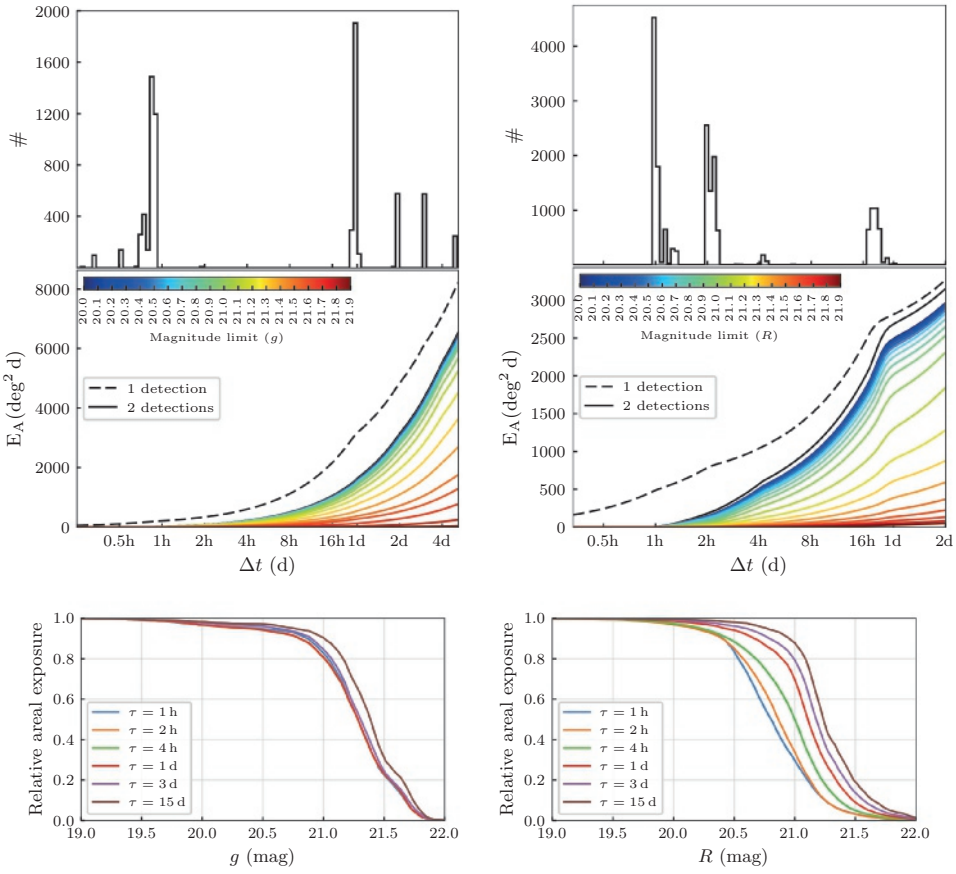

Figure 3.1: The survey characteristics of the 2015 experiment *(left)* and the 2016 experiment *(right)*. *Top* panels display time between observations, *middle* panels the areal exposure of the survey as a function of transient visibility. Coloured lines show the change of areal exposure with limiting magnitude. The *bottom* figure displays the relative areal exposure as a function of source magnitude.

The lower panels of Fig. 3.1 show how the areal exposure decreases as a function of source magnitude for different typical timescales. For the 2015 project, the 90 per cent efficiency ranges from $g = 20.86$ to $g = 21.00$ for timescales of 1 hour to 15 days. For the 2016 project, the 90 per cent areal exposure efficiency ranges from $R = 20.40$ to $R = 20.95$ for the same range of time scales.

3.3.2 Transients in the 2015 campaign

During the 2015 run a total of 83 transients were detected, listed in Table 3.1. Their celestial distribution is shown in the left panel of Fig. 3.2. Light curves and spectra are given in Appendix 3.A.

Stellar Flares

Four transients can be attributed to stellar flares. The lightcurves are shown in Fig. 3.3 and further details are given in Table 3.1. They were identified by their red stellar counterpart in the Pan-STARRS images.

PTF15ctj shows a flare that reached a magnitude of $g = 19.09(3)$ and $g = 19.19(7)$, 40 minutes later. No counterpart was detected in PTF images, but a red stellar counterpart has been detected by Pan-STARRS ($r - i = 2.17(5)$) with only an upper limit to the g-band magnitude of $g > 23.4$, implying a minimal flare amplitude $\Delta g > 4.3$ magnitudes. P60 photometry was obtained 1.14 d after the first detection and showed that the transient had faded to $g = 21.6(2)$, still 1.8 magnitudes brighter than the quiescent magnitude. This is consistent with a linear extrapolation from the first two detections. This suggests that the duration of this flare is long, at least 1.14 d. This is unusually long for an M-flare; the longest flare detected by the Kepler satellite was only 3 hours (Van Doorsselaere et al., 2017) and in (van Roestel et al., 2018) the flares were no longer than 5 hours. The absolute magnitude of the counterpart, $M_J = [7.35\text{–}9.04] \pm 0.23$ (Skrutskie et al., 2006; Bailer-Jones et al., 2018), is consistent with dM2.5–dM5 stars (Pecaut & Mamajek, 2013). However, the *ri-iz* colour is consistent with a spectral type of dM6±0.5 (Best et al. 2018, see also van Roestel et al. 2018).

A spectrum was obtained 1.16 d after the first detection with the DeViny spectrograph mounted at the Discovery Channel Telescope (DCT). The spectrum is not a typical M-star spectrum. It does show a red continuum but without the typical TiO-bands. There is possibly some Hγ, Hδ and Hϵ emission present, but this is uncertain because of the low signal-to-noise ratio of the spectrum. We investigated the possibility that this object is a dwarf Carbon star (dC-star) but both the Pan-STARRS colours and 2MASS colours (Cutri et al., 2003) are not consistent with that of other dC-stars (Gonneau et al., 2016; Harris et al., 2018).

PTF15ctg is a flare of $\Delta g = 1.05(1)$ magnitude on a bright star ($g = 16.85(1)$). It was detected twice on a single night and was faded rapidly, $\Delta g = 2.32(1)\,\mathrm{mag\,d^{-1}}$. The star is blended with a nearby star ($4.0''$distant) and the combination could be confused for an extended object in PTF images, which is likely the reason it was flagged as a potential transient by the PTF pipeline. The counterpart is an M4-dwarf star, on which flares are common (e.g. van Roestel et al., 2018).

PTF15cwu has a point-source counterpart in the PTF reference images ($g = 21.06(3)$) and shows an outburst to $g = 20.18(6)$, an amplitude of $\Delta g = 0.88(7)$ magnitudes. The Pan-STARRS

colours indicate that the counterpart is an M5-dwarf. A DEIMOS spectrum confirms this spectral type.

PTF15cwx shows a peak magnitude of $g = 16.00(1)$ and shows no counterpart in the PTF reference images. Pan-STARRS images do show a faint M6-star ($g = 20.16(1)$). This means that outburst amplitude is $\Delta g = 4.16$. The star has a bright companion ($g = 14.78(1)$) at the same distance ($d = 60.45^{+.11}_{-0.11}$ pc). The glare from this nearby star is likely the reason why the quiescent counterpart was not detected in PTF.

Cataclysmic Variables

The majority of transients designated to be Galactic (i.e. at a redshift of zero, or with a stellar counterpart) are outbursting dwarf-nova type Cataclysmic Variables (CVs, Warner, 2003). We use the light curve, identification spectra, the characteristics of the counterpart, and also long time-baseline photometry to identify 17 transients as dwarf nova outbursts. The Sky2Night photometry shows outburst amplitudes of Δg=1–6 magnitudes, with peak magnitudes of g =16.5–20. The rise time to peak is typically a few days and the duration of the outburst is a few days to weeks.

PTF12jfu, PTF15cnu, PTF15cqj, PTF15cqy, PTF15cuv, and *PTF15cwy* are CVs that have a point-source counterpart which was detected in the PTF reference images ($g = 20$–21.5). The outburst magnitudes are $\Delta g = 4.62(4), 4.40(7), 5.39(8), 0.64(8), 4.22(15)$ and $2.30(11)$ respectively. For *PTF15cvf, PTF15cvt* and *PTF15cvq* a point-source counterpart was detected in the Pan-STARRS images ($g = 21.5$–22.5), leading to outburst amplitudes of $\Delta g = 3.2(2), 5.17(4)$ and $3.2(2)$. For the remaining seven CVs (*PTF15cns, PTF15cqh, PTF15cqi, PTF15csr, PTF15cux, PTF15cvm,* and *PTF15cww*) no counterpart was detected in the Pan-STARRS images, which has an approximate magnitude limit of $g = 23.2$, which makes it the deepest Northern hemisphere survey in the g band. This translates into minimal outburst amplitudes of $\Delta g \gtrsim 5.12, 6.73, 2.83, 3.86, 3.68, 3.28$ and 4.62.

We obtained spectra for 14 of the 17 outbursting CVs. They all show a blue continuum and in 11 spectra display Hα emission, at zero redshift. In most cases also other Balmer emission lines are detected. For a few CVs (*PTF15cqh, PTF15cqy, PTF15cux, PTF15cwy* and *PTF15cww*) He II emission was detected in addition to the Balmer lines. Three CVs only show Balmer absorption lines (*PTF15cqj, PTF15cvt, and PTF15cuv*), commonly detected in dwarf nova outbursts at the peak of the outburst.

Many of the CVs (*PTF15cnu, PTF15cqg, PTF15cqh, PTF15cqj, PTF15cvf, PTF15cvg, PTF15cvm, PTF15cvt, PTF15cww, PTF15csr, PTF15cuv, PTF15cwy,* and *PTF12jfu*) show additional outbursts in their overall PTF light curves, before or after the Sky2Night campaigns, additional evidence that these objects are CVs.

The light curve of *PTF15cwy* is significantly different than the others: it shows a slow rise over a few weeks instead of a rapid rise in a few days. On top of its slow rise, it exhibits short timescale variability on the timescale of hours. This behaviour is most consistent with VY Scl-type CVs (e.g. Leach et al., 1999), where slow transitions from a low to a high state system occurs.

Spectroscopically confirmed supernovae

A total of 55 extragalactic transients were detected, where 'extragalactic' has been defined as 'transients close to a galaxy', not necessarily requiring a spectroscopic identification (Section 3.2.3). We have been able to spectroscopically classify 19 of the 55 extragalactic transients (Fig. 3.4). For *PTF15ccu* (SN2015ac) no spectrum was obtained, but this bright, nearby supernova was already classified by Ochner et al. (2015). Out of the 19 spectroscopically classified supernovae, 15 are Type Ia supernovae (SNIa) and the other 4 are core-collapse supernovae (SNII), see Table 3.1.

The SNIa were typically detected from 2 weeks before peak magnitude up to 15 d after the peak. Peak magnitudes range between $g \approx 18$ and $g \approx 20.5$ (disregarding the very nearby *PTF15ccu*). A few of the supernovae do not have an obvious host galaxies. For *PTF15cqe* there was no extended source within $40''$ in the Pan-STARRS images. For *PTF15cqe* the nearest extended source in Pan-STARRS is $26''$ away, although there were some faint point sources which could be unresolved galaxies.

There are a few exceptional SNIa in the sample. *PTF15ccu* is a nearby SNIa and was first discovered 42 days before the start of our project, when it was already fading. *PTF15cpc* shows similarities to a '91T'-like supernova (i.e. no Si-II 5972 Å in the spectrum (e.g. Taubenberger, 2017)). *PTF15clp* is an old, nearby SNIa, which was first detected 140 days before the start of our survey (Gress et al., 2015b). When we detected it, *PTF15clp* was fading and further declined from $g = 20.3$ ($M_g = -14.4$) to $g = 21.2$ in 10 days. However, shortly after the end of our campaign it rebrightened by ≈0.3 magnitudes, after which it faded again to $g = 21.2$ (see Fig. 3.4). This is possibly due to interactions with circumstellar material around the supernova (a Ia-CSM supernova, Silverman et al., 2013). The narrow Hα emission line supports this explanation (see Fig. 3.4).

There are four core-collapse supernovae in the sample. *PTF15cna* is a Type IIb that occurred in a faint, small galaxy. The slowly evolving light curve reached its peak magnitude of $g = 18.3$ ($M_g = -18.8$) 10 days after the first detection. The supernova started to decline slowly and was last detected by PTF at $g = 21.3$, 48 days after the peak. Spectra were obtained 17 days after peak which classified the supernova as a type IIb at a redshift of $z = 0.060(1)$.

PTF15cno is a faint supernova ($g = 20.5$) which was slowly declining when it was discovered. A DEIMOS spectrum was most similar to Type IIP templates 5–40 days after the peak.

PTF15crj is a nearby Type II that exploded 2-3 days before the start of the survey in an elliptical galaxy (Smith et al., 2015). Spectra obtained 3 days after the first detection (and 5 days before peak) show many narrow emission lines, including Balmer, O-II, and O-III. Between the first two nights, it shows a rapid rise of $\Delta g = 1.98(6)\,\mathrm{mag\,d^{-1}}$ with the midpoint absolute magnitude of $M_g = -15.1$ (see Fig. 3.4). It reached a peak magnitude of $M_g = -17.2$ about 6 days after the first detection.

PTF15cvl was first detected at magnitude $g \approx 20.8$. The following night it had risen to its peak magnitude of $g \approx 20.1$ ($M_g = -17.91(7)$) at a rate of $\Delta g = 0.77(14)\,\mathrm{mag\,d^{-1}}$ at $z = 0.0876$ (see Fig. 3.4). The first spectrum of *PTF15cvl*, obtained 1 day after peak, shows no clear features except for one broad emission line at 5065Å (rest wavelength), which could be Si-II emission. In a spectrum obtained 3 days later this feature has disappeared, but weak Balmer line absorption lines and an O-II emission line (3727Å), as well as other S-II emission lines appeared.

Spectroscopically unconfirmed supernovae

We found 20 transients at a distance between $1''$ and $9''$ to a host galaxy (Fig. 3.4), therefore classified as 'SN' in Table 3.1. They are all faint ($g > 19.5$), which is the reason why no spectra have been obtained. Their light curves all show slowly evolving transients, consistent with typical supernovae, except for *PTF15cpd* which is discussed below. We compared the transients with well-sampled light curves to a supernova Ia lightcurve template (Nugent et al., 2002) with $M_V = -19.3$ using SNCosmo (Barbary et al., 2016). *PTF15cly, PTF15cms, PTF15cmz, PTF15cnm, PTF15coe, PTF15coy, PTF15cpb, PTF15crd, PTF15cse, PTF15ctk* and *PTF15cxz* are all well described by the lightcurve template shifted to redshifts of $z = 0.12$–0.2 (taking into account foreground reddening). For the other transients the lightcurve is too sparsely sampled or the quality too low for a model fit to produce any meaningful results.

PTF15cpd stands out because of the shape of its lightcurve (panel 2 of Fig. 3.5). The transient was first detected 18 days before the start of the survey. Observations the following nights showed that it was declining. The transient kept fading until the beginning of the S2N campaign, at which point it started rebrighten. After 12 days it was 0.7 mag brighter than at the start of the campaign. The transient was also detected in i-band by Pan-STARRS (*PS15bve*, Huber et al., 2015), included in Fig. 3.5, resulting in $g - i \approx 0.90$ (with a reddening of $g - i \approx 0.15$, Yuan et al., 2013). The difference in i-band magnitude between the two first Pan-STARRS observation is $\Delta i = -0.20 \pm 0.09$, which suggests that the supernova also got brighter in the i-band. In addition, Pan-STARRS observed the field 17 days before the first PTF detection and did not detect the supernova, which means that the first peak occurred less than 17 days before the first PTF detection.

PTF15cpd is located $5.4''$ away from a faint galaxy ($g = 21.9(4)$) with a photometric redshift of $z_{\rm phot} = 0.352(98)$. This makes the projected distance 26^{+4}_{-6} kpc. The observed peak absolute magnitude, after correcting for the Galactic extinction of $A_g = 0.39$ (Schlafly & Finkbeiner, 2011), is $M_g = -21.9^{1.5}_{-1.0}$. This would make it a superluminous supernova (e.g. Gal-Yam, 2012).

Nuclear transients

We identified a total of 16 'nuclear' transients (Fig. 3.6), located within $1''$ distance to the host galaxy, which could not be rejected as an AGN based on previous activity. We again compared their light curves to a SN Ia model as in Section 3.3.2. We found that *PTF15cua, PTF15cnp, PTF15cqa, PTF15cpa, PTF15cyw, PTF15crn* and *PTF15cwh* show a rise and decay that are consistent with that of an SNIa with redshifts in a range of $z \approx 0.15$–0.25.

PTF15cnp appeared in a host galaxy with a photometric redshift of $z_{phot} = 0.60(14)$. If this redshift is correct, the supernova would be superluminous ($M_g = -22.6^{+1.4}_{-0.9}$, assuming $A_g = 0.232$). However, superluminous supernovae typically have slow rises and decays. When we compare the light curve with SNIa models, the redshift for the best fit model is $z = 0.20$. It is most likely that the photometric redshift is overestimated and *PTF15cnp* is a regular SNIa at a lower redshift.

PTF15coh is the brightest apparent nuclear transient and only shows a rapidly fading light curve ($-0.078\,\mathrm{mag\,d^{-1}}$). This is consistent with a fading SNIa.

PTF15cre is a transient in a faint galaxy. It shows a rise by 0.5 magnitude in 4 days up to $g = 20.2$, at which it started to fade. The light curve does not match that of a SNIa, but is a good

match to the SNIIn light curve template by Gilliland et al. (1999).

PTF15ctp shows a flat light curve at $g \approx 19.7$ for 15 days and then brightens by $\Delta g = 0.9$ mag within two weeks. The transient location is consistent with the nucleus of the host galaxy. It is therefore most likely that this is an AGN outburst.

PTF15cvn has a point-source counterpart/host in the Pan-STARRS and the SDSS images. Yang et al. (2017) showed the host to be a 'blueberry' galaxy (a dwarf starburst galaxy) at a redshift of $z = 0.046655$. With this redshift, the peak absolute magnitude of this transient is $M_g \approx -16.5$. The transient was first detected at $g \approx 20.1$ and earlier upper limits suggest a risetime of at least 1 magnitude in 5 days. After the first detection it got only slightly brighter (0.2 magnitudes in 9 days), after which it started to fade. This is most consistent with a core-collapse supernova.

For *PTF15cqw* and *PTF15crz* the lightcurve is not of sufficient quality and length to draw any conclusion about the nature of the transient.

Transient with an uncertain classification

For seven transients the classification was uncertain. No spectrum is available for these transients and the counterpart/host galaxy was uncertain or there was no counterpart/host galaxy at all (Fig. 3.7).

PTF15cri has no detected counterpart/host in the SDSS or Pan-STARRS images. The PTF light curve shows a transient with a peak magnitude of $g = 19.8$ which is visible for 30 days. No activity has been detected in observations by PTF in the year before or after the transient occurred. The lightcurve shape is in good agreement with SNIa model, and we therefore conclude that this transient is most likely a SNIa, either 'hostless' or in a faint host galaxy below our detection limit.

PTF15ctv is a transient that was detected twice during only a single night at $g = 20.21$. It showed no significant evolution within a time scale of half an hour. The next night the transient had faded below the detection limit. The field was not observed the nights before the transient was detected. No counterpart/host has been detected in Pan-STARRS images. *PTF15ctv* could be a fading CV outburst. The other possibility is an energetic M-flare, but in those cases a faint red counterpart is usually seen in the Pan-STARRS images.

PTF15cvb is a possibly hostless transient. There is, however, a pair of two faint galaxies at $10.6''$ and $10.7''$ distance. The transient was detected $\approx$5 days before peak ($g = 20.2$) after which it started to decline. The lightcurve is in good agreement with the SNIa model, and we therefore conclude that it is likely a SNIa.

PTF15cvg is a hostless transient (no counterpart in SDSS or Pan-STARRS images) of $g \approx 21.0$ and is visible for 43 days. The light curve shows no particular trend. No PTF observations have been obtained before the first detection. The transient could be a slowly fading supernova.

PTF15cvd is a transient without a counterpart. The first night it peaked at magnitude of $g = 19.8$. Two nights later it faded to a magnitude of $g = 20.8$. Upper limits of $g > 20.2$ two nights before the first detection indicate the transient has a fast rise time. This is most consistent with a short duration dwarf nova or AM CVn outburst.

PTF15cvy is a hostless transient (no counterpart in SDSS or Pan-STARRS) that was visible for 16 days at $g \approx 21$. The lightcurve does not show any clear trend, but the signal-to-noise ratio

is low since it is close to the detection limit. There was some activity (4 detections at $g \approx 21$) 12 days before the start of our campaign. This suggests that the transient is possibly a repeatedly outbursting CV, or the pre-campaign detections belonged to the same prolonged outburst.

PTF15cwc is a hostless transient which peaked at $g \approx 21$. The nearest source in the Pan-STARRS image is $12.5''$ distant and is a point source. There are no galaxies within a radius of $20''$. The 14-day light curve shows a symmetric rise and decay and is consistent with a SNIa lightcurve. The transient could also be a CV, although the rise time of CVs is usually faster.

Table 3.1: Transients in the 2015 Sky2Night-II program. For Galactic sources we report the distance from Bailer-Jones et al. (2018) which are based on the Gaia DR2 parallax measurements (Gaia Collaboration et al., 2018a). For extragalactic objects, we report the redshift as measured from the spectra, if available. If no spectra are available, the SDSS photometric redshift is given (Beck et al., 2016). The quiescence magnitudes are taken from the Pan-STARRS DR1 catalogue, for point sources using the 'MeanPSFMag' and for extended sources the 'MeanKronMag' magnitude values(see Chambers et al., 2016). References for individual objects: [a]: Gress et al. (2015a), [b]: Balanutsa et al. (2013), [c]: Ochner et al. (2015), [d]: Smith et al. (2015), [e]: Petrushevska et al. (2015a) [f]:Gress et al. (2015b), [g]:Papadogiannakis et al. (2015), [h]:Petrushevska et al. (2015b), [i]:Taddia et al. (2015), and [j]:Yang et al. (2017).

Name PTF...	Ra (°)	Dec (°)	First detection (MJD–57273)	Type	distance/redshift (pc)	quiescence	Spec.Tel/Instrument
15ctj	322.301483	28.762165	1.2	Flare	346^{+202}_{-93} pc	$g > 23.2$	DCT
15ctg	330.535797	37.417011	1.3	Flare	$119.9^{+0.9}_{-0.9}$ pc	$g = 16.85(1)$	
15cwu	343.977661	38.643215	6.3	Flare	301^{+27}_{-23} pc	$g = 21.06(3)$	Keck
15cwx	347.409637	44.885475	6.3	Flare	$61.0^{+0.5}_{-0.5}$ pc	$g = 20.16(1)$	
12jfu[a]	344.135703	35.710749	−4.3	CV		$g = 21.41(5)$	
15cns	327.849915	34.760380	−3.7	CV		$g > 23.2$	INT
15cnu	339.138489	37.772701	−3.6	CV	1240^{+920}_{-440} pc	$g = 19.69(4)$	DCT
15cqg	317.100403	23.474806	−1.8	CV		$g = 21.38(5)$	
15cqh	331.641418	31.360506	−1.8	CV		$g > 23.2$	INT
15cqi	323.950073	32.923801	−1.8	CV		$g > 23.2$	
15cqj	333.515747	37.581356	−1.8	CV		$g = 21.63(4)$	INT
15cqy	325.033386	30.938372	−0.8	CV	1020^{+1340}_{-580} pc	$g = 21.03(4)$	INT
15csr	13.973404	46.297951	0.4	CV		$g > 23.2$	DCT,INT
15cuv	328.434601	32.246235	2.2	CV		$g = 20.74(7)$	INT
15cux	2.471562	45.654015	2.4	CV		$g > 23.2$	INT
15cvf[b]	10.034342	49.468571	3.5	CV		$g = 22.14(17)$	INT
15cvm	348.297852	31.366665	5.3	CV		$g > 23.2$	Keck
15cvt	351.016846	51.721687	5.4	CV		$g = 21.42(4)$	INT
15cvq	26.126923	46.552895	5.5	CV		$g = 22.0(2)$	INT
15cwy	331.490540	36.058640	6.2	CV	1610^{+850}_{-460} pc	$g = 20.36(11)$	INT

15cww	332.637756	35.931465	6.3	CV		$g > 23.2$	INT
15ccu[c]	349.180941	33.997619	−20	SNIa-pec	$z = 0.017068$	$g = 14.19(5)$	
15clp[f]	339.795319	34.307137	−14.7	SNIa	$z = 0.0206$	$g = 17.16(2)$	Keck
15cma[g]	23.137955	42.642967	−14.5	SNIa	$z = 0.084$	$g = 18.60(2)$	DCT
15cna	350.045624	28.849466	−4.6	SNIIb	$z = 0.06$	$g = 21.90(12)$	multiple
15cno[i]	332.069458	24.491674	−3.7	SNII	$z = 0.075$	$g = 21.21(5)$	Keck
15cnq[e]	331.971112	29.373819	−3.7	SNIa	$z = 0.0837$	$g = 17.210(5)$	Keck
15cqc	329.311859	27.254459	−2.8	SNIa	$z = 0.105$	$g = 20.14(6)$	INT
15cqe	317.541412	20.707788	−2.8	SNIa	$z = 0.18$	$g > 23.2$	Keck
15cqf	318.943298	20.199705	−2.8	SNIa	$z = 0.0794$	$g = 16.45(1)$	Keck
15cpc[e]	354.573364	32.123894	−2.7	SNIa-'91T'	$z = 0.1702$	$g = 19.55(2)$	Keck
15cpt	11.372441	36.295074	−2.6	SNIa	$z = 0.147$	$g = 19.31(2)$	INT
15cqn[e]	357.490692	41.792088	−1.7	SNIa	$z = 0.1662$	$g = 18.34(1)$	Keck
15crj[d]	336.118561	32.659016	−0.8	SNII	$z = 0.0216$	$g = 15.986(1)$	multiple
15crv[e]	2.623742	41.371796	0.3	SNIa	$z = 0.144$	$g = 21.98(13)$	DCT
15ctl	348.554962	26.965843	1.3	SNIa	$z = 0.167$	$g = 20.18(4)$	INT
15cup	337.044403	30.111048	2.3	SNIa	$z = 0.219$	$g = 20.86(4)$	INT
15cvl	354.849060	36.234711	5.0	SNIIP	$z = 0.0876$	$g = 17.85(2)$	Keck, Hale
15cvp[h]	18.451056	41.390778	5.4	SNIa	$z = 0.121$	?	Hale
15cvw[h]	317.167603	15.230331	6.2	SNIa	$z = 0.096$	$g = 18.24(2)$	Keck
15cly	16.674780	38.372482	−14.5	SN		$g = 21.48(22)$	
15cms	339.689484	33.532867	−4.7	SN		$g = 19.16(4)$	
15cmv	12.943032	43.179085	−4.6	SN	$z = 0.128(22)$	$g = 18.17(39)$	
15cmy	11.980964	43.521999	−4.6	SN	$z = 0.202(46)$	$g = 19.66(3)$	
15cmz	0.836906	42.704239	−4.6	SN		$g = 15.80(1)$	
15cnj	323.633270	17.732044	−3.7	SN	$z = 0.226(51)$	$g = 20.96(4)$	
15cnm	327.798706	21.200390	−3.7	SN	$z = 0.084(18)$	$g = 17.97(1)$	
15coe	358.436096	41.401539	−3.6	SN		$g = 21.03(16)$	
15cps	327.916809	25.289459	−2.8	SN	$z = 0.226(78)$	$g = 20.96(4)$	

15coy	341.828796	30.736967	−2.7	SN	$z = 0.177(35)$	$g = 19.92(2)$	
15cpb	0.461731	32.221191	−2.7	SN	$z = 0.157(17)$	$g = 18.20(11)$	
15cpd	358.027710	36.555401	−2.7	SN	$z = 0.352(98)$	$g = 21.89(35)$	
15cpe	349.132416	32.642498	−2.7	SN	$z = 0.38(12)$	$g = 18.20(11)$	
15crd	359.817932	37.545986	−0.6	SN		$g = 18.68(2)$	
15cse	349.034668	37.036240	0.3	SN		$g = 20.20(10)$	
15ctk	327.829254	23.826366	1.2	SN	$z = 0.25(17)$	$g = 21.56(30)$	
15cts	6.124288	50.538715	1.5	SN		$g = 19.64(4)$	
15cxq	9.965068	39.417095	6.4	SN	$z = 0.178(36)$	$g = 19.89(2)$	
15cxz	22.017426	40.971107	9.4	SN	$z = 0.199(9)$	$g = 17.72(3)$	
15cyd	24.300034	43.868385	9.4	SN		$g = 20.96(4)$	
15cua	351.47522	35.266525	−4.7	nuclear SN (Ia:)		$g = 20.40(4)$	
15cnp	325.972656	24.891933	−3.7	nuclear SN	$z = 0.249(44)$	$g = 20.35(6)$	
15cnn	330.294128	24.162016	−3.7	nuclear SN	$z = 0.092(17)$	$g = 17.76(1)$	
15coh	342.237793	24.938910	−3.7	nuclear SN	$z = 0.0452(1)$	$g = 16.885(9)$	Keck
15cqa	347.643066	27.490721	−2.7	nuclear SN	$z = 0.151(9)$	$g = 19.22(4)$	
15cpa	8.086938	37.884872	−2.7	nuclear SN	$z = 0.280(30)$		
15cyw	323.582458	19.779451	−1.8	nuclear SN	$z = 0.25(17)$		
15cqw	316.879761	17.009695	−0.8	nuclear			
15cre	344.859314	25.974714	−0.7	nuclear SN/CV		$g = 21.2(2)$	
15crn	336.313568	30.125393	0.3	nuclear SN	$z = 0.60(14)$		
15crz	359.009583	36.122330	0.3	nuclear	$z = 0.099(21)$		
15ctp	1.573564	46.184128	1.4	nuclear AGN-flare:			
15ctt	13.728311	41.806980	1.5	nuclear	$z = 0.143(31)$		
15cvn	348.489258	29.586926	5.8	nuclear CC-SN	$z = 0.046655$[j]	$g = 21.16(5)$	
15cwh	356.551239	39.852421	6.3	nuclear			
15cyr	15.443899	46.368176	9.4	nuclear SN	$z = 0.144(35)$		
15cri	342.027863	39.788040	−0.7	hostless SN Ia		$g > 23.2$	
15ctv	38.210499	48.207172	1.5	hostless transient		$g > 23.2$	

15cvb	343.967377	26.250139	2.3	hostless SN	$g > 23.2$
15cvg	4.875271	41.718781	3.4	hostless transient	$g > 23.2$
15cvd	32.999928	49.429108	3.5	hostless transient	$g > 23.2$
15cvy	343.592102	35.911690	6.3	hostless transient	$g > 23.2$
15cwc	340.445007	30.897173	6.3	hostless transient	$g > 23.2$

3.3.3 Transients in the 2016 campaign

During the 2016 campaign a total of 14 transients were detected (Table 3.2, Fig. 3.8). For 9 transients a spectrum has been obtained. We use the spectra, light curves, and SDSS and Pan-STARRS images to identify the transients, see Section 3.2.3.

Stellar flares

We detected one stellar flare during the project, *PTF16bnj*, which peaked at $R = 16.97(1)$. It was detected three times within 2 hours and faded by 0.8 magnitude per hour. The host star is not detected in the PTF reference image because it is blended with a nearby, brighter star. In the Pan-STARRS image, a red star is visible with $r = 19.21(1)$. The Pan-STARRS $r - i$ and $i - z$ colours correspond to a spectral type of M5 (see van Roestel et al., 2018), while the nearby companion is a background star ($d \approx 3\,\mathrm{kpc}$).

Cataclysmic Variables

Nine transients have been identified as CVs. The light curves are similar to those found in the 2015 survey. For the majority of the CVs the spectra feature an Hα absorption line, except for *PTF16bot*, indicating they were detected near the peak of the outburst. For 4 of the CVs, the quiescent counterpart is detected in the Pan-STARRS images. No earlier outbursts have been detected because PTF had not observed most of the survey area before.

Supernovae

PTF16boo is a transient in the outskirts of a large elliptical galaxy (at a center distance of $13.3''$) and is slightly closer to a satellite galaxy, at a center distance of $10.6''$. The spectrum of the transient best matches that of a 10-days old SNIa at a redshift of $z = 0.0549$. The light curve during the project does not show any evolution over 4 days. An upper limit at $g \gtrsim 20.8$ obtained 14 days before discovery confirms that this is a relatively young supernova.

PTF16bnv is a transient in the outskirts of a large galaxy (with a center distance of $9.1''$) at a redshift of $z_{\mathrm{phot}} = 0.096(8)$. The spectrum of *PTF16bnv* shows a strong Hα emission line, and weaker emission lines of Hβ and OI (9266 Å) at a redshift of $z = 0.088(1)$. The lines are relatively broad, and the spectrum is most similar to old SN II supernovae.

PTF16bnx does not have a clear counterpart in the PTF reference images, nor in the Pan-STARRS images. The nearest galaxy is $8.6''$ away and is faint ($r = 20.41(5)$). A spectrum of *PTF16bnx* shows a strong, broad Hα emission line and a broad Hβ emission line. The spectrum best matches templates of an old SNII at a redshift of $z \approx 0.088$, which would imply a projected distance 14.2 kpc. This is far, but not unusual (Hakobyan et al., 2009).

PTF16bny is a supernova that occurred in a face-on spiral galaxy, $4.3''$ from the core. The redshift estimate from SDSS photometry is $z_{\mathrm{phot}} = 0.084(27)$. No spectrum is available which prohibits further classification.

Table 3.2: Transients in the 2016 Sky2Night-II program. For Galactic sources we report the distance from Bailer-Jones et al. (2018) which are based on the Gaia DR2 parallax measurements (Gaia Collaboration et al., 2018a). For extragalactic objects, we report the redshift as measured from the spectra, if available. If not, the SDSS photometric redshift is given (Beck et al., 2016). The quiescence magnitudes are taken from the Pan-STARRS DR1 catalogue, using for point-sources the 'MeanPSFMag' and for extended sources the 'MeanKronMag' magnitude(see Chambers et al., 2016). References for individual objects: [a]: Denisenko et al. (2012)

Name PTF ...	Ra (°)	Dec (°)	First detection (MJD–57564)	Type	distance/redshift (pc)	quiescence (mag)	Spec.Tel
16bnj	284.023497	27.781053	0.5	flare	$d = 380^{+25}_{-24}$ pc	$r = 19.32(3)$	
16bnh	277.845770	15.620630	1.4	CV		$r = 19.88(3)$	
16bnl	287.409228	28.854882	1.4	CV		$r > 22.8$	Hale
16bnp	278.443230	19.006542	2.3	CV		$r > 22.8$	Hale
16bno	283.383818	20.186645	2.2	CV		$r > 22.8$	Hale
16bpb	280.662169	26.613131	7.4	CV	$d = 2800^{1650}_{-930}$ pc	$r = 19.56(1)$	Hale
09bbm	272.364888	24.099640	$\ll 0$	CV	$d = 2010^{+850}_{-510}$ pc	$r = 17.12(1)$	
16boc	267.340758	19.739767	4.4	CV		$r > 22.8$	Hale
16bot	263.601437	13.670348	6.3	CV		$r = 21.52(9)$	Hale
16box[a]	267.258840	19.224930	7.3	CV	$d = 2010^{+1920}_{-890}$ pc	$r = 19.37(1)$	
16bnx	272.040502	21.784610	5.2	SNIIn	$z = 0.088(1)$	$r = 20.41(5)$	Hale
16bny	274.172437	13.904836	5.2	SN	$z = 0.084(26)$	$r = 18.84(5)$	
16bnv	275.111067	23.459988	5.2	SNII	$z = 0.088(1)$	$r = 20.37(18)$	Hale
16boo	261.413669	21.952154	5.4	SNIa	$z = 0.0549(1)$	$r = 16.63(3)$	Hale

3.3.4 Rates

The rate of detected transients is calculated as follows:

$$\mathcal{R} = \frac{N}{\epsilon^2 E_A(\tau)} \ (\mathrm{deg}^{-2}\,\mathrm{d}^{-1}) \tag{3.1}$$

with N the number of transients, ϵ the detection efficiency per image, and E_A the effective exposure. Since N (per class) is a small number in our experiment, Poisson statistics were used to calculate the associated uncertainties (e.g. Gehrels, 1986).

We used a simple estimate for the detection efficiency: all transients brighter than the detection limit are recovered ($\epsilon = 1$) and those fainter than the detection limit are not ($\epsilon = 0$). Frohmaier et al. (2017) performed a detailed test of the recovery rate as function of limiting magnitude, brightness of the transient, seeing, angular distance to the nearest galaxy and other parameters. Such a level of detail is not needed in this work, since the Poisson uncertainty dominates the rates and is of the order of 20 per cent or more. We note that Frohmaier et al. (2017) found a maximum recovery efficiency of 97 per cent. Including this correction would increase the rates and limits in Table 3.4 by a factor $0.97^{-2} = 1.06$.

In Section 3.1, we calculated the areal exposure (E_a) as function of visibility time of transients (τ), estimated for each transient based on its PTF light curve. We use the 90 per cent magnitude limits (see Section 3.1). For flares, the light curve was fit with an exponential function (in flux), from which the visibility time was derived. For dwarf novae and supernovae the PTF light curve was used to estimate the visibility time. For sparsely sampled dwarf novae light curves, the most conservative estimate for the visibility time was used: the timespan between the first and last detection above the magnitude limits. For sparsely sampled supernovae, template light curves (Gilliland et al., 1999; Nugent et al., 2002) combined with the redshift were used to estimate the visibility time.

To calculate the observed rates, the areal exposure, without taking into account losses resulting from the different limiting magnitudes, was taken. As shown in the bottom panels of Fig. 3.1, this is correct until a threshold magnitude, after which the efficiency rapidly decreases. The 90 per cent efficiency ranges between $g = 20.8$ and $g = 21.0$ for the 2015 campaign, and between $R = 20.4$ and $R = 21.0$ for the 2016 campaign (for visibility time scales of 1 hr to 15 d).

Table 3.3 shows the observed rates of the different types transients found in the three Sky2Night campaigns. The table shows the number of detections for each type and the areal rates calculated as described above. For galactic objects (flares and dwarf novae) we also report the rate for transients without a detected counterpart in the PTF reference images.

As we have not observed any unidentifiable fast optical transients, we use our data to also calculate an upper limit on the rate of these events at two different characteristic time scales in each campaign; 1hr and 2hr for the 2015 campaign and 4hr and 1d for the 2016 campaign. This calculation is analogous to that performed in (van Roestel et al., 2018).

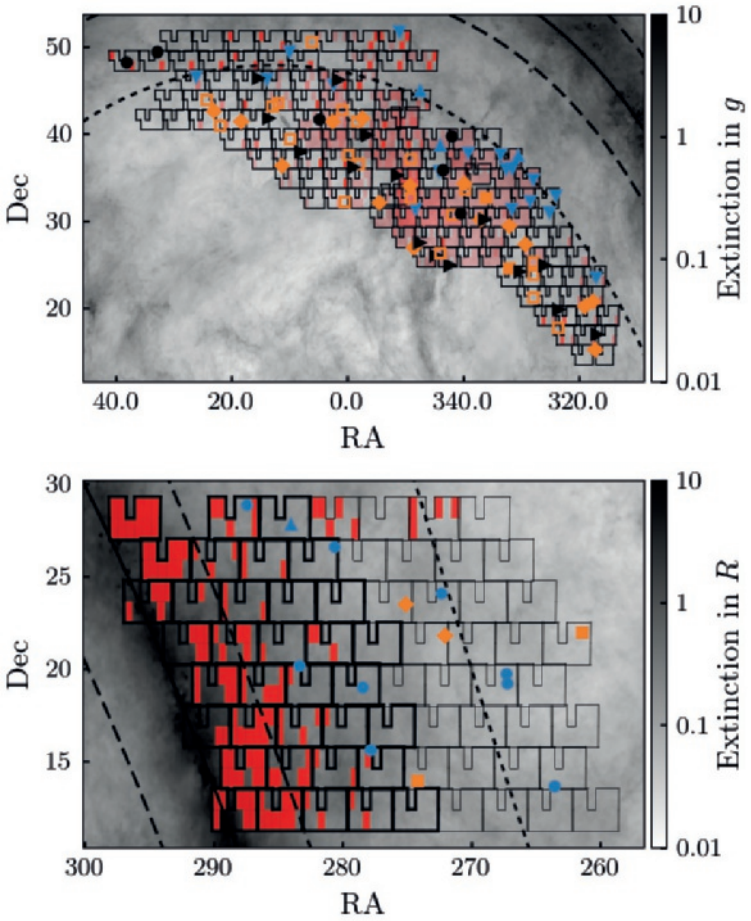

Figure 3.2: Overview of all observed fields and detected transients. Top panel shows the 2015 campaign. Bottom panel shows the 2016 campaign, where the initial fields have a thick outline, and the fields added later have a thin outline. Yellow markers show extra-galactic transients, blue markers show galactic transients, and black markers show unclassified transients. Red shaded regions indicate areas that had some problems with the data processing.

Table 3.3: Observed rate of transients for the Sky2Night project (Sky2Night-I: van Roestel et al. 2018, Sky2Night-II: this work). The uncertainties indicate the 95 per cent confidence interval. Upper-limits for fast optical transients are 95 per cent confidence upper-limits. These limits assume a detection efficiency of $\epsilon = 1$ (see equation 3.1) and all exposures are used to calculate the areal exposure.

Paper	Sky2Night-I		Sky2Night-II (this work)			
Year, band	2012, R-band		2015, g-band		2016, R-band	
number, rate	N	$\mathcal{R}$ (10^{-4} deg^{-2} d^{-1})	N	$\mathcal{R}$ (10^{-4} deg^{-2} d^{-1})	N	$\mathcal{R}$ (10^{-4} deg^{-2} d^{-1})
M-flares	9	118^{+94}_{-58}	3	181^{+257}_{-129}	1	16^{+36}_{-13}
no PTF counterpart	2	35^{+64}_{-26}	3	181^{+257}_{-129}	1	16^{+36}_{-13}
DN	5	$12.8^{+13.6}_{-7.9}$	17	20^{+11}_{-8}	9	22^{+17}_{-11}
no PTF counterpart	2	$6.0^{+10.3}_{-4.6}$	14	17^{+11}_{-7}	6	15^{+13}_{-8}
Supernova - Ia	8	$10.0^{+8.2}_{-5.3}$	15	$5.1^{+2.9}_{-2.1}$	1	$0.8^{+1.9}_{-0.7}$
Supernova - CC	1	$2.0^{+4.4}_{-1.6}$	4	$1.3^{+1.5}_{-0.8}$	2	$1.5^{+2.6}_{-1.2}$
Supernova - unknown	2	$3.1^{+5.2}_{-2.4}$	25	$12.8^{+5.1}_{-4.0}$	1	$0.8^{+2.0}_{-0.7}$
FOTs (1 h)					0	< 76
FOTs (2 h)					0	< 47
FOTs (4 h)	0	< 37	0	< 144	0	< 35
FOTs (1 d)	0	< 9.3	0	< 20	0	< 13

3.4 Discussion

The Sky2Night campaigns have resulted in two separate sets of information. The first is on a number of unusual transients, and the second is on the rate of transients.

3.4.1 Unusual transients

Fast rising supernovae

In the 2015 campaign, we found two rapidly rising supernovae, *PTF15crj* and *PTF15cvl*. Their rise time and absolute magnitudes (corrected for foreground extinction) are $\Delta g = 1.98(6)\,\mathrm{mag\,d^{-1}}$ at $M_g = -16.36(1)$ and $\Delta g = 0.77(14)\,\mathrm{mag\,d^{-1}}$ at $M_g = -18.23(7)$ (Section 3.3.2). We compare these numbers to the samples of fast rising transients found with Pan-STARRS (Drout et al., 2014) and Subaru (Tanaka et al., 2016), shown in Figure 9 in the latter paper.

PTF15crj is similar to three of the fast Subaru transients; SHOOT14ha, SHOOT14jr, and SHOOT14ef. These fast rising transients were interpreted as emission from the expanding and cooling supernova envelope which was heated after the shock-breakout phase (e.g. Waxman et al., 2007; Nakar & Sari, 2010). *PTF15crj* is slightly faster and fainter than these 'cooling envelope' transients and also at a much lower redshift.

PTF15cvl is intrinsically brighter and showed a lower rise rate. However, because *PTF15cvl* is faint (due to distance), we detected it only one day before peak and possibly missed the rapid-rise phase. Compared to the Subaru 'cooling envelope' transients and *PTF15crj*, *PTF15cvl* is approximately 1 magnitude brighter in absolute magnitude, comparable to *PS10ah* and *PS10bjp*.

For a number of fast rising transients found in Pan-STARRS spectra have been obtained. They all showed a blue continuum and lacked any spectral lines, as is predicted for an optically thick cooling envelope. The spectrum of *PTF15cvl* is similar; it shows a blue continuum with possibly one emission line. The spectra for *PTF15crj* show a blue continuum, but with narrow Balmer and Si-II emission lines, most likely from circumstellar material close to the exploding star.

Interestingly, two out of the four detected core-collapse supernovae show a rapid rise. Drout et al. (2014) estimate an event rate for fast transients of 4800–8000 $\mathrm{yr^{-1}Gpc^{-3}}$ and Tanaka et al. (2016) estimate a lowerlimit of 57000 $\mathrm{yr^{-1}Gpc^{-3}}$ for fast-rising 'cooling envelope' transients, and the brighter 'shock break' transients at a rate of 7000 $\mathrm{yr^{-1}Gpc^{-3}}$. We estimate the volumetric rate for fast transients using the same method as Tanaka et al. (2016). For *PTF15crj* we estimate that the transient would have been picked up as a fast transient even if it was 1 magnitude fainter, which sets the maximum distance we could detect it to $d_{max} \approx 150\,\mathrm{Mpc}$. For *PTF15cvl* we assume it has been detected at the distance detection limit, $d_{max} \approx 370\,\mathrm{Mpc}$. If we assume $\tau = 1\,\mathrm{d}$ and use the corresponding effective exposure from Fig. 3.1, we find a volumetric rate of $5.3 \times 10^5\,\mathrm{yr^{-1}Gpc^{-3}}$ and $1.4 \times 10^5\,\mathrm{yr^{-1}Gpc^{-3}}$. These are significantly higher than the estimates by Drout et al. (2014) and Tanaka et al. (2016), and would imply that almost all core-collapse supernovae should show a rapid rise, which is known to be not the case. This discrepancy is likely the result of low number statistics, since especially *PTF15crj* is a nearby event which is quite rare.

Rebrightening supernova *PTF15cpd*

The properties of *PTF15cpd* have been discussed in Section 3.3.2. It is unique among the supernovae found this paper because it shows a rebrightening in the g-band light curve. This light curve feature is also seen in SNIIb, for example SN1993J (Richmond et al., 1994), SN2011fu (Morales-Garoffolo et al., 2015), SN2013df (Van Dyk et al., 2014) and SN2015as (Gangopadhyay et al., 2018). The initial peak in these supernovae is emitted by a cooling envelope after the shock breakout occurred, the second peak is powered by radioactive decay of Ni-56. However, *PTF15cpd* evolves on significantly longer timescales than SNIIb (e.g. Fig 4 in Morales-Garoffolo et al., 2014). The second peak typically occurs 20 d after the first peak, while for *PTF15cpd* the time between the first and second peak is at least 40 days. This can be explained by a time-dilation if the redshift is very high ($z \sim 1$), implying *PTF15cpd* to be a superluminous supernova. Double-peaked superluminous supernovae are rare and the known examples all show a second peak that is brighter than the first peak (Nicholl & Smartt, 2016), which is not the case for *PTF15cpd*. A more accurate redshift measurement of the host is needed to determine the nature of this transient.

3.4.2 Observed rates of transients

One of the goals of the Sky2Night project is to determine an empirical observed rate of transients at various Galactic latitudes to distinguish Galactic and extragalactic contributions, as shown in Table 3.3. Hence, the Sky2Night surveys have been carried out at different Galactic latitudes; Sky2Night at $25° < |b| < 45°$ (van Roestel et al., 2018), Sky2night-II-2015 at $10° < |b| < 30°$ and Sky2night-II-2016 at $0° < |b| < 20°$. The setup of the surveys was slightly different, with different filters and slightly different cadences, and therefore the rates need to be compared with care.

The most common type of Galactic transients are flaring stars and CV outbursts. The stellar density is higher closer to the Galactic plane, so to first order, more flares and dwarf novae can be expected at these lower latitudes.

Flares are typically short, minutes to hours (Van Doorsselaere et al., 2017), and our sampling may therefore not yet probe the complete population. Since we require two detections to identify a transient, we only probe the long duration tail of the distribution. This can be seen in the number of detections. Only a few M-dwarf flares have been detected in each survey. The derived rates are however quite different between the campaigns. The flare rate is at least 5 times higher in the g-band compared to the campaigns in R-band. This the result of the higher flare amplitude at shorter wavelengths (e.g. Davenport et al., 2012), due to the dual effect of flares being intrinsically blue and host stars being intrinsically red, strongly increasing the contrast between the two at bluer wavelengths. The rate of flares in the 2012 and 2016 projects (both in R-band) is similar, which means that the number of flares close to the Galactic plane is not significantly higher than at $b \approx 35°$. This implies that the M-star density and intrinsic flare rate are similar, i.e. we are seeing a very local population. The typical distance to the flare stars is a few hundred parsec (see Table 3.1 and 3.2), and the stellar density is approximately twice as low as at b=0 (based on a thin-disk scale height of 246 pc, Jurić et al., 2008).

Cataclysmic Variables are the second type of common Galactic transients and we have detected a few dozen of them during each campaign. The typical distances to these transients are a few kpc (see Table 3.1 and 3.2). The Sky2Night campaigns probe regions with different CV-space densities.

For example, assuming an exponential disk model ($\rho \propto e^{-z/h}$ with $h = 300\,\mathrm{pc}$ (Groot et al. in prep.)), the density at $d = 1000\,\mathrm{pc}$ is a factor 3 higher at b=10° than at b=30°. As can be seen in Table 3.3, the number of CV outbursts is a factor of 2 higher in the Sky2Night-II campaigns compared to the Sky2Night-I campaign, a similar order of magnitude.

Assuming that the supernova rate is isotropic in volume, we expect to find fewer supernovae at low Galactic latitudes solely due to extinction by Galactic dust (1 magnitude extinction decreases the volume by a factor of ≈ 4). If we again compare the 2012 campaign with the 2016 campaign, we find a factor of 10 fewer SNIa at low Galactic latitudes. This is suprising, since dust extinction only reduces the volume sampled by a factor of 2 instead of a factor 10 (calculated using reddening maps by Li & Paczyński (1998) and the extinction law by Fitzpatrick (1999)). Even if we assume that the unclassified supernovae are SNIa, the difference remains too large to be explained by dust alone. It is possible that the high stellar density makes the transient detection pipeline more inefficient at finding transients. Remarkably, the observed rates of core-collapse supernovae in the 2012 and 2015 surveys are similar, in contrast to the difference in rates for SNIa. We note howerever, that the uncertainty on the observed rates in both surveys in high because only a few CC-SN were detected.

Finally, we calculated upper limits for the rate of fast optical transients. The limits for the Sky2Night-II campaigns are similar to the limits calculated for the Sky2Night-I campaign. This shows that there is not an abundant population of fast optical transients concentrated towards the Galactic plane that do not also occur at higher Galactic latitudes, on the time scales and out to the depths probed by our campaigns.

3.4.3 Kilonova follow up

A second motivation for the Sky2Night campaigns was to assess what the difficulties are in finding the optical counterparts of binary neutron star mergers detected by aLIGO/aVirgo (called kilonovae). Kilonovae are fast (timescales of a hours to a day, e.g. Barnes & Kasen, 2013; Tanaka & Hotokezaka, 2013; Metzger & Fernández, 2014; Kasen et al., 2017) and will likely be faint ($r \approx 19.5$ at 200 Mpc if we assume they are similar to AT2017gfo, Abbott et al., 2017). In Sky2Night-I (van Roestel et al., 2018), the conclusion was that CVs without a quiescent counterpart and fast-rising supernovae are the most significant source of interlopers in the early detection of kilonova signals.

In the Sky2Night-II 2015 and 2016 campaigns, we found a factor of 4 more CVs without a counterpart in PTF than in Sky2Night-I. This means that in a kilonova search covering a $100\,\mathrm{deg}^2$, a new, no-counterpart (down to the limit of Pan-STARRS) CV appears every 5 days. Since a CV outburst and a kilonovae light curve are similar at early times in their colour evolution, this means that a spectrum is needed to make a distinction between the two. However, even a spectrum might not be enough to make the distinction, since CV outbursts can be blue and featureless, as is expected for kilonova at early times. An example is PTF15csr (Fig. 3.3), for which spectra were obtained four days in a row before it could be classified as a CV. Cataclysmic Variables can thus be a sink of spectroscopic follow-up resources, but even in the Galactic plane, it will only be a handful of objects at most, assuming an area of $\approx 100\ \mathrm{deg}^2$. The need for spectroscopic identification can be solved if previous outbursts are detected. Therefore, a historical record of transients is also very useful information when searching for kilonova counterparts, especially closer to the Galactic Plane

which has often been avoided in synoptic surveys. While at low Galactic latitudes the extinction due to dust becomes problematic (e.g. no SN were discovered with $|b| \lesssim 6°$, see Fig. 3.2), the occurrence rate of interlopers does not prohibit the search for kilonovae at low Galactic latitudes.

In Sky2Night-I, rapidly rising supernovae were also identified as potential interlopers. Two fast-rising transients were detected in the Sky2Night-II-2015 campaign. The rise time of these two supernovae (3.4.1) is only slightly slower than the rise time of kilonovae ($\Delta g \approx 2.5\,\mathrm{mag\,d^{-1}}$), with a sparsely sampled light curve they can be difficult to distinguish from kilonovae. However, the rate of fast supernova interlopers in a kilonovae search is at least a factor 10 lower than number of interloper CVs, based on the results from the 2015 campaign.

3.5 Summary and conclusions

We performed two 8-day campaigns with PTF to search for transients at low Galactic latitudes. We determined the rate of detected transients in our surveys for various classes of sources. The campaigns showed that Cataclysmic Variables are the main type of transients at low Galactic latitudes on time scales >2 h, at a rate that is a factor of 2 higher than obtained in the Sky2Night-I campaign which covered an area at a higher Galactic latitude ($|b| \approx 35°$). The rate of flaring stars is not significantly higher at low Galactic latitudes for the host population being very local (< 1kpc). We found no unknown fast optical transients, and conclude that there is not a significant population of fast transients that occurs preferably at low Galactic latitudes.

While the number of interlopers in kilonova-targeted follow-up in the form of no-counterpart CV outbursts is higher at low latitudes, the observed rate does not prohibit the search for kilonovae. Of course, at very low Galactic latitudes ($|b| \lesssim 6$) dust extinction and crowding effects due to the high stellar surface density do pose additional challenges.

3.A Additional figures and tables

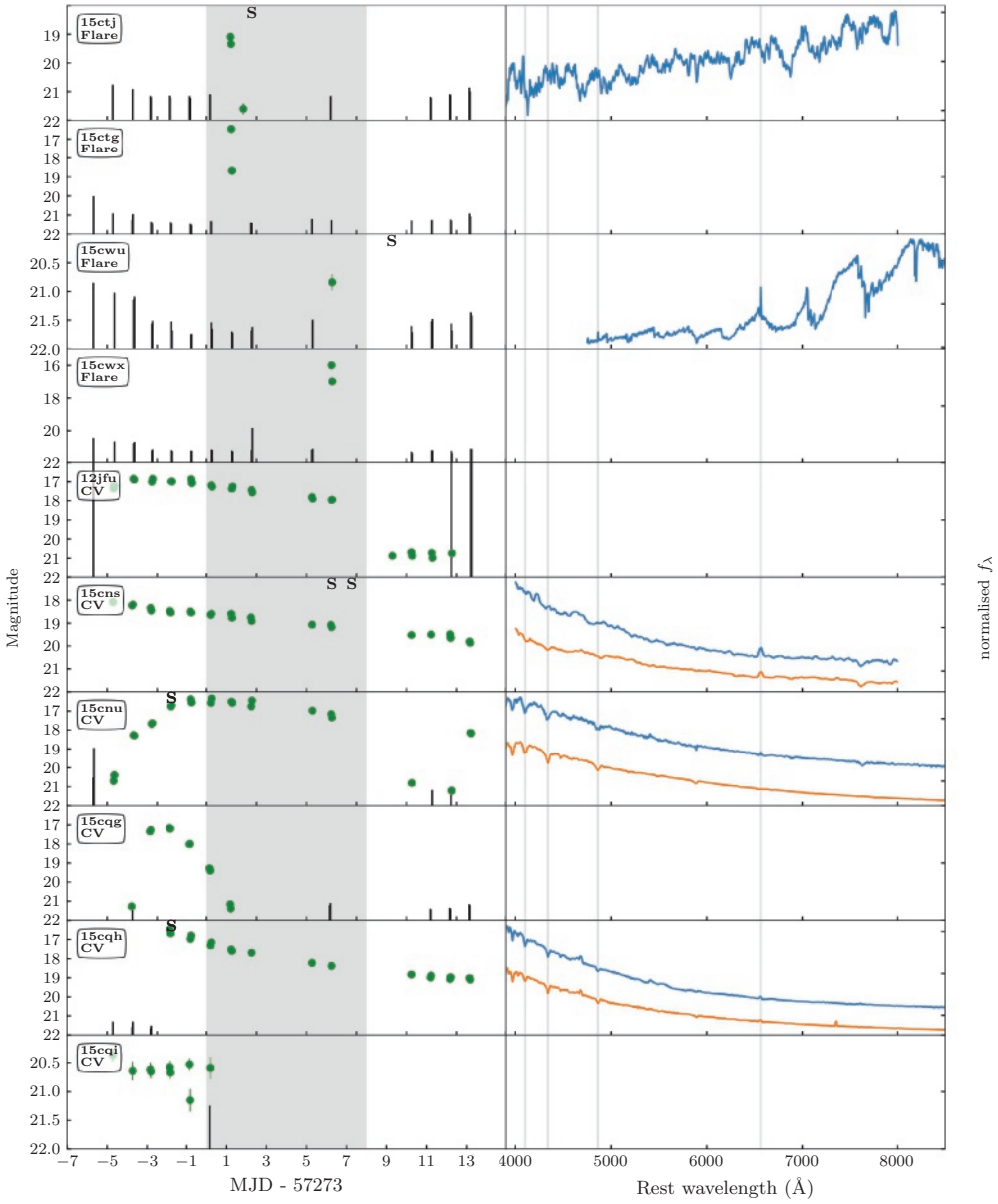

FIGURE 3.3: Light curves and spectra of all the transients found during the 2016 project. The green dots indicate PTF photometry and vertical lines indicate upper limits (g filter). The grey shaded area indicates the duration of the project.

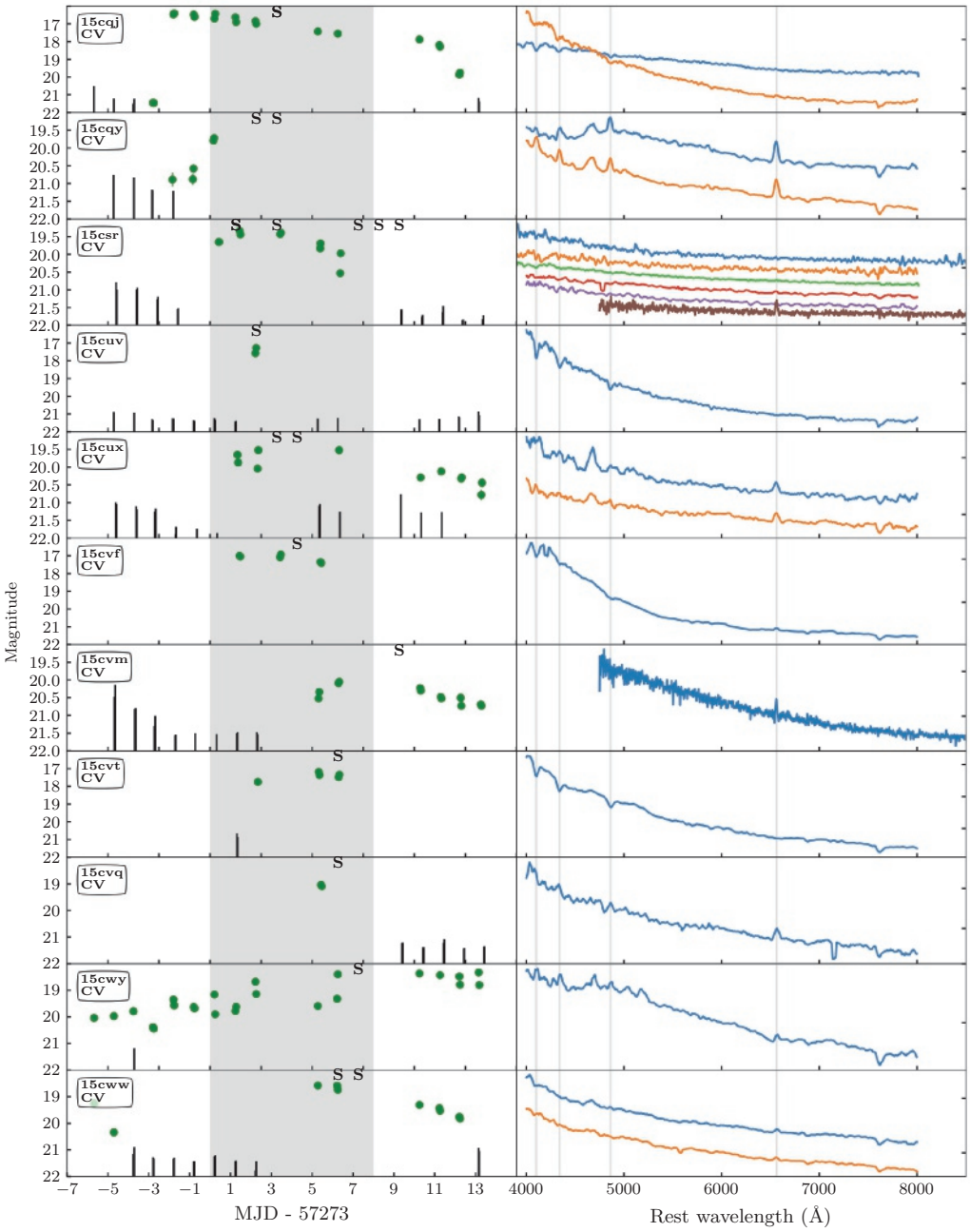
15cqj CV
15cqy CV
15csr CV
15cuv CV
15cux CV
15cvf CV
15cvm CV
15cvt CV
15cvq CV
15cwy CV
15cww CV
Magnitude
MJD - 57273
Rest wavelength (Å)
normalised f_λ

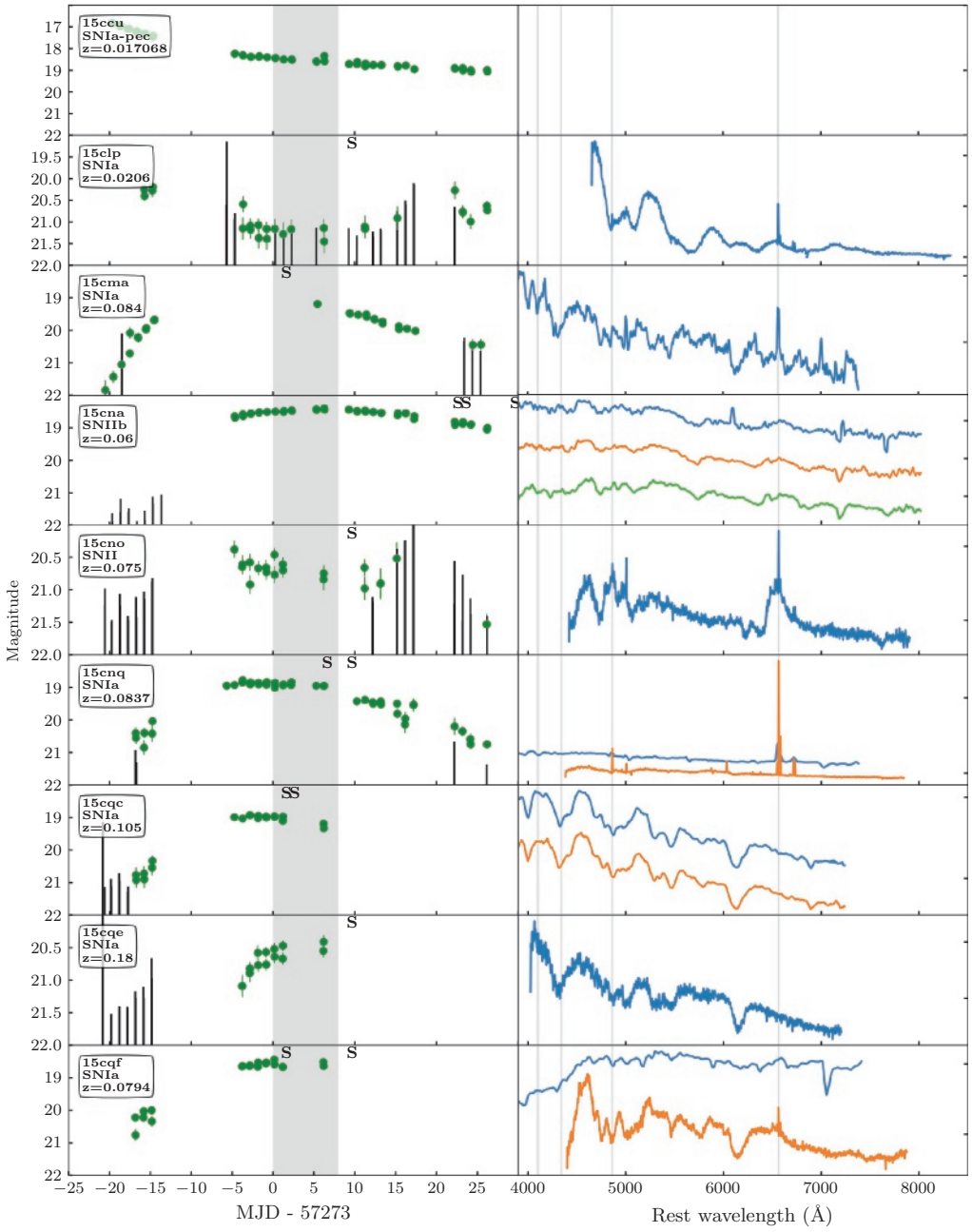

Figure 3.4: Light curves and spectra of classified supernovae detected in the 2015 run.

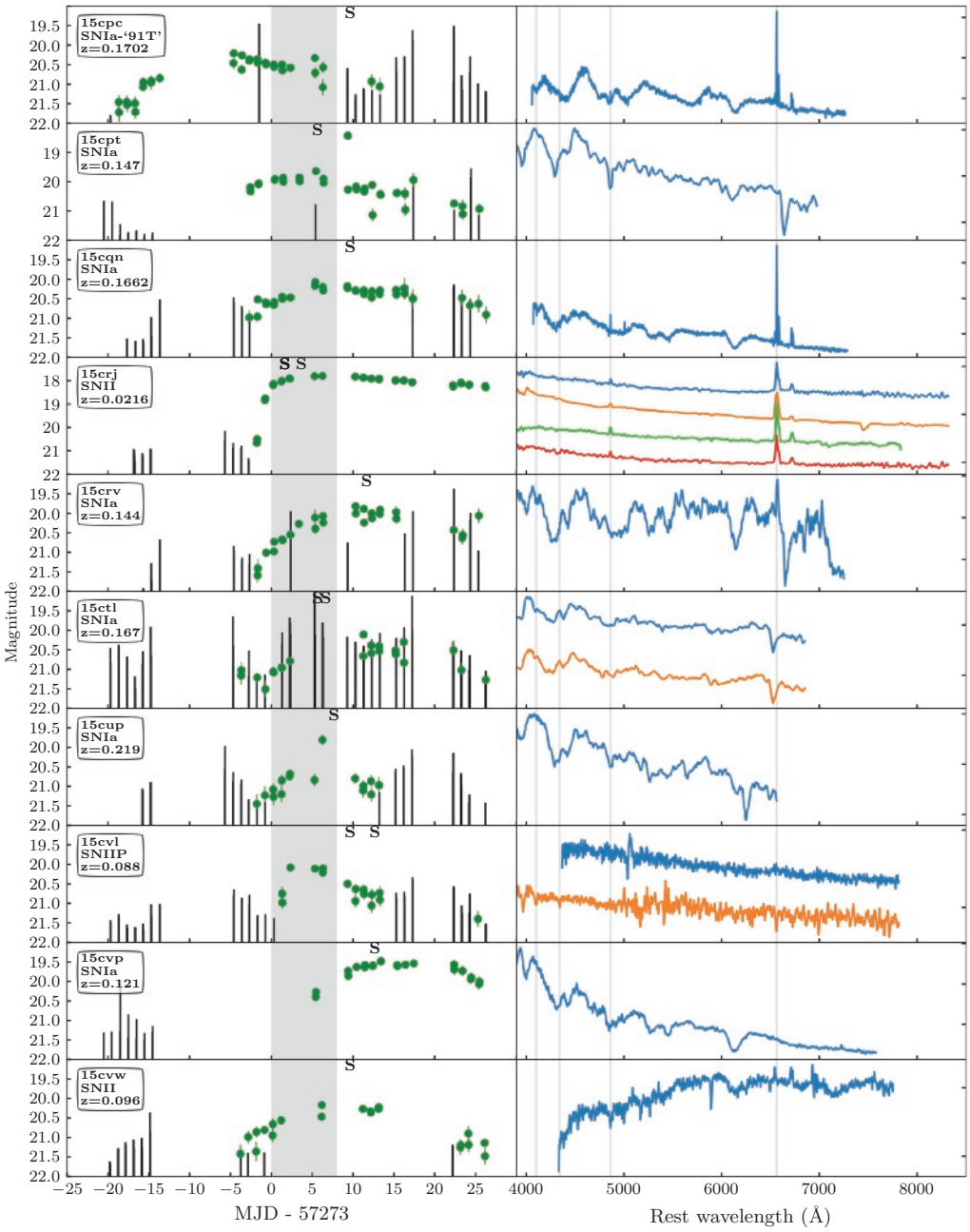
15cpc
SNIa-'91T'
z=0.1702
15cpt
SNIa
z=0.147
15cqn
SNIa
z=0.1662
15crj
SNII
z=0.0216
15crv
SNIa
z=0.144
15ctl
SNIa
z=0.167
15cup
SNIa
z=0.219
15cvl
SNIIP
z=0.088
15cvp
SNIa
z=0.121
15cvw
SNII
z=0.096
Magnitude
MJD - 57273
Rest wavelength (Å)
normalised f_λ

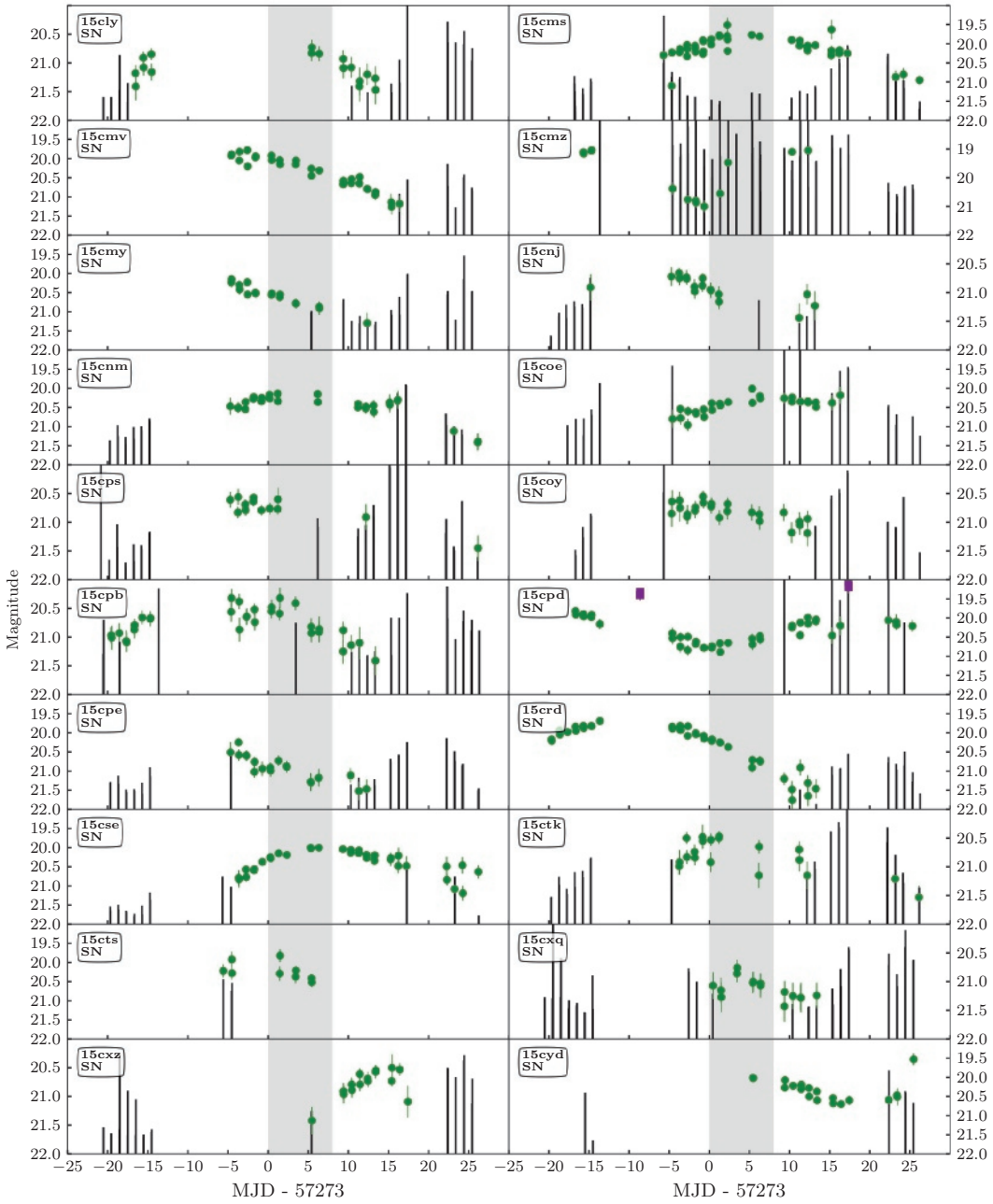

Figure 3.5: Light curves of unclassified supernovae detected in the 2015 run.

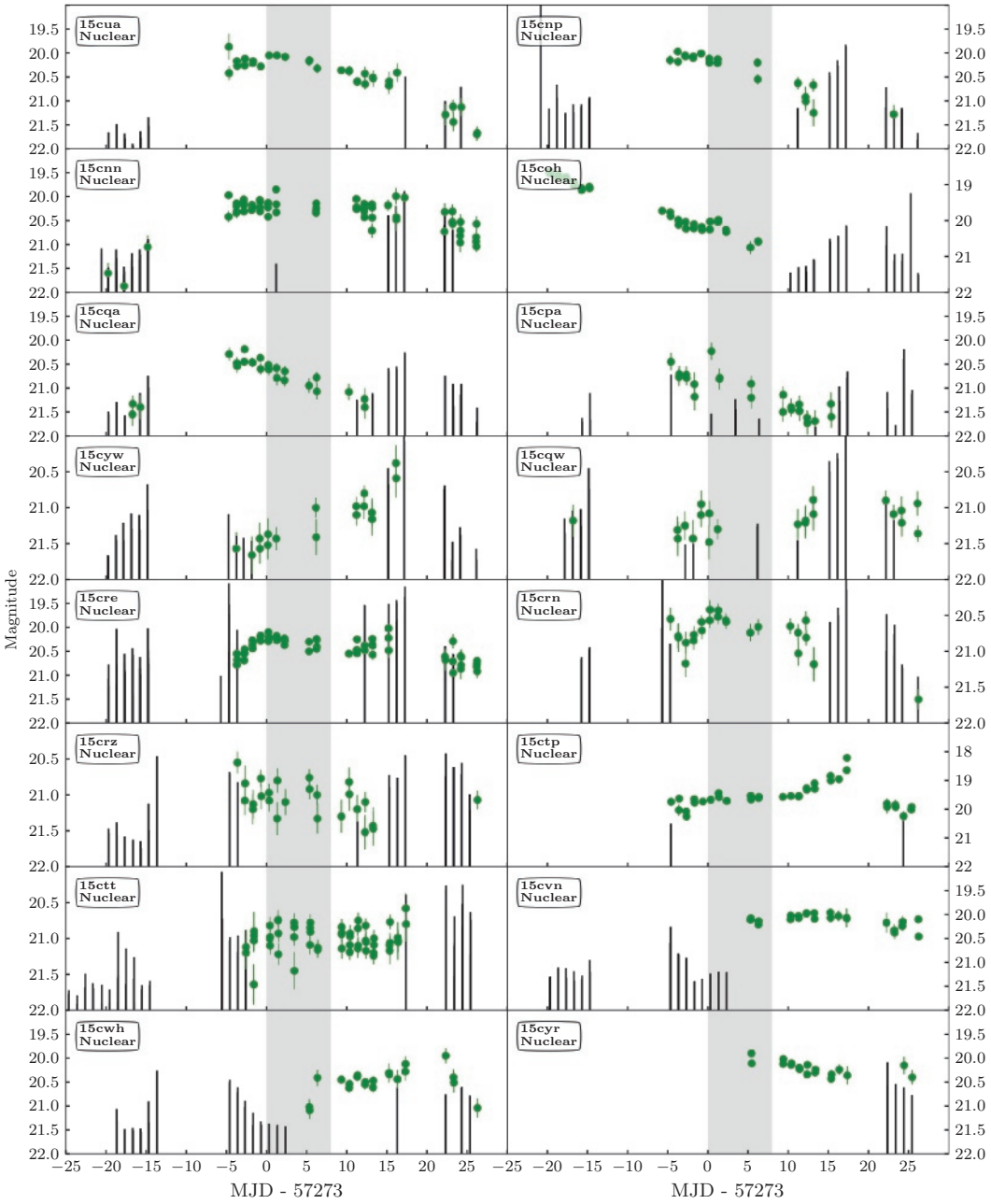

Figure 3.6: Light curves of nuclear transients detected in the 2015 run.

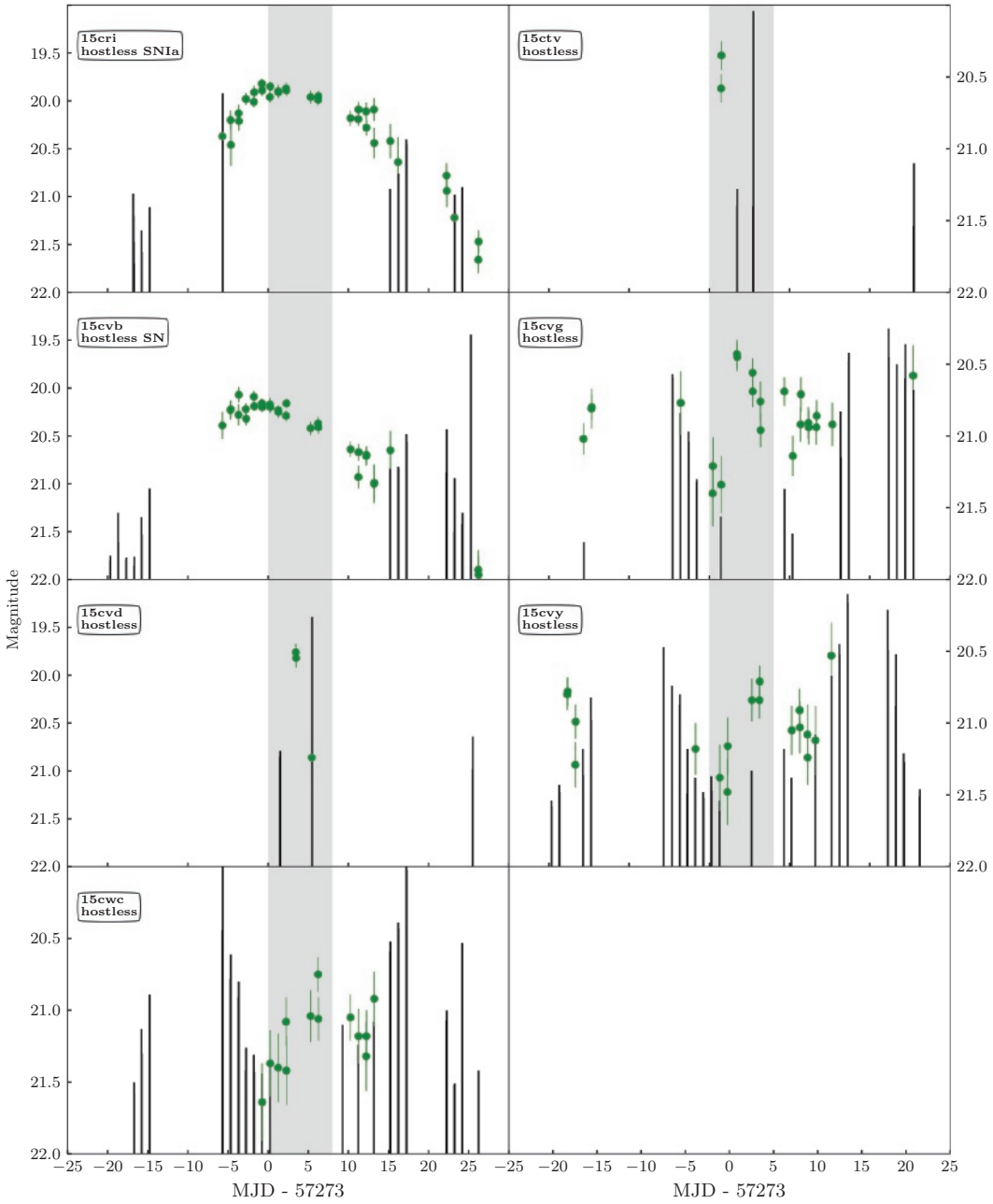

Figure 3.7: Light curves of transients of an uncertain class in the 2015 run.

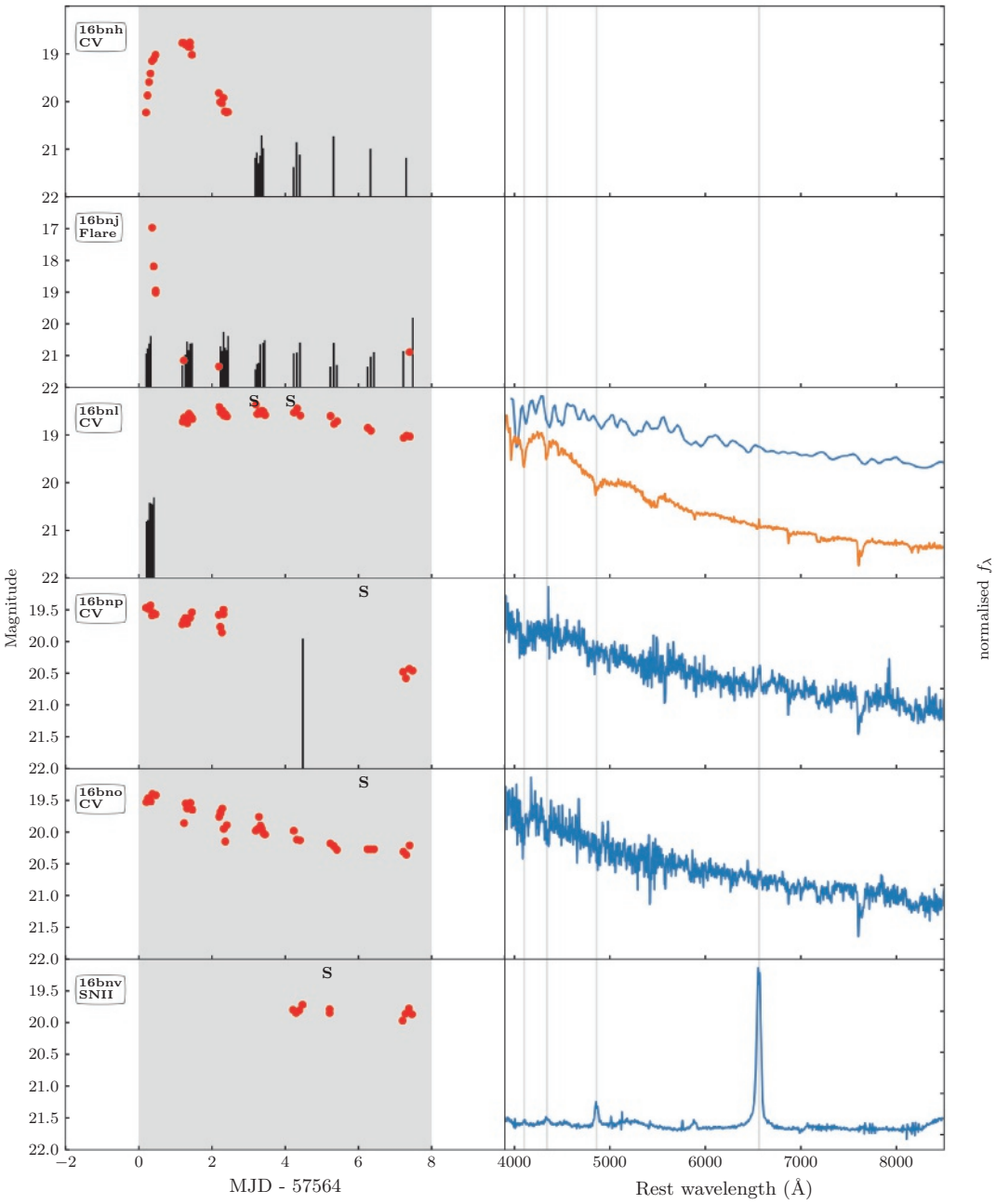

Figure 3.8: Light curves and spectra of all the transients found during the 2016 project. The green dots indicate PTF photometry and vertical lines indicate upper limits (g filter). The grey shaded area indicates the duration of the project.

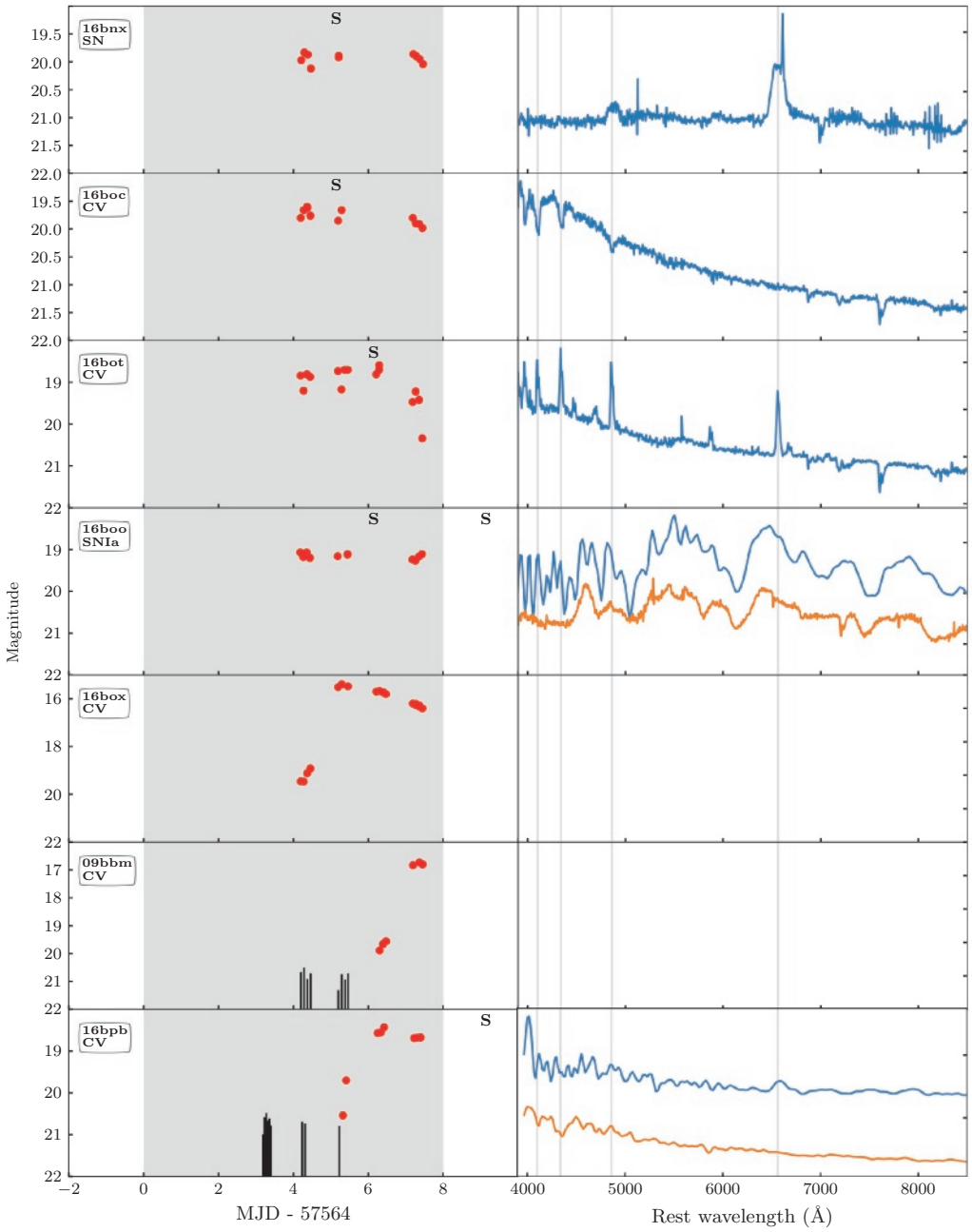
16bnx
SN
16boc
CV
16bot
CV
16boo
SNIa
16box
CV
09bbm
CV
16bpb
CV
S
Magnitude
MJD - 57564
Rest wavelength (Å)
normalised f_λ

Table 3.4: Overview of the conditions during the observations. The time between astronomical twilight was 8 hours and 40 minutes for the 2015 run, and 7 hours and 30 minutes for 2016.

2015 experiment		Night 1	Night 2	Night 3	Night 4	Night 5	Night 6	Night 7	Night 8
	time lost (h)	0.19	0.25	5.99	5.47	9.67	3.24	2.98	all
PTF	seeing (arcsec)	1.7-2.7	1.6-2.5	1.7-2.6	2.2-4.0	-	2.0-3.5	1.7-3.3	-
	cloud conditions	ok	ok	bad	bad	clouded	bad	bad	-
	seeing (arcsec)		1.0-1.5	0.9	0.9	0.6-1.2	0.6-1.2	0.9	0.7
INT	cloud conditions		good	ok	good	ok	good	good	good
	time lost (h)		0	3.5	0	4.0	0	0	0

2016 experiment		Night 1	Night 2	Night 3	Night 4	Night 5	Night 6	Night 7	Night 8
	seeing (arcsec)	2.1-3.5	1.9-3.0	1.9-3.1	1.8-3.3	2.0-3.3	1.8-3.1	1.9-3.1	2.1-3.8
PTF	cloud conditions	good	good	good	good	good	good	good	good
	time lost (h)	0	0	0.47	0	0	0.19	0.54	0

Table 3.5: Number of observation of the different field in Sky2Night-II-2015. Night 1 started at MJD 57273. The last night (night 8) is not displayed since no observations were obtained due to the weather.

ID	RA	Dec	b	E_{B-V}	Night1	Night2	Night3	Night4	Night5	Night6	Night7	Total
3413	315.8823	14.6250	-20.7428	0.09	2	1	0	0	0	0	2	5
3414	319.4118	14.6250	-23.4365	0.08	2	2	0	0	0	0	2	6
3514	315.4455	16.8750	-19.0451	0.09	2	1	0	0	0	0	2	5
3515	319.0099	16.8750	-21.7180	0.16	2	2	0	0	0	0	2	6
3516	322.5743	16.8750	-24.3192	0.13	2	2	0	0	0	0	1	5
3614	315.0000	19.1250	-17.3342	0.11	2	1	0	0	0	0	2	5
3615	318.6000	19.1250	-19.9847	0.14	2	2	0	0	0	0	2	6
3616	322.2000	19.1250	-22.5602	0.10	2	1	0	0	0	0	2	5
3617	325.8000	19.1250	-25.0517	0.12	2	2	0	0	0	0	2	6
3713	317.7551	21.3750	-17.9347	0.15	2	2	0	0	0	0	2	6
3714	321.4286	21.3750	-20.5186	0.09	2	2	0	0	0	0	2	6
3715	325.1020	21.3750	-23.0146	0.09	2	2	0	0	0	0	2	6
3716	328.7755	21.3750	-25.4124	0.09	2	2	0	0	0	0	2	6
3810	317.3196	23.6250	-16.1792	0.17	2	2	0	0	0	0	2	6
3811	321.0309	23.6250	-18.7351	0.15	2	1	0	0	0	0	2	5
3812	324.7423	23.6250	-21.2004	0.08	2	2	0	0	0	0	1	5
3813	328.4536	23.6250	-23.5647	0.06	2	2	0	0	0	0	2	6
3814	332.1649	23.6250	-25.8168	0.08	2	2	0	0	0	0	2	6
3906	320.2105	25.8750	-16.6680	0.10	2	3	0	0	0	0	2	7
3907	324.0000	25.8750	-19.1374	0.10	2	2	0	0	0	0	1	5
3908	327.7895	25.8750	-21.5023	0.07	2	2	0	0	0	0	2	6
3909	331.5790	25.8750	-23.7515	0.09	2	2	0	0	0	0	2	6
3910	335.3684	25.8750	-25.8725	0.08	2	2	2	0	0	1	2	9
3911	339.1579	25.8750	-27.8522	0.05	2	2	2	0	0	1	2	9
3912	342.9474	25.8750	-29.6764	0.18	2	2	2	0	0	1	2	9
3913	346.7368	25.8750	-31.3305	0.12	2	2	2	0	0	1	2	9
4000	323.2258	28.1250	-17.0621	0.17	2	2	0	0	0	0	1	5
4001	327.0968	28.1250	-19.4280	0.08	2	2	0	0	0	0	2	6
4002	330.9677	28.1250	-21.6747	0.09	2	2	0	0	0	0	2	6
4003	334.8387	28.1250	-23.7899	0.10	2	2	2	0	0	1	2	9

4004	338.7097	28.1250	-25.7606	0.04	2	2	2	0	0	1	2	9
4005	342.5806	28.1250	-27.5728	0.07	2	2	2	0	0	1	2	9
4006	346.4516	28.1250	-29.2123	0.10	2	2	2	0	0	1	2	9
4007	350.3226	28.1250	-30.6645	0.10	2	2	2	0	0	2	2	10
4092	326.3736	30.3750	-17.3436	0.12	2	0	0	0	0	0	0	2
4093	330.3297	30.3750	-19.5882	0.09	2	2	1	0	0	1	2	8
4095	338.2418	30.3750	-23.6605	0.08	2	2	2	0	0	1	2	9
4096	342.1978	30.3750	-25.4615	0.07	2	1	2	0	0	1	2	8
4097	346.1538	30.3750	-27.0872	0.06	2	2	2	0	0	1	2	9
4098	350.1099	30.3750	-28.5234	0.09	2	2	2	0	0	2	2	10
4099	354.0659	30.3750	-29.7565	0.08	2	2	1	0	0	2	2	9
4101	2.0225	32.6250	-29.3641	0.04	2	2	0	2	0	2	2	10
4102	6.0674	32.6250	-29.8985	0.06	2	2	0	2	0	2	2	10
4181	325.6180	32.6250	-15.2510	0.15	2	0	0	0	0	0	0	2
4182	329.6629	32.6250	-17.4937	0.12	2	2	2	0	0	1	2	9
4183	333.7079	32.6250	-19.5988	0.09	2	2	2	0	0	1	2	9
4184	337.7528	32.6250	-21.5533	0.10	2	2	2	0	0	1	2	9
4185	341.7978	32.6250	-23.3437	0.11	2	2	2	0	0	1	2	9
4186	345.8427	32.6250	-24.9564	0.09	2	2	2	0	0	1	2	9
4187	349.8876	32.6250	-26.3774	0.08	2	2	2	0	0	2	2	10
4188	353.9326	32.6250	-27.5937	0.07	2	2	1	0	0	2	2	9
4189	357.9775	32.6250	-28.5929	0.05	2	2	1	0	0	2	2	9
4190	2.0690	34.8750	-27.1622	0.06	2	2	0	2	0	2	2	10
4191	6.2069	34.8750	-27.6782	0.08	2	2	0	2	0	2	2	10
4192	10.3448	34.8750	-27.9511	0.13	2	2	0	2	0	2	2	10
4269	328.9655	34.8750	-15.3929	0.16	2	2	2	0	0	1	2	9
4270	333.1035	34.8750	-17.4932	0.15	2	2	2	0	0	1	2	9
4272	341.3793	34.8750	-21.2206	0.08	2	2	2	0	0	1	2	9
4273	345.5172	34.8750	-22.8207	0.09	2	2	2	0	0	2	2	10
4274	349.6552	34.8750	-24.2272	0.12	2	2	2	0	0	2	2	10
4276	357.9310	34.8750	-26.4091	0.06	2	2	1	0	0	2	2	9
4277	2.1429	37.1250	-24.9620	0.09	2	2	0	2	0	2	2	10
4278	6.4286	37.1250	-25.4631	0.06	2	2	0	2	0	2	2	10

4279	10.7143	37.1250	-25.7151	0.05	2	2	0	2	0	2	2	10
4280	15.0000	37.1250	-25.7153	0.05	0	0	0	0	0	2	2	4
4354	332.1429	37.1250	-15.2262	0.18	2	2	2	0	0	1	2	9
4355	336.4286	37.1250	-17.2006	0.10	2	2	2	0	0	1	2	9
4356	340.7143	37.1250	-19.0027	0.16	2	2	2	0	0	1	2	9
4357	345.0000	37.1250	-20.6188	0.15	2	2	2	0	0	2	2	10
4358	349.2857	37.1250	-22.0351	0.13	2	2	1	0	0	2	2	9
4359	353.5714	37.1250	-23.2388	0.14	2	2	1	0	0	2	2	9
4360	357.8571	37.1250	-24.2179	0.14	2	2	1	0	0	2	2	9
4361	2.1951	39.3750	-22.7564	0.08	2	2	2	1	0	2	2	11
4362	6.5854	39.3750	-23.2396	0.07	2	2	0	2	0	2	2	10
4363	10.9756	39.3750	-23.4735	0.06	2	2	0	2	0	2	2	10
4364	15.3659	39.3750	-23.4556	0.05	0	0	0	0	0	2	1	3
4365	19.7561	39.3750	-23.1861	0.06	0	0	0	0	0	2	0	2
4437	335.8537	39.3750	-15.0773	0.12	2	0	0	0	0	0	0	2
4438	340.2439	39.3750	-16.8704	0.13	2	2	2	0	0	1	2	9
4439	344.6341	39.3750	-18.4752	0.17	2	2	2	0	0	1	2	9
4440	349.0244	39.3750	-19.8782	0.13	2	2	2	0	0	2	2	10
4441	353.4146	39.3750	-21.0668	0.11	2	2	1	0	0	2	2	9
4442	357.8049	39.3750	-22.0296	0.13	2	2	1	0	0	2	2	9
4443	2.2785	41.6250	-20.5530	0.07	2	2	2	1	0	2	2	11
4444	6.8354	41.6250	-21.0211	0.08	2	2	0	2	0	2	2	10
4446	15.9494	41.6250	-21.1873	0.05	2	2	0	2	0	2	0	8
4447	20.5063	41.6250	-20.8835	0.06	0	0	0	0	0	2	0	2
4448	25.0633	41.6250	-20.3254	0.05	0	0	0	0	0	2	0	2
4449	29.6202	41.6250	-19.5192	0.07	0	0	0	0	0	2	0	2
4450	34.1772	41.6250	-18.4735	0.05	2	2	0	2	0	2	0	8
4520	353.1646	41.6250	-18.8727	0.14	2	2	1	0	0	2	2	9
4521	357.7215	41.6250	-19.8342	0.11	2	2	1	0	0	2	2	9
4522	2.3684	43.8750	-18.3481	0.06	2	2	2	0	0	2	2	10
4523	7.1053	43.8750	-18.8010	0.08	2	2	0	2	0	2	2	10
4524	11.8421	43.8750	-18.9906	0.07	2	2	0	2	0	2	2	10
4525	16.5789	43.8750	-18.9149	0.08	2	2	0	2	0	2	0	8

4526	21.3158	43.8750	-18.5746	0.07	0	0	0	0	2	0	0	2
4527	26.0526	43.8750	-17.9738	0.08	0	0	0	0	2	0	0	2
4528	30.7895	43.8750	-17.1190	0.08	0	0	0	0	2	0	0	2
4595	348.1579	43.8750	-15.4746	0.37	2	2	2	0	2	2	2	10
4596	352.8947	43.8750	-16.6760	0.15	2	2	1	0	2	2	2	9
4597	357.6316	43.8750	-17.6372	0.10	2	2	1	0	2	2	2	9
4598	2.4657	46.1250	-16.1421	0.09	2	2	2	0	2	2	2	10
4599	7.3973	46.1250	-16.5792	0.07	2	2	0	2	0	2	2	10
4600	12.3288	46.1250	-16.7452	0.11	2	2	0	2	0	2	2	10
4601	17.2603	46.1250	-16.6380	0.10	0	0	0	0	0	2	0	2
4602	22.1918	46.1250	-16.2589	0.09	0	0	0	0	0	2	0	2
4603	27.1233	46.1250	-15.6123	0.09	0	0	0	0	0	2	0	2
4670	357.5342	46.1250	-15.4387	0.10	2	2	1	0	0	2	2	9
4672	7.7143	48.3750	-14.3558	0.15	2	2	0	2	0	2	0	8
4673	12.8571	48.3750	-14.4967	0.18	2	2	0	2	0	2	0	8
4674	18.0000	48.3750	-14.3561	0.14	0	2	0	3	0	2	0	7
4675	23.1429	48.3750	-13.9355	0.16	2	2	0	2	0	2	0	8
4676	28.2857	48.3750	-13.2398	0.27	2	2	0	2	0	2	0	8
4677	33.4286	48.3750	-12.2769	0.22	2	2	0	2	0	3	0	9
4678	38.5714	48.3750	-11.0573	0.16	2	2	0	2	0	2	0	8
4738	347.1429	48.3750	-11.0561	0.22	2	2	1	0	0	2	2	9
4739	352.2857	48.3750	-12.2759	0.15	2	2	1	0	0	2	2	9
4740	357.4286	48.3750	-13.2390	0.12	2	2	1	0	0	2	2	9
4741	2.6866	50.6250	-11.7269	0.14	0	2	1	0	0	2	2	7
4742	8.0597	50.6250	-12.1307	0.17	0	2	0	2	0	2	0	6
4743	13.4328	50.6250	-12.2451	0.18	0	2	0	2	0	2	0	6
4744	18.8060	50.6250	-12.0687	0.20	0	2	0	2	0	2	0	6
4745	24.1791	50.6250	-11.6036	0.24	0	2	0	2	0	2	0	6
4746	29.5522	50.6250	-10.8553	0.32	0	2	0	2	0	2	0	6
4806	351.9403	50.6250	-10.0732	0.22	2	2	1	0	0	2	2	9
4807	357.3134	50.6250	-11.0384	0.23	2	2	1	0	0	2	2	9
100067	337.4130	35.3987	-19.0790	0.11	2	2	2	0	0	1	2	9
100117	352.0560	33.0119	-26.6939	0.12	2	2	1	0	0	2	2	9

100187	350.1040	41.8854	-17.8528	0.13	2	2	1	0	0	2	2	9
100202	333.8820	30.3657	-21.4968	0.08	2	2	2	0	0	1	2	9
131					224	227	99	63	0	180	201	994

Table 3.6: Number of observation of the different field in Sky2Night-II-2016

ID	RA	Dec	b	E_{B-V}	Night1	Night2	Night3	Night4	Night5	Night6	Night7	Night8	Total
3299	274.3689	12.3750	13.0659	0.17	7	7	7	7	4	4	3	4	43
3503	276.2376	16.8750	13.3310	0.22	7	7	7	7	4	4	3	4	43
3604	279.0000	19.1250	11.8876	0.25	7	7	7	7	4	4	3	4	43
3702	277.3469	21.3750	14.2295	0.16	7	7	7	7	4	4	3	4	43
3800	280.2062	23.6250	12.7373	0.12	7	7	7	7	4	4	3	4	43
3402	277.0588	14.6250	11.6637	0.26	7	7	7	7	4	3	3	4	42
3300	277.8641	12.3750	9.9866	0.34	7	7	7	7	3	3	3	4	41
3504	279.8020	16.8750	10.2411	0.43	7	7	7	7	3	3	3	4	41
3703	281.0204	21.3750	11.1156	0.21	7	7	7	7	3	3	3	4	41
3801	283.9175	23.6250	9.6529	0.28	7	7	7	7	3	3	3	4	41
3896	282.3158	25.8750	11.9228	0.18	7	7	7	7	3	3	3	4	41
3990	284.5161	28.1250	11.0846	0.22	7	7	7	7	3	3	3	4	41
3301	281.3592	12.3750	6.9199	0.52	7	7	7	7	3	3	3	3	40
3403	280.5882	14.6250	8.5840	0.58	7	7	7	7	3	3	3	3	40
3404	284.1177	14.6250	5.5217	0.80	7	7	7	7	3	3	3	3	40
3505	283.3663	16.8750	7.1710	0.41	7	7	7	7	3	3	3	3	40
3605	282.6000	19.1250	8.8125	0.37	7	7	7	7	3	3	3	3	40
3606	286.2000	19.1250	5.7620	0.73	7	7	7	7	3	3	3	3	40
3704	284.6939	21.3750	8.0283	0.37	7	7	7	7	3	3	3	3	40
3802	287.6289	23.6250	6.6001	0.65	7	7	7	7	3	3	3	3	40
3897	286.1053	25.8750	8.8389	0.28	7	7	7	7	3	3	3	3	40
3991	288.3871	28.1250	8.0099	0.25	7	7	7	7	3	3	3	3	40
3302	284.8544	12.3750	3.8681	1.41	7	7	6	7	3	3	3	3	39
3405	287.6471	14.6250	2.4793	1.29	7	7	6	7	3	3	3	3	39
3506	286.9307	16.8750	4.1231	0.90	7	7	6	7	3	3	3	3	39
3705	288.3673	21.3750	4.9706	1.05	7	7	6	7	3	3	3	3	39
3898	289.8947	25.8750	5.7920	0.49	7	7	6	7	3	3	3	3	39
3607	289.8000	19.1250	2.7389	2.14	6	7	6	7	3	3	3	3	38
3803	291.3402	23.6250	3.5823	1.21	6	7	6	7	3	3	3	3	38
3804	295.0516	23.6250	0.6034	3.47	6	7	6	7	3	3	3	3	38
3899	293.6842	25.8750	2.7861	1.43	6	7	6	7	3	3	3	3	38

3993	296.1290	28.1250	1.9937	1.41	6	7	6	7	3	3	3	3	38
3303	288.3495	12.3750	0.8338	5.34	6	6	6	7	3	3	3	3	37
3507	290.4950	16.8750	1.1003	4.28	6	6	6	7	3	3	3	3	37
3706	292.0408	21.3750	1.9458	2.27	6	6	6	7	3	3	3	3	37
3295	260.3884	12.3750	25.4668	0.23	0	0	0	0	4	4	4	4	16
3296	263.8835	12.3750	22.3583	0.15	0	0	0	0	4	4	4	4	16
3297	267.3786	12.3750	19.2539	0.12	0	0	0	0	4	4	4	4	16
3298	270.8738	12.3750	16.1557	0.19	0	0	0	0	4	4	4	4	16
3398	262.9412	14.6250	24.1112	0.09	0	0	0	0	4	4	4	4	16
3399	266.4706	14.6250	20.9842	0.09	0	0	0	0	4	4	4	4	16
3400	270.0000	14.6250	17.8659	0.15	0	0	0	0	4	4	4	4	16
3499	261.9802	16.8750	25.8425	0.09	0	0	0	0	4	4	4	4	16
3500	265.5446	16.8750	22.6960	0.07	0	0	0	0	4	4	4	4	16
3501	269.1089	16.8750	19.5605	0.11	0	0	0	0	4	4	4	4	16
3502	272.6733	16.8750	16.4382	0.15	0	0	0	0	4	4	4	4	16
3600	264.6000	19.1250	24.3843	0.06	0	0	0	0	4	4	4	4	16
3601	268.2000	19.1250	21.2351	0.09	0	0	0	0	4	4	4	4	16
3602	271.8000	19.1250	18.1012	0.09	0	0	0	0	4	4	4	4	16
3699	266.3265	21.3750	23.7053	0.11	0	0	0	0	4	4	4	4	16
3700	270.0000	21.3750	20.5267	0.11	0	0	0	0	4	4	4	4	16
3701	273.6735	21.3750	17.3674	0.13	0	0	0	0	4	4	4	4	16
3796	265.3608	23.6250	25.3351	0.11	0	0	0	0	4	4	4	4	16
3797	269.0722	23.6250	22.1516	0.10	0	0	0	0	4	4	4	4	16
3798	272.7835	23.6250	18.9893	0.12	0	0	0	0	4	4	4	4	16
3799	276.4948	23.6250	15.8504	0.12	0	0	0	0	4	4	4	4	16
3892	267.1579	25.8750	24.5637	0.08	0	0	0	0	4	4	4	4	16
3893	270.9474	25.8750	21.3634	0.11	0	0	0	0	4	4	4	4	16
3894	274.7368	25.8750	18.1881	0.14	0	0	0	0	4	4	4	4	16
3986	269.0323	28.1250	23.7368	0.05	0	0	0	0	4	4	4	4	16
3987	272.9032	28.1250	20.5274	0.09	0	0	0	0	4	4	4	4	16
3988	276.7742	28.1250	17.3468	0.13	0	0	0	0	4	4	4	4	16
3401	273.5294	14.6250	14.7584	0.16	0	0	0	0	4	4	4	3	15
3603	275.4000	19.1250	14.9846	0.22	0	0	0	0	4	4	4	3	15

3698	262.6531	21.3750	26.9012	0.06	0	0	0	0	4	3	4	4	15	
3895	278.5263	25.8750	15.0403	0.12	0	0	0	0	4	4	3	4	15	
3989	280.6452	28.1250	14.1981	0.14	0	0	0	0	4	4	3	4	15	
67					237	242	232	245	239	237	229	245	1906	

Chapter 4

PTF1 J085713+331843, a new post common-envelope binary in the orbital period gap of cataclysmic variables

J. van Roestel, P.J. Groot, D. Levitan, T.A. Prince, S. Bloemen, T.R. Marsh, V.S. Dhillon, D. Shupe, R. Laher

MNRAS 468, 3109–3122 (2017)

Abstract

We report the discovery and analysis of PTF1 J085713+331843, a new eclipsing post common-envelope detached white-dwarf red-dwarf binary with a 2.5h orbital period discovered by the Palomar Transient Factory. ULTRACAM multicolour photometry over multiple orbital periods reveals a light curve with a deep flat-bottomed primary eclipse and a strong reflection effect. Phase-resolved spectroscopy shows broad Balmer absorption lines from the DA white dwarf and phase-dependent Balmer emission lines originating on the irradiated side of the red dwarf. The temperature of the DA white dwarf is $T_{\rm WD} = 25700 \pm 400\,{\rm K}$ and the spectral type of the red dwarf is M3-5. A combined modelling of the light curve and the radial velocity variations results in a white dwarf mass of $M_{\rm WD} = 0.61^{+0.18}_{-0.17}\,{\rm M}_\odot$ and radius of $R_{\rm WD} = 0.0175^{+0.0012}_{-0.0011}\,{\rm R}_\odot$, and a red dwarf mass and radius of $M_{\rm RD} = 0.19^{+0.10}_{-0.08}\,{\rm M}_\odot$ and $R_{\rm RD} = 0.24^{+0.04}_{-0.04}\,{\rm R}_\odot$. The system is either a detached cataclysmic variable or has emerged like from the common envelope phase at nearly its current orbital period. In $\sim$70 Myr, this system will become a cataclysmic variable in the period gap.

4.1 Introduction

The majority of stars are members of binary systems. In a main sequence binary with an initial separation of less than ∼1000 solar radii, the two components of the system will interact during their evolution. When the more massive star ascends the red giant branch and/or asymptotic giant branch, it engulfs the secondary star in a common envelope (Paczynski 1976; for reviews see Taam & Sandquist 2000; Webbink 2008; Taam & Ricker 2010; Ivanova et al. 2013). During this phase the system loses orbital angular momentum, causing the secondary star to spiral inward and the giant's envelope to be expelled. This process is expected to take up to a few hundred years at most, resulting in a binary with a short orbital period, consisting of the core of the primary star (now a white dwarf or subdwarf B/O star) and the main-sequence secondary star. These systems are known as post-common-envelope binaries (PCEBs).

Eclipsing PCEBs are ideal to measure fundamental system parameters, such as the mass and radius of both components, with a high accuracy and independent of stellar atmosphere models. In addition, the sharp eclipses allow for very accurate orbital period measurements. Only 71 eclipsing white dwarf PCEBs systems are known (Parsons et al., 2015), and, in addition, 14 eclipsing subdwarf B (sdB) binaries were presented in Kupfer et al. (2015). NN Serpentis is one of the brightest eclipsing PCEBs and has been studied in most detail. Parsons et al. (2010b) determined the masses and radii of both components with an uncertainty of ≤4%. Eclipse timing studies of NN Ser also revealed periodic deviations of the expected eclipse times, which can be explained by two circumbinary planets (Beuermann et al., 2013; Marsh et al., 2014). Other detailed studies of individual eclipsing PCEBs have been presented by Pyrzas et al. (2012); Parsons et al. (2012c,b,a); Derekas et al. (2015). Besides being interesting individually, the population of PCEBs puts constraints on the evolutionary stages of detached white-dwarf red-dwarf binary systems.

After the common-envelope phase, the system will subsequently lose orbital angular momentum through magnetic braking and/or gravitational wave radiation. If the red dwarf secondary fills its Roche lobe while it is still a main-sequence star, a cataclysmic variable (CV) is formed (see Howell et al. 2001; Knigge et al. 2011, for a detailed analysis of CV evolution). A statistically significant lack of CV systems has been observed in the period range between ≈2.15 and ≈3.18h; the so-called period gap (Ritter & Kolb, 2003; Gänsicke et al., 2009). The disrupted magnetic braking model (Rappaport et al., 1983; Schreiber et al., 2010) predicts that mass transfer stops at an orbital period of ≈3.18h and resumes again at an orbital period of ≈2.15h (see Knigge et al. (2011)). Since the passage through the period gap is driven by gravitational wave radiation only, the space density of systems in the gap should be higher than that of systems just above and below the gap if all CVs start mass transfer above the gap and then evolve through the orbital period gap. The relative number of hibernating (in-gap) cataclysmic variables to regular PCEBs is uncertain. Davis et al. (2008) predict that detached CVs outnumber the regular white dwarf PCEBs by a ratio of 4 to 13, with a pile-up at the high end of the period gap since gravitational wave emission strength is a strong function of orbital period ($\dot{P} \propto P^{-5/3}$, see Peters & Mathews, 1963; Peters, 1964). A recent study by Zorotovic et al. (2016) finds PCEBs with orbital periods between ≈2.15 and ≈3.18h at a rate higher than which can be explained with standard PCEB formation theories, requiring a fraction of systems to be hibernating CVs.

In this paper, we report on PTF1 J085713+331843 (PTF0857), a new PCEB discovered by

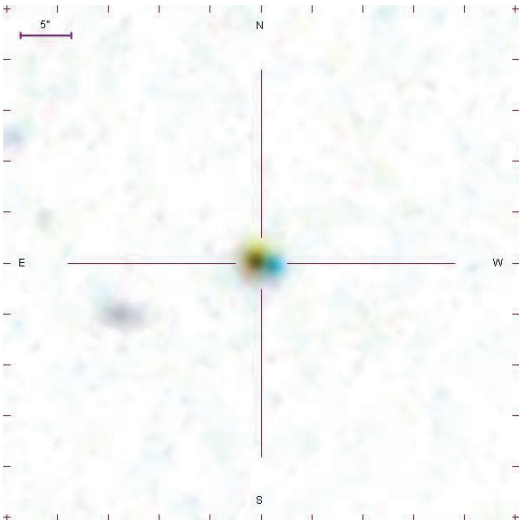

Figure 4.1: SDSS image of PTF0857 with the colours inverted. By eye two objects can clearly be distinguished, the blue object in the east is PTF0857 and the red object in the west is the interloper. The angular distance between the two objects is 1.46 ± 0.10 arcsec.

the Palomar Transient Factory (PTF). PTF0857 was selected as a cataclysmic variable candidate because of its colours in the Sloan Digital Sky Survey (SDSS, Ahn et al. 2012). A visual inspection of the PTF light curve showed that, on a period of a few hours, PTF0857 decreased in brightness by more than 1 magnitude. This was confirmed by inspecting the PTF images and the system was targeted for follow-up with the Double Beam Spectrograph at the Palomar 200″ (P200) and the triple beam, high cadence imager ULTRACAM at the 4.2m William Herschel Telescope (WHT) (Section 4.2). Our analysis of the data is explained in Section 4.3. Section 4.4 presents the results and the determination of the system parameters. In Section 4.5 we discuss the past and future evolution of PTF0857.

4.2 Observations

4.2.1 SDSS photometry

A close inspection of the field of PTF0857 shows that the target is blended with another star, referred to as 'interloper' in the rest of the paper, see Fig. 4.1. This caused the SDSS pipeline to misclassify the target as a galaxy. The colours in the SDSS catalogue are thus a combined colour of the two objects. The stars are separated by 1.5 arcsec (see Sect. 4.3.1), sufficient to determine their individual magnitudes by fitting the PSF of both stars.

4.2.2 Palomar Transient Factory photometry

The PTF (Law et al., 2009b; Rau et al., 2009b) uses the 48-inch (1.2m) Samuel Oschin Telescope at Palomar Observatory to survey the sky in search of transients. The pixel scale is 1.02 arcsec pixel^{-1}

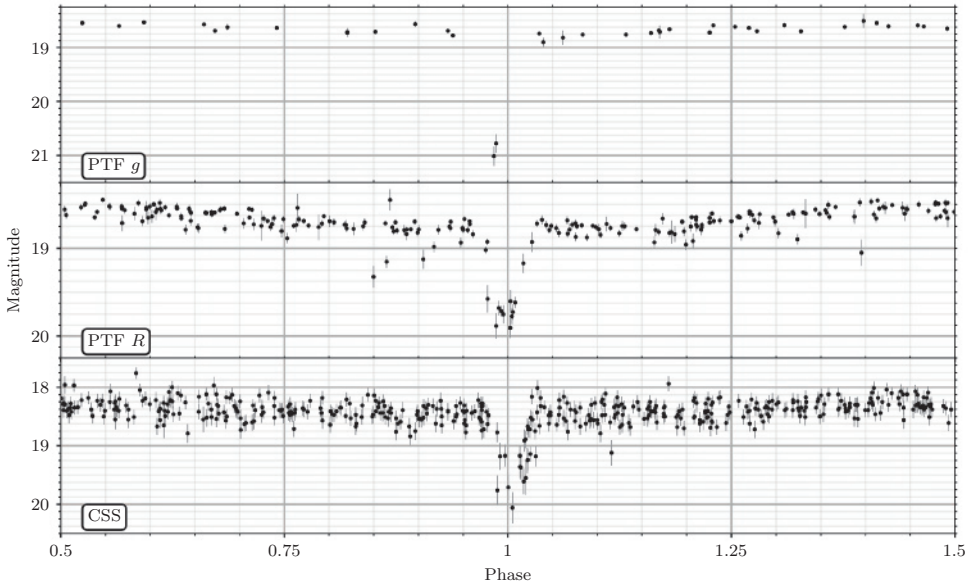

Figure 4.2: Light curves of PTF0857 in PTF R, PTF g, and CSS, folded to the orbital period, 0.10602727 days. The primary eclipse can be clearly seen in all three light curves, as well the small variation due to the reflection effect, best seen in PTF R.

and with a field of view of 7.26 deg^2, it surveys ≈2000 deg^2 per night. Although designed as a transient experiment, the observations are also used to study variable stars. All data are automatically processed to provide light curves, see Laher et al. (2014) for further details.

PTF observed the area of the sky containing PTF0857 at a highly irregular cadence and obtained 238 $R_{\rm mould}$-band and 38 g-band measurements between 2009 March and 2014 May with an individual exposure time of 60 s for all images. Due to a typical seeing of ∼2 arcsec in the PTF images, PTF0857 and the interloper are regarded as a single target. We present the PTF light curves in Fig. 4.2.

4.2.3 Catalina Sky Survey photometry

We examined data obtained by the Catalina Real Time Surveys (CRTS, Drake et al. 2009; Djorgovski et al. 2011). One of their telescopes, the Catalina Schmidt Telescope, observed PTF0857 468 times between 2005 April and 2013 May. The telescope is a 0.68 m Schmidt telescope with a pixel scale of 2.5 arcsec pixel^{-1}. All exposure times are 30 s. No filter is used to maximize the signal, but the observations are calibrated to V-band magnitudes. Observations during a given night are typically grouped in four epochs, 15 minutes apart. The overall cadence varies, but the field is typically observed every ∼20 d, when visible and weather permitting.

4.2.4 ULTRACAM high cadence photometry

We obtained high-speed photometry of PTF0857 on the 30th and 31st of 2012 January using ULTRACAM (Dhillon et al., 2007), mounted on the William Herschel Telescope (WHT) at the Roque de los Muchachos Observatory on the island of La Palma, Spain. ULTRACAM is a triple-beam camera that uses frame-transfer CCDs to minimise dead time. We used 2x2 binning for both nights to reduce the dead-time to 0.024 s. The first night we obtained 5.5 hours of images in the u', g' and r' filters and the second night 5.2 hours in the u', g' and i' filters. The first night we used exposure times of 3.03 s in g' and r', and 9.13 s in u', the second night we used 2.03 s exposures in g' and i', and 8.18 s in u'. Both nights were photometric, with a stable seeing of ∼1.5 arcsec, except for the last two h of the second night, when the seeing became more unstable and increased to 2.5 arcsec.

All data were reduced using the ULTRACAM pipeline software (see Feline et al., 2004). Debiasing, flat-fielding and background subtraction were performed in the standard way. We used two overlapping, variable size apertures covering both the target and the interloper with a radius of two times the full width at half maximum (FWHM) of the PSF, which itself was determined using two reference stars on the same chip. We calibrated the light curves directly using two stars in the field for which SDSS photometry is available (located at 08:57:30.69 +33:16:47.09 and 08:57:28.82 +33:16:46.08, J2000). The difference in photometric calibration between the two stars in less than 1 per cent.

4.2.5 Spectroscopy

Spectra were taken on the nights of 2012 January 30 to 2012 February 1 with the 5.1 m Hale telescope at Palomar Observatory using the double beam spectrograph DBSP (Oke & Gunn, 1982). The seeing was around 1 arcsec and conditions were not photometric. At times clouds prevented

observations altogether. A 316 lines mm^{-1} grating, blazed at 7500Å was used in the red arm and a 600 lines mm^{-1} grating, blazed at 4000Å in the blue arm. The wavelength ranges for the blue and the red arms are 3200–5800 and 5200–10500 Å, respectively, with a resolving power of $R \approx 1400$ in both arms. A total of 41 spectra were obtained in the blue arm, and 36 in the red arm with exposure times of 5 m. The slit was positioned such that the interloper was not included. In addition, one spectrum in the red arm was taken with the slit only on the interloper.

The programme L.A.Cosmic (van Dokkum, 2001) was used to remove cosmic rays, and the spectra were extracted and calibrated using iraf. For the wavelength calibration, FeAr and HeNeAr lamp spectra taken at the same position of the target were used. For relative flux calibration, we used standard star spectra which were obtained at the beginning and end of the night. The absolute calibration of the spectra was done using the ULTRACAM photometry for each spectrum individually. We convolved the individual spectra with the ULTRACAM response curves and a typical atmospheric absorption curve. We then multiplied the spectra so the total flux matched the ULTRACAM observations at the same orbital phase. For the blue arm we used the g' band and for the red arm we used the r' band. The signal-to-noise ratios per Ångström of the spectra vary because of changing conditions but are typically ∼10 in the blue and ∼7 in the red.

The short wavelength end of the blue spectra, below ∼4200 Å is affected by instrumental defects, which mimic broad absorption lines. Although consistently present in blue DBSP spectra, they are of indeterminate origin. We mask out the affected wavelength ranges in the further analysis.

4.3 Analysis

4.3.1 Magnitudes

To extract the luminosity of PTF0857 and the interloper from the *ugriz*- SDSS images, we use a custom-written point-spread-function (PSF) fitting code to fit a Moffat profile (Moffat, 1969) to both stars. Both stars have the same parameters, except for position and brightness. We determine the uncertainties on our fits using an implementation of the Affine-Invariant Markov Chain Monte Carlo method from the emcee python package (Foreman-Mackey et al., 2013). We inspected the residuals of our best models to the images and could not find any pattern in the remaining noise. The results are given in Table 4.1 and Fig. 4.3. The angular distance between the two stars thus determined is 1.46 ± 0.10 arcsec.

To get a more accurate measurement of the interloper's magnitudes we fitted the spatial brightness profile in the in-eclipse images using the same procedure as used to determine the SDSS magnitudes, where we fixed the positional offset between PTF0857 and the interloper. The ULTRACAM data have a larger pixel scale compared to SDSS (0.6 arcsec pixel^{-1} versus 0.39 arcsec pixel^{-}1), but the advantage is that the interloper is brighter than PTF0857 while in eclipse. When inspecting the residuals we noticed some systematic deviations from zero in the spatial brightness distributions. Because of this, we used bootstrapping (Wall & Jenkins, 2012, p. 147) to determine the uncertainties on the fit, which turned out to be a factor ∼3 higher than the formal uncertainties. We have adopted the uncertainties on the photometry obtained using the bootstrap

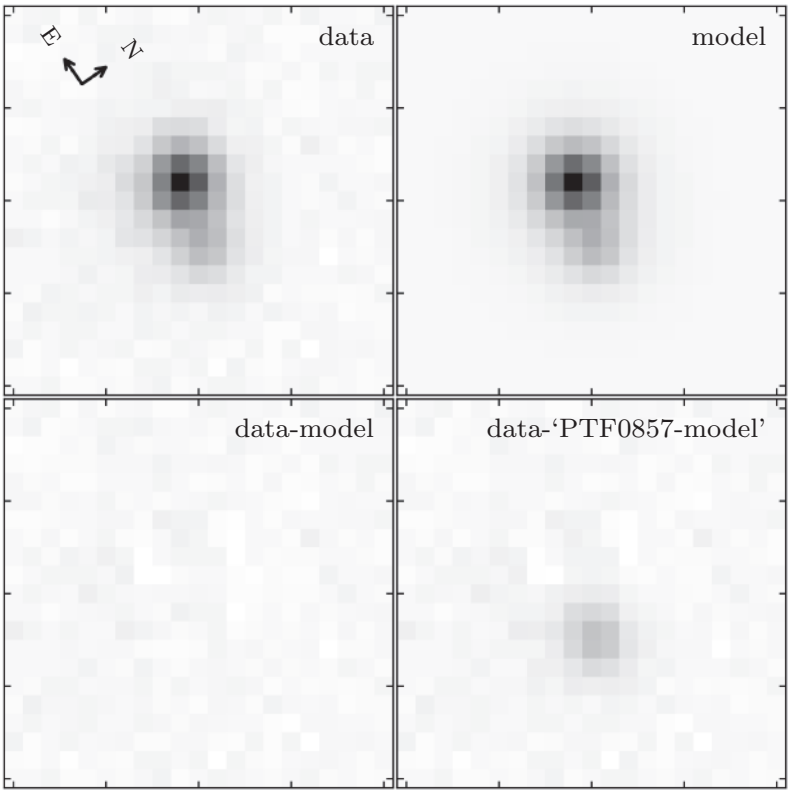

Figure 4.3: The PSF fit to the SDSS r image, with to the east PTF0857 and to the west the interloper. The top left panel shows the data, the top right panel shows the model, the bottom left panel shows the difference between the model and the data, and the bottom right panel shows the difference between the data and the PSF model of PTF0857 only. The greyscale is the same in all images, spanning from minimum to maximum with a linear scale. The size of the images is 21 by 21 pixels, with a pixel scale of $0.39\,\mathrm{arcsec\,pixel^{-1}}$

Table 4.1: The coordinates (J2000) and magnitudes (AB) for PTF0857 and the interloper measured from the SDSS images and ULTRACAM images. The numbers in square brackets indicate the magnitude range of PTF0857 due to the reflection effect. The SDSS images were obtained at an unknown phase, so they should fall somewhere in the range of the ULTRACAM magnitudes. The uncertainties do not include any uncertainties in the calibration, which are typically 0.01 mag. The filters used by SDSS are the *ugriz* system, while ULTRACAM uses the $u'g'r'i'z'$ system. The difference between the systems is small enough that we can neglect it.

	SDSS		ULTRACAM	
	PTF0857	Interloper	PTF0857	Interloper
RA	08:57:13.274(2)	08:57:13.162(8)		
Dec	33:18:43.11(6)	33:18:42.74(10)		
u/u'	18.59 ± 0.01		$[18.53 - 18.64] \pm 0.01$	
g/g'	18.62 ± 0.01	22.13 ± 0.12	$[18.66 - -18.80] \pm 0.01$	21.18 ± 0.06
r/r'	18.83 ± 0.03	20.20 ± 0.03	$[18.85 - -19.15] \pm 0.02$	19.98 ± 0.04
i/i'	18.90 ± 0.03	19.00 ± 0.03	$[18.84 - -19.23] \pm 0.04$	18.90 ± 0.03
z/z'	18.92 ± 0.02	18.41 ± 0.02		

method. The results are shown in Table 4.1.

4.3.2 Orbital period

We determine the orbital period (0.106 027 27(4) d) of the binary system using the ULTRACAM, PTF and CRTS data. All our time measurements were converted to MJD at the Solar system barycentre (BMJD), and they are on barycentric dynamical time (TDB), see Eastman et al. (2010). For the ULTRACAM light curve, we determine an initial orbital period by fitting a model (Section 4.3.5) to the g' band data, resulting in $P_{\rm orb,initial} = 0.106027(26)$ d. While this is just an initial measurement, it can be used to break the degeneracy between alias frequencies in the PTF and CRTS data. We use the PTF g, PTF R, and CRTS light curves to determine the orbital period using a multi-harmonic, multi-band Lomb-Scargle model with parameters $N_{\rm base} = 0$ and $N_{\rm band} = 15$ (VanderPlas & Ivezic, 2015). We bootstrap the data to calculate the uncertainty on the period. The orbital period (assuming it is constant) is $P_{\rm orb} = 0.10602727(4)$ d.

We determine the time of mid-eclipse by modelling the ULTRACAM light curves (see Section 4.3.5). The resulting linear ephemeris is given by:

$$\mathrm{BMJD(TDB)} = 55957.121\,914(3) + 0.106\,027\,27(4)\,E$$

All photometry and spectroscopy are folded on this ephemeris. The folded light curves are shown in Fig. 4.2.

4.3.3 Spectral type and temperature

The average spectrum is shown in Fig. 4.4. The spectral shape is a composite of a blue and red source. The blue spectra are dominated by the white dwarf, as indicated by the broad Balmer absorption lines. The red spectral range is dominated by the red dwarf; the flux increases to higher

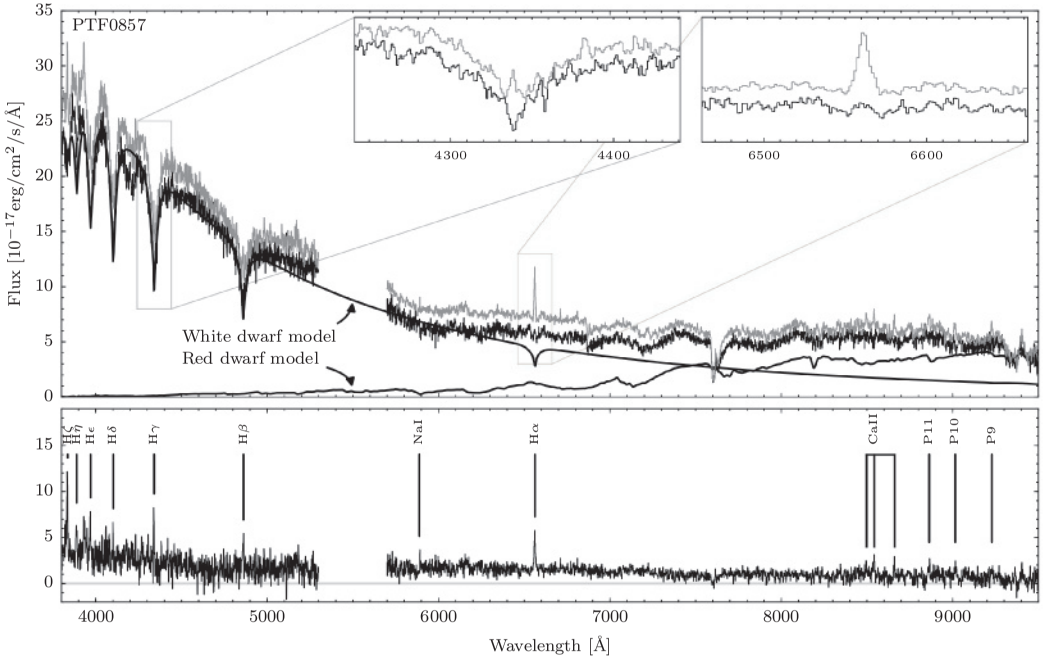

FIGURE 4.4: Average spectrum of PTF0857 for phases 0.8–0.2 (top,black) and for phases between 0.4 and 0.6 (top,grey). The blue side is dominated by the white dwarf and shows wide Balmer absorption lines. The red part of the spectrum is dominated by the red dwarf as can be seen by the TiO bands and slightly rising flux towards longer wavelengths. To guide the eye, the best-fit model spectra are plotted (black lines). The insets show the Hα and Hγ lines in more detail. The bottom panel shows the difference between the spectra taken between phase 0.2-0.8 and 0.4-0.6. It clearly shows phase-dependent Balmer emission lines with Hα the most prominent. Weaker lines in the difference spectra are the Paschen lines (9,10,11), the Na-I lines at 5889/5895Å and the Ca-II triplet (8498, 8542 and 8662Å).

wavelength and the TiO absorption bands can clearly be seen. The Hα absorption line of the white dwarf is barely distinguishable, and a strong, phase-dependent Hα emission line is observed (see the inset of Fig. 4.4). These narrow Balmer emission lines generally originate on the irradiated side of the red dwarf, with the orbital motion causing the variability in observed emission strength as the irradiated hemisphere rotates in and out of the observer's view.

Since no helium absorption lines are seen in the spectrum, we conclude that the white dwarf has a hydrogen-dominated atmosphere [DA, for examples of DB spectra, see Bergeron et al. (2011)]. To determine the white dwarf's temperature and surface gravity and the red dwarf's spectral type, we used the model spectra as in Verbeek et al. (2014); a combination of DA white dwarf model-spectra from Koester et al. (2001) and observed M-dwarf spectra from Pickles (1998), calibrated using fluxes from Beuermann (2006) (with an uncertainty of 10% on the luminosities). The white dwarf spectra available to use are in a grid with temperature steps of about 10 per cent and $\log g$ intervals of 0.5 dex. We use bilinear interpolation (in temperature and surface gravity) to make the white dwarf atmosphere model grid continuous, and we use linear interpolation for the red dwarf spectral types. We do not use any reddening correction, since dust extinction is negligible in the direction of PTF0857 ($E_{B-V} = 0.0263$; Schlegel et al., 1998). We use χ^2 minimization with, as free parameters, the red dwarf spectral type, the white dwarf temperature and its surface gravity, and independent distances for the white dwarf and the red dwarf. To determine the uncertainties on the parameters, we again use EMCEE (Foreman-Mackey et al., 2013). The uncertainties reported are only the formal uncertainties from our fit. Uncertainties due to interpolation are not taken into account.

To obtain the white dwarf temperature we fit a white dwarf model to the average of the blue spectra ($\lambda < 5500$ Å). We only use spectra taken between phases 0.8 and 0.2 (but excluding the eclipse phases from 0.95 to 0.05) because at these phases the contribution by irradiation or reflection is minimal. Although the contribution by the red dwarf in the blue part of the spectrum is expected to be small, we do include a red dwarf component in our model and treat it as a nuisance parameter. The red dwarf also produces emission lines that could introduce a systematic uncertainty in the result and therefore we mask 80Å around each Balmer line. This reduces the accuracy of the fit since we ignore the centre of the white dwarf absorption lines. The models fit the data relatively well ($\chi^2_{\rm red} = 1.08$) with a white dwarf temperature of 25700 ± 400 K and surface gravity of $\log g = 7.86^{+0.06}_{-0.07}$ at a distance of 567^{+19}_{-17} pc.

To determine the red dwarf spectral type, we first subtract our best–fitting white dwarf model from the average of spectra taken between phases 0.8 and 0.2 and fit the red dwarf model spectra to the residuals. The fit is not optimal, and spectral types M3–M5 all fit equally well, with a M4.4 spectrum giving a $\chi^2_{\rm red} = 1.85$ as the best fit, at a distance of $d_{\rm RD,M4} = 1303^{+87}_{-75}$ pc (see Fig. 4.5). The best–fitting distance for spectral types M3 and M5 are $d_{\rm RD,M3} = 1523^{+82}_{-71}$ pc and $d_{\rm RD,M5} = 783^{+87}_{-75}$ pc. Since the fit is not optimal, we adopt an uncertainty of 1 spectral type, M3–M5. The distance range associated with this is 1523–783 pc. If we assume that the red dwarf is at the same distance as the white dwarf, the red dwarf has to be over luminous by a factor of 2–7 for spectral types M5–M3. Or, conversely, the surface gravity of the white dwarf has to be 0.18 dex lower if we fix the white dwarf distance to the red dwarf distance (for a fixed white dwarf temperature of 25700 K).

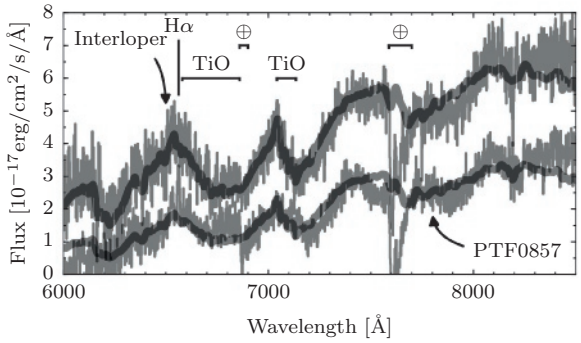

Figure 4.5: The spectrum of the interloper (upper) and the spectrum of PTF0857 after subtracting the best–fitting white dwarf model (lower). The best fitting red dwarf model spectra are over plotted.

We also fit the red dwarf models to the interloper spectrum, with a best fit of an M3.1 model at a distance of 1132^{+42}_{-36} pc. This fit is good, $\chi^2_{\rm red} = 1.04$, see Fig. 4.5. A spectral type of M3 is clearly better than either an M4 or an M2 spectrum and the statistical uncertainty is much lower than 0.1 spectral types. Therefore, we conclude that the spectral type of the interloper is M3.

The spectrum of the interloper is only calibrated photometrically with a standard star observed at the end of the spectroscopic run. The photometric calibration of the spectra of PTF0857 taken just before showed scatter of about 5%. Using the spectrum, we calculated the magnitude in the r and i bands: $r = 19.93 \pm 0.06$ and $r = 18.91 \pm 0.06$. These measurements are consistent with the values in Table 4.1. If we also take into account the calibration uncertainty, the distance to the interloper is $d_{\rm interloper} = 1132^{+96}_{-76}$ pc

4.3.4 Radial velocities

We determined the radial velocity curves from the spectra using the program molly. First, we normalized the spectra by fitting a low-order polynomial to the continuum of the spectra. We fit the Hα emission line using a single Gaussian with a fixed width but variable height and central wavelength to determine the radial velocity shifts of the red dwarf. By doing this we do ignore the Hα absorption line from the white dwarf, but the emission line is much stronger than the absorption line and should not affect the fit to the emission line (see Fig. 4.4).

The other Balmer lines are dominated by the broad absorption lines originating in the white dwarf's atmosphere, but emission from the secondary is clearly detectable (see Fig. 4.4). To determine both the white dwarf and red dwarf radial velocity, we fit the Hβ, Hγ and Hδ absorption and emission features simultaneously. The absorption lines were approximated using Gaussian profiles, all with the same radial velocity offset to the laboratory rest frame. For the emission features, we also used a Gaussian profile but allowed for individual offsets to the rest frame. The depth and width of the absorption features and the FWHM of the emission features were kept fixed (determined from the average of spectra between phases 0.4 and 0.6), but we kept the depth

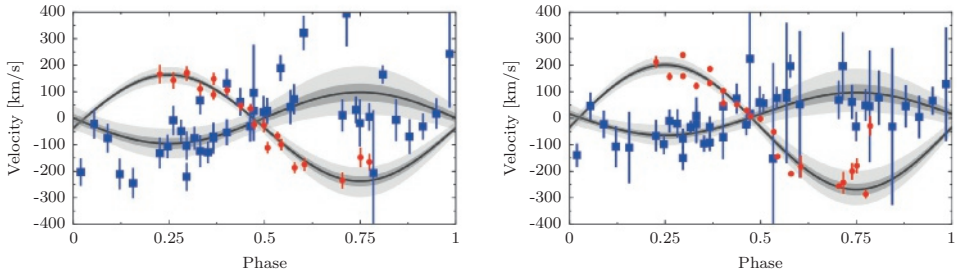

Figure 4.6: Measurements of the radial velocities of the red dwarf as measured from Hα (circles) and the white dwarf (squares). The grey bands show the 1 standard deviation and 3 standard deviations of the fits, determined using the bootstrapping procedure. (*Left*) The radial velocities as measured using line fitting. (*Right*) The data and best fit to the radial velocities obtained using cross-correlation.

and height of the profiles as free parameters. We fit a sinusoid to the phase-folded radial velocity variations, using the period and phase obtained from the photometry and kept the amplitude and zero–point as free parameters. We only used measurements between phases 0.8 and 0.2. A 5σ clipping of outliers was applied in two iterations. The average red dwarf radial velocity amplitude from the Hα, Hβ, Hγ, and Hδ is $K_{\mathrm{RD,obs}} = 212 \pm 10\,\mathrm{km\,s^{-1}}$. This measured radial velocity of the centre of light of the star can still include a K–correction, due to the strong irradiation by the white dwarf (see Section 4.3.6). For the white dwarf, we measure a radial velocity amplitude of $K_{\mathrm{WD}} = 97 \pm 22\,\mathrm{km\,s^{-1}}$. We determined the uncertainties of our fit using a bootstrap method, shown in Fig. 4.6.

To confirm these measurements, we used a cross-correlation of the individual spectra with the average spectrum, using the RV/FXCOR package in IRAF. To determine the radial velocity of the white dwarf, the Balmer Hβ, Hγ, Hδ and Hϵ absorption lines were used with the central 12 Å masked. For the red dwarf radial velocity, only the Hα emission line was used (without any correction of white dwarf absorption). We fitted the resulting radial velocity curve as above, and determined an average red dwarf radial velocity amplitude $K_{\mathrm{RD,obs}} = 235 \pm 15\,\mathrm{km\,s^{-1}}$ and $K_{\mathrm{WD}} = 81 \pm 18\,\mathrm{km\,s^{-1}}$ for the white dwarf, consistent with the first method. The results are shown in Fig. 4.6.

We adopt the values from our first method, $K_{\mathrm{RD,obs}} = 212 \pm 10\,\mathrm{km\,s^{-1}}$ and $K_{\mathrm{WD}} = 97 \pm 22\,\mathrm{km\,s^{-1}}$. The formal uncertainty of this method is larger for the white dwarf radial velocity amplitude, but this method is the least likely to be affected by blending of the features because both absorption and emission profiles are fitted at the same time. The uncertainty on the radial velocity of the white dwarf primary, $\Delta K_{\mathrm{WD}}/K_{\mathrm{WD}}$, is 0.22. This uncertainty is reflected in the mass-ratio ($q = M_{\mathrm{RD}}/M_{\mathrm{WD}} = K_{\mathrm{WD}}/K_{\mathrm{RD}}$, see Section 4.3.5).

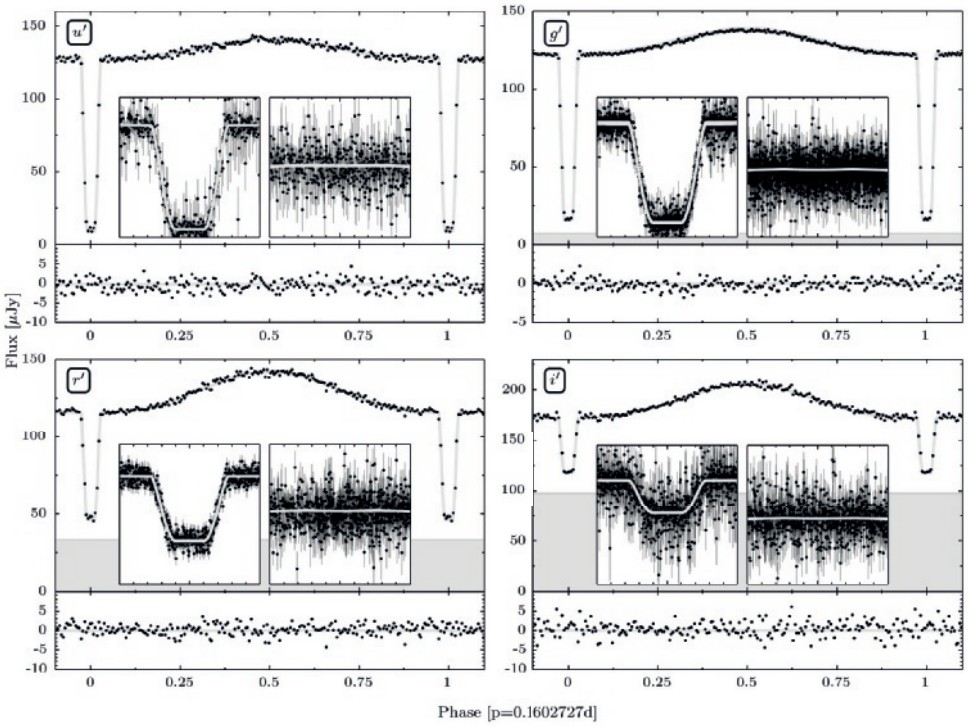

Figure 4.7: The folded and binned ULTRACAM light curves and best fitting models in u', g', r' and i'. The main panels show the binned data and the model. The greyed out area indicates the contribution of the interloper star. The bottom panels shows the residuals of the fit. The insets show the unbinned data and the models near the primary and secondary eclipses.

4.3.5 Light curves

By modelling the light curves we can put strong constraints on the system parameters. To construct a model light curve given a set of binary star parameters, we use LCURVE (written by T.R. Marsh et al., see Copperwheat et al. 2010). The LCURVE code uses grids of points to model the two stars. The shape of the stars in the binary is set by a Roche potential for a certain mass-ratio. LCURVE assumes co-rotation and zero orbital eccentricity.

The amount of light each point on the surface grid emits depends on a number of parameters, the main one being the star's effective temperature. We approximate the spectral energy distribution of both stars with a blackbody and calculate the flux at the effective wavelength of the bandpass. LCURVE takes limb darkening into account. For the red dwarf we use a quadratic limb darkening law with parameters for a 3000 K red dwarf (Claret & Bloemen, 2011). For the white dwarf we use a Claret limb darkening prescription with the parameters for a 25000K, $\log g$=7.5 white dwarf taken from Gianninas et al. (2013). In addition, we also take into account gravity darkening for the red dwarf. We use the relation between the intensity and surface gravity: $I \propto g^y$, with y a free parameter between 0.1 and 1.2 (see Gianninas et al. 2013).

Since the white dwarf is very hot and close to the secondary, irradiation of the secondary by the white dwarf cannot be neglected. A back-of-the-envelope calculation shows that the irradiated energy flux can be a factor 200 higher than the energy flux from the red dwarf. This 'reflection' effect is a combination of heating and reflection, both contributing to the flux emitted by the secondary. In our model, we approximate this effect using an albedo factor, which determines the fraction of the light that is absorbed. This will locally increase the temperature and therefore increase the flux emitted by that area on the surface. The fraction of light that is not absorbed is ignored in the model. In theory, the albedo should be between 0 and 1, but this method is a very crude approximation for the reflection effect, and thus we do not constrain the range of the albedo parameter.

We combine our LCURVE model with a Monte Carlo Markov Chain method, as implemented in the package EMCEE (Foreman-Mackey et al., 2013) to explore the solution space. We calculate the solution for the light curves per passband, using as priors $T_{\rm WD} = 25700 \pm 400$ K and the contribution from the interloper as measured from the ULTRACAM images (Table 4.1). When inspecting the residuals we find a trend over time, likely due to a difference in airmass. To remove the trends in the data, we add a low second order polynomial function to our model and use this to correct the data. Besides the long scale trend, we also noticed some minor flaring behaviour, simultaneously in the g' band and r' band data, possibly from chromospheric activity of the red dwarf. We removed the affected data points from our light curve as studying the flare is not within the scope of this paper.

We first fitted the data without any constraint on the mass ratio. The best-fitting models to the individual light curves are shown in Fig. 4.7. No systematic deviations can be seen in the residuals. The primary eclipse is fitted well in all bands. The best-fitting models do not show any indication of a secondary eclipse in any of the bands.

After a more detailed inspection of the parameter uncertainties, we deduced that the mass ratio is only very marginally constrained by the light curve. The effect of the mass-ratio on the light curve is in the amount of ellipsoidal variation, which is a very small effect compared to the

reflection effect. There is a small preference for models with a mass ratio of $q \approx 0.1 - 0.2$, but the $\Delta\chi^2$ improvement compared to $q = 0.5$ models is only 35 out of 15337. Statistically, this means that a mass ratio of $q = 0.5$ is ruled out, but this assumes that our model and data are both perfect, especially in how we treat limb darkening. This not the case, and we, therefore, decide to treat the mass-ratio as a systematic uncertainty and calculate a solution for a range of mass-ratios (0.1, 0.2, 0.25, 0.3, 0.35, 0.4, 0.5).

4.3.6 System parameters

We determine the mass of both components using the mass function,

$$M_{\rm A} = \frac{(K_{\rm WD} + K_{\rm RD})^2 K_{\rm B} P}{2\pi G \sin(i)^3} \tag{4.1}$$

with A and B being either the white dwarf (WD) or the red dwarf (RD), M the mass, K the radial velocity amplitude, P the orbital period and i the inclination. Once the masses are known, we can calculate the orbital separation (a) using Kepler's third law.

The light curve model gives us very good constraints on the relative sizes of the components and the inclination (i), but we need spectroscopy to determine the absolute masses of both components. For many binaries, it is straightforward to obtain phased resolved spectroscopy and use periodic velocity shifts in spectral features to obtain the radial velocities. For PTF0857 there are two complications. One is the strong reflection effect, which shifts the centre-of-light of the red dwarf away from its centre-of-mass. This means that the measured radial velocity of the red dwarf is lower than the centre-of-mass radial velocity. We describe this effect using the following equation (first used by Wade & Horne 1988):

$$K_{\rm RD} = K_{\rm RD,obs}/(1 - f\ r_{2,\rm L1}(1 + q)), \tag{4.2}$$

with $K_{\rm RD,obs}$ the observed radial velocity amplitude of the irradiated component (the red dwarf in the case of PTF0857), f a value between 0 and 1 that indicates the offset of the centre–of–light to the centre-of-mass of the secondary, and $r_{\rm RD,L1}$ the radius of the red dwarf in the direction of the inner Lagrangian point, divided by the orbital semi-major axis, i.e. $r_{\rm RD,L1} = R_{\rm RD,L1}/a$. This adds an additional parameter to our model, f, which lies, by definition, between 0 and 1, but has a fixed dependence on the geometry. We use the Roche geometry (set by the mass ratio q) and the relative size of the red dwarf from the light–curve models to calculate f. This shows that the value of f is 0.69 for a mass-ratio of 0.3, and only changes by 0.03 for mass ratios of $\Delta q = 0.1$. Therefore, we decide to use a range of f=0.66–0.72 for all models. See Appendix 4.A for the calculation of, and a further discussion on, the expected value for f.

A second complication is that the spectral features of the white dwarf and red dwarf are blended, as outlined in Section 4.3.4, and therefore the uncertainty on the radial velocity measurement of the white dwarf is high. In combination with the high signal-to-noise light curve, the uncertainty in $K_{\rm WD}$ (and therefore the mass-ratio q) will dominate the error budget. To better understand the source of uncertainties in the different parameters, we calculate both a statistical uncertainty on the model parameters, as well as how the uncertainty in $K_{\rm WD}$ propagates through. We choose the models with mass ratios that are most compatible with the observed value of $K_{\rm WD} = 97\,{\rm km\,s^{-1}}$,

and derive how each parameter changes if $K_{\rm WD}$ is one standard deviation lower or higher, $K_{\rm WD} = 75\,{\rm km\,s^{-1}}$ and $K_{\rm WD} = 119\,{\rm km\,s^{-1}}$. We use linear interpolation between models with different mass ratios to obtain these values.

The result of the combined fitting for the system parameters is given in Table 4.2. The light curve parameters are fit independently per band, except for the mass-ratio (q), which we determined using $K_{\rm WD}$, $K_{\rm RD}$, f and $r_{\rm RD}$.The light curves in the four different bands essentially give us four independent measurements of the light curve parameters (see Table 4.2). Most of the parameters are consistent with each other, but there are a few inconsistencies. First, the temperature of the secondary is significantly higher as measured in the u' band than in the other bands. This is possibly a result of using a blackbody approximation to calculate the flux (this is also seen in Parsons et al., 2010b), but could also indicate excess flux at shorter wavelengths due to the irradiation (Barman et al., 2004). The red dwarf temperatures ($T_{\rm RD}$) are also not entirely consistent for the g', r', and i' bands. This could be due to systematic uncertainties in the determination of the contribution by the interloper, which was already noted in Section 4.3.1, or the fact that also the spectrum of a low-mass star is not a blackbody, certainly in the redder parts of the spectrum where strong TiO absorption comes in. Related to the inconsistently high red dwarf temperature is the unphysically high albedo (>1) in the u' band results.

A second inconsistency are the values for $r_{\rm WD}$, $r_{\rm RD}$, and i for the i' band models compared to the results from the other bands. These three parameters are correlated and set by the duration of the ingress and egress, and the eclipse. The difference is $\sim 2-4$ standard deviations between the i' and g' solutions. This could be caused by the fact that in the i' band the interloper outshines the eclipsing binary PTF0857, which can cause systematic uncertainties. Because the solution is consistent for the u', g', and r' bands, we choose to accept those solutions, and we will ignore the solution in the i' band in further discussions.

Table 4.2: Results of the fits to the ULTRACAM light curves in the four different bands. We use linear interpolation to calculate the mass ratio for which the white dwarf radial velocity matches the observed 97 km s^{-1}. We calculate the value and uncertainty of each parameter for that mass ratio. For each parameter two uncertainties are given (both indicate the 16%–84% interval, equivalent to 1 standard deviation); the first is the uncertainty as a result of the uncertainty on the mass ratio q, the second is the statistical uncertainty. The zero–phase time is 55957.121914 BMJD (TDB), the best–fitting value for the g' band, and the table gives Δt_0, the offset from this value. A $^{\mathrm{p}}$ indicates that we used a prior of some sort for that parameter, see text for details.

		u'	g'	r'	i'
Light curve parameters					
Mass ratio	q	$0.31^{0.06}_{-0.06}$	$0.31^{0.06}_{-0.06}$	$0.32^{0.05}_{-0.06}$	$0.34^{0.06}_{-0.06}$
Phase 0 offset	Δt_0 (10^{-6} d)	$-11^{+0\ +9}_{-1\ -9}$	$0^{+0\ +3}_{+0\ -3}$	$2^{-0\ +11}_{-1\ -11}$	$8^{-4\ +23}_{-1\ -25}$
WD effective temperature$^{\mathrm{p}}$	T_1 (K)	$25700^{-0\ +400}_{+0\ -400}$	$25700^{-0\ +400}_{-0\ -400}$	$25700^{-0\ +400}_{-0\ -400}$	$25700^{-0\ +400}_{+0\ -400}$
RD effective temperature	T_2 (K)	$4200^{-70\ +250}_{+60\ -220}$	$3280^{-50\ +60}_{+90\ -60}$	$3110^{-90\ +80}_{+120\ -90}$	$3290^{-150\ +210}_{+230\ -190}$
WD radius/a	r_{WD}	$0.0199^{-0.0011\ +0.0010}_{+0.0014\ -0.0007}$	$0.0212^{-0.0012\ +0.0003}_{+0.0017\ -0.0002}$	$0.0205^{-0.0012\ +0.0009}_{+0.0016\ -0.0008}$	$0.0275^{-0.0020\ +0.0025}_{+0.0029\ -0.0022}$
RD radius/a	$r_{\mathrm{RD,L_1}}$	$0.352^{+0.017\ +0.022}_{-0.019\ -0.038}$	$0.345^{+0.016\ +0.010}_{-0.023\ -0.010}$	$0.339^{+0.020\ +0.014}_{-0.024\ -0.015}$	$0.285^{+0.022\ +0.020}_{-0.025\ -0.020}$
RD radius/a	r_{RD}	$0.281^{+0.012\ +0.003}_{-0.016\ -0.012}$	$0.279^{+0.013\ +0.002}_{-0.017\ -0.003}$	$0.277^{+0.014\ +0.003}_{-0.017\ -0.004}$	$0.256^{+0.017\ +0.012}_{-0.020\ -0.012}$
Binary inclination	i (°)	$76.5^{-0.8\ +0.6}_{+1.0\ -0.1}$	$76.5^{-0.8\ +0.1}_{+1.1\ -0.1}$	$76.6^{-0.9\ +0.3}_{+1.1\ -0.2}$	$77.7^{-1.1\ +0.8}_{+1.3\ -0.6}$
albedo		$1.91^{-0.04\ +0.23}_{+0.09\ -0.21}$	$0.96^{-0.03\ +0.05}_{+0.04\ -0.05}$	$0.89^{-0.04\ +0.05}_{+0.07\ -0.04}$	$0.62^{-0.07\ +0.06}_{+0.12\ -0.05}$
Interloper contribution^{P}	L_3 (μJy)	$3.8^{-0.3\ +2.1}_{+0.6\ -2.6}$	$11.2^{-0.3\ +0.5}_{+0.1\ -0.6}$	$36.9^{-0.1\ +1.2}_{+0.1\ -1.3}$	$97.8^{-0.1\ +2.9}_{+0.1\ -2.9}$
RD gravity darkening	γ_2	$0.7^{+0.0\ +0.4}_{-0.0\ -0.4}$	$1.1^{+0.0\ +0.1}_{-0.0\ -0.2}$	$0.8^{+0.0\ +0.3}_{-0.1\ -0.3}$	$0.9^{-0.0\ +0.2}_{-0.0\ -0.4}$
System parameters					
Semi–major axis	a ($\mathrm{R}_\odot$)	$0.88^{+0.08\ +0.05}_{-0.08\ -0.06}$	$0.87^{+0.08\ +0.04}_{-0.08\ -0.04}$	$0.87^{+0.08\ +0.05}_{-0.08\ -0.04}$	$0.83^{+0.08\ +0.05}_{-0.08\ -0.05}$
WD mass	M_{WD} ($\mathrm{M}_\odot$)	$0.61^{+0.15\ +0.12}_{-0.13\ -0.11}$	$0.61^{+0.15\ +0.10}_{-0.14\ -0.09}$	$0.60^{+0.16\ +0.10}_{-0.13\ -0.09}$	$0.50^{+0.13\ +0.09}_{-0.11\ -0.08}$
RD mass	M_{RD} ($\mathrm{M}_\odot$)	$0.19^{+0.09\ +0.04}_{-0.07\ -0.04}$	$0.19^{+0.09\ +0.03}_{-0.07\ -0.03}$	$0.19^{+0.09\ +0.03}_{-0.07\ -0.03}$	$0.17^{+0.08\ +0.03}_{-0.06\ -0.03}$
WD radius	R_{WD} ($\mathrm{R}_\odot$)	$0.0175^{+0.0006\ +0.0010}_{-0.0004\ -0.0010}$	$0.0185^{+0.0006\ +0.0009}_{-0.0004\ -0.0009}$	$0.0178^{+0.0005\ +0.0011}_{-0.0004\ -0.0011}$	$0.0227^{+0.0004\ +0.0021}_{-0.0000\ -0.0019}$
RD radius	R_{RD} ($\mathrm{R}_\odot$)	$0.24^{+0.03\ +0.02}_{-0.04\ -0.02}$	$0.24^{+0.03\ +0.01}_{-0.04\ -0.01}$	$0.24^{+0.04\ +0.01}_{-0.04\ -0.01}$	$0.21^{+0.04\ +0.02}_{-0.04\ -0.02}$
WD surface gravity	$\log g$	$7.74^{+0.07\ +0.04}_{-0.08\ -0.06}$	$7.69^{+0.07\ +0.03}_{-0.09\ -0.03}$	$7.71^{+0.08\ +0.04}_{-0.09\ -0.04}$	$7.43^{+0.09\ +0.08}_{-0.11\ -0.09}$
WD radial velocity$^{\mathrm{p}}$	K_{WD} [km s^{-1}]	$97^{+22\ +6}_{-22\ -6}$	$97^{+22\ +5}_{-22\ -5}$	$97^{+22\ +5}_{-22\ -5}$	$97^{+22\ +5}_{-22\ -5}$
RD radial velocity$^{\mathrm{p}}$	K_{RD} [km s^{-1}]	$309^{+14\ +19}_{-13\ -19}$	$309^{+13\ +16}_{-15\ -16}$	$306^{+15\ +16}_{-15\ -16}$	$288^{+13\ +16}_{-13\ -16}$
Roche lobe fill factor		$0.987^{+0.001\ +0.009}_{-0.001\ -0.041}$	$0.982^{+0.002\ +0.007}_{-0.006\ -0.010}$	$0.974^{+0.007\ +0.012}_{-0.008\ -0.016}$	$0.883^{+0.019\ +0.042}_{-0.022\ -0.041}$

4.4 Discussion

4.4.1 Mass, Radius and Temperature

The masses and radii of the two components are plotted in Fig. 4.8. As can be seen in this figure and Table 4.2, the uncertainty on the mass of the white dwarf is dominated by the uncertainty on the mass ratio. For a mass ratio in the range q=0.25–0.38, the white dwarf in PTF0857 has a mass between $M_{\rm WD}$ =0.47–0.71 $\rm M_{\odot}$, with a statistical uncertainty of ∼0.10 $\rm M_{\odot}$.

The mass and radius of the white dwarf are both consistent with He-core white dwarf models and CO-core white dwarf models, as can be seen in Fig. 4.8. The models of 25000 K He white dwarfs (Benvenuto & Althaus, 1999) match the solution in the mass range of $M_{\rm WD}$ =0.45–0.50 $\rm M_{\odot}$. Models for 25000 K CO-core white dwarfs (Fontaine et al., 2001) have a slightly smaller radius for a given mass compared to the He white dwarf models. Solutions with a mass in the range of $M_{\rm WD}$ =0.42–0.45 $\rm M_{\odot}$ match these models. Current uncertainties on the white dwarf mass and radius exclude a distinction on the white dwarf core composition, but both solutions are at the lower end of the mass range, which corresponds with low mass ratios in the binary system.

The red dwarf in PTF0857 has a mass between $M_{\rm RD}$ = 0.12 − −0.28 $\rm M_{\odot}$ for q =0.25–0.38, with a statistical uncertainty of ∼0.03 $\rm M_{\odot}$. The total uncertainty on the mass and radius of the red dwarf is even more dominated by the uncertainty in the mass ratio. If we compare our solution space to mass–radius models for single red dwarfs (Baraffe et al., 2015, solid black line in Fig. 4.8), the solution with a mass of 0.27 $\rm M_{\odot}$ and at a high value of q fits best. The model temperature for stars of this mass is ≈3340 K, consistent with results from our light curve modelling. Red dwarfs of this mass typically have spectraltype of ≈M3.5 (Rajpurohit et al., 2013), which agrees with our measurement in Section 4.3.3, M3-M5.

There are some caveats in using models for single M-dwarfs. Ritter et al. (2000) showed that for M dwarfs that are strongly irradiated, such as PTF0857, the radius of the red dwarf can increase by about 7 per cent (indicated by the dashed line in Fig. 4.8). A second effect of being part of a binary is that the red dwarf has a short rotation period making it mostly likely tidally synchronised to the orbital period. This short rotational period can make the M dwarf very magnetically active. High stellar activity inhibits convection, and for the star to remain in hydrostatic equilibrium, it has to increase its radius (Ribas, 2006; Chabrier et al., 2007). If either effect has increased the equilibrium radius of the red dwarf in PTF0857 a lower mass is required for it to fit the current solutions. For slightly oversized ('bloated') red dwarfs, our solutions intersect at 0.22 $\rm M_{\odot}$ (black dashed line in Fig. 4.8). Fig. 4.8 shows that, given the current uncertainty on the mass ratio, we cannot make a distinction between a bloated and a normal red dwarf radius.

The derived ranges on the masses, radii and temperatures of both the white dwarf and the red dwarf are consistent with stellar structure models. Given the derived radii, the stellar structure models would predict lower than measured masses. In comparing our solutions with varying mass ratios this points towards mass-ratios at the middle to higher end of the allowed range.

4.4.2 Surface gravity, spectral type, and distance

We calculated the distance to the system when fitting the model spectra to the data (Section 4.3.3). There is a slight discrepancy between the surface gravity of the white dwarf as measured

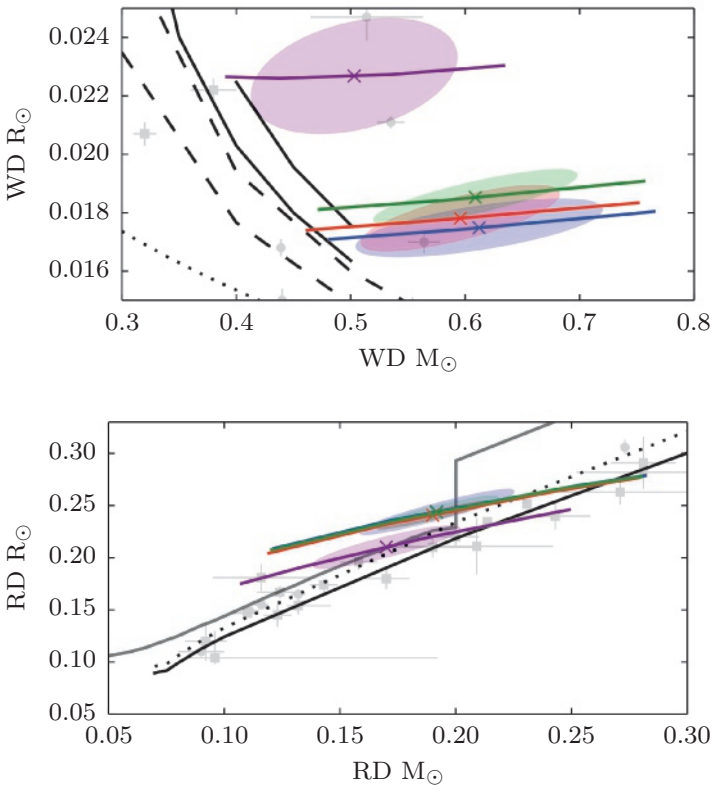

Figure 4.8: The mass versus radius of the white dwarf (top) and red dwarf (bottom). The 'x' markers show the most probable solutions for the masses and radii for the fit to the u',g',r', and i' light curves (blue, green, red and purple). The ellipses indicate the statistical uncertainty on the solution, and the solid coloured lines show the range of solutions due to the uncertainty in the mass ratio. (*Top*) The dotted line indicates the zero-temperature mass-radius relation by Verbunt & Rappaport (1988), the dashed lines show the models for a 25000 K CO white dwarf with a thin and thick hydrogen layer ($q_H = 10^{-10}$, $q_H = 10^{-4}$), taken from Fontaine et al. (2001), and the black line shows a model of a 25000K He white dwarf from Benvenuto & Althaus (1999). The grey circles indicate the mass and radius of white dwarfs in other PCEB binaries (Parsons et al., 2010a, 2012b,a, 2016). Grey squares indicate the mass and radius from the two white dwarfs in the eclipsing binary CSS 41177 (Bours et al., 2014). (*Bottom*) The solid black line represents a 5Gyr isochrone by Baraffe et al. (2015), the dashed line shows the same isochrone, but with the radius increased by 7% as predicted for irradiated red dwarfs, and the grey line indicates the mass-radius relation for red dwarfs in cataclysmic variables (Knigge et al., 2011). Grey circles indicate the mass and radius of red dwarfs in other PCEB binaries (Parsons et al., 2010a, 2012b,a, 2016). Grey squares indicate the mass and radius of single red dwarfs or red dwarfs with a main-sequence companion from Beatty et al., 2007; López-Morales, 2007; Nefs et al., 2013; Tal-Or et al., 2013; Zhou et al., 2014.

by fitting the spectra, $\log g = 7.86 \pm 0.07$, and as derived from the white dwarf mass and radius in the light curve modelling $\log g = 7.69^{+0.07}_{-0.09}\,^{+0.03}_{-0.03}$ (for the g' band). If the actual mass ratio is on the lower end of the allowed range, as discussed in the previous paragraph, the discrepancy between the spectra and the light curve modelling would grow.

The discrepancy in the surface gravity is likely due to systematic errors in fitting the spectra. The surface gravity from the spectra is mainly determined by the shape of the Balmer absorption lines of the white dwarf. These are contaminated by the red dwarf line emission. Considering this, we adopt the surface gravity from the light curve fit as the 'true' surface gravity of the white dwarf in PTF0857.

Because the surface gravity and distance are strongly correlated, we need to correct the distance determination to PTF0857. If we assume the surface gravity of the white dwarf given by the light curve results, the earlier distance estimate to the white dwarf based on the spectra, needs to be increased by a factor of 1.21 to $d = 686^{+128}_{-50}\,^{+23}_{-21}$ pc (the first uncertainties are the systematic uncertainties due to mass-ratio and second the statistical uncertainties), which we adopt as the distance to PTF0857.

The distance range associated with a red dwarf of spectral type M3-M5 is $1523 - 783$ pc. The lower end of this distance estimate (for an M5 red dwarf) is barely consistent with the upper end of the white dwarf distance range. This is not uncommon; Rebassa-Mansergas et al. (2007) compared distance estimates from white dwarfs and red dwarfs for white dwarf–red dwarf binaries and found that red dwarf distance estimates are often higher than the white dwarf distances. Rebassa-Mansergas et al. (2007) discuss a number of causes, including systematic problems in fitting the white dwarf or systematic problems in determining the red dwarf spectral type, problems with the spectral type - radius relation, effects due to close binarity, and effects due to age. If the red dwarf is oversized for its mass this would help to alleviate the distance discrepancy.

From the single spectrum of the interloper, we determined the spectral type M3 at a distance of 1132^{+96}_{-76} pc. The spectrum and SDSS-colour match the spectral type, so this measurement is robust. This distance indicates that the interloper is likely a background object if we assume the white dwarf distance is the distance to the binary system. We compared images from the DSS (Digitized Sky Survey) obtained in 1955 with recent SDSS images. The PSF of the DSS image is not good enough to distinguish PTF0857 from the interloper, but the angular distance between PTF0857 and the interloper does not seem to have changed. There is also no significant difference in the relative position of the blended source compared to field stars in the SDSS images, so neither of the objects has a large (relative) proper motion.

4.5 System evolution

There are two possible scenarios for the formation history of PTF0857; either it emerged from the common envelope as we see it now, or it is a CV that is currently detached (dCV) and is crossing the period gap. It is difficult to distinguish between these two scenarios as the system parameters of dCVs are the same as a subset of the PCEBs.

If PTF0857 is a PCEB that has emerged from the common-envelope phase, the system would not have changed much since emerging. Given its current temperature, we estimate white dwarf

cooling age $\tau_{\rm WD}\sim$25 Myr, if it is a CO white dwarf (Wood, 1995), or $\tau_{\rm WD}\sim$50 Myr for a helium white dwarf (Panei et al., 2007). This would also be the time since it emerged from the common-envelope. If the system is losing angular momentum due to gravitational waves only, the orbital period decreased just ∼1-2 minutes since then, which means it emerged from the common-envelope right in the orbital period gap of cataclysmic variables. Alternatively, the system could have gone through an sdB phase (lasting about ∼150 Myr) after emerging from the common envelope. This scenario requires that the white dwarf mass is around 0.48 $M_\odot$, which is at the lower mass bound of the solution space. It also means that gravitational wave radiation has had a longer time to shrink the system, which implies a common-envelope-exit at a period that is slightly longer, but no more than ≈8 min, depending on the lifetime of the shell burning in the sdB star.

If PTF0857 is a dCV, the system parameters should be similar to CVs just above and below the period gap and consistent with CV evolution models. Measured white dwarf temperatures for CVs above the gap range from 15 000K to 50 000K (Townsley & Gänsicke, 2009; Pala et al., 2017), while the CV evolution models predict temperatures in the range of 23 000-30 000K at the upper end of the period gap. The white dwarf in PTF0857 (25 700K) fits within this range, but it should have cooled down after entering the period gap. Under the emission of gravitational wave radiation only it will have taken ≈0.8 Gyr to decrease the orbital period to its current value. The cooling age of the white dwarf is much shorter than this and therefore the system is unlikely to have entered the period gap at ≈3.18 hours. The actual temperature of the white dwarf at the entry into the orbital period gap is not relevant for this discrepancy between the cooling time and the gravitational in-spiral time. Fig. 5 in Townsley & Gänsicke (2009) indicates that very hot WDs in CVs at the upper end of the period gap do exist, but after close to a billion years they should all have cooled down to values far lower than 25 700 K. In a recent paper, Zorotovic et al. (2016) used binary population models and numerical simulations to predict the system parameters of the observed population of PCEBs and dCVs. They show that white dwarfs with a temperature of 25 700K occur in both PCEB and dCV systems with an orbital period of 2.5 h, and conclude that the white dwarf temperature cannot be used to distinguish if a system is a dCV or PCEB. It is however not clear how these systems would 'escape' the cooling age argument given above. The same study does show that the distribution of the white dwarf masses is different for the two populations; massive white dwarfs ($M > 0.8\,M_\odot$) only occur in dCV systems. The mass of the white dwarf in PTF0857 is $M_{\rm WD} = 0.61^{+0.15}_{-0.14}\,M_\odot$, which occurs in both scenarios and is consistent with measured white dwarfs in CVs both above and below the period gap. In conclusion, with the uncertainties in the white dwarf mass and in the evolutionary models, we cannot exclude either scenario based on the white dwarf properties, although a detached CV scenario is unlikely given the high temperature of the white dwarf.

The Red dwarf spectral type is consistent with measured spectral types of CVs, as well as the model value of M4.0 (Knigge et al., 2011). If we compare the mass and radius of the red dwarf to measurements of red dwarfs in CVs above and below the period gap (Table 1 in Knigge, 2006), we note that they are consistent both in mass and radius with CVs below the gap, but fall below the range of masses and radii of CV-red dwarfs above the gap, see also the grey line in Fig. 4.8. The CV-model by Knigge et al. (2011), which is based on measurements, predicts that the mass of a red dwarf that has just stopped mass transfer (a dCV) is $M_{\rm RD} = 0.20 \pm 0.02\,M_\odot$. While the red

dwarf radius is still inflated just after mass-transfer stops, it quickly shrinks down to a radius of $R_{\rm RD} = 0.23\,{\rm R}_{\odot}$ (Stehle et al., 1996). This combination of mass and radius is within the solution space for PTF0857 (see Fig. 4.8). The red dwarf is filling ∼98 per cent of the Roche lobe in radius (∼94% of the volume), well within the predicted range for dCVs (>76%) for the orbital period of PTF0857. In conclusion: the red dwarf mass and radius are consistent with measurements of CV-red dwarfs at the upper end of the period gap, and also consistent with model values of the red dwarf radius in the dCV scenario.

Regardless of which of the two scenarios is correct, the future of the binary is the same: the binary separation will shrink due to gravitational wave emission and the system will come into contact in ≈70 Myr. If the radius of the secondary does not change, stable mass transfer will start at an orbital period of about 2.47 h, very close to its current value, and the system will continue its evolution as a cataclysmic variable, very similar to the known systems SDSS J1627+1204 and SDSS J0659+2525 (Ritter & Kolb 2003; Shears et al. 2009). If it is currently a PCEB that emerged from the common envelope at a period close to the current period, it implies that a direct injection of systems to the cataclysmic variable below the period gap is possible and that therefore the space density of systems above the gap should be lower than that of systems below the gap.

4.6 Summary

PTF1 J085713+331843 is an eclipsing binary with an orbital period of 0.1060272(4) d, consisting of a 25 700 K DA white dwarf and an M3–M5 red dwarf. The light curve shows a total primary eclipse of the white dwarf and a strong reflection effect but no secondary eclipse. The system has a nearby neighbour ∼1.5 arcsec distant, with a spectral type M3 and is most likely a background object.

We analysed high cadence ULTRACAM light curves in the u', g', r' and i' bands and phase-resolved spectroscopy to determine the system parameters. The white dwarf's radial velocity accuracy is the main source of uncertainty on the system parameters. The white dwarf has a derived mass of $M_{\rm WD} = 0.61^{+0.15}_{-0.14}\,{\rm M}_{\odot}$. The white dwarf mass-radius solution is compatible with models of both He and CO white dwarfs. The red dwarf mass is $M_{\rm RD} = 0.19^{+0.09}_{-0.07}\,{\rm M}_{\odot}$, and matches red dwarf mass-radius models. The best solutions to mass-radius models for the white dwarf and red dwarf are consistent which each other within the observational uncertainties.

To improve our measurements, we require higher signal-to-noise phase-resolved spectroscopy over at least one orbit to measure the white dwarf radial velocity amplitude with higher precision. In addition, the NaI absorption doublet near 8200 Å can be used to measure the radial velocity of the centre of mass of the red dwarf, although the radial velocity measurements need to be corrected for the irradiation effect, as was done in Parsons et al. (2010b).

The semi-major axis of the system is smaller than a solar radius, and therefore the system must have experienced a common-envelope phase in its evolution. Within the current uncertainties, we cannot clearly distinguish between a detached CV or a PCEB. In the former case, the system has already been a cataclysmic variable and is currently in hibernation. In the latter case, the system emerged from the common-envelope at an orbital period close to its current period, which then happened about 25–50 Myr ago. The system will keep losing angular momentum due to

gravitational wave emission and start stable mass transfer in only ≈70 Myr, at an orbital period close to its current value. It will become one of the few known cataclysmic variables in the period gap.

4.A Centre of light offset

For stars that do not have a uniform surface brightness, the centre of light emitted by that star is not the same as the centre of mass of the star. If the star is in a close binary, this can significantly offset the measured radial velocity. We describe this effect using $f \equiv \text{offset}/R$, the distance between the centre of light from the centre of mass divided by the radius of the star. If $f = 0$, the offset is zero, while $f = 1$ is the most extreme case, where the centre of light is at the surface of the star. In the following discussion, we estimate the value of f at quadrature, starting from a simple model.

Wade & Horne (1988) discussed the case where one hemisphere of the star is showing an absorption line. In this case, assuming the star is spherical, f is equivalent to the centre of mass of a semi-circle:

$$f = \frac{\int_0^{\pi/2} \cos(\theta) \sin^2(\theta) d\theta}{\int_0^{\pi/2} \sin^2(\theta) d\theta} = \frac{4}{3\pi} \approx 0.424 \tag{4.3}$$

In the paper by Horne & Schneider (1989), a lower limit is calculated for the offset factor of an irradiated red dwarf. Assuming a spherical star, an irradiation source at infinity, and the reflected light is proportional to the incoming light, the value of f can be calculated by analytically solving equation 4.4.

$$f = \frac{\int_0^{\pi/2} \cos^2(\theta) \sin^2(\theta) d\theta}{\int_0^{\pi/2} \cos(\theta) \sin^2(\theta) d\theta} = \frac{3\pi}{16} \approx 0.589 \tag{4.4}$$

If the reflection effect is detected, the irradiated star's radius is significant compared to the semi-major axis, and the assumption that the irradiation source is at infinity is not correct anymore. Assuming a point source at a finite distance has two effects; the irradiation is stronger closer to the irradiating object, and not the entire hemisphere is irradiated. Equation 4.5 includes these two corrections, and Figure 4.9 illustrates the geometry. The solution of the equation only a function of $r = R/a$, which is shown in Figure 4.10 by the black line.

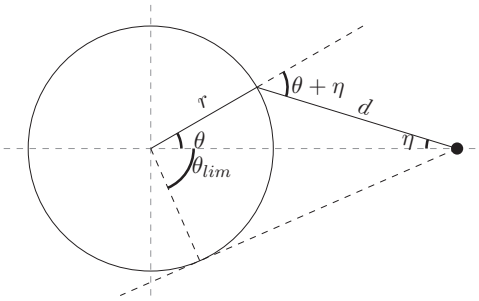

Figure 4.9: This figure shows the angles involved in the calculation. The circle represents the irradiated star's surface and the dot indicates the points source.

$$f = \frac{\int_0^{\theta_{\rm lim}} \cos(\theta) d^{-2} \cos(\theta + \eta) \sin^2(\theta) d\theta}{\int_0^{\theta_{\rm lim}} d^{-2} \cos(\theta + \eta) \sin^2(\theta) d\theta} \tag{4.5}$$

$$\text{where } \eta = \arctan \frac{r \sin\theta}{1 - r\cos\theta}$$
$$d = \frac{r\sin\theta}{\sin\eta}$$
$$\theta_{\text{lim}} = \pi/2 - \arcsin(r)$$

So far we have assumed a spherical star, which makes it possible to write down an analytic expression for f. However, stars in close binaries are deformed by their companion star and their shape has a Roche geometry. This makes the analytic solution extremely complicated and solving the problem requires numerically integrating the incoming light and the observing angle over the entire surface of the star. The most extreme deviation is for Roche lobe filling stars, shown by the grey line in Figure 4.10. As you can see, taking this into account decreases the offset factor compared to a spherical star. The reason is that due to the Roche geometry, the maximum radius increases, while the rest of the stars remain approximately spherical, and thus the factor f decreases.

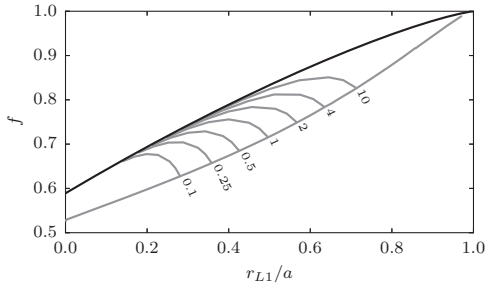

Figure 4.10: The offset factor f versus the radius of the star divided by the orbital separation (r). The black line indicates an irradiated sphere by a point source at a finite distance and the grey line indicates the offset factor for irradiated stars filling their Roche lobe. The number next to the grey line indicates the mass ratio q of the binary system.

Chapter 5

Discovery of 36 eclipsing EL CVn binaries found by the Palomar Transient Factory

J. van Roestel, T. Kupfer, R. Ruiz-Carmona, P.J. Groot, T.A. Prince, K. Burdge, R. Laher, D.L. Shupe, E. Bellm

MNRAS 475, 2560–2590 (2018)

Abstract

We report the discovery and analysis of 36 new eclipsing EL CVn-type binaries, consisting of a core helium-composition pre-white dwarf and an early-type main-sequence companion, more than doubling the known population of these systems. We have used supervised machine learning methods to search 0.8 million lightcurves from the Palomar Transient Factory, combined with SDSS, Pan-STARRS and 2MASS colours. The new systems range in orbital periods from 0.46 to 3.8 d and in apparent brightness from ∼14 to 16 mag in the PTF R or g' filters. For twelve of the systems, we obtained radial velocity curves with the Intermediate Dispersion Spectrograph at the Isaac Newton Telescope. We modelled the lightcurves, radial velocity curves and spectral energy distributions to determine the system parameters. The radii (0.3–0.7 $R_\odot$) and effective temperatures (8000–17000 K) of the pre-He-WDs are consistent with stellar evolution models, but the masses (0.12–0.28 $M_\odot$) show more variance than models have predicted. This study shows that using machine learning techniques on large synoptic survey data is a powerful way to discover substantial samples of binary systems in short-lived evolutionary stages.

5.1 Introduction

EL CVn binaries are eclipsing binaries containing a low mass ($\sim$0.15–0.33 $M_\odot$) pre-helium white dwarf (pre-He-WD) and an A/F-type main sequence star. The prototype system, EL CVn, is part of a sample of 17 EL CVn systems (Maxted et al., 2014a) discovered by SWASP (Pollacco et al., 2006) with magnitudes in the range of $9<V<13$. All lightcurves show "boxy", shallow eclipses ($\lesssim$ 0.1 mag depth) with periods between $\sim$0.5d and $\sim$3 d, and in most cases ellipsoidal variation due to the deformation of the A/F-star. The low radial velocity amplitudes ($\sim$15–30 km s^{-1}) of the primaries confirm the low mass nature of the pre-He-WDs.

A total of 10 EL CVn systems were found in the Kepler survey: KOI-74 (van Kerkwijk et al., 2010; Bloemen et al., 2012); KOI-81 (van Kerkwijk et al., 2010; Matson et al., 2015); KOI-1375 (Carter et al., 2011); KOI-1224 (Breton et al., 2012); KIC-9164561, KIC-10727668 (Rappaport et al., 2015); KIC-4169521, KOI-3818, KIC-2851474, and KIC-9285587 (Faigler et al., 2015). All these systems were studied in great detail, and by modelling the Kepler lightcurves in combination with radial velocity curves, all system parameters have been determined. Four of these systems contain small pre-He-WDs ($< 0.05\,R_\odot$) and as a consequence their lightcurves feature shallow eclipses only detectable from space. The fact that 10 EL CVn-like systems are found in the Kepler field suggests that there should be many more in our Galaxy, in line with an estimate of the local space density from stellar evolution and population synthesis models, 4–10 $\times$ 10^{-6} pc^{-3} (Chen et al., 2017).

Besides the samples found by Kepler and SWASP, there were serendipitous discoveries of binaries related to EL CVn systems. The star V209 in ω Cen is likely an EL CVn binary (Kaluzny et al., 2007), but the primary does not seem to be a typical main sequence star: its mass is 0.95$M_\odot$ but it has a temperature of 9370 K. OGLE–BLG–RRLYR–02792 is an eclipsing binary which contains a large pre-He-WD which seems to be pulsating like an RR-Lyrae star (Pietrzyński et al., 2012). A possible non-eclipsing variant of an EL CVn binary is the star Regulus (α Leo). Gies et al. (2008) and Rappaport et al. (2009) found that Regulus A is a single-lined spectroscopic binary with a period of 40 d, consisting of an A-type primary and a companion with a mass of $>0.3\,M_\odot$, at the upper end of the pre-He-WDs mass range.

EL CVn binaries share many characteristics with a new type of binary: "R CMa"-type binaries are Algol binaries with a bloated, low mass, donor (e.g. Budding & Butland, 2011; Lee et al., 2016). They are very similar to EL CVn systems, except that they are semi-detached, and therefore considered the progenitors of EL CVn systems. Two "detached R CMa" systems have been identified using Kepler photometry and are now considered to be newly born EL CVn binaries (KIC-10661783; Lehmann et al. 2013, and KIC-8262223; Guo et al. 2017).

EL CVn systems are part of a larger family of binaries where one component of the binary is an extremely low mass white dwarf (ELMWD). The majority of ELMWD-containing binaries without a main-sequence companion have white dwarf or neutron star companions instead (e.g. Marsh et al., 1995; van Kerkwijk et al., 2005). In these systems, the ELMWD dominates the luminosity, making them identifiable with a single spectrum. The ELM survey (Brown et al., 2010) uses this approach and has been successful in finding many ELMWDs in binary white dwarf systems.

In this paper, we present system parameters for 36 new EL CVn systems, all eclipsing, discovered using the Palomar Transient Factory (PTF). In Section 5.2 we describe the identification of the

systems using supervised machine learning classifiers. In Section 5.3 we discuss the spectroscopic follow-up of 12 of the new systems. In Section 5.4 we discuss the analysis of the lightcurves, spectra and spectral energy distributions, and we present the results in Section 5.5. In Section 5.6 we compare our results with theoretical prediction and compare our sample with already known EL CVn binaries. We end with a summary and conclusion in Section 5.7.

5.2 Target selection

5.2.1 The Palomar Transient Factory

The Palomar Transient Facility (PTF) used the 1.2 m Oschin Telescope at Palomar Observatory with a mosaic camera consisting of 11 CCDs. The CCDs have 4Kx2K pixels and the camera has a pixel scale of $1.02''$/pixel, giving it a total field of view of 7.26 square degrees. PTF uses an automated image processing pipeline which does bias and flatfield corrections, source finding and photometry. All data is automatically processed, see Rau et al. (2009a); Law et al. (2009a) for further information.

5.2.2 Data

For all objects detected by PTF, lightcurves are automatically generated (see Laher et al., 2014) and lightcurve statistics are calculated. These statistics include, among others, the mean, root-mean-square, percentiles, χ^2-statistic, see Masci & Bellm (2016) for a full list. These lightcurve statistics are based on the lightcurve features used in Richards et al. (2011, 2012), that are useful to distinguish different types of variable stars. Important to note is that we do not use features related to any periodicity in the lightcurve. This has a practical reason; it is very difficult to automatically obtain a reliable period for all the PTF lightcurves because they are sparsely sampled and span many years.

For this study, we used all available lightcurve data that was obtained between the start of PTF in December 2008 and March 2016. We treat the data for the R and g' filter as two separate datasets in the subsequent analysis. These datasets are very substantial (R: $\sim$250 million, g': $\sim$50 million objects). We make an initial cut and select only objects which are variable by requiring that $\chi^2_{\rm reduced} > 10$, that lightcurves have more than 40 epochs, and that objects are brighter than 16 mag in either PTF R or PTF g'. This still leaves more than $\sim 10^5$ candidates (see Table 5.1 and Fig. 5.1).

We match the objects in these datasets to the latest SDSS catalogue (*ugriz* bands, DR13, SDSS Collaboration et al., 2016), the NOMAD catalogue (*JHK* bands, Zacharias et al., 2004), and the Pan-STARRS catalogue (*grizy* bands, Chambers et al., 2016). An overview of the total number of objects and the colour availability are given in Table 5.1.

5.2.3 Machine Learning Classification

To cut back on the number of candidates for an initial visual lightcurve inspection, we use supervised machine learning classifiers to make a pre-selection. The idea is that instead of finding EL CVn binaries by using fixed, pre-defined, user-supplied selection criteria, a sample of known EL CVn

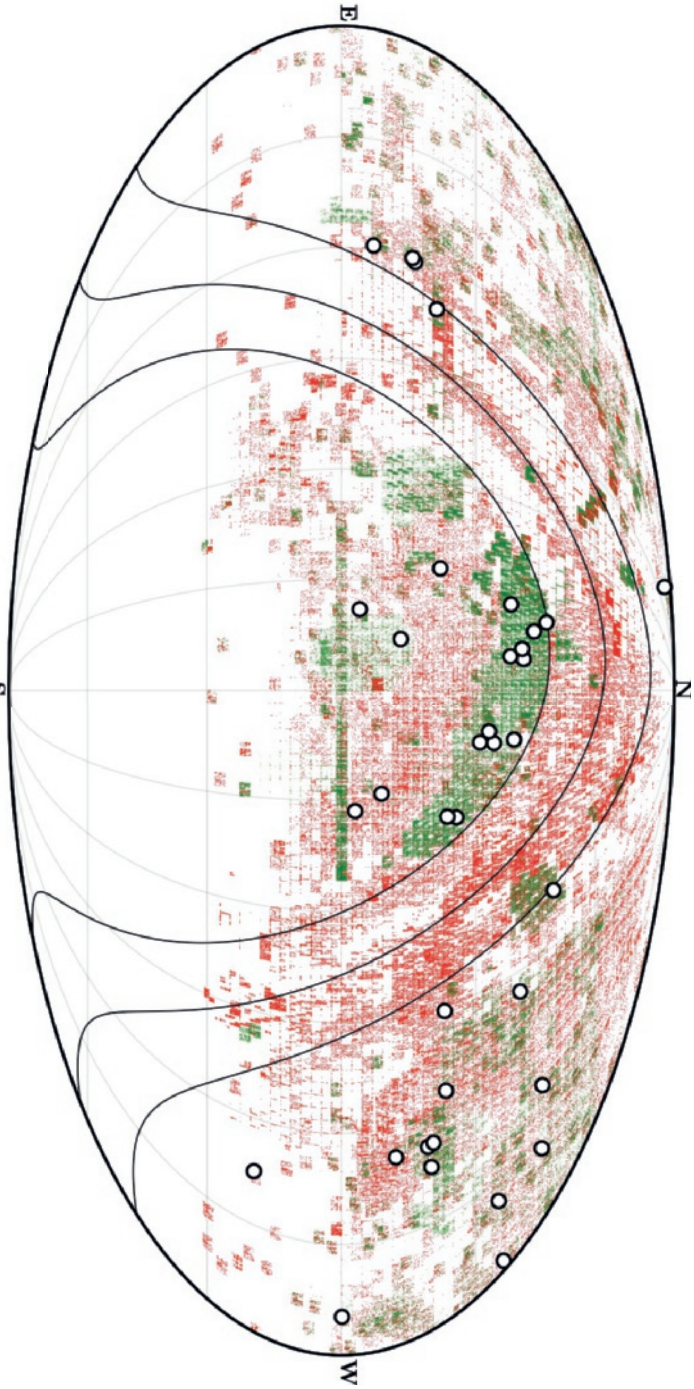

Figure 5.1: All objects in the PTF sample after our initial cut (> 40 epochs, $\chi^2_{\rm reduced} > 10$, < 16 mag), red for PTF R, green for PTF g'. The EL CVn binaries we discovered in the data are shown as white dots. The black lines show Galactic latitudes of −15°, 0°, and 15°.

Table 5.1: The number of objects after our initial selection with PTF lightcurves (>40 epochs, $\chi^2_{\rm reduced} > 10$, <16 mag). The percentage for which additional colour information is available is shown in the table below.

Filter	# objects	SDSS	NOMAD	Pan-STARRS
		ugriz	*JHK*	*grizy*
R	532 477	43.65%	97.58%	98.92%
g'	257 918	55.45%	98.69%	99.26%
$R \cap g'$	36 943	64.39%	96.48%	98.66%

binaries and not–EL CVn objects (a 'training set') is provided and a machine learning code ('classifier') decides what the best way is to separate the two groups given the characteristics (called 'features', e.g. $g - r$ colour or the lightcurve's root-mean-square value). There are many different types of classifiers, and the behaviour of each classifier can be adjusted by changing so-called hyperparameters. Setting the correct hyperparameters is required to avoid over- or underfitting of the data. For an introduction to machine learning in astronomy, see Ivezić et al. (2014), and for a practical guide to machine learning (with Python) see Müller & Guido (2016).

Because supervised machine learning classifiers can process huge amounts of data very quickly, they have become a popular tool to handle with the large amount of lightcurves produced by survey telescopes. Many different techniques have been tried for lightcurve classification (e.g. Debosscher, 2009; Palaversa et al., 2013; Angeloni et al., 2014; Peters et al., 2015; Mackenzie et al., 2016; Armstrong et al., 2016; Sesar et al., 2017). In recent years, the Random Forest method (Breiman, 2001) has become very popular as it typically performs the best and is also easy to interpret (e.g. Richards et al., 2011; Masci et al., 2014).

To find EL CVn binaries we have experimented with three different supervised machine learning classifiers based on combining decision trees: the standard 'Random Forest', an 'Extra-Trees' classifier (Geurts et al., 2006), both implemented in the Python package sklearn (Pedregosa et al., 2011), and the more sophisticated 'Gradient boosted decision tree' classifier, implemented in XGBoost (Chen & Guestrin, 2016). All three classifiers combine many randomised decision trees, which are a sequence of binary decisions.

Here we briefly discuss the differences between the methods. Both Random Forest and Extra-Trees combine the prediction of many independent, randomised decision trees. The larger the number of trees the better but at the cost of increased computation time. For both methods, each tree is built using only a subset of all features (rule-of-thumb is the square root of the total number of features). Random Forest uses the best possible split of the data given the available features and uses that to separate the different classes. Extra-Trees differs from Random Forest as it does not use the best split, but a random split. This extra randomization step has the consequence that decision boundaries are more smooth compared to Random Forest. Both methods are relatively simple; they have only a few hyperparameters and are relatively robust against overfitting. XGBoost also uses many randomised decision trees. But instead of combining many independent trees, new trees are created to optimally complement the existing trees. This is done by giving samples which were wrongly classified by the previous trees a larger weight when building the next tree. The next tree is, therefore, more likely to classify these objects correctly. The disadvantage of this

method is that it is more sensitive to overfitting compared to Random Forest. The XGBoost implementation has many hyperparameters which can be set to counteract this, but it can be difficult to determine the best values for these parameters. The advantages of all three methods are that they are insensitive to uninformative features, do not require scaling of the data, and are easy to interpret: they automatically determine the importance of features.

5.2.4 EL CVn identification

Because supervised machine learning algorithms require a training sample we first need to identify EL CVn binaries in our data. There are no known EL CVn binaries in the PTF magnitude range, so we need to find new ones the old-fashioned way. We do this by selecting a sample of A–type main sequence stars using SDSS colours ($0.8 < u - g_{\rm SDSS} < 1.5$ and $-0.5 < g - r_{\rm SDSS} < 0.2$) and require that Stetson-K > 0.6 (one of the lightcurve statistics, see also Stetson 1996). To limit the sample size and have increased post-facto confidence in the selected objects, we further require that the lightcurve is significantly variable ($\chi^2 > 40$) and with more than 150 epochs in R and 100 in g'. EL CVn binaries are characterized by their $\lesssim 0.1$ mag, flat-bottomed primary eclipse and slightly shallower secondary eclipse. We, therefore, do a period search using both Analysis-of-Variance and Boxed-Least-Square methods (AoV, Schwarzenberg-Czerny 1989; Devor 2005; BLS, Kovács et al. 2002, vartools implementation Hartman & Bakos 2016) on each of the lightcurves and inspect each folded lightcurve for these criteria. In case of doubt the candidate was included in the lightcurve modelling (see Section 5.4.1). If the lightcurve fitting showed a 'V'-shaped, non-total, eclipse, we rejected it from the sample, as these systems could also be regular MS-MS binary. In other words, we require our systems to be totally eclipsing.

Using this method, we found 6 EL CVn binaries, which we then used as a training set for a Random Forest classifier, combined with a sample of 4000 randomly chosen objects (which we confirmed are not EL CVn binaries). Since the training set is so small, we do not attempt any parameter optimisation, but used the default hyperparameters (500 trees, the square-root of the total number of features as the number of features per tree, and no limits on the tree depth). We applied the classifier to the data (the PTF R and PTF g' lightcurve statistics combined with SDSS colours) and inspected the $\sim$100 best candidates identified by the classifiers. We added newly found EL CVn candidates to the training sample and repeated the procedure an additional two times. This resulted in the discovery of an additional 11 systems, bringing the total to 17.

Because we required that SDSS colours were available, we only inspected roughly half of the data so far (see Table 5.1). We, therefore, replaced the SDSS colours with the $BVRHJK$ colours from the NOMAD catalogue (Pan-STARRS colours were not yet available at this time). We again checked the best 100 candidates in an iterative way, adding the new EL CVn systems to the training sample. The combined SDSS and NOMAD process resulted in a total of 30 EL CVn binaries.

With this sample, we trained the three different classifiers (Random Forest, Extra-Trees and XGBoost) and determined the best hyperparameters. We use the PTF variability features combined with the Pan-STARRS colours. The goal of our classifier is not to classify all samples correctly (high precision), but instead to rank the candidates according to 'EL CVn' likeness. We, therefore, do not optimise the precision of our classifier, but instead we use the 'area-under-

curve' for the 'receiver operating characteristic' (roc-auc). We do this using stratified K-fold cross-validation to calculate the roc-auc score. For more details on classifier metrics (like roc-auc) and model optimisation, see Ivezić et al. (2014); Müller & Guido (2016).

For both Random Forest and Extra-Trees we find similar optimal hyperparameters. Using more than 600 trees does not improve performance significantly. The number of features per tree influences the roc-auc score marginally, but there is a clear preference for only using two features per tree. We checked different hyperparameters that limit the depth or complexity of the tree, but we find that the roc-auc score only decreases when the tree depth or complexity is limited using any of the hyperparameters.

For XGBoost there are more hyperparameters to tune. We start by optimising the most important three: the number of estimators, the learning rate and the tree depth while setting the other parameters to typical values. After finding the optimal combination of these hyperparameters we continue to optimise the minimum child weight, sub-sampling fraction and the column sub-sample fraction.

After training all classifiers we selected the top 1000 candidates (in both R and g' datasets) from the three classifiers and visually inspected their lightcurves. We found an additional 6 EL CVn binaries, bringing the final number to 36 systems, listed in Table 5.2.

A quick comparison between the classifiers shows that both the Extra-Trees classifier and the XGBoost classifier perform equally well while the Random Forest performs a bit worse. This is confirmed by the ranking of the last six discovered EL CVn binaries that were all further down the list for the Random Forest method. Although Extra-Trees and XGBoost performance is comparable, tuning the XGBoost classifier took significantly more time and effort. Due to the combination of yield versus investment, we deem the Extra-Trees classifier the best (in this particular case).

PTF observed the Kepler field and has thus observed the EL CVn binaries found by Kepler. None of these were recovered by our search and we investigated the reason why. First of all, most Kepler systems feature eclipses much shallower than PTF can detect. The Kepler EL CVn systems with deep enough eclipses to be detected by PTF were not recovered because either the star was saturated in the PTF data, or the object was not observed at a sufficient number of epochs.

5.3 Spectroscopy

For 19 of our EL CVn systems, we obtained phase-resolved spectroscopy with the Isaac Newton Telescope (INT). We used the Intermediate Dispersion Spectrograph (IDS) with the R632V grating (0.90 Å pixel^{-1}, 3800–5800 Å) for 8 bright nights and the R900V grating for 9 bright nights on 3 separate runs (0.63 Å pixel^{-1}, 4000–5500 Å). Conditions were good with seeing of $\lesssim$ 1 arcsec, except for the last four nights. During these nights the seeing was 2–5 arcsec and two nights were mostly clouded. An overview of the spectroscopic runs, the set-up and the weather quality is given in Table 5.6.

Since the orbital period and phase for all systems is determined very precisely from the photometry (see Section 5.5), we timed the observations such that we observed the systems around orbital phases 0.25 and 0.75. The signal–to–noise per pixel of each spectrum ranges between 40 and

Table 5.2: Overview of the EL CVn binaries we discovered in the PTF data. In the rest of the paper we will use the PTF name. The "PTF R"-column lists the median magnitude of the light curve in R-band.

PTF name	IAU name (PTF1 J...)	P (d)	PTF R
PTFS1600y	J004040.23+412521.61	1.184	13.7
PTFS1600ad	J004300.75+381537.26	1.084	14.7
PTFS1700do	J005424.06+411126.98	3.051	15.7
PTFS1600aa	J005659.72+130920.66	0.693	15.9
PTFS1601p	J011909.91+435907.11	1.222	15.3
PTFS1501bh	J012814.72+040551.90	0.620	13.9
PTFS1601q	J013336.92+470600.18	1.252	16.2
PTFS1601cl	J014839.10+382314.56	0.892	13.6
PTFS1402de	J021913.15+215921.98	0.619	15.0
PTFS1607aa	J071207.01+211654.98	0.846	15.0
PTFS1607v	J075310.42+835154.79	0.720	15.3
PTFS1607t	J075642.49+162143.99	0.876	14.2
PTFS1607ab	J075950.03+154319.09	0.773	14.0
PTFS1608ab	J080425.26+070845.24	0.610	14.6
PTFS1612al	J121254.27+363341.76	0.637	15.7
PTFS1512bf	J124154.58+001333.06	0.607	14.2
PTFS1613s	J133220.59+352847.28	1.142	14.3
PTFS1613u	J133929.37+455055.64	0.564	15.3
PTFS1615ag	J150041.84−191417.23	0.681	14.3
PTFS1615v	J150327.61+460322.78	0.559	15.9
PTFS1515ay	J150336.10+195842.16	0.464	14.8
PTFS1615w	J152726.81+120453.54	1.441	14.9
PTFS1615ao	J152758.90+190751.63	0.895	15.0
PTFS1615u	J153005.01+202157.06	0.778	15.8
PTFS1616cr	J162342.13+231456.58	0.565	14.0
PTFS1617n	J173257.98+403600.93	2.337	15.3
PTFS1617m	J175433.50+230041.83	3.773	14.7
PTFS1619l	J191826.08+485302.94	1.160	13.7
PTFS1521ct	J213318.98+254126.30	1.172	15.8
PTFS1621ax	J213534.11+233313.86	1.018	15.0
PTFS1521cm	J214858.33+030417.50	0.685	15.1
PTFS1622by	J220719.56+085415.66	0.749	15.8
PTFS1522cc	J225539.41+342137.72	0.572	14.7
PTFS1622aa	J225652.53+390822.70	0.766	15.6
PTFS1622bt	J225755.64+310133.67	0.688	15.1
PTFS1723aj	J231010.08+331249.78	1.109	14.8

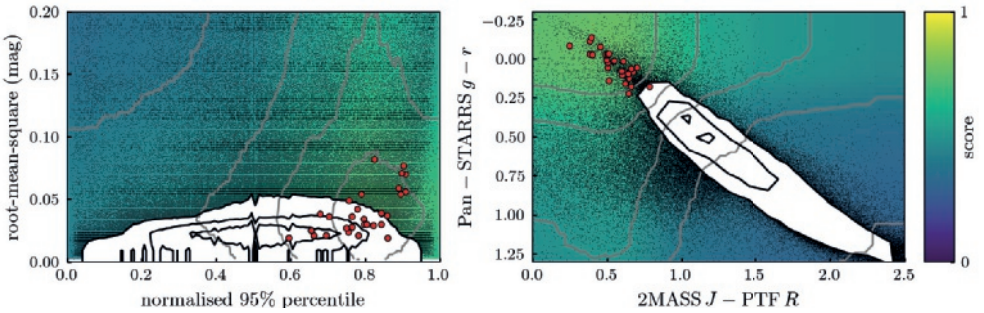

Figure 5.2: The left panel shows the weighted root-mean-squared of the PTF lightcurve versus the normalised 95th percentile of the lightcurve (percentile 95 minus median, divided by 90 percentile range, see Table 5.5), the right panel shows 2MASS J-PTF R versus Pan-STARRS g-r colour–colour space. The red dots show all EL CVn binaries, the black contours show all samples in the PTF R dataset, with the black contours containing 25, 50, and 75 per cent of the data, samples outsides the contours are indicated with black points. The background colour indicates the 'EL CVn'–score by the Extra-Trees classifier with grey lines at every 0.1 score interval. The score is calculated assuming the median values of the EL CVns for all parameters, except the parameters on the x- and y-axis.

80, sufficient to detect the weaker metal lines in the A/F-star's spectrum. Spectra were taken in pairs and before or after each stellar spectrum a calibration lamp spectrum (CuAr) was obtained to make sure the wavelength calibration was stable.

The data were reduced using IRAF. We used L.A.Cosmic (van Dokkum, 2001) to remove cosmic rays and performed the standard bias and flat calibrations. For the wavelength calibration, we used ∼40 arc lines, which resulted in a typical root-mean-square uncertainty on the wavelength solution of $\lesssim$0.1 pixels (4-6 km s^{-1}).

5.4 Methods and analysis

5.4.1 Lightcurve

By modelling the lightcurves we put strong constraints on the system parameters. To construct a model lightcurve given a set of binary star parameters, we use lcurve (by T.R. Marsh and collaborators, see Copperwheat et al., 2010, see also Copperwheat et al., 2011; Parsons et al., 2011). The lcurve code uses grids of points to model the two stars. The shape of the stars in the binary is set by a Roche potential. We assume that the orbit is circular and that the rotation periods of the stars are synchronised to the orbital period. We discuss the validity of the latter assumption in Section 5.6.1. We calculate the lightcurves assuming the effective wavelength of the PTF filters; 4641 Å for the g' filter and 6516 Å for the R filter. In this section (and the rest of the paper), we refer to the A/F–type main sequence as the primary (subscript '1') and the pre-He-WD as the secondary (subscript '2').

The free parameters of the model are: the orbital period (P) and mid-eclipse time (t_0), both in

$\mathrm{BMJD_{TDB}}$ (the barycentric Julian date in the terrestrial dynamic time frame, minus 2400000.5), the effective temperatures of both stars ($T_{1,2}$), the scaled radii of both stars ($r_{1,2} = R_{1,2}/a$, where a is the binary separation), the inclination angle (i), the mass ratio ($q = M_2/M_1$), an albedo (absorption) for both stars, a linear limb darkening coefficient ($x_{1,2}$), and a gravity darkening coefficient ($y_{1,2}$) in the relation $I \propto g^y$ (where g is the local surface gravity, von Zeipel, 1924). Not all these parameters are well constrained by the data and therefore we fix or set an allowed range for some parameters. We constrain the temperature of the primary star (T_1) to 6500–10000 K; the temperature range of A/F–type main-sequence stars. This is needed because with only a lightcurve the temperature ratio is well constrained, but the absolute values of the temperatures of each star are not. We will not use the resulting temperatures of the lightcurve fit, but instead determine the effective temperatures of both stars by modelling the spectral energy distribution (see Section 5.4.2). We fix the limb darkening coefficient of star 2 (x_2) to 0.5, since the effect on the lightcurve is minimal. We allow the limb darkening coefficient of the A/F-star (x_1) to vary between 0.08 to 1.05, the lowest and highest values for stars in the allowed temperature range (Gianninas et al., 2013).

To determine the uncertainty on the parameters we use the Markov Chain Monte Carlo (MCMC) method as implemented by emcee (Foreman-Mackey et al., 2013). The standard method to determine the uncertainties on the parameters is by using the least-square (χ^2) statistic. However, this assumes that the uncertainty estimates of the data are correct and Gaussian distributed. This is not the case for the PTF lightcurves (as in many observational datasets). Ignoring this problem leads to an underestimate of the uncertainties in the derived parameters, and can in some cases also change the solution. To solve this problem we add additional white noise[1] to our model (see Section 8 in Hogg et al. 2010 and for a simple example see Foreman-Mackey 2013). This means that our model has the white noise amplitude as an extra parameter, which we can simply optimize over, exactly the same as for the lightcurve parameters.

This method requires the following modification to the standard least-square function:

$$\tilde{\chi}^2 = \sum_n \frac{(y_n - m_n(p))^2}{\sigma_n^2 + f^2 m_n(p)^2} + \log(\sigma_n^2 + f^2 m_n(p)^2) \tag{5.1}$$

where y_n is the data, m_n the lightcurve model as a function of the lightcurve parameters p, σ_n the uncertainties, and f a factor which adds an extra noise source. Note that the first term of the equation is almost the same as in a regular least-square (χ^2) regression, except for the additional noise term $[f^2 m_n(p)^2]$. The first term can be minimised by letting f go to infinity, instead of minimising the difference between data and model $[y_n - m_n(p)]$. Therefore, the second term is needed to penalise models with a large value of f. Using this equation, the optimal amount of white noise is added to account for any difference between the data and model. To obtain the best model, we simply minimise $\tilde{\chi}^2$ over the lightcurve parameters p and the parameter f, just like regular least-square regression.

For each of the systems, we first find the approximate solution using a simple simplex minimiser of the modified least-square function. We then use emcee to find the best set of parameters of

[1] If the noise cannot be treated as white noise, but the noise is correlated (red noise), Gaussian process regression can be used. See for a simple example Foreman-Mackey (2014) and an example of this method used to model flickering in a cataclysmic variable by McAllister et al. (2017).

all the available lightcurves for that system. For each filter we use different values for x_1, y_1, and 'absorb', while the rest of the parameters are filter independent. We use 256 parallel MCMC chains (called 'walkers') and use at least 2000 generations or more if needed. Any further calculations are done using the last 2560 positions of the walkers.

5.4.2 Effective temperature

To determine the temperatures of both components we fit the spectral energy distribution of the target with model spectra, similar as in Maxted et al. (2011). We use data from GALEX (far UV & near UV, Bianchi et al., 2014), SDSS DR13 (*ugriz*, SDSS Collaboration et al., 2016), Pan-STARRS (*grizy*, Chambers et al., 2016), 2MASS (HJK, Skrutskie et al., 2006), and WISE ($W1$ & $W2$, Wright et al., 2010) for each target (where available). We used as model spectra the BaSeL3.1 spectral library (Westera et al., 2002). To calculate the flux per band, we convolve the model spectra with each band's response curve.

The overall spectrum is the sum of two model spectra of a given temperature and metallicity, created using bilinear interpolation from the BaSeL library. With only an SED, it is not possible to measure the metallicity of the stars reliably. However, since metallicity and temperature are correlated, we treat the metallicity of both stars as free parameters and marginalise over them in the final result. For the surface gravity, we assume $\log g$=4 for the A/F-star and $\log g$=5 for the pre-He-WD. We set the relative contribution to the total light by the ratio between r_1 and r_2 obtained from the lightcurve. At first, we also used the temperature ratio obtained from the lightcurve, but we learnt that this gave inconsistent predictions for the eclipse depths. This is likely due to the use of blackbody spectra by LCURVE. Instead, we directly use the eclipse depth of the primary eclipse instead of the temperature ratio. The final variable is the extinction, set by $E(B-V)$. To calculate the reddening following from the extinction we used the reddening law by Cardelli et al. (1989) with $R_V = 3.1$ (as implemented by PYSYNPHOT).

To determine the temperatures of both stars we minimized the function:

$$\begin{aligned}\tilde{\chi}^2 = &\sum_n \frac{(y_n - m_n(p))^2}{\sigma_n^2 + f^2 m_n(p)^2} + \log(\sigma_n^2 + f^2 m_n(p)^2) \\ &+ \mathrm{prior}(r_1/r_2, \mathrm{E_{B-V}})\end{aligned} \tag{5.2}$$

with y the data, m the model, and f an additional noise factor. We used a value for $E(B-V)$ according to Schlafly & Finkbeiner (2011), with an uncertainty of 0.034 (as in Maxted et al., 2011). For some added flexibility in our model, we added an extra term of uncertainty to the magnitudes (f), similar to the way it was applied in Equation 5.1. We again use EMCEE to determine the best values and uncertainties, similar as in Section 5.4.1.

5.4.3 Radial velocity

To obtain the radial velocity curve of the primary star, we cannot use the Balmer absorption lines in the spectrum because these are present both in the A/F-star and the pre-He-WD. Using these would not yield reliable results. Instead, we use the metal lines present in the spectra of the A/F–type stars. We cross-correlate the spectra with a template; a high-resolution spectrum of the A5 star HD145689 (Bagnulo et al., 2003). We first interpolate the target spectrum to the

(much higher) sampling of HD145689. We then remove the continuum with a low-order polynomial and determine the radial velocity shift using cross-correlation. To estimate the uncertainty on the radial velocity shift, we add random Gaussian noise to the target spectra according to the uncertainty per pixel and measure the radial velocity shift. We repeat this process 11 times and use the standard deviation of the results as the uncertainty. We use the metal lines between 4150–4301 Å, 4411–4791 Å, and 4941–5400 Å to get three separate measurements of the radial velocity shift. The radial velocity measurements are corrected to the heliocentric velocity frame with the RVCORRECT task in IRAF.

To determine the radial velocity amplitude, we fit a sinusoidal curve with a fixed value for the period and phase to the measurements. This leaves only the amplitude and systemic velocity as free parameters. We again use a modified least-squares objective function which can also take into account underestimated uncertainties (similar to Equation 5.1):

$$\tilde{\chi}^2 = \sum_n \frac{(y_n - m_n(p))^2}{\sigma_n^2 + f^2} + \log(\sigma_n^2 + f^2) \tag{5.3}$$

with y_n the radial velocity measurements, σ the statistical uncertainty on the cross-correlation results and f the extra white noise. Fitting the data shows (Table 5.3) that f ranges between 7 and 12 $\mathrm{km\,s^{-1}}$, a factor of 2 higher than the statistical noise σ. This extra noise is partially due to the uncertainties in the wavelength calibration (4–6 $\mathrm{km\,s^{-1}}$) but does not account for all residual variance. This means that we either underestimate the uncertainties in the cross-correlation procedure (for example by the normalisation of the spectra) or that we underestimate the uncertainties in the calibration process of the spectra. This could be due to instabilities of the optical elements in the IDS/INT combination, which typically changes for each observing run. Since we combine data from four different observing runs, this could result in minor differences in the setup. A potential method to verify this is to check the wavelength of sky emission lines, but these are not available in the spectral range we use.

5.4.4 Galactic kinematics

For the 12 systems for which we have obtained a radial velocity measurement, we calculate their Galactic location and velocity. We determine the distance to the systems by using the K-band magnitude and absolute radius, combined with the K-band surface brightness calibration by Kervella & Fouqué (2008). The proper motions of the systems are taken from the UCAC5 catalogue (Zacharias et al., 2017) or the Initial Gaia Source List (Smart & Nicastro, 2013). Combined with right ascension and declination, we calculate velocity in the direction of the Galactic Centre (V_ρ) and the Galactic rotation direction (V_ϕ), the Galactic orbital eccentricity (e), and the angular momentum in the Galactic z direction (J_z). The Galactic radial velocity V_ρ is negative towards the Galactic centre, while stars that are revolving on retrograde orbits around the Galactic Centre have negative V_ϕ. Stars on retrograde orbits have positive J_z. Thin disk stars generally have very low eccentricities e. Population membership can be derived from the position in the V_ρ - V_ϕ diagram and the J_z - e diagram (Pauli et al., 2006).

Table 5.3: Radial velocity amplitude of the A/F-star, the systemic velocity, the residual variance of the fit, the derived distance, the measured proper motions and the associated stellar population for the 12 EL CVn systems with radial velocity curves. The proper motion is taken from either the UCAC5 catalogue ([a], Zacharias et al. 2017) or or the Initial Gaia Source List ([b], Smart & Nicastro 2013).

ID	K_1 (km s^{-1})	γ (km s^{-1})	f (km s^{-1})	Distance (pc)	$\mu_\alpha \cos(\delta)$ (mas yr^{-1})	μ_δ (mas yr^{-1})	Pop.
PTFS1600y	22.8 ± 0.9	-88.7 ± 0.9	6.9	2340 ± 70	-7.3 ± 2.0^a	-4.2 ± 1.3^a	Thin
PTFS1600ad	29.7 ± 1.4	-23.3 ± 1.2	7.2	3770 ± 180	1.1 ± 1.5^a	-1.8 ± 1.5^a	Thin
PTFS1601p	18.4 ± 2.1	-45.9 ± 1.8	12.4	4960 ± 500	1.4 ± 4.6^a	-7.6 ± 4.2^a	Thin/Thick
PTFS1501bh	24.0 ± 1.5	16.6 ± 1.2	8.2	1280 ± 70	10.1 ± 1.5^a	-4.9 ± 1.5^a	Thin
PTFS1601cl	35.2 ± 2.1	-14.4 ± 1.2	9.1	2890 ± 90	2.0 ± 1.3^a	2.2 ± 1.3^a	Thin
PTFS1607t	26.7 ± 1.7	31.0 ± 1.2	5.5	2160 ± 70	-2.1 ± 0.3^a	1.6 ± 1.6^a	Thin
PTFS1607ab	32.7 ± 1.3	-37.6 ± 1.1	6.3	1810 ± 70	-3.1 ± 2.6^b	-8.2 ± 3.1^b	Thin
PTFS1512bf	31.4 ± 1.9	70.3 ± 1.5	11.8	1820 ± 50	-19.2 ± 6.4^a	4.7 ± 5.7^a	Thick
PTFS1617n	17.7 ± 1.7	-198.7 ± 1.9	7.2	5700 ± 380	-1.8 ± 2.6^a	-2.9 ± 2.7^a	Thick/Halo
PTFS1617m	13.1 ± 2.4	-40.4 ± 2.1	10.9	4060 ± 180	-0.9 ± 1.5^a	-9.2 ± 1.7^a	Thin/Thick
PTFS1619l	22.7 ± 1.3	-12.5 ± 1.0	5.8	2040 ± 140	-1.9 ± 1.6^a	-2.0 ± 1.6^a	Thin
PTFS1521cm	34.7 ± 2.0	-6.5 ± 1.9	7.9	2870 ± 110	9.6 ± 2.8^a	-7.8 ± 2.7^a	Thick

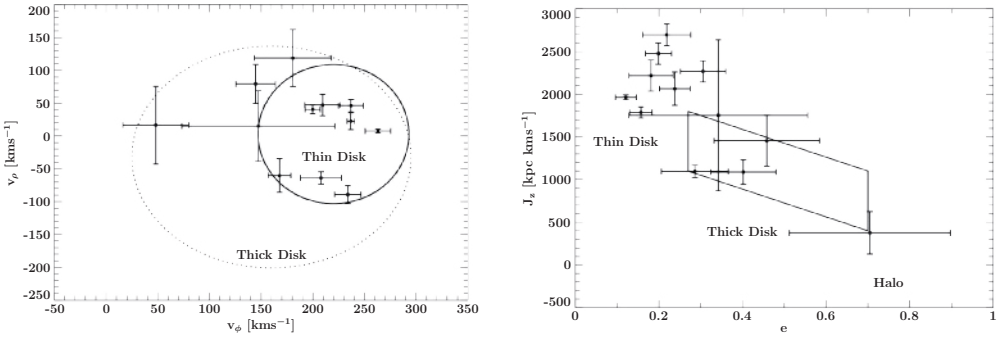

Figure 5.3: V_ϕ–V_ρ (left) and e–J_z diagrams (right). The solid and dotted ellipses render the 3σ thin and thick disk contours in the V_ϕ–V_ρ diagram, while the solid box in the e–J_z marks the thick disk region as specified by Pauli et al. (2006).

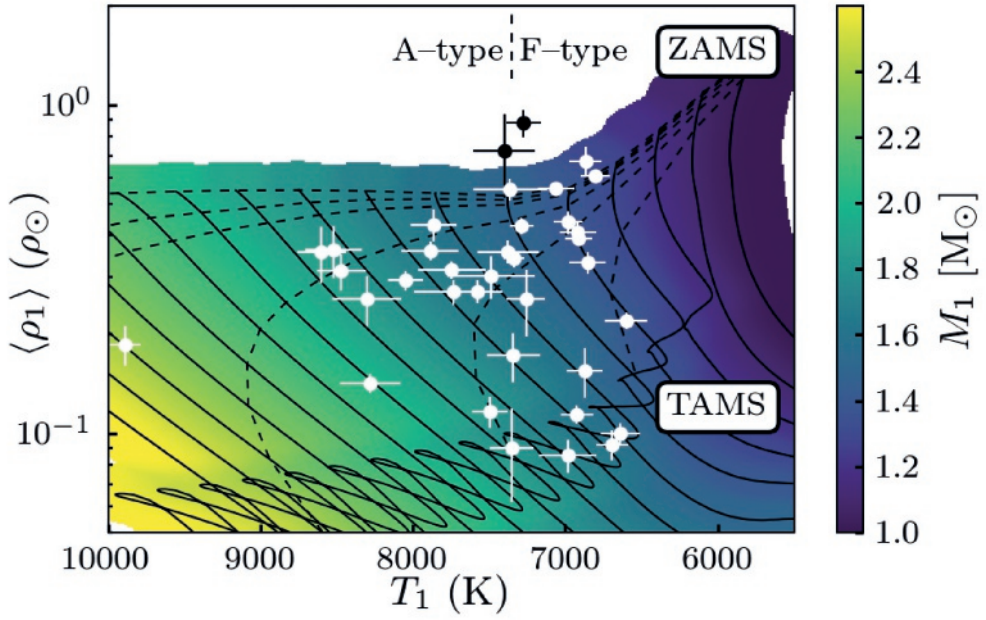

Figure 5.4: The temperature versus the average density of the main-sequence stars of the binary system, indicated with a black or white dot. The black lines show main-sequence evolution tracks (solar metallicity) from Spada et al. (2017) between 1.0 and 2.5 $M_\odot$ with 0.1 $M_\odot$ intervals. The colour map shows the mass of the star according to the interpolation method by Breton et al. (2012). The dashed lines are isochrones of 0, 0.1, 0.2, 0.5, 1, and 2 Gyr since the start of the main sequence.

5.4.5 Masses and radii

To fully solve for the elements of the binary system, we need to combine the information from the lightcurve fit with an additional piece of information to set the scale of the system. This is typically done by measuring the radial velocity amplitude of both stars. We only have the radial velocity amplitude of one of the stars in the binary. In principle, we can combine this with the mass-ratio q, but the uncertainties on the mass-ratio derived from the lightcurve fitting are high, and the uncertainty on the masses scale with a high power of q (for low q: $M_1 \propto K_1^2 q^{-3}$, $M_2 \propto K_1^3 q^{-2}$), and are therefore not constraining.

To circumvent this problem, we make use of the assumption that the primary star is a main-sequence star. Using only the lightcurve parameters, we can calculate the average density of the main-sequence component:

$$\langle \rho \rangle = \frac{3\pi}{GP^2 r_1^3 (1+q)} \tag{5.4}$$

To propagate the uncertainties correctly, we calculate the stellar density for each point in the MCMC chain and assign a random temperature according to our measurement of the SED. With the average density and temperature of the main-sequence star, we can use stellar models to determine its mass. We use the Yale-Potsdam stellar models (Spada et al., 2017) and follow the same procedure as in Breton et al. (2012) to make a continues mapping of the mass in $T - \langle \rho \rangle$ space. We convolve each track with a Gaussian probability function with a standard deviation of 200K in temperature and 0.1 dex in density. For each point in the temperature-density grid, we assign the mass with the highest probability. We use this mapping to calculate the primary mass for the posterior distribution of the lightcurve fits (see Section 5.4.1). As can be seen in Fig. 5.4, most but not all measurements agree with the models. Two systems, PTFS1612al and PTFS1615u, have slightly higher densities than would be the case for a solar metallicity composition for zero-age main sequence models. For these two systems, we extrapolate the models to determine the mass.

With the mass of the primary (M_1) combined with q, i and P, we calculate the semi-major axis (a) using Kepler's law;

$$a^3 = GM_1 \, (1+q) \, \left(\frac{2\pi}{P} \right)^2 \tag{5.5}$$

Note that in both equations the mass ratio is present in the form of $1 + q$, and since the mass ratio is small ($q \sim 0.1$), the high uncertainty on q only mildly affects the accuracy on a and M_1. However, the uncertainty on the pre-He-WDs mass ($M_2 = qM_1$) is proportional to the uncertainty on q, which means that the uncertainty on M_2 is too high to be constraining.

This can be solved by including the measured radial velocity (K_1) in our calculation, which is available for 12 systems. We use an iterative approach to find the optimal solution as in Rappaport et al. (2015), again for each sample from the lightcurve fit posterior distribution. This involves calculating M_1, q and $\langle \rho \rangle$ until the solution converges, which it does after 2 iterations.

Table 5.4: System parameters of all EL CVn systems and the uncertainty (standard deviation) on the parameters. Systems for which a radial velocity measurement is used to calculate the parameters is indicated with the 'RV' superscript. This mainly affects the reliability and systematics on the mass and surface gravity of the pre-He-WD (M_2 and $\log g_2$).

Name	P (d)	i (°)	M_1 ($M_\odot$)	M_2 ($M_\odot$)	R_1 ($R_\odot$)	R_2 ($R_\odot$)	T_1 (K)	T_2 (K)	$\log g_1$	$\log g_2$
1600y^{RV}	1.1838920	84.5	1.62	0.17	2.41	0.46	6930	8900	3.88	4.33
	0.0000008	2.7	0.04	0.01	0.07	0.02	100	110	0.02	0.03
1600ad^{RV}	1.0840448	86.5	1.76	0.23	1.83	0.35	8050	10490	4.16	4.72
	0.0000010	2.2	0.04	0.01	0.05	0.02	120	200	0.02	0.04
1700do	3.0507582	87.4	2.40	0.81	2.34	0.33	9890	17100	4.08	5.31
	0.0000278	1.8	0.06	0.25	0.13	0.03	90	1400	0.04	0.15
1600aa	0.6934558	78.7	1.67	0.50	1.67	0.55	7880	9300	4.21	4.67
	0.0000006	0.9	0.05	0.09	0.04	0.02	190	400	0.02	0.09
1601p^{RV}	1.2215885	83.8	1.82	0.14	1.65	0.34	8600	11700	4.26	4.54
	0.0000051	3.2	0.06	0.02	0.14	0.04	160	500	0.06	0.10
1501bh^{RV}	0.6204144	78.4	1.30	0.12	1.23	0.20	6870	11100	4.38	4.91
	0.0000005	1.9	0.04	0.01	0.07	0.01	110	400	0.04	0.06
1601q	1.2515058	80.5	1.85	0.30	1.93	0.46	8300	10700	4.13	4.58
	0.0000051	2.9	0.08	0.18	0.15	0.04	200	700	0.05	0.40
1601cl^{RV}	0.8917354	82.9	2.02	0.28	2.44	0.52	8290	10100	3.97	4.45
	0.0000005	2.9	0.06	0.01	0.07	0.02	200	300	0.02	0.03
1402de	0.6189694	87.0	1.61	0.36	1.56	0.45	7860	9300	4.27	4.69
	0.0000011	2.5	0.04	0.13	0.07	0.02	150	300	0.03	0.23
1607aa	0.8463120	84.6	1.85	0.30	1.81	0.38	8470	10300	4.19	4.76
	0.0000016	3.4	0.05	0.07	0.08	0.02	160	300	0.03	0.13
1607v	0.7198356	82.6	1.58	0.20	1.83	0.16	7260	10900	4.11	5.32
	0.0000020	5.8	0.06	0.05	0.16	0.03	120	500	0.06	0.24
1607t^{RV}	0.8759507	76.6	1.40	0.16	1.87	0.38	6600	8600	4.04	4.48
	0.0000004	1.0	0.05	0.01	0.05	0.01	140	200	0.02	0.03
1607ab^{RV}	0.7730986	83.8	1.40	0.19	1.45	0.32	6980	8810	4.26	4.71
	0.0000002	2.3	0.03	0.01	0.05	0.01	100	80	0.03	0.04

1608ab	0.6101718	86.8	1.50	0.11	1.39	0.52	7400	7900	4.32	4.04
	0.0000014	1.9	0.06	0.10	0.04	0.02	200	400	0.02	0.24
1612al	0.6369260	86.8	1.38	0.16	1.16	0.37	7280	10300	4.45	4.50
	0.0000006	2.0	0.08	0.09	0.05	0.02	110	300	0.03	0.22
1512bf^{RV}	0.6074343	87.2	1.39	0.17	1.53	0.32	6910	9740	4.21	4.65
	0.0000002	1.9	0.02	0.01	0.02	0.01	90	180	0.01	0.04
1613s	1.1420695	76.2	1.83	0.17	2.72	0.25	7350	13700	3.83	4.88
	0.0000024	6.0	0.08	0.05	0.30	0.05	140	800	0.08	0.28
1613u	0.5644902	81.6	1.52	0.27	1.65	0.37	7340	9690	4.19	4.73
	0.0000003	2.7	0.02	0.04	0.04	0.01	70	160	0.02	0.08
1615ag	0.6806897	85.7	1.52	0.27	1.63	0.32	7370	10200	4.20	4.87
	0.0000046	3.3	0.05	0.07	0.05	0.02	200	400	0.02	0.13
1615v	0.5594054	73.7	1.39	0.13	1.50	0.33	6920	9400	4.23	4.54
	0.0000003	1.4	0.03	0.03	0.04	0.01	120	300	0.02	0.17
1515ay	0.4642873	89.0	1.33	0.15	1.30	0.46	6800	7930	4.33	4.27
	0.0000001	1.1	0.03	0.04	0.02	0.01	100	150	0.01	0.10
1615w	1.4407151	77.7	1.61	0.24	2.59	0.40	6690	10300	3.82	4.63
	0.0000024	2.7	0.05	0.05	0.14	0.03	110	200	0.04	0.14
1615ao	0.8954515	77.6	1.64	0.41	1.82	0.64	7580	8700	4.13	4.43
	0.0000007	0.8	0.05	0.12	0.05	0.03	170	160	0.02	0.15
1615u	0.7777349	82.4	1.50	0.24	1.27	0.16	7400	12200	4.40	5.41
	0.0000011	4.2	0.09	0.10	0.14	0.02	200	600	0.08	0.27
1616cr	0.5649690	82.5	1.40	0.07	1.36	0.46	7060	8000	4.32	3.93
	0.0000002	0.9	0.03	0.02	0.02	0.01	120	170	0.01	0.07
1617n^{RV}	2.3367776	87.3	1.80	0.18	2.41	0.38	7500	11600	3.93	4.55
	0.0000052	2.1	0.04	0.02	0.12	0.03	110	400	0.04	0.07
1617m^{RV}	3.7728999	87.8	1.68	0.14	2.57	0.69	6990	9320	3.84	3.89
	0.0000083	1.5	0.06	0.03	0.08	0.03	190	190	0.02	0.10
1619l^{RV}	1.1599993	83.2	1.56	0.17	2.13	0.34	6870	9200	3.97	4.60
	0.0000017	4.1	0.05	0.01	0.14	0.04	120	150	0.05	0.09
1521ct	1.1724964	83.0	1.82	0.36	1.72	0.56	8520	9800	4.23	4.50

	0.0000014	1.4	0.06	0.29	0.11	0.04	190	300	0.04	0.28
1621ax	1.0181522	84.0	1.69	0.30	2.14	0.17	7350	11800	4.00	5.48
	0.0000045	4.6	0.06	0.07	0.14	0.03	170	700	0.04	0.22
1521cm[RV]	0.6854774	80.0	1.49	0.21	1.49	0.43	7290	9240	4.27	4.49
	0.0000002	1.0	0.02	0.01	0.03	0.01	70	90	0.02	0.03
1622by	0.7486683	85.8	1.69	0.31	1.84	0.33	7700	11100	4.13	4.88
	0.0000016	3.4	0.07	0.07	0.07	0.02	300	1400	0.03	0.13
1522cc	0.5717853	81.2	1.40	0.26	1.62	0.27	6860	9570	4.17	4.99
	0.0000003	3.1	0.04	0.04	0.05	0.01	120	190	0.02	0.08
1622aa	0.7661291	84.7	1.60	0.16	1.74	0.26	7500	10900	4.16	4.85
	0.0000038	4.0	0.08	0.05	0.10	0.03	300	1300	0.04	0.19
1622bt	0.6884160	79.2	1.65	0.29	1.74	0.29	7700	12200	4.18	4.97
	0.0000004	2.0	0.06	0.04	0.05	0.01	200	1000	0.02	0.08
1723aj	1.1088064	85.6	1.57	0.18	2.51	0.23	6640	11000	3.84	4.98
	0.0000009	3.3	0.05	0.03	0.07	0.02	130	400	0.02	0.11

5.5 Results

For the 36 EL CVn binaries in the PTF data, we fit the lightcurves with a binary star model, see Fig. 5.8 and Table 5.8 in the Appendix. The best model fits to the lightcurves all show a flat-bottomed primary eclipse and a round-bottom secondary eclipse. The orbital period of the binary, the radii of both stars, and the orbital inclination are typically well constrained, but the uncertainty on the mass-ratios of the systems is typically $\gtrsim 10$ per cent. The extra noise term in the fit for the lightcurves is typically $\lesssim 1$ per cent. This is consistent with the expected uncertainty in the absolute photometric calibration which is not part of the error bars of the lightcurves. The orbital periods of the binaries range from 0.46 d to 3.8 d, with inclinations between 74–90 degrees. The radii of the primary stars divided by the semi-major axis (r_1) are typically 0.2–0.5, and the primary stars fill about 0.4–0.9 of their Roche lobe. The average density derived from the lightcurve is typically between 10–70 per cent of Solar density, consistent with A/F–type main sequence stars. The mass-ratio as determined from the lightcurves are typically between 0.08–0.2, but there are outliers to larger ratios. However, the uncertainties on the outliers are high. The mass-ratio determined from the amplitude of the inter-eclipse variability, which is in some cases not significant (e.g. 1700do) and explains the high uncertainty on the value for the mass-ratio is some cases. From the lightcurve we determined the temperature ratio of the two stars, assuming blackbody spectral energy distributions is typically 0.5–0.95.

The results of the SED fitting are shown in Table 5.4 and Fig. 5.9. The temperatures of the A/F-stars in the EL CVn systems range between 6600–10000 K, consistent with temperatures for A/F–type main sequence stars (F-type: 6000–7350 K, A-type: 7350–10000 K, Pecaut & Mamajek 2013). The temperature of the pre-He-WDs range from 7900 to 17000 K. In all systems, the pre-He-WDs are hotter than the A/F-star companion. The uncertainty on the A/F-star's temperature is typically 100–200 K. The temperature of the pre-He-WD is less well constrained (100–1400 K), because it depends on the availability of UV data and on how accurately the eclipse depth can be measured from the lightcurves. The RMS scatter between the data and model is typically $\lesssim 5$ per cent, with a few outliers to 10 per cent (see Table 5.7). This residual scatter can be due to calibration differences between telescopes, but also because the observations are taken at a random phase. An observation taken in-eclipse results in a $\sim$10 per cent lower flux as out of eclipse.

For 12 of the EL CVn systems we obtain usable radial velocity curves and measure the radial velocity amplitude, see Fig. 5.10. The remaining 7 systems were not enough measurements were obtained or they were observed at unfavourable orbital phases, precluding an accurate radial velocity measurement. However, all radial velocity amplitudes are low, in the range of 20–40 $\mathrm{km\,s^{-1}}$. This confirms that the secondary stars in these binaries are indeed low mass stars.

Using all information available, we determine the stellar parameters of the stars in the EL CVn systems, summarised in Table 5.4. The masses of the A/F-type star range between 1.3 and 2.4 $\mathrm{M_\odot}$. The radii of these stars (1.15–2.7 $\mathrm{R_\odot}$) are consistent with these stars being regular main-sequence stars.

The radii of the pre-He-WDs range between 0.17–0.65 $\mathrm{R_\odot}$. To calculate the mass of the pre-He-WD (M_2), we include the measured radial velocity amplitude if available, which 'replaces' the uncertain mass-ratio measurement from the lightcurve. For most of the systems we do not have a radial velocity amplitude measurement, so we do depend on the mass-ratio to determine the mass

of the pre-He-WDs, which range between 0.12 and 0.5 $M_\odot$. As discussed in Section 5.4.1 and 5.4.5, the mass determination of the secondary using only the mass-ratio is very uncertain because of the high uncertainty on the mass-ratio. If we limit ourselves only to systems for which we have a radial velocity amplitude, the mass range is 0.12–0.28 $M_\odot$, significantly smaller.

For the sample for which we have radial velocity curves, we determine the motion in the Galactic plane and derive their population membership as described in Sec. 5.4.4 and shown in Table 5.3. Fig. 5.3 shows that more than half of the systems are part of the thin disk population. A few are part of the thick disk, and PTFS1617n could also be a halo object.

5.6 Discussion

5.6.1 Co-rotation

In the lightcurve modelling (Section 5.4.1), we assume that both stars are synchronised with the orbit. Previous studies of EL CVn binaries have made the same assumption, but all authors acknowledge that it might not be correct, since mass-accretion can spin up the A/F–star significantly (see Section 5.6.2). van Kerkwijk et al. (2010) extensively discuss how all parameter estimates are affected by incorrectly assuming co-rotation. Since the precision of PTF lightcurves is far lower than the precision of the Kepler lightcurves, the only significant effect this assumption has in our analysis is on the estimate of the mass-ratio. If a star is rotating faster than the orbital period, the mass-ratio (q) is overestimated. We quantify this by simulating a typical EL CVn lightcurve with a primary star which is rotating 2 and 4 times faster than the orbital period, while keeping all other parameters the same. Fitting these lightcurves with the model assuming co-rotation, results in values for q of 0.02 and 0.10 higher the initial value of $q = 0.17$. All other lightcurve parameters do not change significantly. We therefore conclude that for mildly faster-than-synchronous rotating primary stars ($P_{\rm rot}/P_{\rm orb} > 0.5$), the effect on the mass-ratio is similar or smaller than the statistical uncertainty on the mass-ratio. If the primary star is rotating faster, the mass-ratio is overestimated.

This overestimate propagates through to the rest of our parameter estimates; the average density of the primary is overestimated, and therefore the mass of the primary underestimated (Fig. 5.4), and the semi-major axis is overestimated. However, the effect is small since these parameters only weakly depend on the mass-ratio (see Equations 5.4 and 5.5). For a large part of our sample, we do not have any radial velocity amplitudes, and for these systems we rely on the mass-ratio to calculate the mass of the pre-He-WD. As mentioned in Section 5.4.5, the mass of the pre-He-WD depends on the mass-ratio to the third power. This, combined with a high statistical and systematic uncertainty on the mass-ratio, makes the calculations of M_2 (without a radial velocity amplitude) unreliable.

To check if the A/F-stars are rotating faster than synchronous, we compare the rotation periods to the orbital period for stars in known EL CVn systems. The orbital period of the main sequence star has been determined for five Kepler EL CVn binaries by measuring the projected rotational velocity ($v \sin i$): 1.79(60) d, 0.79(14) d, 5.0(2.4) d, and 1.71(62) d; (Faigler et al., 2015) and (0.93 d, Lehmann et al., 2013). In addition, the rotational period has tentatively been identified from a frequency analysis for KOI-81 (0.48 d Matson et al., 2015), KOI-74 (0.59 d Bloemen et al., 2012),

KOI-1224 (3.49 d Breton et al., 2012), and KIC-8262223 (0.62 d Guo et al., 2017). All rotational periods are of the same order as the orbital period. A detailed comparison of the rotational and orbital period shows that most stars rotate faster than synchronous, but in one case the rotation period is longer than the orbital period. For three cases (all from Faigler et al. 2015) the rotation period is consistent with the orbital period of the binary, but since the uncertainties on the rotational periods are large, it is difficult to say if they are synchronised. The data therefore indicates that at least some (or maybe most) of the A/F-stars are not synchronised with the orbital period.

There is however an important difference between the PTF sample and the sample of EL CVn systems with known rotation periods of the primary (all found by Kepler). The relative size of the A/F-star (r_1) is a factor of $\sim$3 larger in the PTF sample, which strongly affects the synchronisation timescale of the star ($\propto r_1^{-8.5}$, Zahn, 1977). We used the equation by Zahn (1977) and tabulated values for E_2 from Claret (2004) to calculate the synchronisation timescale for each of the EL CVn systems in our sample. This shows that the synchronisation timescale of the A/F-type star is less than 10 Myr in 20 systems, and less than 100 Myr for 32 systems. For these 32 systems, the synchronisation time is shorter than the time since mass transfer (0–260 Myr, see Fig. 5.5). The remaining 4 systems (with the smallest values for r_1) have synchronisation timescales that are significantly longer than the estimated age. Based on this theoretical prediction, we can assume that that most of the A/F-stars are rotating synchronously. Whether this is actually the case requires an independent measurement of the rotation period.

5.6.2 Binary evolution and stellar parameters

In the canonical formation channel of EL CVn binaries (e.g. Chen et al., 2017), two main-sequence stars of similar mass are born at a short orbital period of a few days. The more massive star evolves faster and increases in radius. Before it ascends the red giant branch (RGB), it fills its Roche lobe and starts stable mass-transfer to the lower mass secondary star. This process continues until almost the complete outer envelope is transferred (identified as "R CMa"-type binaries, e.g. Lee et al., 2016). The remnant of the initially more massive star has become a pre-white dwarf with a helium core and a thick hydrogen envelope ($\approx 0.01 - 0.04\,M_\odot$, see Istrate et al. 2016b; Chen et al. 2017). The accretor has become a rejuvenated main-sequence star of spectral type A or F which dominates the luminosity of the system. If present in a specific stellar population as e.g. found in clusters, such a system would be identified as a 'blue straggler'. If the orbital inclination is such that it shows eclipses, we identify it as an EL CVn binary.

The structure and evolution of pre-He-WDs have been extensively studied, as they also occur at more advanced binary evolutionary stages with either a white dwarf (Marsh et al., 1995) or a neutron star (van Kerkwijk et al., 2005) as companions. Modelling of the formation process of binaries with a low mass pre-He-WD (Althaus et al., 2013; Istrate et al., 2014b,a, 2016b; Chen et al., 2017) shows that there are strong correlations between the binary orbital period, and the mass, temperature, radius and age of the pre-He-WD. First, higher mass pre-He-WDs are formed at longer orbital periods. This is a direct result of the mass accretion process. This relation was already found in pre-He-WD – neutron star binaries and has been parametrised by Lin et al. (2011). Binary evolution studies by Istrate et al. (2014a) and Chen et al. (2017) also predict this

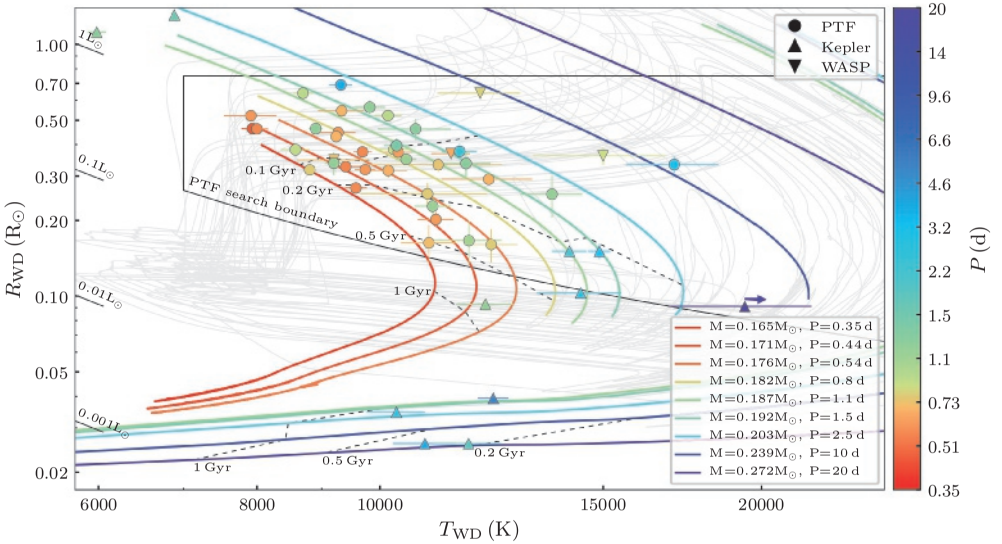

Figure 5.5: Temperature versus radius of the pre-He-WDs, with the colours indicating different orbital periods. The coloured lines indicate evolution tracks by Althaus et al. (2013) for different masses. The dots indicate pre-He-WDs from this study, triangles are other low mass pre-He-WDs in EL CVn systems; upward pointing triangles indicate Kepler discoveries, downward pointing triangles indicate SWASP discoveries (for references, see Sec. 5.1). During the evolution of pre-He-WDs, multiple hydrogen shell flashes can occur, indicated as grey lines. The tracks before the first H-flash and after the last H-flash are shown as coloured lines. Isochrones are shown as dashed lines, counted from the end of mass-transfer in the binary. The solid black line indicates the approximate detection limits, estimated by assuming a T_1 =7000 K, R_1=1.5 $R_\odot$ primary star. The bottom boundary is set by an eclipse depth of 0.03 mag in R-band, the top boundary is set by the requirement of a flat-bottom eclipse ($R_1 > 2R_2$), and the left limit is set by the requirement that the flat-bottom eclipse is deeper than the secondary eclipse ($T_1 < T_2$).

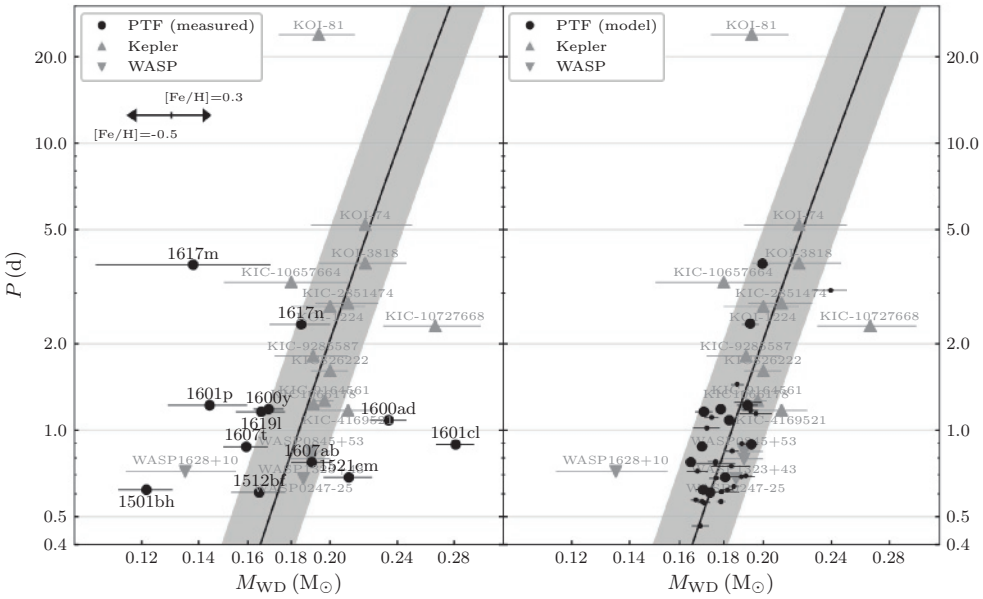

Figure 5.6: Pre-He-WD mass versus the orbital period of the binary. The left panel shows the measured mass (using the radial velocity amplitude) of the PTF sample, the right panel shows the mass derived from the radius and temperature models (see Fig. 5.5). Large points indicate PTF systems with a radial velocity measurement, small points indicate systems without a radial velocity measurement (not shown in the right panel because of the high uncertainties). Grey triangles indicate mass-period measurements of other EL CVn systems; upward pointing triangles indicate Kepler discoveries, downward pointing symbols indicate SWASP discoveries (for references, see Sec. 5.1). The black line shows the period-mass relation by Lin et al. (2011), and the shaded area indicates a 10 per cent uncertainty on this relation.

P-M relation for EL CVn binaries. The latter shows that the relation between orbital period and mass is very robust, but at the low-mass end of the relation (0.16–0.20$M_\odot$) there is some spread.

Pre-He white dwarfs (of a given mass) are also predicted to follow a particular evolutionary track, corresponding to a particular combination of radius and temperature as a function of age. The temperature and radius are directly related to the envelope mass and core mass of the white dwarf. Directly after the mass accretion process ends, the pre-He-WD is large ($\gtrsim 0.5\,R_\odot$) and has a low ($\lesssim 8000\,K$) surface temperature. While the hydrogen envelope is slowly being consumed by shell burning, the pre-He-WD shrinks and increases in temperature while maintaining an approximately constant luminosity (this phase is often referred to as the constant luminosity phase). When almost the entire envelope has been consumed, the pre-He-WD starts to cool down while the radius keeps decreasing (the cooling track). At the beginning of the cooling track, multiple hydrogen shell flashes (H-flash, e.g. Driebe et al., 1998) can occur in the more massive pre-He-WDs. These flashes briefly increase the temperature and radius of the star, after which the white dwarf settles back on the cooling track. The exact mass boundary at which this starts to occur is uncertain. Models by Althaus et al. (2013) show shell flashes for masses above $\sim$0.18$M_\odot$, while Istrate et al. (2014a) put this boundary at $\sim$0.21$M_\odot$.

Fig. 5.5 shows the temperature versus radius of the pre-He-WD, with the colour of the points indicating the orbital period of the system. This shows that the temperatures and radii we find are consistent with predictions for pre-He-WDs in the constant luminosity phase, and before the occurrence of any H-flash. While some of the measurements are also consistent with pre-He-WDs undergoing an H-flash (grey lines), the short time spent in this phase makes this extremely unlikely. For the PTF sample, the orbital period (indicated by the colours) follows the same trend as the models, with long period systems containing larger and hotter pre-He-WDs. To test if the data match the models, we interpolate the models in orbital period, which allows us to test directly how well the radius and temperature match the model for a given orbital period. The fraction of measurements within 1, 3, and 5 standard deviations is 25, 75 and 86 per cent. Given the fact that we interpolate, and the uncertainties on radius and temperature could contain some systematic uncertainties, we conclude that most of the measurements agree with the models. This comparison to the models also allows us to infer the time since the end of mass transfer, which ranges from 0 to 260 Myr with an average of 110 Myr.

Fig. 5.6 shows the orbital period of the binary versus the mass of the pre-He-WD. The left panel shows the measured values, while the right panel shows the expected masses using the models inferred from the measured temperature and radius (Fig. 5.5). The measured values indicate that all pre-He-WD are low mass systems, but the PTF sample scatters around the model predictions. The right panel shows that if the radius and temperature measurements and models are used to derive the mass, the results fall within 10 per cent of the prediction of the mass-period relation for pre-He-WDs.

There are two possible explanations for this discrepancy. Either we have underestimated the uncertainties on the mass measurements, or there is some additional intrinsic spread on the predicted mass versus period, radius, and temperature not properly modelled. There are a number of possible systematic uncertainties that could affect the mass determination. First of all, we have assumed that the A/F-star is a regular main sequence star with a solar metallicity to estimate its

mass (see Fig. 5.4). In Fig. 5.6 we have indicated how the mass estimate changes if we assume a different metallicity. If the real metallicity is lower than assumed, the mass is overestimated. This could explain a part of the inconsistency with the theory, but extreme metallicities would be needed to explain the largest outliers. Since thick disk systems generally have a lower metallicity, the masses for these systems could be overestimated. However, the thick disk systems do not show any particular trend, indicating that this assumption may not be the dominant cause of the inconsistency with the model predictions.

Another possibility is that we have underestimated our measurement uncertainties. The mass of the pre-He-WD is mostly determined by the radial velocity measurement. As shown in Fig. 5.10 in the Appendix, we need to add an additional uncertainty to the formal uncertainties in order to explain all variance in the radial velocity measurements. For PTFS1601cl (one of the outliers), where we did not obtain radial velocity measurements at the quadratures, small systematic offsets between measurements can have a large impact on the radial velocity amplitude. We did check the radial velocity amplitude measurements of PTFS1512bf by obtaining a few high-resolution spectra with the Echellette Spectrograph and Imager (ESI) on the Keck telescope. The resulting radial velocity amplitude measured from these spectra is consistent with the result from the IDS spectra, which leads to the conclusion that uncertainties due to an unstable detector are most likely very small.

An alternative explanation is that there is some intrinsic variance between mass and period, radius and temperature. For example, Istrate et al. (2016a) shows that assumptions about rotation, diffusion and metallicity give different results when modelling the mass, radius and temperature of pre-He-WDs. The magnitude of the effect is estimated to be low, about 10 per cent. This would be enough to explain the variance in the right panel but cannot explain the outliers on the left panel.

To solve this ambiguity, a measurement of both the main-sequence and pre-He-WD radial velocity is needed. This allows the mass of both stars to be calculated by only using Kepler's law (combined with the period and inclination measurement from the lightcurve). This has been done for SWASP J0247-25 (Maxted et al., 2013), KOI-81 (Matson et al., 2015), KIC-10661783, (Lehmann et al., 2013), and KIC-8262223 (Guo et al., 2017). For SWASP J0247-25, KIC-10661783, and KIC-10661783 the mass of the pre-He-WD agrees well with the P-M relation, but for KOI-81, the mass is significantly lower ($0.10 M_\odot$) than the P-M relation predicts. This hints that there is more scatter in the P-M relation than models estimated.

5.6.3 Galactic population and space density

Using stellar evolution and population synthesis codes, Chen et al. (2017) predict a space density of $4\text{–}10 \times 10^{-6}\,\mathrm{pc}^{-3}$ for EL CVn binaries (including non-eclipsing ones) with orbital periods less than 2.2 d. In addition, they predicted that EL CVn binaries should mainly be found in young stellar populations, and therefore be more abundant in the thin disk. We use the Galaxy model based on SDSS data by Jurić et al. (2008) to estimate how many EL CVn binaries we would expect to see given this space density and in what ratios between thin disk, thick disk and halo. We populate our model Galaxy with stars with absolute magnitudes according to a normal distribution with a mean and standard deviation of $R = 2.46 \pm 0.54$ mag, values determined from our sample of 36

systems. We simulate the PTF coverage by using (overly) simple requirements: $|b| > 15$, $\delta > 0$, $13.5 < R < 16$ (see Fig. 5.1). We ignore the Galactic Plane because these fields tend to be observed only $\sim$50 times. The minimum number of epochs in our uncovered sample is 58, indicating that at least 58 observations are needed to identify an EL CVn binary. Using the 58 epoch limit, we derive an effective coverage of 32.8 per cent for the remaining area. We also correct for the requirement that the systems must be eclipsing. This decreases the number of observable EL CVn systems by a factor of 0.307; determined from our sample using radii and inclination. Even if the binaries are eclipsing, if the pre-He-WD is too small (and thus old), we would not find it in the PTF data. To correct for this, we assume a lifetime of EL CVn binaries of 1 Gyr (the main sequence lifetime of a $2\,M_{\odot}$ star) and compare this to the typical age of PTF EL CVn binaries (0–260 Myr). We therefore assume that PTF can only detect 26 percent of all EL CVn binaries.

According to the model and the assumed selection criteria, 26 per cent of the PTF sample should be from the thin disk. If we assume our model is correct, there is only a 1.8 per cent chance $(\sum_{n=7}^{12} \binom{12}{n} 0.26^n\,[1-0.26]^{12-n})$ to find ≥ 7 thin disk systems out of a total of 12 EL CVn systems. If any of the ambiguous cases are from the thin disk, this probability drops well below 1 per cent. This indicates that our model is unlikely to be correct, and confirms that EL CVn systems are more abundant in the thin disk compared to the average stellar population, as was already suggested by Chen et al. (2017).

Using the model and estimated PTF detection efficiency, we also predict that we should have found $\sim$300–750 EL CVn systems, a factor of $\sim 10-25$ higher than we actually recovered. This could simply be because we are over-predicting the contributions of the thick disk and halo. However, even if we assume a factor of 4 higher contribution from the thin disk (to bring the model in line with with the ratio of thin to thick disk systems), the model still predicts at least a factor of $5-12$ more EL CVn systems than we found. Another uncertain estimate which could explain the discrepancy is the assumed efficiency of PTF in finding EL CVn binaries. The PTF observing cadence and coverage is highly inhomogeneous, and the assumptions we have used are very simple approximations. Assuming that we can find all EL CVn systems observed more than 58 times and are younger than 200 Myr is overly optimistic, and could explain the discrepancy of a factor of 5 (or more).

The inhomogeneity of the PTF dataset makes it difficult to do a proper study of the Galactic distribution and space density of EL CVn systems. We do find tentative results that EL CVn systems occur more often in the thin disk, as was predicted by Chen et al. 2017. We also find that the space density is at the lower bound, or even below the prediction of 4–10 $\times 10^{-6}\,\mathrm{pc}^{-3}$. To properly measure the properties of the population of EL CVn systems, a larger sample of EL CVn binaries is needed, preferably from a more uniform variability survey.

5.6.4 Comparison with the SWASP sample

To better understand the biases of our survey, we compare the PTF sample to the sample found by SWASP (Maxted et al., 2014a). While we both have used the lightcurve characteristics to identify EL CVn binaries, there are some intrinsic differences between the surveys, and therefore different biases in finding EL CVn systems. The most obvious difference between the surveys is the magnitude range; SWASP probes magnitudes between 9–13 mag, while our sample is fainter,

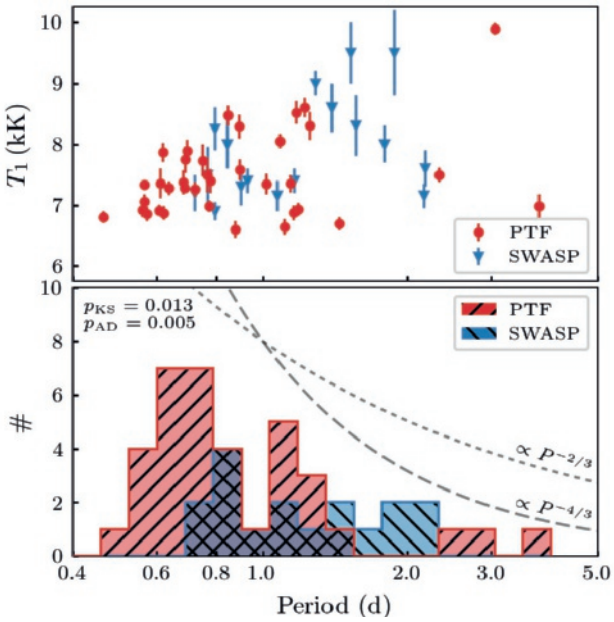

Figure 5.7: (*top*) The temperature of the A/F-star versus the orbital period of the EL CVn system. (*bottom*) The distribution of orbital periods of the PTF sample (red) and the SWASP sample (blue). In the top left, the result of the KS-test and AD-test are shown (see text). The top panel shows that there is a strong correlation between orbital period and temperature, which is a result of the binary evolution process (see text). The histograms show that the PTF data is more biased to the short period systems compared to the SWASP sample. It also shows a possible gap at periods of 1 day, caused by a detection bias against these systems. For comparison, we also plotted the detection probability of an eclipsing population with well-sampled lightcurves ($\propto P^{-2/3}$, dotted line), and for lightcurves with a limited amount of epochs ($\propto P^{-4/3}$, dashed line).

between 13.5 and 16 mag. A second major difference is the cadence and the number of epochs in a lightcurve; PTF lightcurves have an irregular cadence and a low number of epochs (∼100) compared to the regular cadence and better-sampled SWASP lightcurves (∼4000–13000 epochs).

There are indeed differences between the two samples. First , the distance range for the SWASP sample is 100–1200 pc, while the PTF sample reaches 1200–5000 pc. This is expected given the different magnitude range of the two surveys. We therefore also expect to find relatively more thick disk and halo systems compared to thin disk systems in the PTF sample. However, using the one-sided Fisher's exact test (Fisher, 1934), we find no significant difference between the relative number of thin disk systems. This is consistent with our finding that EL CVn systems are more numerous in the thin disk compared to the average stellar population and explains why at larger distances it is still the most dominant population.

The two samples are also different with regards to orbital period and temperature of the A/F-star (which dominates the luminosity), see Fig 5.7. We performed a Kolmogorov–Smirnov (KS) test and Anderson–Darling (AD) test (e.g. Sec. 3.1 in Feigelson & Babu, 2012) to compare the distribution of orbital periods. Both tests show that it is unlikely that the samples are drawn from the same distribution ($p_{\rm KS} = 0.013$ and $p_{\rm AD} = 0.005$). The histogram in Fig. 5.7 shows that we find more short orbital period systems and the top panel in Fig. 5.7 shows that at short orbital periods, the temperature of the primary star is low. This correlation can be understood because the mass of A/F-star is correlated with the orbital period. High mass main-sequence stars ($2\,{\rm M}_\odot$) begin their main-sequence lifetime at a temperature of 9500 K, and cool down to 7500 K towards the end of their main sequence lifetime (see Fig. 5.4). Main sequence stars of $1.3\,{\rm M}_\odot$ start at a temperature of 7500 K and only cools by 500 K during their time on the main sequence. Therefore, PTFs sensitivity for lower luminosity (lower temperature) EL CVn systems (partially) explains why the PTF sample contains more short period systems.

A second explanation is that, because of the sparse sampling, it is harder to find long period systems with PTF compared to SWASP. Both surveys use eclipses to find EL CVn binaries, and therefore are biased towards short period systems ($\mathrm{Prob}_{\rm ecl} \propto R_1 P^{-2/3}$). In addition, short period systems spend a larger fraction of their orbit in eclipse ($\tau_{\rm ecl} \propto R_1 P^{-2/3}$). This does not bias the SWASP search since the lightcurves are well sampled. With PTF however, a lack of observations during the eclipse can hinder the identification of a system as an EL CVn binary.

The difference between the two samples shows that selection effects make it difficult to determine the intrinsic properties of EL CVn binaries. To do so requires an integrated approach: stellar evolution and population synthesis models should be used to simulate a sample of EL CVn binaries, which are then 'observed' by simulating the variability survey which was used to find the real sample. Such a calculation is difficult given the in-homogeneity of the PTF sample, and beyond the scope of this work.

5.6.5 Pulsations

Pre-He-WDs are predicted to exhibit both p- and g-mode pulsations (e.g. Córsico & Althaus, 2014, 2016; Córsico et al., 2016; Istrate et al., 2016a). Pulsations have been found in two of the SWASP EL CVn binaries: WASP 0247-25 (Maxted et al., 2013; Istrate et al., 2017) and WASP 1628+10 (Maxted et al., 2014b). The pulsation periods are 5–10 minutes and the amplitudes ∼1–2 per cent

of the pre-He-WD luminosity. Models of pre-He-WDs predict that in a large area in T–log g space, pre-He-WDs should feature pulsations (Fig. 10 in Córsico et al., 2016; Istrate et al., 2016a). Many of the pre-He-WDs in the PTF sample lie in this region, making them useful to test the general predictions for pulsation theory. In addition, because stellar parameters can be measured very precisely, a pulsating pre-He-WD in an eclipsing binary is extremely useful to test evolutionary and seismic models in great detail (e.g. Istrate et al., 2017).

Unfortunately, the very sparse sampling of the PTF lightcurves makes it very difficult to identify such pulsations. We did attempt to find pulsations by using a Lomb-Scargle algorithm (Lomb 1976; Scargle 1982, implementation by VanderPlas & Ivezić 2015) on the residuals of the lightcurves. We found periodic behaviour in the residuals at predicted periods of ∼10 minutes for a number of the systems, but because of the sparse sampling and low amplitude, it is difficult to determine if these are real or not. High cadence follow-up photometry is needed to establish the reality of these pulsations.

5.7 Summary and conclusion

In this paper, we report the discovery and analysis of 36 new EL CVn systems extracted from Palomar Transient Factory data. With this sample, we more than double the number of known EL CVn systems. To find the EL CVn systems we used machine learning classifiers to make a pre-selection of candidates. This has proven to be an efficient method to minimise the number of lightcurves that have to be visually inspected.

The radii (0.16–0.7 $R_\odot$) and temperatures (8000–17000 K) of the pre-He-WDs in the sample indicate they are all young systems in the "constant luminosity" phase (0–250 Myr) of their evolution. The masses of the pre-He-WDs are all low ($<0.3 M_\odot$), but our measurements show a large spread around the predicted mass-period relation, which remains unexplained. If we use the measured radii and temperatures combined with models, we do find masses consistent with the mass-period relation. This discrepancy is either due to systematic or underestimated uncertainties in our measurements, or there is more variance in the masses than the stellar evolution models predict. This problem can be resolved by obtaining more accurate radial velocity measurements (ideally for both stars in the binary to obtain an independent mass ratio measurement), and by more extensively testing the effect on the mass-period relation of e.g. different metallicities and rotation rates.

Although a detailed population study is difficult with the PTF dataset, we find that EL CVn binaries occur more often in the thin disk than an average Galactic stellar population. In addition, we find that the space density is most likely lower than the predicted value of $4–10 \times 10^{-6}$ pc^{-3}. To properly determine the properties of the EL CVn population, a more systematic search combined with stellar and Galactic modelling is required.

This new sample of young pre-He-WDs will be useful to put many theoretical models to the test, including stellar structure models for low mass white dwarfs, pulsation models, and binary evolution models. In addition, the methods we have used to identify EL CVn systems can easily be adapted to find other rare types of variable stars and these (and similar machine learning methods) will be vital to fully utilise (future) variability surveys like ZTF (Bellm, 2014), NGTS

(Wheatley et al., 2017), GOTO (Steeghs & Galloway, 2017), BlackGEM (Bloemen et al., 2015), *TESS* (Ricker et al., 2015), *PLATO* (Rauer et al., 2014), and LSST (Ivezić et al., 2008).

5.A Additional tables and figures

Table 5.5: List of a features used by the machine learning classifiers.

PTF variability	
wRMS (mag)	weighted root-mean-square of the PTF lightcurve
skew (mag)	skewness of the PTF lightcurve
medAbsDev (mag)	median absolute deviation of the PTF lightcurve
StetsJ	Stetson-J statistic of the PTF lightcurve
StetsK	Stetson-K statistic of the PTF lightcurve
Neumann	the Von Neumann ratio statistic of the PTF lightcurve
MBR	median buffer range: the fraction of points more than 20% of the lightcurve amplitude from the weighted mean magnitude, divided by total number of epochs.
AMBS{1,2,3}	The fraction of lightcurve points that are # standard deviation above the mean magnitude.
BMBS{1,2,3}	The fraction of lightcurve points that are # standard deviation below the mean magnitude.
prange{#} (mag)	range containing {90,80,65,50,35,20} per cent of the data.
percentile{#}	#th percentile minus the median of the PTF lightcurve, divided by prange90 , with # in {5,10,17.5,25,32.5,40,60,67.5,75,82.5,90,95}.

Pan-STARRS colours	
PSr (mag)	Pan-STARRS r - median of the lightcurve
PSgr (mag)	Pan-STARRS $g - r$
PSri (mag)	Pan-STARRS $r - i$
PSiz (mag)	Pan-STARRS $i - z$
PSzy (mag)	Pan-STARRS $z - y$

2MASS colours	
J (mag)	2MASS J - median of the lightcurve
JH (mag)	2MASS $J - H$
HK (mag)	2MASS $H - K$

Table 5.6: Overview of the nights at the INT with the IDS.

Date	Grating	CCD	seeing (″)	weather
2016-09-07	R632V	RED+2	0.6	excellent
2016-09-08	R632V	RED+2	0.7	excellent
2016-09-09	R632V	RED+2	0.6	excellent
2016-09-10	R632V	RED+2	0.7	good
2016-09-11	R632V	RED+2	0.6–1.0	good
2016-09-12	R632V	RED+2	0.7–1.0	good
2016-09-13	R632V	RED+2	0.8–1.2	good
2016-09-14	R632V	RED+2	1.0	good
2016-12-14	R900V	RED+2	0.8–1.4	good
2016-12-15	R900V	RED+2	1.4	ok
2017-01-09	R900V	RED+2	0.8	good
2017-01-10	R900V	RED+2	1.2–2.6	ok–bad
2017-03-10	R900V	EEV10	1.5–3.0	bad
2017-03-11	R900V	EEV10	–	clouds
2017-03-12	R900V	EEV10	2–4	bad
2017-03-13	R900V	EEV10	1.5	bad

Table 5.7: The temperatures of the A/F-star (T_1) and pre-Helium white dwarf (T_2) determined from the spectral energy distribution of the binary stars, see Fig. 5.9. The $E(B-V)$ values are taken from Schlegel et al. (1998); Schlafly & Finkbeiner (2011), with an uncertainty of 0.034 (as in Maxted et al., 2011). The 'RMS' column indicates the additional uncertainty added to account for all variance, which is achieved by the parameter f in Equation 5.2.

ID	T_1 (K)	T_2 (K)	$E(B-V)$	RMS
1600y	6930 ± 100	8900 ± 110	0.047	0.05
1600ad	8050 ± 120	10490 ± 200	0.024	0.04
1700do	9890 ± 110	17100 ± 1400	0.015	0.03
1600aa	7890 ± 190	9300 ± 400	0.107	0.02
1601p	8600 ± 160	11700 ± 500	0.030	0.03
1501bh	6870 ± 110	11100 ± 400	0.035	0.03
1601q	8300 ± 230	10700 ± 700	0.081	0.03
1601cl	8280 ± 200	10100 ± 300	0.030	0.04
1402de	7870 ± 150	9300 ± 300	0.100	0.03
1607aa	8470 ± 160	10300 ± 300	0.087	0.04
1607v	7260 ± 130	10900 ± 500	0.090	0.03
1607t	6600 ± 140	8600 ± 200	0.009	0.10
1607ab	6980 ± 100	8810 ± 80	0.005	0.09
1608ab	7360 ± 240	7900 ± 400	0.037	0.05
1612al	7280 ± 110	10300 ± 300	0.039	0.01
1512bf	6920 ± 90	9740 ± 180	0.022	0.03
1613s	7350 ± 140	13700 ± 800	0.051	0.04
1613u	7340 ± 70	9690 ± 160	0.006	0.04
1615ag	7380 ± 200	10200 ± 400	0.093	0.05
1615v	6920 ± 120	9400 ± 300	0.030	0.03
1515ay	6800 ± 100	7930 ± 150	0.029	0.04
1615w	6690 ± 110	10300 ± 200	0.046	0.04
1615ao	7580 ± 170	8700 ± 160	0.070	0.03
1615u	7400 ± 200	12200 ± 600	0.069	0.06
1616cr	7060 ± 120	8000 ± 170	0.095	0.10
1617n	7500 ± 110	11600 ± 400	0.022	0.03
1617m	6990 ± 190	9320 ± 190	0.071	0.04
1619l	6870 ± 120	9200 ± 150	0.031	0.04
1521ct	8520 ± 180	9800 ± 300	0.090	0.02
1621ax	7340 ± 170	11800 ± 700	0.108	0.04
1521cm	7290 ± 80	9240 ± 90	0.051	0.02
1622by	7730 ± 260	11100 ± 1400	0.079	0.07
1522cc	6860 ± 120	9570 ± 190	0.042	0.06
1622aa	7490 ± 290	10900 ± 1300	0.160	0.11
1622bt	7750 ± 220	12200 ± 1000	0.061	0.07
1723aj	6640 ± 130	11000 ± 400	0.061	0.04

Table 5.8: The parameters of the lightcurve models shown in Fig. 5.8. This table shows the median and root-mean-square of final 5120 points in our MCMC chains. Note that these distributions are not normally distributed and parameters can be strongly correlated.

ID Band	P (d)	t_0 (BMJD$_{\rm tdb}$)	i (°)	q	$\langle r_1 \rangle$	$\langle r_2 \rangle$	T_2/T_1	absorb$_R$	absorb$_{g'}$	log(f_R)	log($f_{g'}$)	fill	ρ ($\rho_\odot$)
1600y	1.1838920	55570.2084	84.5	0.12	0.421	0.081	0.73	0.8	0.8	−2.1	−2.5	0.748	0.114
R+g	0.0000008	0.0006	2.7	0.02	0.010	0.003	0.03	0.2	0.2	0.0	0.1	0.019	0.007
1600ad	1.0840448	56247.4677	86.5	0.11	0.328	0.063	0.80	1.3	1.0	−2.3	−2.4	0.575	0.292
R+g	0.0000010	0.0006	2.2	0.03	0.008	0.003	0.03	0.5	0.5	0.0	0.1	0.025	0.019
1700do	3.0507595	55556.8044	87.4	0.33	0.178	0.025	0.77	2.8		−2.3		0.380	0.187
R	0.0000281	0.0014	1.8	0.10	0.010	0.002	0.04	1.2		0.0		0.020	0.024
1600aa	0.6934558	56892.6368	78.7	0.29	0.391	0.128	0.94	3.6	3.2	−2.5	−2.6	0.801	0.362
R+g	0.0000006	0.0003	0.8	0.05	0.007	0.004	0.01	0.8	0.8	0.2	0.4	0.026	0.021
1601p	1.2215885	57152.5232	84.0	0.21	0.274	0.056	0.84	1.4	1.1	−2.2	−2.3	0.534	0.358
R+g	0.0000051	0.0010	3.1	0.09	0.019	0.005	0.03	1.0	1.1	0.0	0.3	0.036	0.059
1501bh	0.6204144	55097.3927	78.4	0.14	0.356	0.058	0.64	0.5	0.4	−2.1	−2.1	0.646	0.674
R+g	0.0000005	0.0008	1.9	0.04	0.017	0.004	0.04	0.3	0.2	0.1	0.0	0.023	0.085
1601q	1.2515054	57190.1373	80.6	0.12	0.308	0.074	0.91	1.6	2.2	−2.3	−2.5	0.535	0.266
R+g	0.0000051	0.0012	2.7	0.07	0.021	0.007	0.03	1.1	1.2	0.1	0.3	0.049	0.051
1601cl	0.8917354	56063.3087	82.9	0.11	0.475	0.101	0.95	2.3	1.9	−2.1	−2.3	0.830	0.142
R+g	0.0000005	0.0004	2.9	0.02	0.011	0.004	0.02	0.8	0.7	0.0	0.0	0.021	0.009
1402de	0.6189694	55768.8152	87.0	0.17	0.405	0.119	0.91	2.5		−2.9		0.757	0.454
R	0.0000011	0.0008	2.4	0.07	0.015	0.006	0.03	1.1		0.3		0.052	0.049
1607aa	0.8463124	56246.6579	84.4	0.14	0.375	0.079	0.92	2.2	3.7	−2.6	−2.6	0.678	0.314
R+g	0.0000017	0.0007	3.6	0.03	0.017	0.005	0.03	1.0	0.9	0.3	0.2	0.024	0.035
1607v	0.7198355	55769.1206	82.7	0.13	0.447	0.039	0.66	2.0	2.2	−2.4	−2.3	0.808	0.256
R+g	0.0000020	0.0014	5.7	0.04	0.037	0.007	0.08	1.0	1.0	0.1	0.0	0.038	0.048
1607t	0.8759507	56158.7102	76.6	0.09	0.417	0.085	0.74	0.7	0.5	−2.3	−2.3	0.712	0.220

R+g	0.0000004	0.0004	1.0	0.02	0.009	0.003	0.03	0.2	0.2	0.0	0.0	0.020	0.014
1607ab	0.7730986	55151.7862	83.8	0.18	0.351	0.077	0.77	1.9	1.5	−2.3	−2.2	0.665	0.439
R+g	0.0000002	0.0004	2.3	0.03	0.010	0.003	0.03	0.4	0.4	0.1	0.0	0.020	0.035
1608ab	0.6101718	57034.9178	86.8	0.07	0.390	0.146	0.90	0.4		−3.0		0.656	0.551
R	0.0000014	0.0003	1.9	0.07	0.006	0.004	0.02	0.3		0.3		0.058	0.044
1612al	0.6369260	55782.6928	86.8	0.12	0.322	0.103	0.69	0.1		−2.3		0.574	0.880
R	0.0000006	0.0007	2.0	0.06	0.009	0.004	0.03	0.1		0.1		0.043	0.084
1512bf	0.6074343	56100.9311	87.2	0.10	0.438	0.091	0.66	0.1	0.1	−2.1	−2.2	0.762	0.391
R+g	0.0000002	0.0002	1.9	0.02	0.005	0.003	0.03	0.1	0.1	0.0	0.0	0.017	0.012
1613s	1.1420695	56511.1762	76.2	0.10	0.470	0.044	0.60	1.2	1.2	−2.2	−2.2	0.812	0.091
R+g	0.0000024	0.0014	6.0	0.03	0.050	0.008	0.05	0.5	0.5	0.1	0.0	0.050	0.023
1613u	0.5644902	56787.5255	81.6	0.18	0.472	0.107	0.77	1.4	1.6	−2.4	−2.5	0.889	0.340
R+g	0.0000003	0.0003	2.7	0.03	0.012	0.004	0.03	0.4	0.4	0.1	0.2	0.023	0.024
1615ag	0.6806898	55380.8645	85.8	0.17	0.410	0.079	0.76	2.2	1.9	−2.2	−2.4	0.772	0.358
R+g	0.0000046	0.0010	3.3	0.04	0.013	0.005	0.05	1.0	0.8	0.3	0.1	0.026	0.029
1615v	0.5594054	54962.6621	73.7	0.10	0.457	0.099	0.71	0.2	0.1	−2.2	−2.9	0.784	0.410
R+g	0.0000003	0.0007	1.4	0.02	0.012	0.004	0.03	0.1	0.1	0.1	0.3	0.029	0.031
1515ay	0.4642873	56138.1751	89.0	0.11	0.452	0.161	0.83	0.0	0.1	−2.2	−1.9	0.794	0.606
R+g	0.0000001	0.0002	1.1	0.03	0.003	0.002	0.02	0.0	0.1	0.1	0.0	0.027	0.018
1615w	1.4407151	56530.5582	77.7	0.15	0.393	0.060	0.60	0.7	0.4	−2.9	−2.5	0.723	0.092
R+g	0.0000024	0.0010	2.7	0.04	0.021	0.004	0.04	0.3	0.2	0.3	0.1	0.026	0.015
1615ao	0.8954515	56308.1400	77.6	0.24	0.368	0.129	0.94	2.1	1.9	−2.4	−2.5	0.729	0.273
R+g	0.0000007	0.0005	0.8	0.06	0.007	0.005	0.02	1.1	1.0	0.3	0.2	0.038	0.020
1615u	0.7777349	56185.6219	82.4	0.16	0.297	0.038	0.59	1.4	1.8	−2.1	−2.2	0.554	0.726
R+g	0.0000011	0.0011	4.2	0.07	0.034	0.006	0.05	0.7	0.8	0.1	0.0	0.041	0.191
1616cr	0.5649690	55972.1677	82.5	0.05	0.416	0.141	0.84	0.4	0.5	−2.3	−3.0	0.657	0.558
R+g	0.0000002	0.0002	0.9	0.01	0.005	0.002	0.02	0.2	0.1	0.2	0.2	0.021	0.025

1617n	2.3367776	55591.4345	87.3	0.21	0.258	0.040	0.63	2.6	1.5	−2.1	−2.4	0.501	0.117
R+g	0.0000052	0.0027	2.1	0.07	0.012	0.003	0.04	0.8	0.5	0.1	0.1	0.025	0.013
1617m	3.7728999	56584.2146	87.8	0.24	0.206	0.056	0.68	0.6	0.7	−2.1	−2.2	0.410	0.085
R+g	0.0000083	0.0010	1.5	0.15	0.005	0.002	0.03	0.5	0.4	0.1	0.1	0.046	0.011
1619l	1.1599993	56560.2644	82.7	0.14	0.385	0.061	0.67	1.2	3.6	−2.2	−2.3	0.704	0.153
R+g	0.0000017	0.0016	4.2	0.04	0.022	0.006	0.04	0.4	0.8	0.1	0.3	0.029	0.021
1521ct	1.1724964	56907.7345	83.2	0.17	0.282	0.093	0.92	1.2	2.2	−2.3	−2.9	0.528	0.373
R+g	0.0000013	0.0005	1.4	0.09	0.009	0.004	0.02	0.8	1.1	0.1	0.3	0.046	0.044
1621ax	1.0181525	56741.7492	83.1	0.17	0.401	0.029	0.57	2.9	2.2	−2.2	−2.2	0.758	0.171
R+g	0.0000044	0.0017	4.8	0.04	0.028	0.006	0.07	0.9	1.1	0.0	0.1	0.031	0.027
1521cm	0.6854774	56068.9363	80.0	0.22	0.381	0.110	0.78	0.7	0.8	−2.9	−2.6	0.740	0.428
R+g	0.0000002	0.0002	1.0	0.04	0.008	0.003	0.02	0.3	0.2	0.3	0.2	0.025	0.027
1622by	0.7486683	55718.0157	85.6	0.16	0.424	0.076	0.81	3.5	3.1	−2.4	−2.9	0.791	0.270
R+g	0.0000015	0.0010	3.6	0.03	0.017	0.005	0.04	0.9	0.8	0.3	0.3	0.024	0.025
1522cc	0.5717853	56641.9749	81.2	0.18	0.472	0.078	0.69	1.4	1.2	−2.4	−2.6	0.894	0.331
R+g	0.0000003	0.0003	3.1	0.03	0.013	0.004	0.04	0.3	0.3	0.1	0.2	0.018	0.023
1622aa	0.7661291	57136.1682	84.7	0.10	0.410	0.060	0.75	0.6	1.4	−2.4	−2.9	0.716	0.302
R+g	0.0000038	0.0014	4.0	0.03	0.022	0.006	0.05	0.5	0.7	0.2	0.3	0.026	0.038
1622bt	0.6884160	56746.2432	79.2	0.17	0.425	0.071	0.70	1.7	1.4	−2.3	−2.5	0.795	0.314
R+g	0.0000004	0.0003	2.0	0.02	0.012	0.003	0.03	0.4	0.3	0.0	0.2	0.017	0.023
1723aj	1.1088064	56733.1351	85.6	0.11	0.460	0.042	0.52	0.5	0.5	−2.4	−3.1	0.818	0.100
R+g	0.0000009	0.0004	3.3	0.02	0.011	0.003	0.05	0.2	0.2	0.0	0.2	0.022	0.006

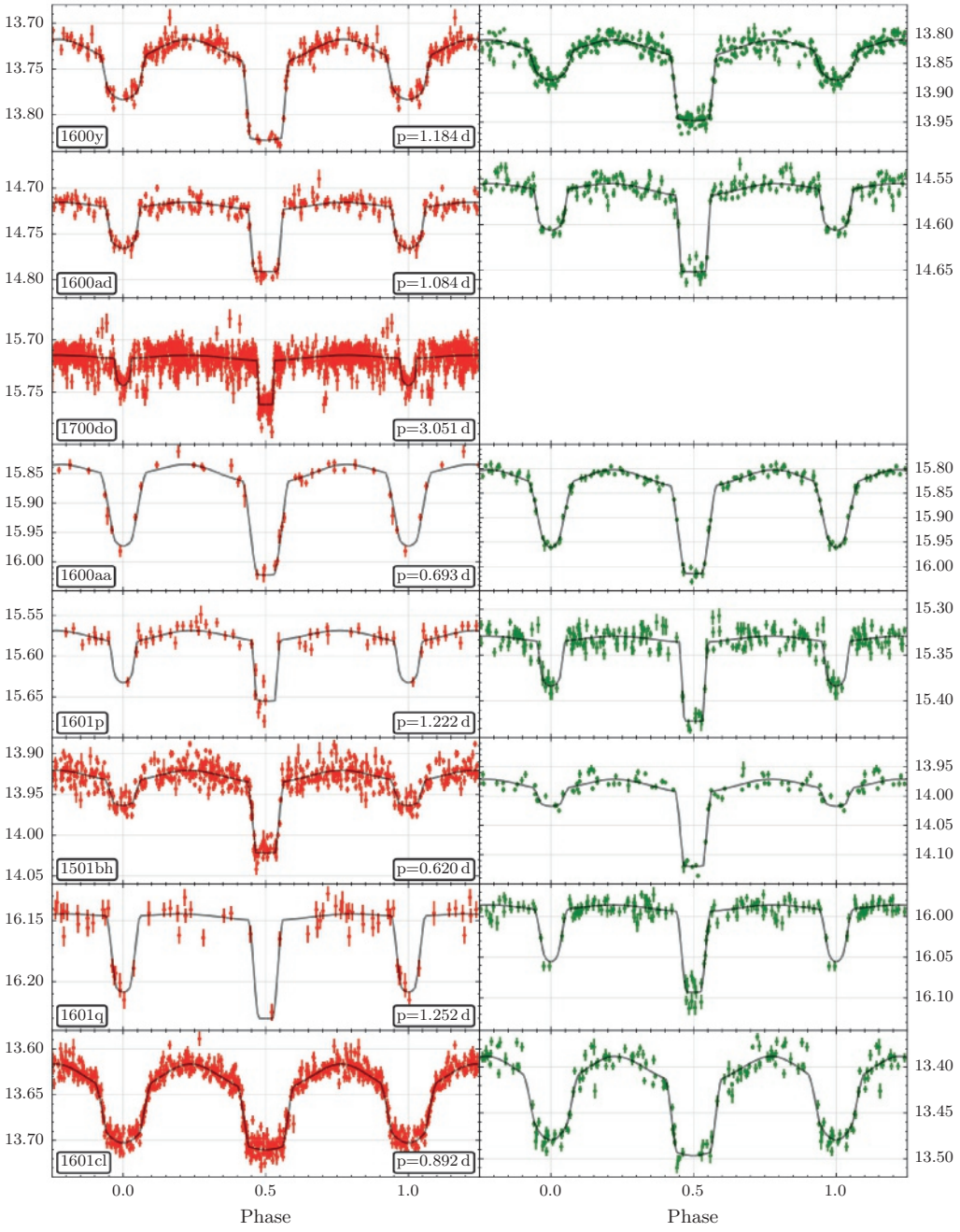

Figure 5.8: The PTF lightcurves in R (left) and g' (right) with the best model over-plotted (see Table 5.8).

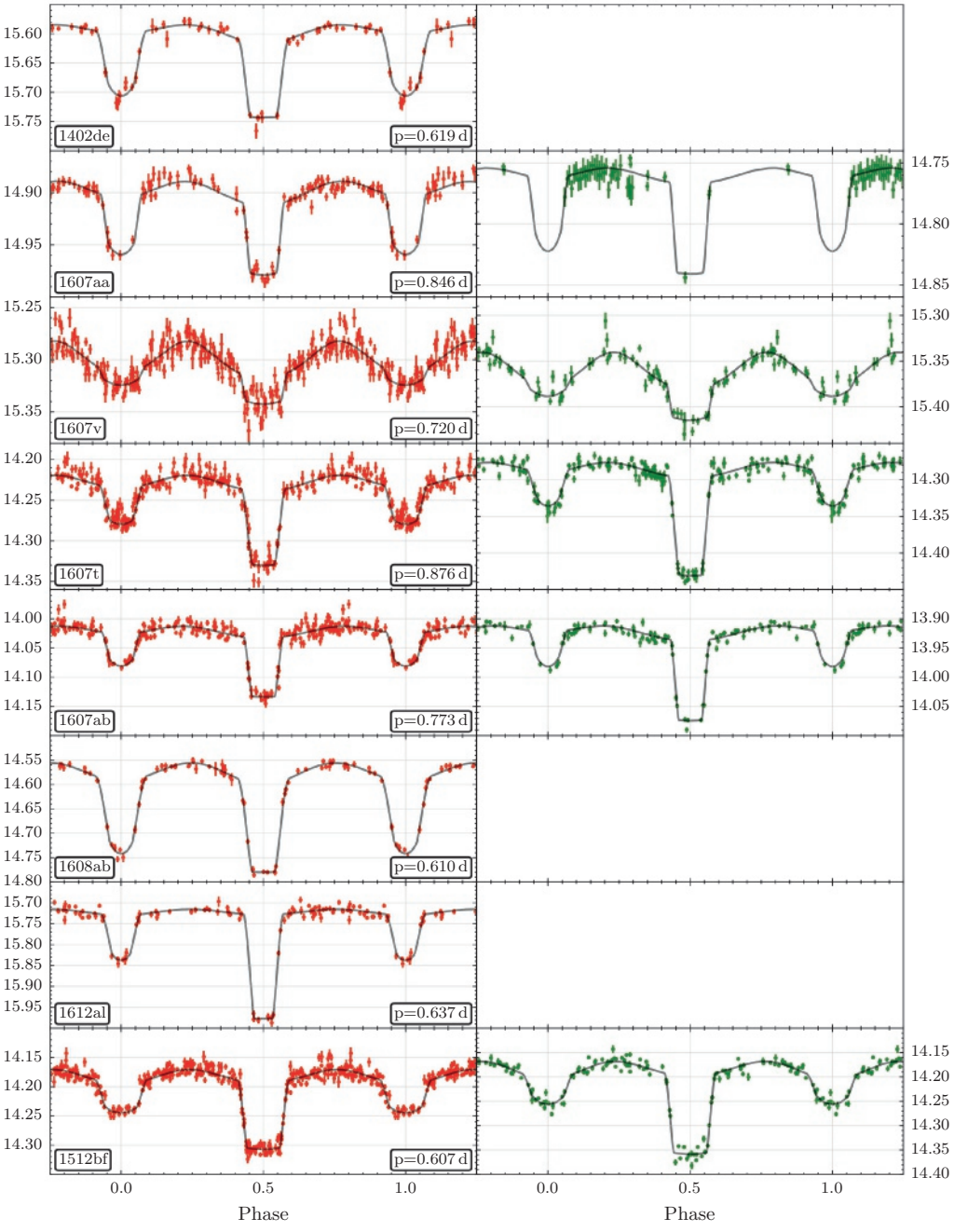
1402de
p=0.619 d
1607aa
p=0.846 d
1607v
p=0.720 d
1607t
p=0.876 d
1607ab
p=0.773 d
1608ab
p=0.610 d
1612al
p=0.637 d
1512bf
p=0.607 d
Phase
Phase

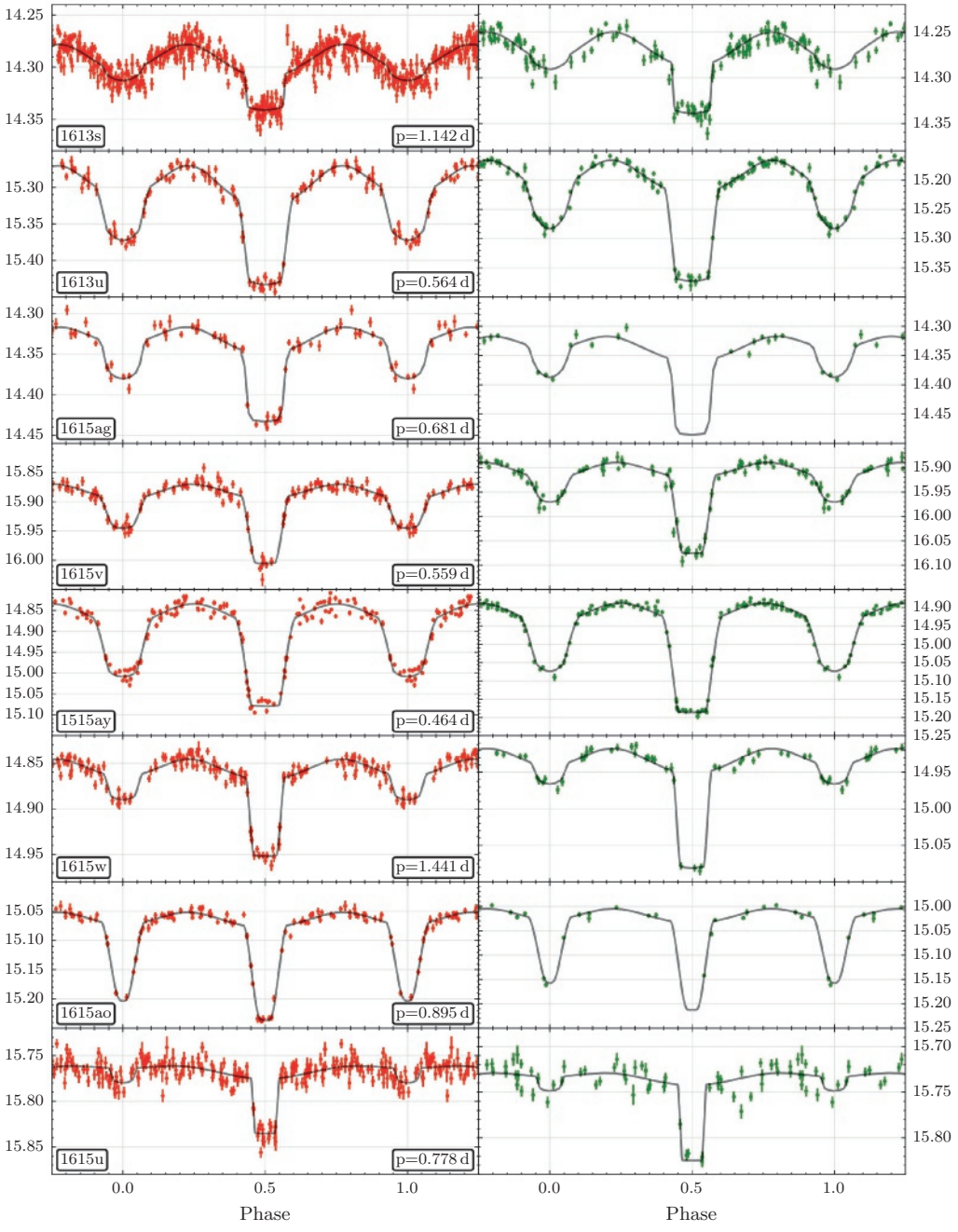
1613s
p=1.142 d
1613u
p=0.564 d
1615ag
p=0.681 d
1615v
p=0.559 d
1515ay
p=0.464 d
1615w
p=1.441 d
1615ao
p=0.895 d
1615u
p=0.778 d
Phase
Phase

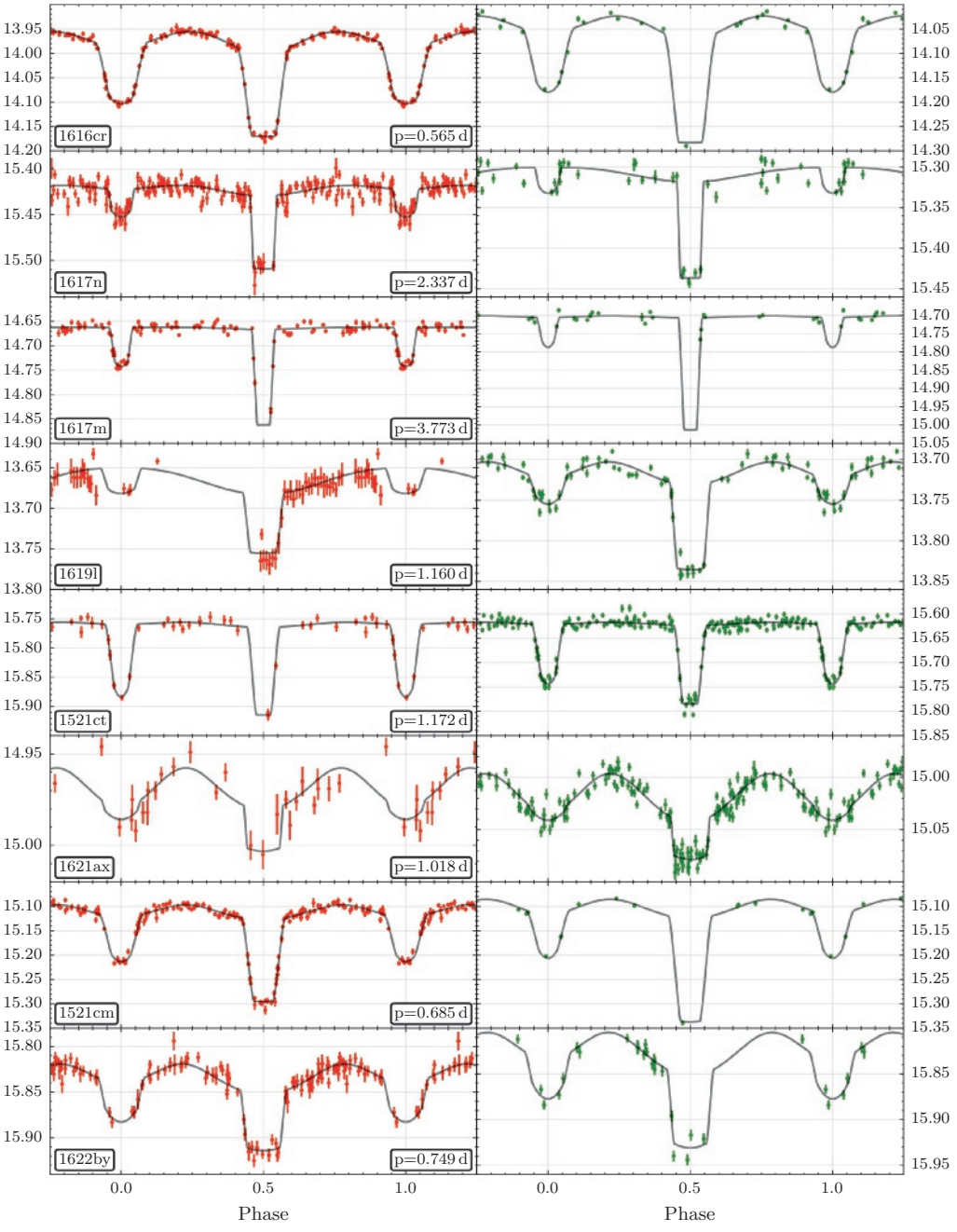
1616cr
p=0.565 d
1617n
p=2.337 d
1617m
p=3.773 d
1619l
p=1.160 d
1521ct
p=1.172 d
1621ax
p=1.018 d
1521cm
p=0.685 d
1622by
p=0.749 d
Phase
Phase

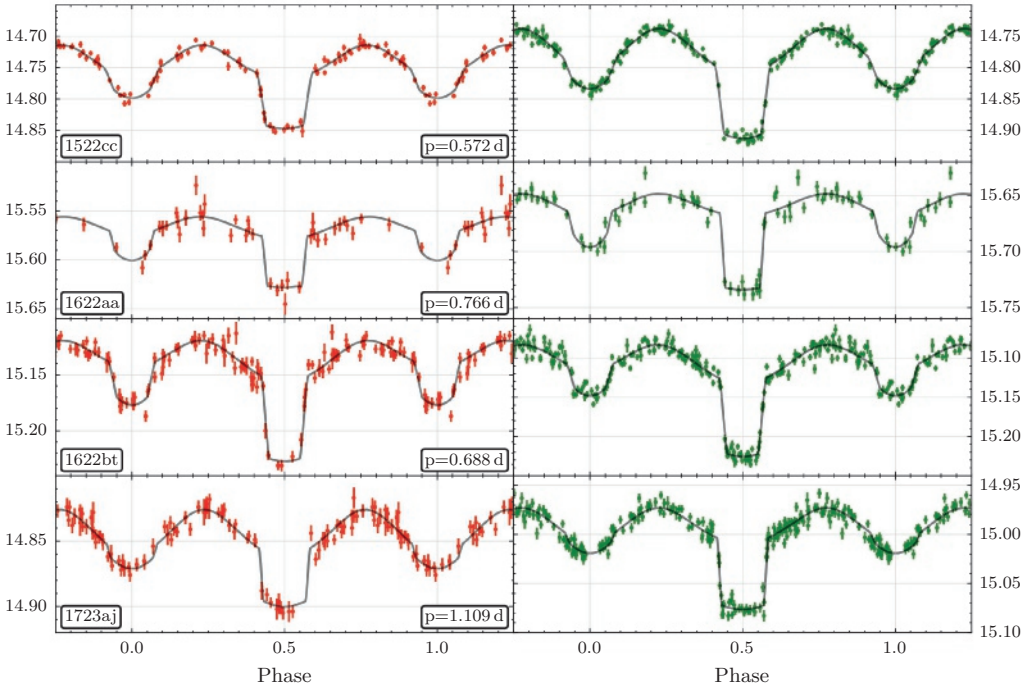
1522cc
p=0.572 d
1622aa
p=0.766 d
1622bt
p=0.688 d
1723aj
p=1.109 d
Phase
Phase

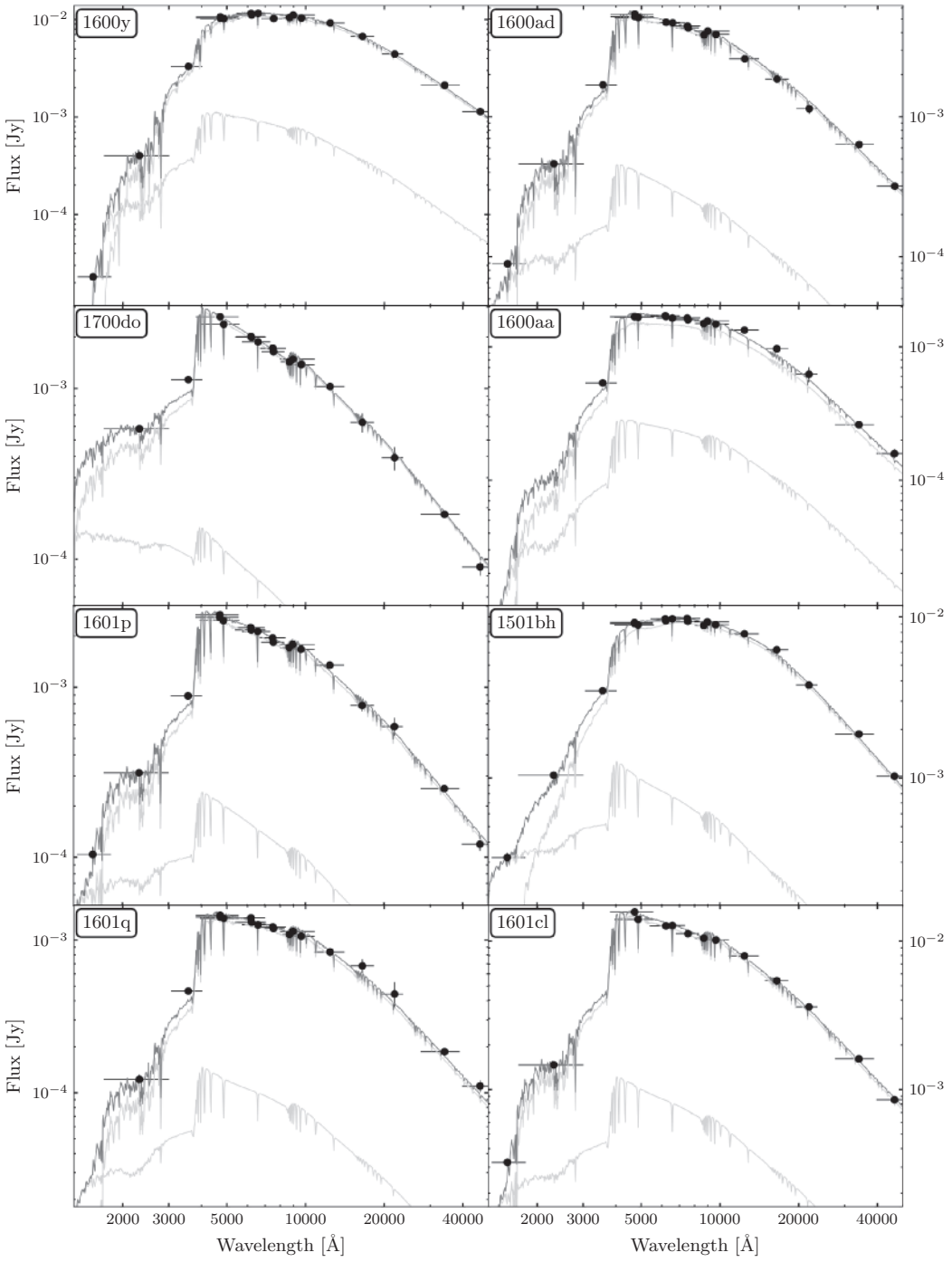

Figure 5.9: The spectral energy distribution and the best-fitting model spectra (see Table 5.7). The grey lines show the SED of the A/F-star and pre-He-WD. The black line shows the sum of both components. The A/F-star dominates the SED over the whole wavelength range, except in the far-UV in some of the cases.

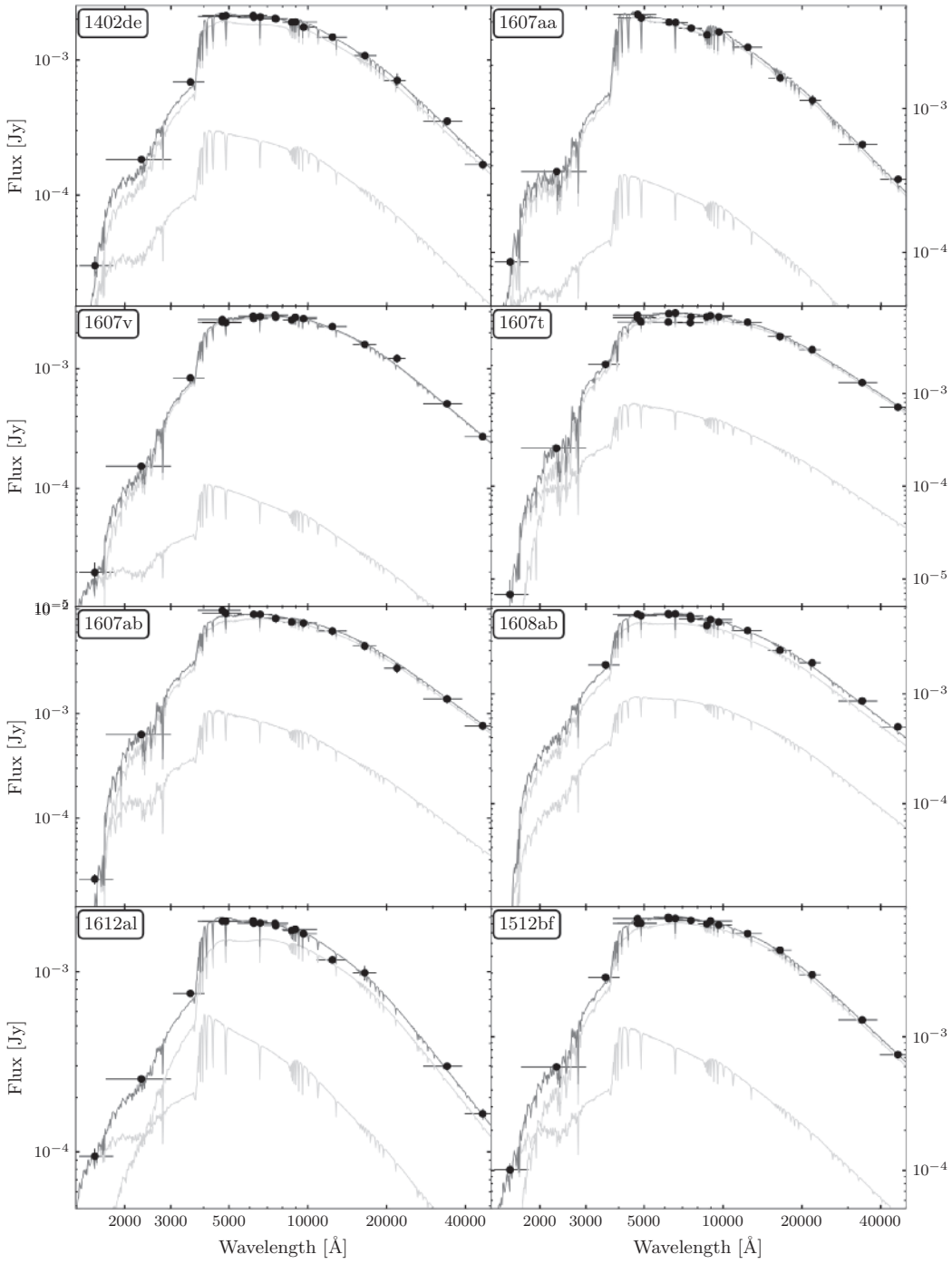
1402de
1607aa
1607v
1607t
1607ab
1608ab
1612al
1512bf
Flux [Jy]
Wavelength [Å]
2000
3000
5000
10000
20000
40000

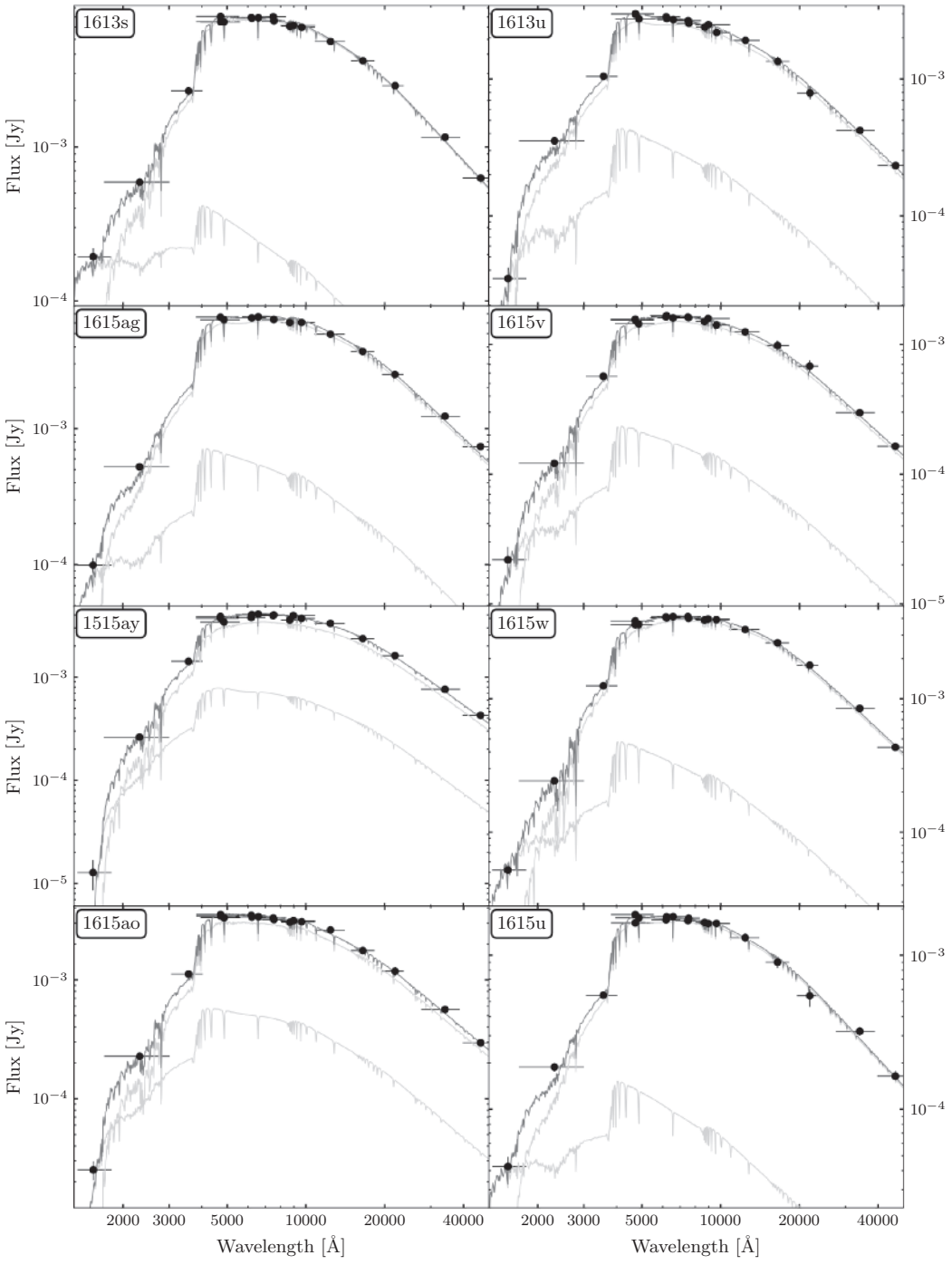
1613s
1613u
1615ag
1615v
1515ay
1615w
1615ao
1615u
Flux [Jy]
Wavelength [Å]
2000
3000
5000
10000
20000
40000

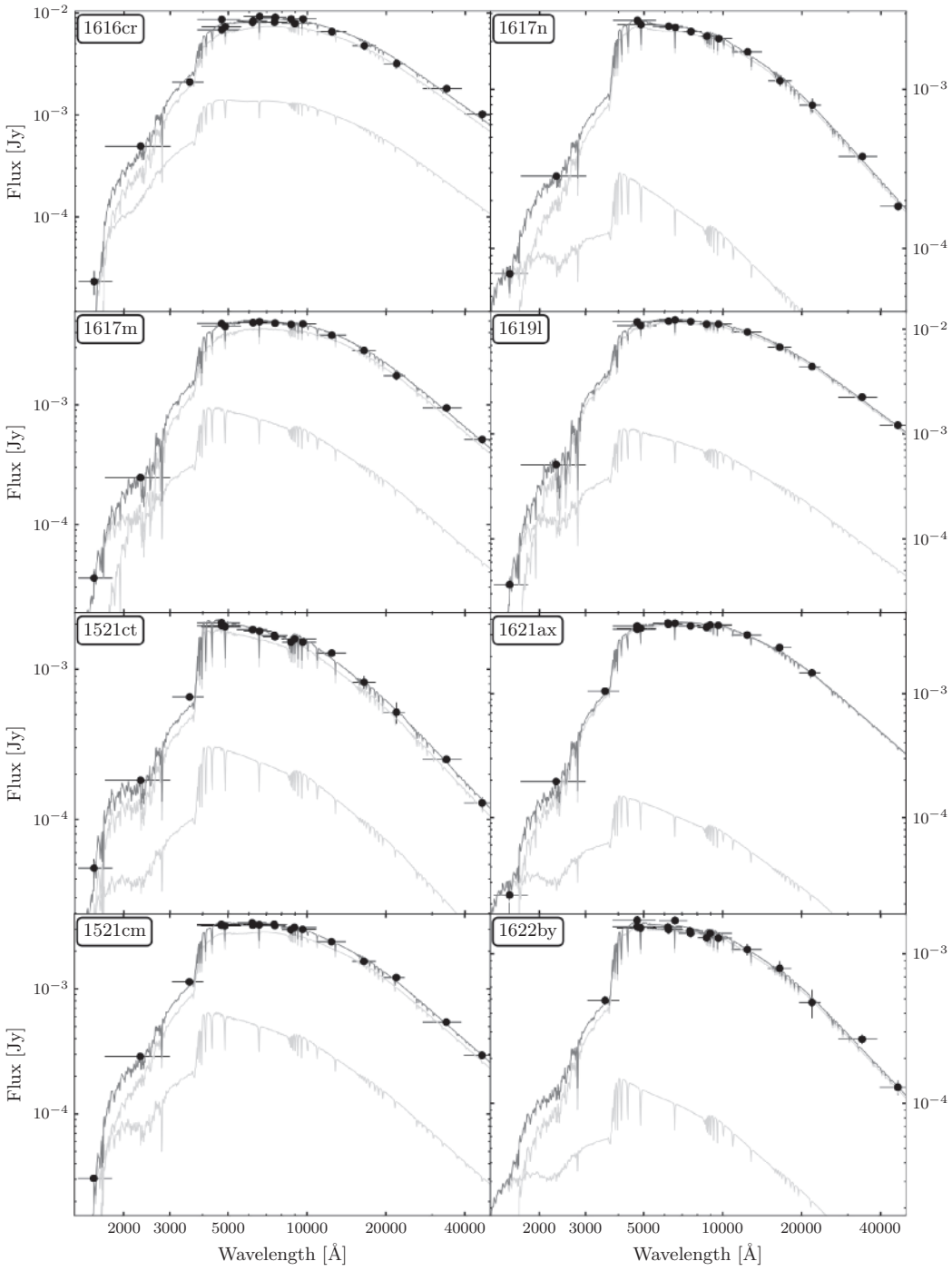
1616cr
1617n
1617m
1619l
1521ct
1621ax
1521cm
1622by
Flux [Jy]
Wavelength [Å]
2000
3000
5000
10000
20000
40000

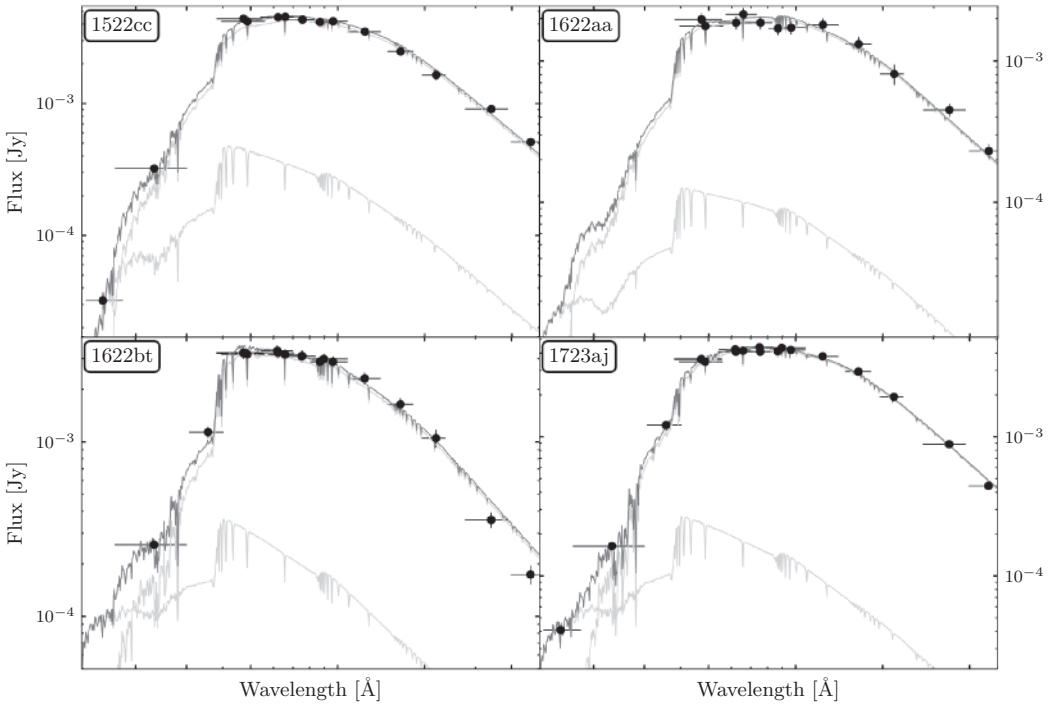
1522cc
1622aa
1622bt
1723aj
Flux [Jy]
Flux [Jy]
10^{-3}
10^{-4}
Wavelength [Å]
Wavelength [Å]

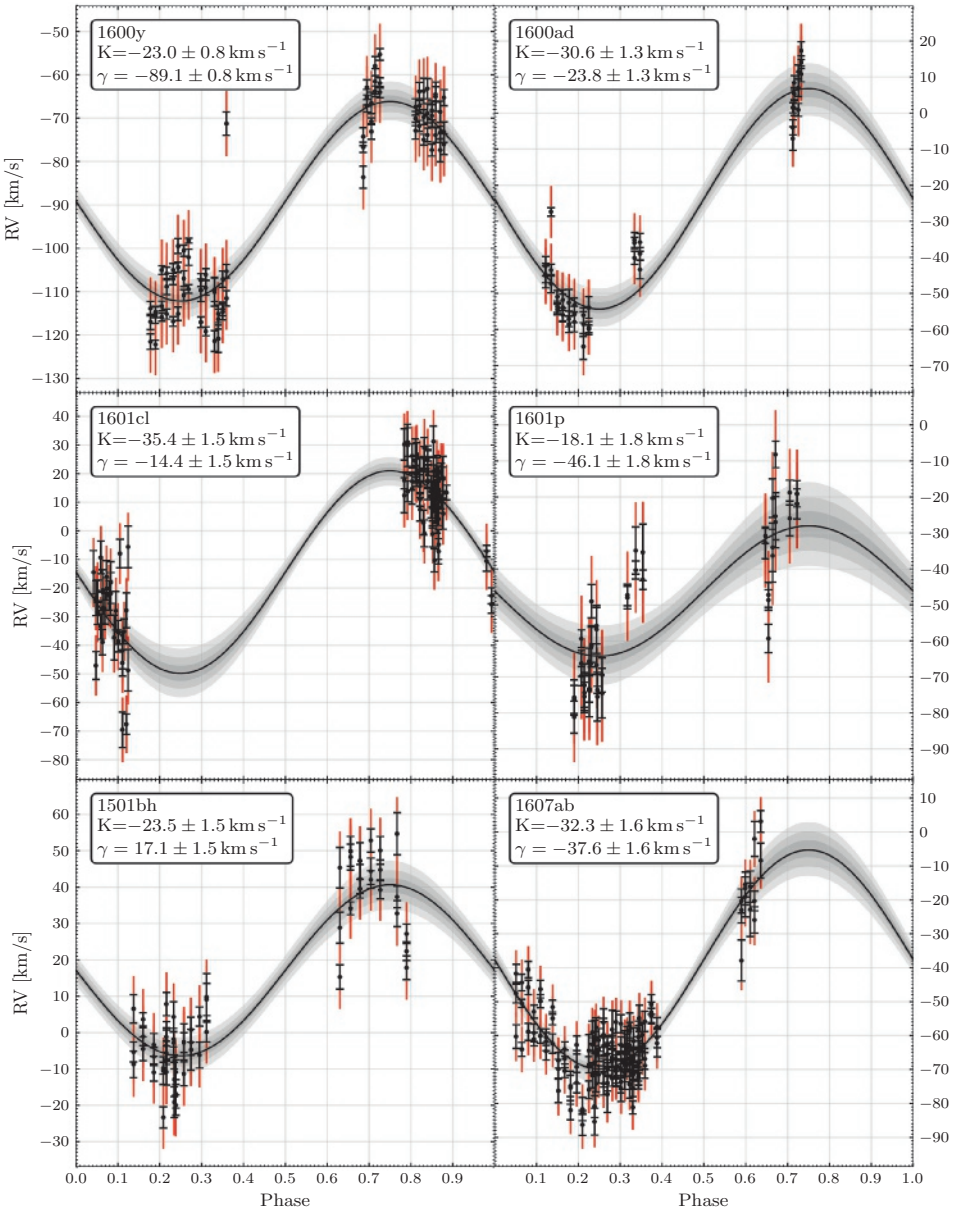

Figure 5.10: The radial velocity measurements with the INT and the best fitting model. Black errorbars show the estimated uncertainty from the cross-correlation procedure, while the red errorbars show the uncertainties required to account for all residual variance. The shaded grey contours show the 1, 2 and 3 standard deviation intervals of model, obtained using the larger uncertainties.

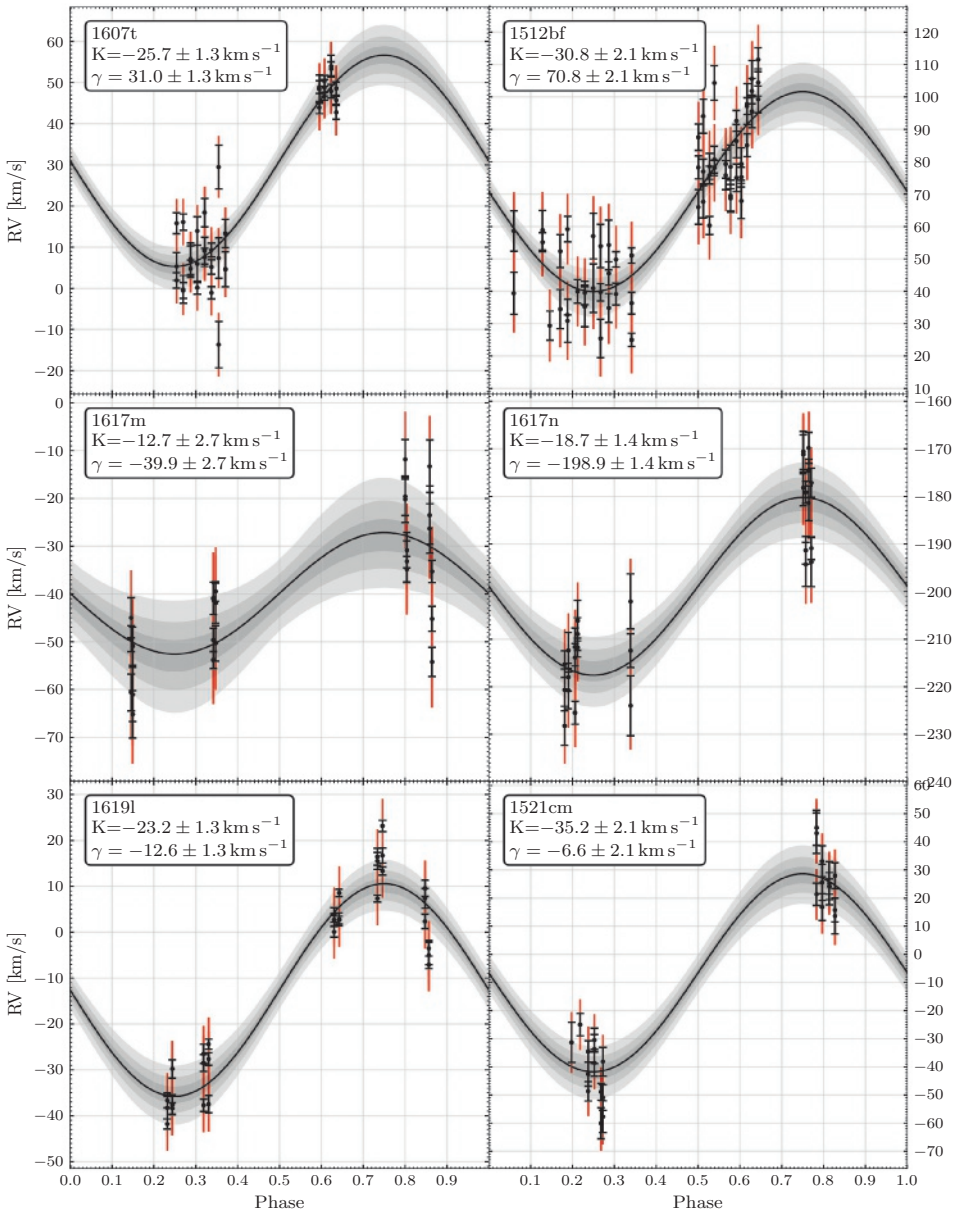
1607t
K=−25.7 ± 1.3 km s−1
γ = 31.0 ± 1.3 km s−1
1512bf
K=−30.8 ± 2.1 km s−1
γ = 70.8 ± 2.1 km s−1
1617m
K=−12.7 ± 2.7 km s−1
γ = −39.9 ± 2.7 km s−1
1617n
K=−18.7 ± 1.4 km s−1
γ = −198.9 ± 1.4 km s−1
1619l
K=−23.2 ± 1.3 km s−1
γ = −12.6 ± 1.3 km s−1
1521cm
K=−35.2 ± 2.1 km s−1
γ = −6.6 ± 2.1 km s−1
RV [km/s]
Phase

Bibliography

K. N. Abazajian, J. K. Adelman-McCarthy, M. A. Agüeros, et al., 2009. *ApJS*, 182:543-558.

B. P. Abbott, R. Abbott, T. D. Abbott, et al., 2016. *Living Reviews in Relativity*, 19:1.

B. P. Abbott, R. Abbott, T. D. Abbott, et al., 2017. *ApJ*, 848:L13.

B. P. Abbott, R. Abbott, T. D. Abbott, et al., 2017. *Phys. Rev. Lett.*, 119:161101.

B. P. Abbott, R. Abbott, T. D. Abbott, et al., 2017. *ApJ*, 848:L12.

B. Abolfathi, D. S. Aguado, G. Aguilar, et al., 2018. *ApJS*, 235:42.

F. Acernese, M. Agathos, K. Agatsuma, et al., 2015. *Classical and Quantum Gravity*, 32(2):024001.

M. Ackermann, I. Arcavi, L. Baldini, et al., 2015. *ApJ*, 807:169.

S. M. Adams, N. Blagorodnova, M. M. Kasliwal, et al., 2018. *PASP*, 130(3):034202.

C. P. Ahn, R. Alexandroff, C. Allende Prieto, et al., 2012. *ApJS*, 203:21.

V. S. Airapetian, V. Adibekyan, M. Ansdell, et al., 2018. *ArXiv e-prints*.

L. G. Althaus, M. M. Miller Bertolami, & A. H. Córsico, 2013. *A&A*, 557:A19.

I. Andreoni, K. Ackley, J. Cooke, et al., 2017. *PASA*, 34:e069.

R. Angeloni, R. Contreras Ramos, M. Catelan, et al., 2014. *A&A*, 567:A100.

I. Arcavi, G. Hosseinzadeh, D. A. Howell, et al., 2017. *Nature*, 551:64–66.

I. Arcavi, D. Xu, T. Matheson, et al., 2010. *The Astronomer's Telegram*, 3027.

D. J. Armstrong, J. Kirk, K. W. F. Lam, et al., 2016. *MNRAS*, 456:2260–2272.

W. Baade & F. Zwicky, 1934. *Proceedings of the National Academy of Science*, 20:254–259.

S. Bagnulo, E. Jehin, C. Ledoux, et al., 2003. *The Messenger*, 114:10–14.

C. A. L. Bailer-Jones, J. Rybizki, M. Fouesneau, et al., 2018. *AJ*, 156:58.

P. Balanutsa, D. Denisenko, V. Lipunov, et al., 2013. *The Astronomer's Telegram*, 4837.

I. Baraffe, D. Homeier, F. Allard, et al., 2015. *A&A*, 577:A42.

K. Barbary, T. Barclay, R. Biswas, et al., 2016. "SNCosmo: Python library for supernova cosmology." Astrophysics Source Code Library.

Kyle Barbary, 2014.

T. S. Barman, P. H. Hauschildt, & F. Allard, 2004. *ApJ*, 614:338–348.

J. Barnes & D. Kasen, 2013. *ApJ*, 775:18.

T. G. Beatty, J. M. Fernández, D. W. Latham, et al., 2007. *ApJ*, 663:573–582.

R. Beck, L. Dobos, T. Budavári, et al., 2016. *MNRAS*, 460:1371–1381.

A. C. Becker, D. M. Wittman, P. C. Boeshaar, et al., 2004. *ApJ*, 611:418–433.

E. Bellm, 2014. In *The Third Hot-wiring the Transient Universe Workshop*, editors P. R. Wozniak, M. J. Graham, A. A. Mahabal, et al., pages 27–33.

C. Benn, K. Dee, & T. Agócs, 2008. In *Ground-based and Airborne Instrumentation for Astronomy II*, volume 7014 of *Proc. SPIE*, page 70146X.

O. G. Benvenuto & L. G. Althaus, 1999. *MNRAS*, 303:30–38.

E. Berger, C. N. Leibler, R. Chornock, et al., 2013. *ApJ*, 779:18.

P. Bergeron, F. Wesemael, P. Dufour, et al., 2011. *ApJ*, 737:28.

W. M. J. Best, E. A. Magnier, M. C. Liu, et al., 2018. *ApJS*, 234:1.

K. Beuermann, 2006. *A&A*, 460:783–792.

K. Beuermann, S. Dreizler, & F. V. Hessman, 2013. *A&A*, 555:A133.

L. Bianchi, A. Conti, & B Shiao, 2014. *VizieR Online Data Catalog*, 2335.

T. A. Bida, E. W. Dunham, P. Massey, et al., 2014. In *Ground-based and Airborne Instrumentation for Astronomy V*, volume 9147 of *Proc. SPIE*, page 91472N.

N. Blagorodnova, J. D. Neill, R. Walters, et al., 2018. *PASP*, 130(3):035003.

S. Bloemen, P. Groot, G. Nelemans, et al., 2015. In *Living Together: Planets, Host Stars and Binaries*, editors S. M. Rucinski, G. Torres, & M. Zejda, volume 496 of *Astronomical Society of the Pacific Conference Series*, page 254.

S. Bloemen, T. R. Marsh, P. Degroote, et al., 2012. *MNRAS*, 422:2600–2608.

S. Bloemen, T. R. Marsh, R. H. Østensen, et al., 2011. *MNRAS*, 410:1787–1796.

S. Blondin & J. L. Tonry, 2007. *ApJ*, 666:1024–1047.

J. S. Bloom, J. W. Richards, P. E. Nugent, et al., 2012. *PASP*, 124:1175.

A. Boksenberg, 1985. *Vistas in Astronomy*, 28:531–553.

H. E. Bond, L. R. Bedin, A. Z. Bonanos, et al., 2009. *ApJ*, 695:L154–L158.

M. C. P. Bours, T. R. Marsh, S. G. Parsons, et al., 2014. *MNRAS*, 438:3399–3408.

Leo Breiman, 2001. *Machine Learning*, 45(1):5–32.

M. Brescia, S. Cavuoti, & G. Longo, 2015. *MNRAS*, 450:3893–3903.

R. P. Breton, S. A. Rappaport, M. H. van Kerkwijk, et al., 2012. *ApJ*, 748:115.

H. Brink, J. W. Richards, D. Poznanski, et al., 2013. *MNRAS*, 435:1047–1060.

W. R. Brown, M. Kilic, C. Allende Prieto, et al., 2010. *ApJ*, 723:1072–1081.

E. Budding & R. Butland, 2011. *MNRAS*, 418:1764–1773.

Y. Cao, P. E. Nugent, & M. M. Kasliwal, 2016. *PASP*, 128(11):114502.

J. A. Cardelli, G. C. Clayton, & J. S. Mathis, 1989. *ApJ*, 345:245–256.

J. A. Carter, S. Rappaport, & D. Fabrycky, 2011. *ApJ*, 728:139.

S. B. Cenko, S. R. Kulkarni, A. Horesh, et al., 2013. *ApJ*, 769:130.

S. B. Cenko, A. L. Urban, D. A. Perley, et al., 2015. *ApJ*, 803:L24.

G. Chabrier, J. Gallardo, & I. Baraffe, 2007. *A&A*, 472:L17–L20.

K. C. Chambers, E. A. Magnier, N. Metcalfe, et al., 2016. *ArXiv e-prints*.

T. Chen & C. Guestrin, 2016. *ArXiv e-prints*.

X. Chen, P. F. L. Maxted, J. Li, et al., 2017. *MNRAS*, 467:1874–1889.

A. Claret, 2004. *A&A*, 424:919–925.

A. Claret & S. Bloemen, 2011. *A&A*, 529:A75.

S. A. Colgate & R. H. White, 1966. *ApJ*, 143:626.

J. J. Condon, W. D. Cotton, E. W. Greisen, et al., 1998. *AJ*, 115:1693–1716.

D. L. Coppejans, P. A. Woudt, B. Warner, et al., 2014. *MNRAS*, 437:510–523.

C. M. Copperwheat, T. R. Marsh, V. S. Dhillon, et al., 2010. *MNRAS*, 402:1824–1840.

C. M. Copperwheat, T. R. Marsh, S. P. Littlefair, et al., 2011. *MNRAS*, 410:1113–1129.

A. H. Córsico & L. G. Althaus, 2014. *A&A*, 569:A106.

A. H. Córsico & L. G. Althaus, 2016. *A&A*, 585:A1.

A. H. Córsico, L. G. Althaus, A. M. Serenelli, et al., 2016. *A&A*, 588:A74.

D. A. Coulter, R. J. Foley, C. D. Kilpatrick, et al., 2017. *Science*, 358:1556–1558.

P. S. Cowperthwaite, E. Berger, A. Rest, et al., 2017a. *ArXiv e-prints*.

P. S. Cowperthwaite, E. Berger, V. A. Villar, et al., 2017b. *ApJ*, 848:L17.

R. M. Cutri, M. F. Skrutskie, S. van Dyk, et al., 2003. *VizieR Online Data Catalog*, 2246.

R. D'Abrusco, F. Massaro, A. Paggi, et al., 2014. *ApJS*, 215:14.

J. R. A. Davenport, A. C. Becker, A. F. Kowalski, et al., 2012. *ApJ*, 748:58.

P. J. Davis, U. Kolb, B. Willems, et al., 2008. *MNRAS*, 389:1563–1576.

J. Debosscher, 2009. *Automated Classification of variable stars: Application to the OGLE and CoRoT databases*. Ph.D. thesis, Institute of Astronomy, Katholieke Universiteit Leuven, Belgium.

D. Denisenko, V. Lipunov, N. Tiurina, et al., 2012. *The Astronomer's Telegram*, 4324:1.

A. Derekas, P. Németh, J. Southworth, et al., 2015. *ApJ*, 808:179.

J. Devor, 2005. *ApJ*, 628:411–425.

V. S. Dhillon, T. R. Marsh, M. J. Stevenson, et al., 2007. *MNRAS*, 378:825–840.

M. C. Díaz, L. M. Macri, D. Garcia Lambas, et al., 2017. *ApJ*, 848:L29.

S. G. Djorgovski, A. J. Drake, A. A. Mahabal, et al., 2011. *ArXiv e-prints*.

Pieter G. van Dokkum, 2001. *Publ.Astron.Soc.Pac.*, 113:1420–1427.

A. J. Drake, S. G. Djorgovski, A. Mahabal, et al., 2009. *ApJ*, 696:870–884.

A. J. Drake, S. G. Djorgovski, A. Mahabal, et al., 2010a. *Central Bureau Electronic Telegrams*, 2601.

A. J. Drake, S. G. Djorgovski, A. A. Mahabal, et al., 2010b. *The Astronomer's Telegram*, 3081.

A. J. Drake, B. T. Gänsicke, S. G. Djorgovski, et al., 2014. *MNRAS*, 441:1186–1200.

T. Driebe, D. Schoenberner, T. Bloecker, et al., 1998. *A&A*, 339:123–133.

M. R. Drout, R. Chornock, A. M. Soderberg, et al., 2014. *ApJ*, 794:23.

M. R. Drout, A. L. Piro, B. J. Shappee, et al., 2017. *Science*, 358:1570–1574.

A. Duquennoy & M. Mayor, 1991. *A&A*, 248:485–524.

J. Eastman, R. Siverd, & B. S. Gaudi, 2010. *PASP*, 122:935–946.

P. A. Evans, S. B. Cenko, J. A. Kennea, et al., 2017. *Science*, 358:1565–1570.

S. M. Faber, A. C. Phillips, R. I. Kibrick, et al., 2003. In *Instrument Design and Performance for Optical/Infrared Ground-based Telescopes*, editors M. Iye & A. F. M. Moorwood, volume 4841 of *Proc. SPIE*, pages 1657–1669.

S. Faigler, I. Kull, T. Mazeh, et al., 2015. *ApJ*, 815:26.

Ye Fan et al., 445. *Book of the Later Han*.

E. D. Feigelson & G. J. Babu, 2012. *Modern Statistical Methods for Astronomy*.

W. J. Feline, V. S. Dhillon, T. R. Marsh, et al., 2004. *MNRAS*, 355:1–10.

A. V. Filippenko, 1997. *ARA&A*, 35:309–355.

A. V. Filippenko, M. W. Richmond, D. Branch, et al., 1992a. *AJ*, 104:1543–1556.

A. V. Filippenko, M. W. Richmond, T. Matheson, et al., 1992b. *ApJ*, 384:L15–L18.

R.A. Fisher, 1934. *Statistical Methods for Research Workers*. 5 edition.

E. L. Fitzpatrick, 1999. *PASP*, 111:63–75.

H. A. Flewelling, E. A. Magnier, K. C. Chambers, et al., 2016. *ArXiv e-prints*.

W. Fong, E. Berger, R. Margutti, et al., 2015. *ApJ*, 815:102.

G. Fontaine, P. Brassard, & P. Bergeron, 2001. *PASP*, 113:409–435.

D. Foreman-Mackey, D. W. Hogg, D. Lang, et al., 2013. *PASP*, 125:306–312.

Dan Foreman-Mackey, 2013. "Example: Fitting a Model to Data." `http://dan.iel.fm/emcee/current/user/line/#maximum-likelihood-estimation`. [Online; accessed 15-September-2017].

Dan Foreman-Mackey, 2014. "Tutorial: model fitting with correlated noise." `http://dfm.io/george/current/user/model/`. [Online; accessed 21-September-2017].

C. Frohmaier, M. Sullivan, P. E. Nugent, et al., 2017. *ApJS*, 230:4.

Gaia Collaboration, A. G. A. Brown, A. Vallenari, et al., 2018a. *A&A*, 616:A1.

Gaia Collaboration, L. Eyer, L. Rimoldini, et al., 2018b. *ArXiv e-prints*.

A. Gal-Yam, 2012. *Science*, 337:927.

T. J. Galama, P. M. Vreeswijk, J. van Paradijs, et al., 1998. *Nature*, 395:670–672.

A. Gangopadhyay, K. Misra, A. Pastorello, et al., 2018. *MNRAS*, 476:3611–3630.

B. T. Gänsicke, M. Dillon, J. Southworth, et al., 2009. *MNRAS*, 397:2170–2188.

C. F. Gauss, 1809. *Summarische Uebersicht der zur Bestimmung der Bahnen der beyden neuen Hauptplaneten angewandten Methoden*.

N. Gehrels, 1986. *ApJ*, 303:336–346.

N. Gehrels, J. K. Cannizzo, J. Kanner, et al., 2016. *ApJ*, 820:136.

R. E. Gershberg, 1972. *Ap&SS*, 19:75–92.

Pierre Geurts, Damien Ernst, & Louis Wehenkel, 2006. *Mach. Learn.*, 63(1):3–42.

S. Gezari, R. Chornock, A. Rest, et al., 2012. *Nature*, 485:217–220.

A. Gianninas, B. D. Strickland, M. Kilic, et al., 2013. *ApJ*, 766:3.

D. R. Gies, S. Dieterich, N. D. Richardson, et al., 2008. *ApJ*, 682:L117.

F. Gieseke, S. Bloemen, C. van den Bogaard, et al., 2017. *MNRAS*, 472:3101–3114.

R. L. Gilliland, P. E. Nugent, & M. M. Phillips, 1999. *ApJ*, 521:30–49.

A. Gonneau, A. Lançon, S. C. Trager, et al., 2016. *A&A*, 589:A36.

O. Graur, S. A. Rodney, D. Maoz, et al., 2014. *ApJ*, 783:28.

O. Gress, V. Vladimirov, V. Lipunov, et al., 2015a. *The Astronomer's Telegram*, 8013.

O. Gress, V. Vladimirov, E. Popova, et al., 2015b. *The Astronomer's Telegram*, 7410.

Z. Guo, D. R. Gies, R. A. Matson, et al., 2017. *ApJ*, 837:114.

J. Guy, P. Astier, S. Baumont, et al., 2007. *A&A*, 466:11–21.

A. A. Hakobyan, G. A. Mamon, A. R. Petrosian, et al., 2009. *A&A*, 508:1259–1268.

H. C. Harris, C. C. Dahn, J. P. Subasavage, et al., 2018. *AJ*, 155:252.

T. E. Harrison, J. J. Johnson, B. E. McArthur, et al., 2004. *AJ*, 127:460–468.

J. D. Hartman & G. Á. Bakos, 2016. *Astronomy and Computing*, 17:1–72.

S. L. Hawley, J. R. A. Davenport, A. F. Kowalski, et al., 2014. *ApJ*, 797:121.

J. F. W. Herschel, Sir, 1847. *Results of astronomical observations made during the years 1834, 5, 6, 7, 8, at the Cape of Good Hope; being the completion of a telescopic survey of the whole surface of the visible heavens, commenced in 1825*.

E. Hertzsprung, 1911. *Publikationen des Astrophysikalischen Observatoriums zu Potsdam*, 63.

E. J. Hilton, 2011. *The Galactic M Dwarf Flare Rate*. Ph.D. thesis, University of Washington.

E. J. Hilton, A. A. West, S. L. Hawley, et al., 2010. *AJ*, 140:1402–1413.

Anna Y. Q. Ho, S. R. Kulkarni, Peter E. Nugent, et al., 2018. *The Astrophysical Journal Letters*, 854(1):L13.

D. W. Hogg, J. Bovy, & D. Lang, 2010. *ArXiv e-prints*.

K. Horne & D. P. Schneider, 1989. *ApJ*, 343:888–901.

S. B. Howell, L. A. Nelson, & S. Rappaport, 2001. *ApJ*, 550:897–918.

E. Y. Hsiao, A. Conley, D. A. Howell, et al., 2007. *ApJ*, 663:1187–1200.

L. Hu, X. Wu, I. Andreoni, et al., 2017. *Science Bulletin, Vol. 62, No.21, p.1433-1438, 2017*, 62:1433–1438.

E. Hubble, 1949. *PASP*, 61:121.

M. Huber, K. C. Chambers, H. Flewelling, et al., 2015. *The Astronomer's Telegram*, 7153.

John P. Huchra, Lucas M. Macri, Karen L. Masters, et al., 2012. *The Astrophysical Journal Supplement Series*, 199:26.

R. A. Hulse & J. H. Taylor, 1975. *ApJ*, 195:L51–L53.

A. G. Istrate, G. Fontaine, A. Gianninas, et al., 2016a. *A&A*, 595:L12.

A. G. Istrate, G. Fontaine, & C. Heuser, 2017. *ApJ*, 847:130.

A. G. Istrate, P. Marchant, T. M. Tauris, et al., 2016b. *A&A*, 595:A35.

A. G. Istrate, T. M. Tauris, & N. Langer, 2014a. *A&A*, 571:A45.

A. G. Istrate, T. M. Tauris, N. Langer, et al., 2014b. *A&A*, 571:L3.

N. Ivanova, S. Justham, X. Chen, et al., 2013. *A&A Rev.*, 21:59.

Ž. Ivezić, J. A. Tyson, E. Acosta, et al., 2008.

Ž. Ivezić, A.J. Connolly, J.T. Vanderplas, et al., 2014. *Statistics, Data Mining and Machine Learning in Astronomy*. Princeton University Press.

M. Jurić, Ž. Ivezić, A. Brooks, et al., 2008. *ApJ*, 673:864–914.

J. Kaluzny, S. M. Rucinski, I. B. Thompson, et al., 2007. *AJ*, 133:2457–2463.

D. Kasen, R. Fernández, & B. D. Metzger, 2015. *MNRAS*, 450:1777–1786.

D. Kasen, B. Metzger, J. Barnes, et al., 2017. *Nature*, 551:80–84.

A. Kashi & N. Soker, 2016. *Research in Astronomy and Astrophysics*, 16:99.

M. M. Kasliwal, 2011. *Bridging the gap : elusive explosions in the local universe*. Ph.D. thesis, California Institute of Technology.

M. M. Kasliwal, S. R. Kulkarni, A. Gal-Yam, et al., 2012. *ApJ*, 755:161.

M. M. Kasliwal, E. Nakar, L. P. Singer, et al., 2017. *Science*, 358:1559–1565.

T. Kato, A. Imada, M. Uemura, et al., 2009. *PASJ*, 61:S395–S616.

J. Kepler, 1619. *Ioannis Keppleri harmonices mundi libri V : quorum primus harmonicus ... quartus metaphysicus, psychologicus et astrologicus geometricus ... secundus architectonicus ... tertius proprie ... quintus astronomicus & metaphysicus ... : appendix habet comparationem huius*

operis cum harmonices Cl. Ptolemaei libro III cumque Roberti de Fluctibus ... speculationibus harmonicis, operi de macrocosmo & microcosmo insertis.

Johannes Kepler, 1606. *De stella nova in pede serpentarii, et qui sub eius exortum de novo iniit, Trigono igneo.* Impens. authoris.

P. Kervella & P. Fouqué, 2008. *A&A*, 491:855–858.

C. Knigge, 2006. *MNRAS*, 373:484–502.

Christian Knigge, Isabelle Baraffe, & Joseph Patterson, 2011. *Astrophys.J.Suppl.*, 194:28.

C. S. Kochanek, 2016. *MNRAS*, 461:371–384.

D. Koester, R. Napiwotzki, N. Christlieb, et al., 2001. *A&A*, 378:556–568.

G. Kovács, S. Zucker, & T. Mazeh, 2002. *A&A*, 391:369–377.

A. F. Kowalski, S. L. Hawley, E. J. Hilton, et al., 2009. *AJ*, 138:633–648.

A. F. Kowalski, S. L. Hawley, J. A. Holtzman, et al., 2010. *ApJ*, 714:L98–L102.

Pavel Kroupa & Monika G Petr-Gotzens, 2011. *Astronomy & Astrophysics*, 529:A92.

S. R. Kulkarni, 2005. *ArXiv Astrophysics e-prints.*

S. R. Kulkarni & A. Rau, 2006. *ApJ*, 644:L63–L66.

S. S. Kumar, 1962. *AJ*, 67:579.

T. Kupfer, S. Geier, U. Heber, et al., 2015. *A&A*, 576:A44.

C. J. Lada, 2006. *ApJ*, 640:L63–L66.

R. R. Laher, J. Surace, C. J. Grillmair, et al., 2014. *PASP*, 126:674–710.

N. M. Law, S. R. Kulkarni, R. G. Dekany, et al., 2009a. *PASP*, 121:1395.

N. M. Law, S. R. Kulkarni, R. G. Dekany, et al., 2009b. *PASP*, 121:1395–1408.

R. Leach, F. V. Hessman, A. R. King, et al., 1999. *MNRAS*, 305:225–230.

Yann LeCun, Yoshua Bengio, & Geoffrey E. Hinton, 2015. *Nature*, 521(7553):436–444.

J. W. Lee, S.-L. Kim, K. Hong, et al., 2016. *AJ*, 151:25.

A. M. Legendre, 1806. *Nouvelles Methodes pour la determination des Orbites des Cometes.*

H. Lehmann, J. Southworth, A. Tkachenko, et al., 2013. *A&A*, 557:A79.

L.-X. Li & B. Paczyński, 1998. *ApJ*, 507:L59–L62.

W. Li, J. Leaman, R. Chornock, et al., 2011. *MNRAS*, 412:1441–1472.

LIGO Scientific Collaboration, J. Aasi, B. P. Abbott, et al., 2015. *Classical and Quantum Gravity*, 32(7):074001.

J. Lin, S. Rappaport, P. Podsiadlowski, et al., 2011. *ApJ*, 732:70.

V. Lipunov, V. Kornilov, E. Gorbovskoy, et al., 2018. *New A*, 63:48–60.

V. M. Lipunov, V. G. Kornilov, A. V. Krylov, et al., 2007. *Astronomy Reports*, 51:1004–1025.

N. R. Lomb, 1976. *Ap&SS*, 39:447–462.

M. López-Morales, 2007. *ApJ*, 660:732–739.

C. Mackenzie, K. Pichara, & P. Protopapas, 2016. *ApJ*, 820:138.

K. Maguire, M. Sullivan, R. S. Ellis, et al., 2012. *MNRAS*, 426:2359–2379.

K. S. Mandel, D. M. Scolnic, H. Shariff, et al., 2017. *ApJ*, 842:93.

T. R. Marsh, V. S. Dhillon, & S. R. Duck, 1995. *MNRAS*, 275:828.

T. R. Marsh, S. G. Parsons, M. C. P. Bours, et al., 2014. *MNRAS*, 437:475–488.

F Masci & E Bellm, 2016. "PTF light curve statistics." `http://www.ptf.caltech.edu/system/media_files/binaries/30/original/Objects_SourcesTable_cols_v3.html`. [Online; date

2016-08-26].
F. J. Masci, D. I. Hoffman, C. J. Grillmair, et al., 2014. *AJ*, 148:21.
R. A. Matson, D. R. Gies, Z. Guo, et al., 2015. *ApJ*, 806:155.
P. F. L. Maxted, 2016. *A&A*, 591:A111.
P. F. L. Maxted, D. R. Anderson, M. R. Burleigh, et al., 2011. *MNRAS*, 418:1156–1164.
P. F. L. Maxted, S. Bloemen, U. Heber, et al., 2014a. *MNRAS*, 437:1681–1697.
P. F. L. Maxted, A. M. Serenelli, T. R. Marsh, et al., 2014b. *MNRAS*, 444:208–216.
P. F. L. Maxted, A. M. Serenelli, A. Miglio, et al., 2013. *Nature*, 498:463–465.
M. J. McAllister, S. P. Littlefair, V. S. Dhillon, et al., 2017. *MNRAS*, 464:1353–1364.
B. D. Metzger, A. Arcones, E. Quataert, et al., 2010. *MNRAS*, 402:2771–2777.
B. D. Metzger & R. Fernández, 2014. *MNRAS*, 441:3444–3453.
A. M. Mickaelian, L. R. Hovhannisyan, D. Engels, et al., 2006. *A&A*, 449:425–433.
A. A. Miller, M. K. Kulkarni, Y. Cao, et al., 2017. *AJ*, 153:73.
A. F. J. Moffat, 1969. *A&A*, 3:455.
A. Morales-Garoffolo, N. Elias-Rosa, S. Benetti, et al., 2014. *MNRAS*, 445:1647–1662.
A. Morales-Garoffolo, N. Elias-Rosa, M. Bersten, et al., 2015. *MNRAS*, 454:95–114.
Andreas C. Müller & Sarah Guido, 2016. *Introduction to Machine Learning with Python*. O'Reilly.
E. Nakar & R. Sari, 2010. *ApJ*, 725:904–921.
S. V. Nefs, J. L. Birkby, I. A. G. Snellen, et al., 2013. *MNRAS*, 431:3240–3257.
G. Nelemans, L. R. Yungelson, & S. F. Portegies Zwart, 2004. *MNRAS*, 349:181–192.
I. Newton, 1687. *Philosophiae Naturalis Principia Mathematica. Auctore Js. Newton.*
M. Nicholl & S. J. Smartt, 2016. *MNRAS*, 457:L79–L83.
P. Nugent, A. Kim, & S. Perlmutter, 2002. *PASP*, 114:803–819.
P. Ochner, S. Benetti, E. Cappellaro, et al., 2015. *The Astronomer's Telegram*, 7877:1.
J. B. Oke, J. G. Cohen, M. Carr, et al., 1995. *PASP*, 107:375.
J. B. Oke & J. E. Gunn, 1982. *PASP*, 94:586.
A. S. Oliveira, C. V. Rodrigues, D. Cieslinski, et al., 2017. *AJ*, 153:144.
Y. Osaki & T. Kato, 2013. *PASJ*, 65:50.
B. Paczyński, 1971. *ARA&A*, 9:183.
B. Paczynski, 1976. In *Structure and Evolution of Close Binary Systems*, editors P. Eggleton, S. Mitton, & J. Whelan, volume 73 of *IAU Symposium*, page 75.
B. E. J. Pagel, 1986. *QJRAS*, 27:432.
A. F. Pala, B. T. Gänsicke, D. Townsley, et al., 2017. *MNRAS*, 466:2855–2878.
L. Palaversa, Ž. Ivezić, L. Eyer, et al., 2013. *AJ*, 146:101.
Y.-C. Pan, M. Sullivan, K. Maguire, et al., 2014. *MNRAS*, 438:1391–1416.
J. A. Panei, L. G. Althaus, X. Chen, et al., 2007. *MNRAS*, 382:779–792.
S. Papadogiannakis, R. Ferretti, C. Fremling, et al., 2015. *The Astronomer's Telegram*, 8080.
S. G. Parsons, C. Agurto-Gangas, B. T. Gänsicke, et al., 2015. *MNRAS*, 449:2194–2204.
S. G. Parsons, B. T. Gänsicke, T. R. Marsh, et al., 2012a. *MNRAS*, 426:1950–1958.
S. G. Parsons, C. A. Hill, T. R. Marsh, et al., 2016. *MNRAS*, 458:2793–2812.
S. G. Parsons, T. R. Marsh, C. M. Copperwheat, et al., 2010a. *MNRAS*, 407:2362–2382.
S. G. Parsons, T. R. Marsh, C. M. Copperwheat, et al., 2010b. *MNRAS*, 402:2591–2608.

S. G. Parsons, T. R. Marsh, B. T. Gänsicke, et al., 2011. *ApJ*, 735:L30.
S. G. Parsons, T. R. Marsh, B. T. Gänsicke, et al., 2012b. *MNRAS*, 420:3281–3297.
S. G. Parsons, T. R. Marsh, B. T. Gänsicke, et al., 2012c. *MNRAS*, 419:304–313.
G. Paturel, C. Petit, P. Prugniel, et al., 2003. *A&A*, 412:45–55.
E.-M. Pauli, R. Napiwotzki, U. Heber, et al., 2006. *A&A*, 447:173–184.
M. J. Pecaut & E. E. Mamajek, 2013. *ApJS*, 208:9.
F. Pedregosa, G. Varoquaux, A. Gramfort, et al., 2011. *Journal of Machine Learning Research*, 12:2825–2830.
C. M. Peters, G. T. Richards, A. D. Myers, et al., 2015. *ApJ*, 811:95.
P. C. Peters, 1964. *Physical Review*, 136:1224–1232.
P. C. Peters & J. Mathews, 1963. *Physical Review*, 131:435–440.
T. Petrushevska, R. Ferretti, C. Fremling, et al., 2015a. *The Astronomer's Telegram*, 8130.
T. Petrushevska, R. Ferretti, C. Fremling, et al., 2015b. *The Astronomer's Telegram*, 8131.
B. R. Pettersen, 1989. *Sol. Phys.*, 121:299–312.
M. M. Phillips, 1993. *ApJ*, 413:L105–L108.
E. Pian, P. D'Avanzo, S. Benetti, et al., 2017. *Nature*, 551:67–70.
A. J. Pickles, 1998. *PASP*, 110:863–878.
G. Pietrzyński, I. B. Thompson, W. Gieren, et al., 2012. *Nature*, 484:75–77.
T. Piran, 1999. *Phys. Rep.*, 314:575–667.
D. L. Pollacco, I. Skillen, A. Collier Cameron, et al., 2006. *PASP*, 118:1407–1418.
A. S. Pozanenko, M. V. Barkov, P. Y. Minaev, et al., 2018. *ApJ*, 852:L30.
M. L. Pretorius & C. Knigge, 2012. *MNRAS*, 419:1442–1454.
S. Pyrzas, B. T. Gänsicke, S. Brady, et al., 2012. *MNRAS*, 419:817–826.
R. M. Quimby, S. R. Kulkarni, M. M. Kasliwal, et al., 2011. *Nature*, 474:487–489.
A. S. Rajpurohit, C. Reylé, F. Allard, et al., 2013. *A&A*, 556:A15.
S. Rappaport, L. Nelson, A. Levine, et al., 2015. *ApJ*, 803:82.
S. Rappaport, P. Podsiadlowski, & I. Horev, 2009. *ApJ*, 698:666–675.
S. Rappaport, F. Verbunt, & P. C. Joss, 1983. *ApJ*, 275:713–731.
A. Rau, S. R. Kulkarni, N. M. Law, et al., 2009a. *PASP*, 121:1334.
A. Rau, S. R. Kulkarni, N. M. Law, et al., 2009b. *PASP*, 121:1334–1351.
A. Rau, E. O. Ofek, S. R. Kulkarni, et al., 2008. *ApJ*, 682:1205–1216.
H. Rauer, C. Catala, C. Aerts, et al., 2014. *Experimental Astronomy*, 38(1):249–330.
A. Rebassa-Mansergas, B. T. Gänsicke, P. Rodríguez-Gil, et al., 2007. *MNRAS*, 382:1377–1393.
M. J. Rees, 1988. *Nature*, 333:523–528.
I. Ribas, 2006. *Ap&SS*, 304:89–92.
J. W. Richards, D. L. Starr, H. Brink, et al., 2012. *ApJ*, 744:192.
J. W. Richards, D. L. Starr, N. R. Butler, et al., 2011. *ApJ*, 733:10.
M. W. Richmond, R. R. Treffers, A. V. Filippenko, et al., 1994. *AJ*, 107:1022–1040.
G. R. Ricker, J. N. Winn, R. Vanderspek, et al., 2015. *Journal of Astronomical Telescopes, Instruments, and Systems*, 1(1):014003.
A. G. Riess, A. V. Filippenko, P. Challis, et al., 1998. *AJ*, 116:1009–1038.
H. Ritter & U. Kolb, 2003. *A&A*, 404:301–303.

H. Ritter, Z.-Y. Zhang, & U. Kolb, 2000. *A&A*, 360:959–990.
L. F. Roberts, D. Kasen, W. H. Lee, et al., 2011. *ApJ*, 736:L21.
E. Roche, 1859. *Annales de l'Observatoire de Paris*, 5:353–393.
S. Rosswog, U. Feindt, O. Korobkin, et al., 2017. *Classical and Quantum Gravity*, 34(10):104001.
H. N. Russell, 1914. *Popular Astronomy*, 22:275–294.
E. S. Rykoff, F. Aharonian, C. W. Akerlof, et al., 2005. *ApJ*, 631:1032–1038.
E. E. Salpeter, 1955. *ApJ*, 121:161.
J. D. Scargle, 1982. *ApJ*, 263:835–853.
E. F. Schlafly & D. P. Finkbeiner, 2011. *ApJ*, 737:103.
D. J. Schlegel, D. P. Finkbeiner, & M. Davis, 1998. *ApJ*, 500:525–553.
S. J. Schmidt, J. L. Prieto, K. Z. Stanek, et al., 2014. *ApJ*, 781:L24.
M. R. Schreiber, B. T. Gänsicke, A. Rebassa-Mansergas, et al., 2010. *A&A*, 513:L7.
A. Schwarzenberg-Czerny, 1989. *MNRAS*, 241:153–165.
SDSS Collaboration, F. D. Albareti, C. Allende Prieto, et al., 2016. *ArXiv e-prints*.
N. J. Secrest, R. P. Dudik, B. N. Dorland, et al., 2015. *ApJS*, 221:12.
B. Sesar, N. Hernitschek, S. Mitrović, et al., 2017. *AJ*, 153:204.
B. J. Shappee, J. D. Simon, M. R. Drout, et al., 2017. *Science*, 358:1574–1578.
J. Shears, S. Brady, B. Gaensicke, et al., 2009. *Journal of the British Astronomical Association*, 119:144–148.
S. M. Silverberg, A. F. Kowalski, J. R. A. Davenport, et al., 2016. *ApJ*, 829:129.
J. M. Silverman, P. E. Nugent, A. Gal-Yam, et al., 2013. *ApJS*, 207:3.
L. P. Singer, M. M. Kasliwal, S. B. Cenko, et al., 2015. *ApJ*, 806:52.
M. F. Skrutskie, R. M. Cutri, R. Stiening, et al., 2006. *AJ*, 131:1163–1183.
R. L. Smart & L. Nicastro, 2013. *VizieR Online Data Catalog*, 1324.
S. J. Smartt, 2009. *ARA&A*, 47:63–106.
S. J. Smartt, T.-W. Chen, A. Jerkstrand, et al., 2017. *Nature*, 551:75–79.
A. M. Smith, S. Lynn, M. Sullivan, et al., 2011. *MNRAS*, 412:1309–1319.
K. W. Smith, D. Wright, S. J. Smartt, et al., 2015. *The Astronomer's Telegram*, 8258.
N. Soker & R. Tylenda, 2003. *ApJ*, 582:L105–L108.
F. Spada, P. Demarque, Y.-C. Kim, et al., 2017. *ApJ*, 838:161.
D Steeghs & D Galloway, 2017. "Gravitational wave Optical Transient Observatory." `https://www2.warwick.ac.uk/fac/sci/physics/research/astro/research/goto/`. [Online; accessed 20-September-2017].
R. Stehle, H. Ritter, & U. Kolb, 1996. *MNRAS*, 279:581–590.
P. B. Stetson, 1996. *PASP*, 108:851.
A. V. Sweigart & P. G. Gross, 1978. *ApJS*, 36:405–437.
P. Szkody, M. E. Everett, S. B. Howell, et al., 2014. *AJ*, 148:63.
R. E. Taam & P. M. Ricker, 2010. *New A Rev.*, 54:65–71.
R. E. Taam & E. L. Sandquist, 2000. *ARA&A*, 38:113–141.
F. Taddia, R. Ferretti, C. Fremling, et al., 2015. *The Astronomer's Telegram*, 8067.
L. Tal-Or, T. Mazeh, R. Alonso, et al., 2013. *A&A*, 553:A30.
M. Tanaka & K. Hotokezaka, 2013. *ApJ*, 775:113.

M. Tanaka, N. Tominaga, T. Morokuma, et al., 2016. *ApJ*, 819:5.
N. R. Tanvir, A. J. Levan, C. González-Fernández, et al., 2017. *ApJ*, 848:L27.
S. Taubenberger, 2017. *ArXiv e-prints*.
D. M. Townsley & B. T. Gänsicke, 2009. *ApJ*, 693:1007–1021.
E. Troja, L. Piro, H. van Eerten, et al., 2017. *Nature*, 551:71–74.
R. Tylenda, M. Hajduk, T. Kamiński, et al., 2011. *A&A*, 528:A114.
Y. Utsumi, M. Tanaka, N. Tominaga, et al., 2017. *PASJ*, 69:101.
Y. Utsumi, N. Tominaga, M. Tanaka, et al., 2018. *PASJ*, 70:1.
S. Valenti, David, J. Sand, et al., 2017. *ApJ*, 848:L24.
P. G. van Dokkum, 2001. *PASP*, 113:1420–1427.
T. Van Doorsselaere, H. Shariati, & J. Debosscher, 2017. *ApJS*, 232:26.
S. D. Van Dyk, W. Zheng, O. D. Fox, et al., 2014. *AJ*, 147:37.
M. H. van Kerkwijk, C. G. Bassa, B. A. Jacoby, et al., 2005. In *Binary Radio Pulsars*, editors F. A. Rasio & I. H. Stairs, volume 328 of *Astronomical Society of the Pacific Conference Series*, page 357.
M. H. van Kerkwijk, S. A. Rappaport, R. P. Breton, et al., 2010. *ApJ*, 715:51–58.
J. van Roestel, P.J. Groot, et al., 2018. *MNRAS*.
S. van Velzen, G. R. Farrar, S. Gezari, et al., 2011. *ApJ*, 741:73.
J. T. VanderPlas & Z. Ivezic, 2015. *ArXiv e-prints*.
J. T. VanderPlas & Ž. Ivezić, 2015. *ApJ*, 812:18.
K. Verbeek, P. J. Groot, S. Scaringi, et al., 2014. *MNRAS*, 438:2–13.
F. Verbunt & S. Rappaport, 1988. *ApJ*, 332:193–198.
K. Vida, Z. Kővári, A. Pál, et al., 2017. *ApJ*, 841:124.
V. A. Villar, J. Guillochon, E. Berger, et al., 2017. *ApJ*, 851:L21.
H. von Zeipel, 1924. *MNRAS*, 84:665–683.
R. A. Wade & K. Horne, 1988. *ApJ*, 324:411–430.
J. V. Wall & C. R. Jenkins, 2012. *Practical Statistics for Astronomers*.
B. Warner, 1976. In *Structure and Evolution of Close Binary Systems*, editors P. Eggleton, S. Mitton, & J. Whelan, volume 73 of *IAU Symposium*, page 85.
B. Warner, 1987. *MNRAS*, 227:23–73.
B. Warner, 2003. *Cataclysmic Variable Stars*.
E. Waxman, P. Mészáros, & S. Campana, 2007. *ApJ*, 667:351–357.
R. F. Webbink, 1984. *ApJ*, 277:355–360.
R. F. Webbink, 2008. In *Astrophysics and Space Science Library*, editors E. F. Milone, D. A. Leahy, & D. W. Hobill, volume 352 of *Astrophysics and Space Science Library*, page 233.
P. Westera, T. Lejeune, R. Buser, et al., 2002. *A&A*, 381:524–538.
P. J. Wheatley, R. G. West, M. R. Goad, et al., 2017. *ArXiv e-prints*.
D. M. Wittman, J. A. Tyson, I. P. Dell'Antonio, et al., 2002. In *Survey and Other Telescope Technologies and Discoveries*, editors J. A. Tyson & S. Wolff, volume 4836 of *Proc. SPIE*, pages 73–82.
M. A. Wood, 1995. In *White Dwarfs*, editors D. Koester & K. Werner, volume 443 of *Lecture Notes in Physics, Berlin Springer Verlag*, page 41.

E. L. Wright, P. R. M. Eisenhardt, A. K. Mainzer, et al., 2010. *AJ*, 140:1868-1881.

Huan Yang, Sangeeta Malhotra, James E. Rhoads, et al., 2017. *ApJ*, 847:38.

N. Yasuda, M. Fukugita, V. K. Narayanan, et al., 2001. *AJ*, 122:1104–1124.

H. B. Yuan, X. W. Liu, & M. S. Xiang, 2013. *MNRAS*, 430:2188–2199.

N. Zacharias, C. Finch, & J. Frouard, 2017. *VizieR Online Data Catalog*, 1340.

N. Zacharias, D. G. Monet, S. E. Levine, et al., 2004. In *American Astronomical Society Meeting Abstracts*, volume 36 of *Bulletin of the American Astronomical Society*, page 1418.

B. Zackay, E. O. Ofek, & A. Gal-Yam, 2016. *ApJ*, 830:27.

J.-P. Zahn, 1977. *A&A*, 57:383–394.

G. Zhou, D. Bayliss, J. D. Hartman, et al., 2014. *MNRAS*, 437:2831–2844.

M. Zorotovic, M. R. Schreiber, S. G. Parsons, et al., 2016. *MNRAS*, 457:3867–3877.

Summary

In this thesis, I have used the Palomar Transient Factory (PTF) to explore the optical variable sky. PTF uses an automated, wide field-of-view telescope to automatically take images of the night sky. By analysing the images in detail, regular and irregular variable astrophysical objects can be found and studied in more detail. This thesis consists of two parts; the first describes the search for fast astrophysical transient events with the PTF-Sky2Night project, the second part focuses on eclipsing binary stars found in the PTF data.

The motivation for the Sky2Night project was twofold. The first is exploration: with automated survey telescopes, many new types of transients have been discovered. These new transients were typically visible for a few weeks. One goal of the Sky2Night projects was to determine if there are also unknown types of transients which are visible for only a few hours. The second motivation was the prospect of finding kilonovae, the optical transient caused by two merging neutron stars. Merging neutron stars emit gravitational waves, which can be detected by gravitational wave observatories (aLIGO & Virgo). However, when aLIGO & Virgo detect the gravitational waves emitted by a binary neutron star merger, they can only give a rough indication were this merger occurred in the sky. Therefore, if we want to find the kilonova, a large area needs to be searched to find it. Such a large area contains many other transients besides the kilonovae. The second goal of the Sky2Night project is to determine what these other transients are and how to recognise them.

The second part of this thesis focusses on eclipsing binary stars. The majority of stars have a nearby companion, which can significantly influence their evolution. If the stars are close enough, mass can be transferred from one star to the other. Mass transfer can change the structure of the stars and also shorten or widen the orbit of the two stars. Many transients are the result of binary star evolution (either the mass-transfer process or the drastically altered structure of the star) and therefore understanding binary stars is important to understand transients. Eclipsing binary stars (were star move in front of each other periodically) are especially useful because the eclipse allows the determination of the masses and radii of both stars. The last two chapters of this thesis present the study of two types of binary stars which have already undergone a phase of mass transfer.

Transients

Chapter 2 describes the Sky2Night-I project, a search for fast optical transients. I used the PTF to monitor 400 square degrees every 2 hours and systematically searched the images for transients. Transients were followed up as fast as possible with the WHT to classify them. I used this data to calculate the observational rates of many common transients: thermonuclear supernovae and core-collapse supernovae, and also of Galactic transients; outbursting Cataclysmic Variables and flaring stars. No fast optical transients were found during the search, so an upper-limit on the rate of fast transients is calculated. I determined that the most important false positives in kilonovae searches are Cataclysmic Variables for which the quiescent counterpart is not detected.

Chapter 3 continues the Sky2Night project with additional campaigns at lower Galactic latitudes. I used a similar setup as the Sky2Night-I campaign; an area on the sky is observed by the Palomar Transient Factory at a high cadence while another telescope is used to obtain spectra of the transients as fast as possible. Two campaigns were performed; one in 2015, aimed at Galactic latitudes of $10^\circ < |b| < 30^\circ$ with the Isaac Newton Telescope as the follow-up telescope, and the other in 2016 aimed at the Galactic plane ($0^\circ < |b| < 25^\circ$), with the Hale telescope as the follow-up telescope. The survey revealed many of the usual transients; supernovae, Cataclysmic Variables and a few flare stars. But a few unusual transients were also found; two fast-rising supernovae and a re-brightening supernova. At the lowest Galactic latitudes, the vast majority of the transients were Cataclysmic Variables, but we also found a few supernovae and flares. The conclusion of Sky2Night-II projects is that there is no population of unknown fast transients at low galactic latitudes. In addition, we conclude false positives in kilonova searches are not a major problem even at low galactic latitudes and do not prohibit the search for kilonovae close to the Galactic plane.

Eclipsing binary stars

Chapter 4 presents the find of a short period (2.5 h) eclipsing white dwarf red dwarf binary. This type of binary star system is a precursor to a Cataclysmic Variables. An interesting feature of Cataclysmic Variables is that there is a lack of systems with periods between 2 and 3 hours. It is suggested that Cataclysmic Variables 'turn off' if their orbital period becomes less than three hours and turn on again at an orbital period of 2 hours. I used high cadence photometry and spectroscopy to determine the system parameters of this system. The conclusion is that it is unlikely to be a Cataclysmic Variable that has turned off, but instead was 'born' as we see it today.

In the last Chapter, I present a study of 'EL CVn' binaries, eclipsing pre-He-WD–dA binaries, found in PTF data. EL CVn binaries show very shallows eclipses which means they are not easy to recognise in the PTF data. To solve this needle-in-a-haystack problem, I used a machine-learning algorithm to sift through the PTF data in order to identify promising candidates. This resulted in the discovery of 36 new EL CVn binaries, more than doubled number of known EL CVn systems. I used radial velocity measurements to confirm that these systems contain a low-mass white dwarf. The conclusions are that EL CVn systems are relatively common, and have been hiding in plain

sight. The measured radii and temperatures of the pre-He-WDs, and orbital period are consistent with the model predictions.

Samenvatting

Deze thesis beschrijft een studie van de variabele sterrenhemel in optische golflengten met de Palomar Transient Factory (PTF). De PTF gebruikt een gerobotiseerde telescoop met een groot beeldveld om automatisch de sterrenhemel te fotograferen. Door de foto's in detail te analyseren kunnen zowel periodiek variable objecten als onregelmatig variable objecten gevonden worden. Het eerste deel van deze thesis beschrijft de zoektocht naar kort waarneembare optische explosies ('transients') met het 'Sky2Night' project. Het tweede deel van de thesis focust op eclipserende dubbelsterren die gevonden zijn met de PTF.

De motivatie van het Sky2Night project is tweevoudig. Robotische telescopen hebben de afgelopen jaren de sterrenhemel systematisch onderzocht op zoek naar optische explosies die zichtbaar zijn op tijdschalen van weken. Met het Sky2Night project heb ik deze zoektocht uitgebreid naar een tijdschaal van uren. De tweede motivatie is het vooruitzicht van het vinden van kilonovae: het in het optisch waarneembare explosie die het gevolg is van een samensmelting van twee neutronensterren. Samensmeltende neutronensterren zenden ook zwaartekrachtgolven uit en zijn waarneembaar door de zwaartekrachtgolf observatoria aLIGO en Virgo. Ookal kunnen aLIGO en Virgo de extreem subtiele trillingen van zwaartekrachtgolven opvangen, zijn ze niet goed in het bepalen van de richting waaruit deze golven komen. Daarom moet een groot stuk van de hemel afgespeurd worden om de bijbehorende kilonova te vinden. In zo'n groot deel van de sterrenhemel zijn ook andere explosies te vinden die op het eerste gezicht verward kunnen worden met een kilonova. Het tweede doel van het Sky2Night project is dus om te bepalen hoe groot dit probleem is en hoe deze kilonova het makkelijkst te onderscheiden is van de andere waarneembare explosies.

Het tweede deel van deze thesis richt zich op eclipserende dubbelsterren. Het grootste deel van de sterren hebben een nabije begeleider en draaien samen rond hun gemeenschappelijke massamiddelpunt. Deze begeleider kan een grote invloed hebben op de evolutie van de ster. Als de sterren dichtbij genoeg van elkaar staan, kan er massa van de ene naar de andere ster worden overgedragen. Massa overdracht kan de structuur van de sterren veranderen en ook de baanperiode korter of langer maken. Veel van de astrofysische explosies die we waarnemen zijn het directe of indirecte gevolg van massa overdracht in dubbelster systemen. Voor het begrijpen van deze explosies is het dus nodig om dubbelsterren in detail te bestuderen. Eclipserende dubbelsterren (waar een ster elke baanperiode voor de andere langs beweegt) zijn erg nuttig omdat aan de hand

van de eclips de afmeting van beide sterren gemeten kan worden (en met radiële snelheidsmetingen ook de massa van de sterren). De laatste twee hoofdstukken beschrijven twee typen ongebruikelijke eclipserende dubbelster systemen waarbij massaoverdracht al eerder heeft plaatsgevonden.

Astrofysische explosies

Hoofdstuk 2 beschrijft het Sky2Night-I project, een zoektocht naar kortdurende explosies. Hiervoor het ik met de PTF 400 vierkante graad elke twee uur gefotografeerd en de data systematisch onderzocht naar nieuw verschenen lichtbronnen. Nieuwe bronnen zijn daarna zo snel mogelijk geobserveerd met de 4.2 m William Herschel Telescoop om een spectrum te verkrijgen en de nieuwe lichtbron te classificeren. Hiermee heb ik het aantal explosies per dag per vierkante graad bepaald van veel voorkomende explosies zoals type Ia supernova, overige supernovae, dwerg novae en 'zonnevlammen' in de atmosfeer van sterren. Er waren geen onbekende, kortdurende explosies gevonden, dus met heb ik een bovenlimiet kunnen stellen aan hoe vaak deze voorkomen. Verder heb ik vastgesteld dat voor de zoektocht naar kilonovae, dwerg novae die in rust niet waarneembaar zijn de grootste bron van verwarring zijn.

Hoofdstuk 3 gaat verder met het Sky2Night project en beschrijft twee experimenten die gericht zijn op lagere galactische breedte. De opzet van de experimenten zijn het zelf als het eerste experiment; de PTF wordt gebruikt om een groot deel van de sterrenhemel af te speuren op zoek naar explosies, terwijl een tweede telescoop wordt gebruikt om zo snel mogelijk een spectrum te verkrijgen van de nieuw ontdekte explosies. Het eerste experiment was gericht op Galactische breedte van $10° < |b| < 30°$ en het tweede experiment richtte zich op het Galactisch vlak zelf. In het eerste experiment vonden we veel van de gebruikelijke explosies; supernovae, cataclysmische variabelen en 'zonnevlammen'. Maar ook een paar uitzonderlijke explosies zijn waargenomen; twee snel helder wordende supernovae en ook een supernova die na een tijd lang zwakker te worden weer opleefde. In het experiment dat op het Galactisch vlak gericht was zijn vooral dwerg novae gevonden en enkele supernovae. De conclusie van dit onderzoek is dat er geen onbekende snelle explosies te vinden zijn in het Galactisch vlak. Het aantal gevonden dwerg novae is hoger ter vergelijking met het Sky2Night-I experiment, maar niet zo hoog dat het de zoektocht naar kilonova in het Galactisch vlak onmogelijk maakt.

Eclipserende dubbelsterren

Hoofdstuk 4 beschrijft de ontdekking en analyse van een kort periodieke eclipserende witte dwerg – rode dwerg dubbelster systeem. Dit type dubbelster is de voorloper van een cataclysmische variabelen (CVs). Een eigenschap van de populatie van CVs is dat er een tekort is aan CVs met baanperioden van tussen de 2 en 3 uur. Mogelijk is het dat als de baanperiode geleidelijk afneem van CVs, ze rond de 3 uur 'uitschakelen' en bij een baanperiode van 2 uur weer 'aan' gaan. Aan de hand van hoge snelheid waarnemingen en spectroscopie heb ik het systeem in detail bestudeerd om de vraag te beantwoorden of dit systeem een CV is die tijdelijk uitgeschakeld is. De conclusie is dat dit waarschijnlijk niet het geval is, en dat het systeem ongeveer geboren is zoals het nu waar te nemen is.

Het laatste hoofdstuk gaat over 'EL CVn' dubbelsterren. Dit zijn eclipserende proto- helium wittedwerg – A-ster systemen. Lichtkromme van EL CVn dubbelsterren vertonen een ondiepe eclips en zijn daarom moeilijk te vinden met traditionele methoden. Om dit naald-in-een-hooiberg probleem op te lossen heb ik 'machine learning' methoden toegepast om de PTF data te doorzoeken. Dit resulteerde in de ontdekking van 36 nieuwe systemen, waarmee het aantal bekende EL CVn systemen meer dan verdubbelde. Aan de hand van radiële snelheids metingen heb ik bevestigd dat het inderdaad om lage massa wittedwergen gaat. De conclusie is dat EL CVn systemen redelijk vaak voorkomen en een lange tijd over het hoofd gezien zijn. De gemeten stralen en temperaturen van de proto- helium wittedwergen en de baanperiodes van de systemen zijn in goede overeenkomst met theoretische modellen.

Curriculum vitæ

I was born on the second of April 1990 in Tilburg, where I attended primary school the 'Armhoefse Akker'. I have been very curious about how the world works from a young age. I liked reading children's books about science and also did some experimenting; I still remember building a small electromotor using copper wire and magnets.

I attended 'Cobbenhagen College' high school, where science and history were my favourite subjects. After briefly considering studying history, I instead chose to start a Bachelor's degree in physics with a minor in astronomy at Radboud University in Nijmegen. For my Bachelor research project, I worked with Prof. Gijs Nelemans to study spectra of a pulsating stripped core of a giant star.

After obtaining my Bachelor's degree in 2011, I continued my studies in Nijmegen. During my Master's in physics and astronomy, I enjoyed learning about a wide range of topics in astrophysics. Aside from the coursework at Radboud University, I visited the University of Amsterdam to learn about exoplanets, and attended a summer school about binary stars in Leuven (BE), and a summer school about astronomical instrumentation in Toronto (CA). My Master's research project involved the study of a short period eclipsing white dwarf–red dwarf binary, supervised by Prof. Paul Groot. For this project, we used the William Herschel Telescope on La Palma. Besides observing the eclipsing white dwarf–red dwarf binary system, we also observed two white dwarf stars orbiting each other every 12 minutes! This extraordinary system made me wonder about what other kinds of weird astrophysical objects can be found in the universe and motivated me to continue my career as an astronomer.

After obtaining my Master's degree in 2013 (*cum laude*), I began my PhD research at the Radboud University, under the supervision of Prof. Paul Groot. The goal of the research (presented in this thesis) was to explore the intranight variability of the night sky with the Palomar Transient Factory. By systematically searching the sky and following up any new transients, I determined how many new transients appear each night and of what nature they are. Besides working on transients I remained interested in binary stars and used PTF data to find and study them in more detail.

For my research, I observed with a number of different telescopes; the Isaac Newton Telescope and the William Herschel Telescope at La Palma, the Palomar Transient Factory and the Hale

Telescope (Palomar Mountain, USA), and with the Keck telescope (Hawaii, USA). I also worked on the installation of the MeerLICHT telescope at Sutherland observatory (SA). I presented parts of my work with posters or oral presentations at seminars and national and international conferences in Noordwijkerhout (NL), Villanova (USA), Boston (USA), Santa Barbara (USA), and Leuven (BE). Aside from research, I have been a teaching assistant for undergraduate courses including Introduction to Astronomy, Observational Astronomy, and Programming I. I was also the supervisor of two Bachelor students who did their research project at the astronomy department.

As of October 2018, I am a postdoctoral researcher at the California Institute of Technology in Pasadena (USA), where I am working on variable stars observed by the Zwicky Transient Facility.

List of publications

- **van Roestel, J.**; Groot, P. J.; Levitan, D.; Prince, T. A.; Bloemen, S.; Marsh, T. R.; Dhillon, V. S.; Shupe, D.; Laher, R.
  PTF1 J085713+331843, a new post-common-envelope binary in the orbital period gap of cataclysmic variables
  Monthly Notices of the Royal Astronomical Society, Volume 468, Issue 3, p.3109-3122, 2017

- **van Roestel, J.**; Kupfer, T.; Ruiz-Carmona, R.; Groot, P. J.; Prince, T. A.; Burdge, K.; Laher, R.; Shupe, D. L.; Bellm, E.
  Discovery of 36 eclipsing EL CVn binaries found by the Palomar Transient Factory
  Monthly Notices of the Royal Astronomical Society, Volume 475, Issue 2, p.2560-2590, 2017

- Green, M.J.; Marsh, T.R.; Steeghs, D.T.H.; Kupfer, T.; Ashley, R.P.; Bloemen, S.; Breedt, E.; Campbell, H.C.; Chakpor, A.; Copperwheat, C.M.; Dhillon, V.S.; Hallinan, G.; Hardy, L.K.; Hermes, J.J.; Kerry, P.; Littlefair, S. P.; Milburn, J.; Parsons, S. G.; Prasert, N.; **van Roestel, J.**; Sahman, D.I.; Singh, N.
  High-speed photometry of Gaia14aae: an eclipsing AM CVn that challenges formation models
  Monthly Notices of the Royal Astronomical Society, Volume 476, Issue 2, p.1663-1679, 2018

- Gieseke, F; Bloemen, S; van den Bogaard, C; Heskes, T; Kindler, J; Scalzo, R.A.; Ribeiro, V.A.R.M.; **van Roestel, J.**; Groot, P.J.; Yuan, F; Möller, A; Tucker, B.E.
  Convolutional neural networks for transient candidate vetting in large-scale surveys
  Monthly Notices of the Royal Astronomical Society, Volume 472, Issue 3, p.3101-3114, 2017

- Kupfer, T.; Ramsay, G.; **van Roestel, J.**; Brooks, J.; MacFarlane, S.A.; Toma, R.; Groot, P.J.; Woudt, P.A.; Bildsten, L.; Marsh, T.R.; Green, M.J.; Breedt, E.; Kilkenny, D.; Freudenthal, J.; Geier, S.; Heber, U.; Bagnulo, S.; Blagorodnova, N.; Buckley, D.A.H.; Dhillon, V.S.; Kulkarni, S.R.; Lunnan, R.; Prince, T.A.
  The OmegaWhite Survey for Short-period Variable Stars. V. Discovery of an Ultracompact

Hot Subdwarf Binary with a Compact Companion in a 44-minute Orbit
The Astrophysical Journal, Volume 851, Issue 1, article id. 28, 10 pp., 2017

- Macfarlane, S. A.; Woudt, P. A.; Dufour, P.; Ramsay, G.; Groot, P. J.; Toma, R.; Warner, B.; Paterson, K.; Kupfer, T.; **van Roestel, J.**; Berdnikov, L.; Dagne, T.; Hardy, F.
  The OmegaWhite Survey for short-period variable stars - IV. Discovery of the warm DQ white dwarf OW J175358.85-310728.9
  Monthly Notices of the Royal Astronomical Society, Volume 470, Issue 1, p.732-741, 2017

- Kupfer, T; **van Roestel, J.**; Brooks, J; Geier, S; Marsh, T.R.; Groot, P.J.; Bloemen, S; Prince, T.A.; Bellm, E; Heber, U; Bildsten, L; Miller, A.A.; Dyer, M.J.; Dhillon, V.S.; Green, M; Irawati, P.; Laher, R.; Littlefair, S.P.; Shupe, D.L.; Steidel, C.C.; Rattansoon, S.; Pettini, M
  PTF1 J082340.04+081936.5: A Hot Subdwarf B Star with a Low-mass White Dwarf Companion in an 87-minute Orbit
  The Astrophysical Journal, Volume 835, Issue 2, article id. 131, 8 pp., 2017

- Marsh, T. R.; Gänsicke, B. T.; Hümmerich, S.; Hambsch, F.-J.; Bernhard, K.; Lloyd, C.; Breedt, E.; Stanway, E. R.; Steeghs, D. T.; Parsons, S. G.; Toloza, O.; Schreiber, M. R.; Jonker, P. G.; **van Roestel, J.**; Kupfer, T.; Pala, A. F.; Dhillon, V. S.; Hardy, L. K.; Littlefair, S. P.; Aungwerojwit, A.; Arjyotha, S.; Koester, D.; Bochinski, J. J.; Haswell, C. A.; Frank, P.; Wheatley, P. J.
  A radio-pulsing white dwarf binary star
  Nature, Volume 537, Issue 7620, pp. 374-377, 2016

- Barentsen, Geert; Farnhill, H. J.; Drew, J. E.; González-Solares, E. A.; Greimel, R.; Irwin, M. J.; Miszalski, B.; Ruhland, C.; Groot, P.; Mampaso, A.; Sale, S. E.; Henden, A. A.; Aungwerojwit, A.; Barlow, M. J.; Carter, P. J.; Corradi, R. L. M.; Drake, J. J.; Eislöffel, J.; Fabregat, J.; Gänsicke, B. T.; Gentile Fusillo, N. P.; Greiss, S.; Hales, A. S.; Hodgkin, S.; Huckvale, L.; Irwin, J.; King, R.; Knigge, C.; Kupfer, T.; Lagadec, E.; Lennon, D. J.; Lewis, J. R.; Mohr-Smith, M.; Morris, R. A. H.; Naylor, T.; Parker, Q. A.; Phillipps, S.; Pyrzas, S.; Raddi, R.; Roelofs, G. H. A.; Rodríguez-Gil, P.; Sabin, L.; Scaringi, S.; Steeghs, D.; Suso, J.; Tata, R.; Unruh, Y. C.; **van Roestel, J.**; Viironen, K.; Vink, J. S.; Walton, N. A.; Wright, N. J.; Zijlstra, A. A.
  The second data release of the INT Photometric Hα Survey of the Northern Galactic Plane (IPHAS DR2)
  Monthly Notices of the Royal Astronomical Society, Volume 444, Issue 4, p.3230-3257, 2014

Acknowledgments

Writing a doctoral thesis is quite an undertaking. While it was sometimes solitary work, I could not have done it without help, advice, and support from colleagues, friends, and family.

First of all, I'd like to thank my supervisors. Paul, without your guidance, advice and encouragement this thesis would not be here. I'm very grateful for the opportunity to work with you and the freedom you've given me to also work on other projects besides my main PhD research. I am also very grateful for all the advice and support from Thomas. Thanks to Tom and Shri, who kindly hosted me at Caltech numerous times.

I also like to thank my colleagues; working at the astronomy department in Nijmegen can only be described as 'gezellig'. The many traditions; having lunch together, celebrating published papers with cake, the journal clubs, the Christmas dinner, informal coffee breaks, Friday-afternoon beers and other fun activities made it a joy to be a part of the astronomy department at the RU. I would especially like to thank my office mates; Roque, Bjarni, Jakub, Thomas B., Jamie, Rocco, Pim, Sweta, and Satyendra for advice, support and the fun discussion we had about many random topics. I wish to thank all my fellow scientists, both at the Radboud University and elsewhere, who share my passion for astronomy. I always enjoyed talking with you about exciting ideas, new results, and the latest astrophysics news.

I would also like to thank old friends; Philip, Boris, en Lukas, thanks for the relaxing evenings with beer, pizza, and games of Munchkin. Gijs, Tijs, and Lars for showing me how board games should be played. Annelot, Rosa, and Valerio for our infrequent but very enjoyable gatherings. Lars, thank you for the interactive history lessons about the 20th century.

Zonder de steun en aanmoediging van mijn familie zou deze thesis er niet zijn. Gerard en Gijs; dank voor de adolescente humor, af en toe een 'druppeltje', en het samen onveilig maken van het nachtleven van Tilburg. Mama en papa, bedankt dat jullie me altijd gesteund en aangemoedigd hebben, en me het zelfvertrouwen hebben gegeven om aan deze onderneming te beginnen. Tijdens het wandelen in het bos en het spelen van bordspelletjes kwam ik echt tot rust (behalve bij Mr. X). Pa, ik vind het altijd heel leuk als je me vraagt of het sterrenkunde nieuws dat je in de krant of op internet leest wel waar is (meestal niet). Ma, ik vind het erg lief dat altijd zo betrokken bent bij wat ik doe. Je bent m'n grootste fan.

Dieke, dankje dat je er altijd voor me bent. Je bent een enorme steun voor me geweest tijdens het maken van deze thesis, het is eigenlijk niet te beschrijven. Vanaf onze eerste date herinner je me eraan om ook van het leven te genieten. Dat we nog vaak samen wandelen door het bos, bier drinken in de zon, exotische gerechten koken, duiken, bakken, bordspelletjes spelen, ...
Dieke, je bent de beste.